An ACI Technical Publication

SYMPOSIUM VOLUME

A Vision for the Future of Corrosion Resistant Structures—A Special Session Honoring Professor Carolyn Hansson

SP-366

Editors: O. Burkan Isgor, David Tepke, Ceki Halmen, and Neal Berke

American Concrete Institute
Always advancing

A Vision for the Future of Corrosion Resistant Structures—A Special Session Honoring Professor Carolyn Hansson

Sponsored by
ACI Committee 222

ACI Concrete Convention
March 30 – April 2, 2025
Toronto, ON

Editors:
O. Burkan Isgor, David Tepke, Ceki Halmen, and Neal Berke

American Concrete Institute
Always advancing

SP-366

First printing, October 2025

Printed in the United States of America

Editorial production: Gail Tatum

ISBN-13: 978-1-64195-334-4

A Vision for the Future of Corrosion Resistant Structures—A Special Session Honoring Professor Carolyn Hansson

Professor Carolyn Hansson's remarkable journey began in England, during the turbulence of the Second World War. Despite the hardships of wartime and the limitations imposed by rationing, Carolyn was raised in a nurturing environment by parents who instilled in her a deep respect for learning and perseverance. These values would guide her through an exceptional academic and professional life.

As the sole woman at the Royal School of Mines, Carolyn studied metallurgy at Imperial College, where she later earned her PhD, focusing on superconductivity and crystal structures at liquid helium temperatures. Her postdoctoral path led her from industrial research at Martin Marietta Laboratories to academic positions at Columbia University and the State University of New York at Stony Brook, and later to Bell Laboratories in 1976.

Her pivotal shift into corrosion science began in 1980 at the Danish Corrosion Centre, where she worked on a new type of cement and corrosion of steel in concrete. From Denmark to Canada, Professor Hansson continued her research at Queen's University and later at the University of Waterloo, building an enduring legacy in the field of steel corrosion in concrete structures.

Over the decades, Carolyn's contributions to corrosion research have shaped and guided generations of engineers and scientists. Her pioneering studies—on electrical resistivity of concrete, quantifying reinforcement corrosion rates, and understanding the complex role of chlorides—remain foundational in the field. Her investigations into corrosion inhibitors, electrochemical chloride extraction, effects of concrete cracking on reinforcement corrosion, and corrosion-resistant steels continue to influence global practices in infrastructure resilience.

This Special Publication celebrates more than 60 years of Professor Hansson's contributions as a scientist, educator, and mentor. The papers collected here, presented at the 2025 Spring Convention in Toronto, reflect not only the lasting relevance of her work but also its future promise. Her vision stands as both a mirror to the past and a beacon for innovations yet to come in corrosion-resistant construction.

O. Burkan Isgor
David Tepke
Ceki Halmen
Neal Berke

TABLE OF CONTENTS

Remarks on the Last Sixty Years of Advancement in Corrosion of Metals in Concrete during Carolyn Hansson's 60 Year Career

David G. Tepke and O. Burkan Isgor

Synopsis: A review of corrosion literature on corrosion of steel in concrete clearly shows that Carolyn Hansson's work and vision mirrors the exponentially increasing interest on the subject since 1980s. During the time Dr. Hansson has been contributing to the scientific community, significant advancements have occurred in understanding and controlling corrosion of metals in concrete. This paper discusses some of the key advancements over the last six decades as Dr. Hansson was making her mark on the industry. The recognition of the role of corrosive environments, development and roles of committees in providing forums for experts, service-life modeling, electrochemical control, and other topics are discussed. Finally, a perspective on where the industry may be going in the future years is offered.

Keywords: reinforcement corrosion, chloride, chloride threshold, chloride binding, carbonation, inhibitor, cathodic protection, electrochemical chloride extraction

David G. Tepke, FACI, is a Principal Engineer with SKA Consulting Engineers, Inc., in Charleston, SC, USA. He specializes in structural and materials evaluation, troubleshooting, repair, and service-life extension. He is a NACE/AMPP Certified Corrosion Specialist and Protective Coating Specialist. Tepke is the Chair of ACI Committee 222, Corrosion of Metals in Concrete, and a member of ACI Committees 201, Durability of Concrete; 301, Specifications for Concrete Construction; 321, Durability Code; and 329, Performance Criteria for Ready Mixed Concrete. He is a licensed professional engineer.

O. Burkan Isgor, FACI, is the Eric H.I. and Janice Hoffman Professor in Civil and Construction Engineering at Oregon State University, Corvallis, OR, USA. He is a past Chair of ACI Committee 222, Corrosion of Metals in Concrete, and a member of ACI Committees 236, Material Science of Concrete; and 365, Service Life Prediction. His research interests include corrosion of steel in concrete, service-life modeling, and reactive-transport modeling of cementitious systems. He is also a Fellow of the Canadian Society for Civil Engineering

INTRODUCTION

While reinforcing steel corrosion in concrete has been known as a deterioration mechanism for more than a century and a topic of scientific importance for more than 80 years, it has become a more specialized topic of investigation over the last six decades, and a major field of research over the last four decades. After C.L. Page's 1975 paper in *Nature* on the mechanism of corrosion protection in reinforced concrete marine structures (1), and his subsequent article with K.W.J. Treadaway in 1982 on aspects of the electrochemistry of steel in concrete (2), scientific progress on the subject exponentially increased over the following decades, as shown in Figure 1.

Caroyn Hansson's involvement in research on steel corrosion in concrete started in 1980, around the same time as the publication of Page's papers in *Nature*, when she joined the Danish Corrosion Centre, initially as a research scientist and later as the head of the research department. During her time there, she led a project on a new type of cement, marking her first venture into the field of corrosion of steel in concrete. Later, she moved to Canada to join the faculty of Queens University, followed by many years at the University of Waterloo, where she continued her research on the subject.

A close study of corrosion literature clearly shows that Carolyn Hansson's work and vision on corrosion of steel in concrete mirrors the exponentially increasing interest on the subject since 1980s. Soon after her first involvement in research on corrosion of steel in concrete, Carolyn started publishing on some of the most critical subjects on reinforcement corrosion that are still guiding experts to this day. For example, Carolyn was one of the first experts who recognized the importance of electrical resistivity of concrete. In her 1983 paper (3) she discussed how electrical resistivity is affected by not only the water-to-cement ratio but also the chemical composition of the cementitious system while providing a measurement approach to quantify it. In this front, Carolyn was ahead of her time considering that the concept of electrical resistivity of concrete, decades later, became one of the most important durability performance indicators. In her 1984 article on the electrochemical measurements of the rate of corrosion of steel in concrete (4), she meticulously tied the thermodynamics and kinetics of corrosion and demonstrated the methods and their challenges to quantify corrosion rate of steel in concrete.

Carolyn was also one of the first researchers who systematically studied the role of chlorides on steel corrosion in concrete, highlighting the importance of the role of chloride cation type (5), chloride transport and binding (6), and steel surface finish (7) on corrosion initiation and propagation, providing a framework for the necessary research for many decades to come. Starting from the 1990s, her collaborations with prominent researchers like former ACI 222 chair, Dr. Brian Hope, resulted in highly impactful works on corrosion inhibitors (8, 9), electrochemical chloride extraction (10, 11), and the quantification of critical chloride threshold (12). Her impactful work continued until her retirement in 2022, particularly on the role of concrete cracking on steel corrosion (13, 14), and corrosion-resistant steels (15-19).

It is easy to see that there are not many aspects of steel corrosion in concrete that remained unexamined by Carolyn and her collaborators. This paper discusses some of the key advancements over the last six decades as Dr. Hansson was making her mark on the industry. Although the paper is not intended to provide a comprehensive literature review on the subject, in the following, we provide a non-exhaustive summary of research milestones, ACI 222 advancements and contributions to codes, practice-related advancements and code provisions, and a look ahead for future research.

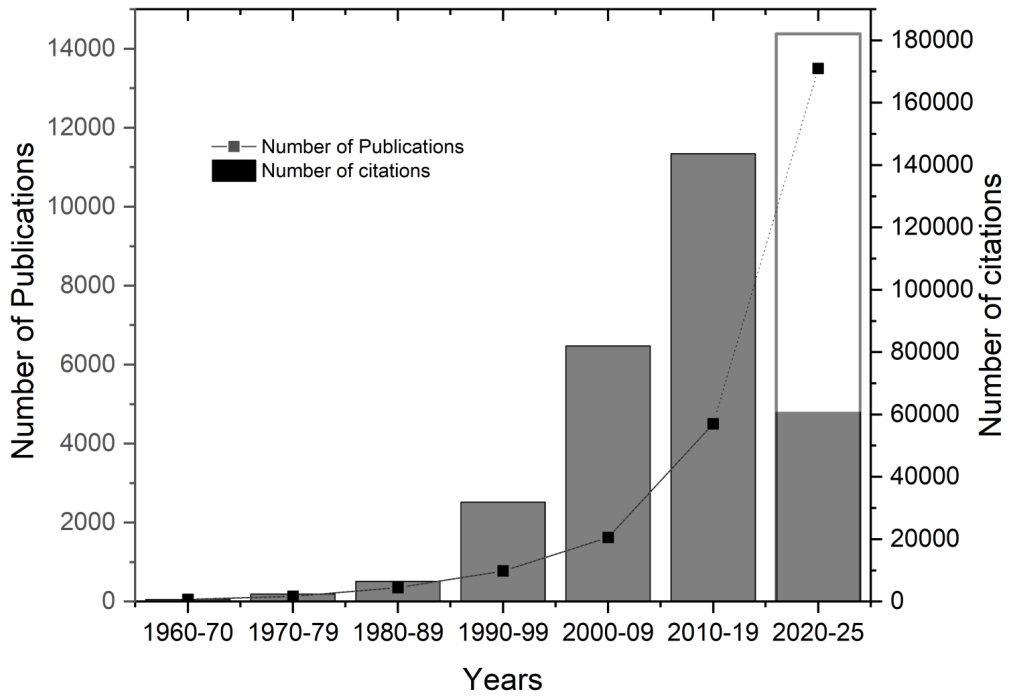

Figure 1: The number of publications and citations on the corrosion of steel in concrete in the last six decades. The data were obtained from Web of Knowledge for the following title search criterion: (("cathodic protection" or "chloride" or "carbonation") or ("electrochemical" or "electrochemistry" or "corrosion" or "passivation" or "passivity" or "passive")) and ("cement" or "cementitious" or "concrete" or "paste" or "mortar" or "pore solution" or "rebar" or "reinforcement" or "reinforcing steel" or "reinforcing bar"). The data in 2020-25 present projected number of papers and citations.

RESEARCH ADVANCEMENTS

Thompson et al. (20) reported on the potential for reinforcing steel corrosion in porous concrete in 1909 and Davis (21) described the formation of rust stains and concrete breaking at undersides of concrete in marine exposures in 1910. In 1950, Friedland (22) reported the well-known mechanism (to the author at the time) of spalling from corrosion of reinforcing. Pletta et al. (23) reported review of many references in the 40 years preceding their 1950 paper on corrosion of reinforcing steel in concrete, but with none on evaluating corrosion rates. Cathodic protection was being used on reinforced concrete by the 1950's (Broomfield (24); ICRI Committee 510 (25); Vrable (26); Stratfull (27). Mozer et al.(28) reported on rapid advancement of knowledge on corrosion of reinforcing steel between the 1940's and 1960's, and ACI Committee 201 (29) provided an in-depth review on reinforcing steel corrosion in its first committee report published in 1962. Broomfield (30) and Bohni (31) describe an increase in the awareness of chloride contribution to reinforcing steel corrosion in the 1950's and Broomfield (30) described an increase in overall awareness and research to study corrosion starting around the 1960's.

Over the past 60 years, significant progress has been made toward developing fundamental understanding and mitigation strategies for reinforcement corrosion in concrete structures. Electrochemical techniques have been extensively used to study passivity and chloride- and/or carbonation- induced depassivation of carbon steel in concrete pore (32) – the size of this literature is so large that it would be unpractical to list a comprehensive list of references here. These electrochemical studies have provided macro-scale observations of the nature of the passive films and have also demonstrated the large variability of chloride thresholds to depassivate carbon steel in concrete (33, 34). This large variability in chloride thresholds is the result of a number of factors including the chemistry of the concrete pore solution (35-37), rebar surface conditions (7, 38, 39), and properties of the rebar-concrete interface (40-42). The literature review by Hong et al. (43) provides a comprehensive review of the methods for characterising the steel–concrete interface to enhance understanding of reinforcement corrosion. Nanoscale surface characterization techniques such as FIB/TEM (44), electron energy loss spectroscopy (EELS) (45) and X-ray photoelectron spectroscopy (XPS) (46, 47) have helped develop fundamental understanding of passivity and chloride-induced depassivation of steel in alkaline environments.

Advancements in analytical and computational methods also provided additional opportunities for exploring corrosion of steel in various scales (48-50). For example, high-resolution chemical imaging techniques including X-ray computed tomography (XCT) and X-ray absorption spectroscopy (XAS) allow for detailed observations of the presence of water in micropores of cementitious materials (51) and the morphology and composition of corrosion products at the metal-electrolyte interface (52, 53). Other ex-situ and in-situ studies conducted by several researchers, the type of corrosion product that forms in concrete depends on the chemistry of the concrete pore solution (which is related to the binder type and mixture design properties), water availability, dissolved oxygen concertation, chloride-to-hydroxide ratio (Cl/OH), reinforcement type, and corrosion rate (13, 54-58).

Recent decades have witnessed an exponential increase in computational resources and power. This progress made it feasible to use atomistic/molecular scale modeling techniques (e.g., Density functional theory, DFT (59-64), and reactive-force field molecular dynamics, Reax-FF MD (65-68), to computationally study processes in the atomistic/molecular scale that are difficult, and in some cases impossible, to investigate using conventional experimental methods. One area that has seen progress using these techniques is the development of fundamental understanding on the passivity and chloride-induced depassivation processes of iron or carbon steel in highly alkaline environments (such as concrete). In addition to the atomistic/molecular scale modeling techniques, thermodynamic modeling has also become as powerful tool for advancing our understanding of the chemistry of cementititous systems (69, 70) and their interaction with embedded steel reinforcement (71-73). Coupled with transport solvers (74, 75), they can further compute the spatial distribution of dissolved species such as chlorides, carbonates and sulfates, which allow more accurate corrosion modeling and better service life predictions. In general, significant progress have been made on transport modeling in concrete (76) and corrosion propagation modeling of steel (77, 78).

The research advancements related to reinforcement corrosion definitely go beyond these. Over the past six plus decades, we have developed a strong understanding on several other fields such as corrosion mitigation techniques including electrochemical chloride extraction (79), cathodic protection (80), and re-alkalization (81); corrosion resistant reinforcement (82); and corrosion measurement techniques (82). ACI 222 committee, among other committees in RILEM, AMPP (formerly NACE), and ECS have also made major contributions. In the following section some of the ACI 222 advancements and contributions are summarized.

ACI 222 ADVANCEMENTS AND CONTRIBUTIONS TO CODES

ACI Committee 222 was formed in 1963. The first committee report was published in 1985. Documents developed by ACI Committee 222 include:

- 222R (Committee Report: Corrosion of Metals in Concrete, and then Guide to Protection of Metals in Concrete Against Corrosion)
    - Published 1985
    - Revised in 1996, 2001 (reapproved in 2010), and 2019.
- 222.1 (Provisional Standard Test Method for Water-Soluble Chloride Available for Corrosion of Embedded Steel in Mortar)
    - Published 1996
    - Withdrawn
- 222.2 (Corrosion of Prestressing Steels)
    - Published 2001
    - Revised 2014
- 222.3 (Guide to Design and Construction Practices to Mitigate Corrosion of Reinforcement in Concrete Structures)
    - Published 2011

Though the first committee report was published in 1985, the early documented committee involvement was in the form of recommendations for other committees.

ACI 318-71 (83), the first version of ACI 318 subsequent to the 1963 version of 318 and formation of Committee 222, included the following new provision for permissible chloride contents in concrete.

> *"3.4 Water…the mixing water for prestressed concrete or for concrete which will contain aluminum embedments, including that portion of the mixing water contributed in the form of free moisture on the aggregates, shall not contain deleterious amounts of chloride ion."*

The commentary in ACI 318-71 provided the following context and information from Committee 222.

3.4-Water

> *3.4.1s- A new provision has been added concerning chloride ion content of water (including that portion of the mixing water contributed as free moisture on the aggregates) to be used in prestressed concrete or in concrete with aluminum embedment. No numerical quantities are stipulated. It is suggested that a chloride ion content greater than 400 or 500 ppm might be considered dangerous and ACI Committee 222, Corrosion of Metals in Concrete, recommends that levels well below these values be maintained, if practicable.*

ACI 201.2, "Guide to Durable Concrete", published in 1977 (84), was essentially an update of the 1962 committee report, "Durability of Concrete in Service" (29). The guide indicated that the topic of corrosion was under in-depth study by Committee 222, and that the following chloride limits (expressed as percent by weight of cement) were recommended based on agreement with Committee 222:

- Prestressed concrete:
  - 0.06 percent
- Conventionally reinforced concrete in a moist environment and exposed to chlorides:
  - 0.1 percent
- Conventionally reinforced concrete in a moist environment but not exposed to chloride (includes locations where the concrete will be occasionally wetted – such as kitchens, parking garages, waterfront structures, and areas with potential moisture condensation):
  - 0.15 percent
- Above ground building construction where the concrete will stay dry:
  - no limit

ACI 318-83 (85) was the first version to include specific limits on chloride content for corrosion protection. Maximum water-soluble chloride ion (Cl^-) contents in concrete (percent by weight of cement) were 0.06, 0.15, 1.00 and 0.30 for prestressed concrete, reinforced concrete exposed to chloride in service, reinforced concrete that will be dry or protected from moisture in service, and other reinforced concrete construction, respectively. The commentary in ACI 318-83 included context regarding the input from ACI Committees 201 and 222:

> *"The chloride ion limits in Table 4.5.4 differ from those recommended in ACI 201. For reinforced concrete that will be dry in service, a limit of one percent has been included to control total soluble chlorides. Table 4.5.4 includes limits of 0.15 and 0.30 percent for reinforced concrete that will be exposed to chlorides or will be damp in service, respectively. These limits compare to 0.10 and 0.15 recommended in ACI 201. The more liberal limits were developed after consultation with Committees 201 on durability and 222 on corrosion, and are considered to represent the best information available at the time of adoption."*

This suggested that the limits reported by Committee 201 in agreement with Committee 222 were reconsidered. The first Committee 222 Report (86), published in 1985, acknowledged published recommended values by Committee 201 and in ACI 318; but recommended more conservative acid-soluble chloride limits expressed as a percent by weight of cement) of 0.08 percent for prestressed concrete and 0.20 percent for reinforced concrete. Limits in ACI 318 essentially have remained similar through today, except for changes in structuring classification and descriptions, and the modification to use of total cementitious materials as the basis for percentages in the 2019 version of ACI 318 based on recommendations from Committee 222.

The amount of allowable admixed chlorides, chloride thresholds and associated testing parameters have been the subject of research and debate since the formation of Committee 222. The 1996 version of ACI 222R (87)included revised recommended chloride limits based on acid-soluble and water-soluble testing and additionally included subcategories of wet and dry conditions with the previous prestressed condition. Isgor et al. (88) provides a discussion on more recent advancements and initiatives over the past decade that have included support for development of a

chloride threshold test, amendment of recommended chloride limits for new construction, and development of a subcommittee for evaluating exposures, limits and thresholds and producing a stand-alone guide document. Committee 222 Task Group 1 was formed in 2017 to support ACI Foundation funded research on the development of a standard critical chloride threshold test method and follow up Foundation research on the effect of material sources (89-92). The 2019 version of ACI 222R (93) revised chloride limits and additionally recommended rendering them in relation to total cementitious materials contents, with restrictions. Revisions for 222.3 and 222.2, and a new document reporting the findings of the new subcommittee focusing on chloride limits, thresholds and exposures, are underway at the time of this writing.

PRACTICE-RELATED ADVANCEMENTS AND CODE PROVISIONS

These references demonstrate the known condition of reinforcing steel corrosion dating back to the early 1900's or before, with a significant increase in awareness starting around the 1950's or 1960's as documents were being developed, committees formed, code provisions implemented, control being implemented, and research efforts increased. Indeed, the beginning of commercial use of calcium chloride admixtures in the US in the 1920's, development of a deicing salt use policy in 1941 by the New Hampshire Department of Transportation(94), increased used of deicing salts by US Transportation Departments in the 1950's, 1960's and 1970's, and the Federal Highway Act of 1956 leading to the construction of the interstate highway system all likely contributed considerably to the increase in awareness, perceived severity, and more intense study of corrosion-related issues.

Although the word, "corrosion" first appeared in the ACI standard building code (ACI 501-36) (95)in 1936 for protection of portions of exposed bars during construction, it wasn't until the 1963 version of ACI 318 (96)that corrosion protection of unbonded prestressing steel and assemblies, as well as increased cover over conventional reinforcing steel in "extremely corrosive atmospheres' were required, and the 1983 version of ACI 318 that chloride limits were provided.

Tepke (97)provided a summary of industry knowledge development and ACI industry standard code adoption of corrosion-related provisions (the above being a clarification and expansion on the timeline of the general awareness of issues that, perhaps, trivialized the early understanding). Tepke and Mandry-Campbell (98) provided a summary of industry knowledge development for corrosion control measures of existing concrete. Some technological developments and code integrations of the 20th century include:

- 1910 or before: corrosion of reinforcing steel in concrete known.
- 1928: Galvanized reinforcing steel specification(99)
- 1937: Stainless-steel reinforcing used in north America (29)
- 1950's: Cathodic protection of steel being used in existing reinforced concrete (24-26, 100)
- 1963: First ACI 318 Code preclusion of use of calcium chloride admixtures in prestressed concrete or post-tensioned grout (96)
- 1960's: Consideration of FRP reinforcing steel bars for concrete (101)
- 1970's: Epoxy-coated reinforcing steel bars evaluated and introduced
- Late 1970's: Corrosion inhibiting admixtures commercially available (102) (103)
- 1983: Chloride limits first included in ACI 318-83 (85)
- 1983: Galvanized and epoxy-coated reinforcing steel included in ACI 318-83 (85)
- 1989, 1999: Additional corrosion protection requirements for post-tensioned steel in ACI 318-89 (104) and ACI 318-99 (105).
- 2008: Stainless steel reinforcing steel included in ACI 318-2008 (106).
- 2014: First direct reference to corrosion-inhibiting admixtures in ACI 318-14 (107).

A LOOK AHEAD

Those who have worked closely with Carolyn Hansson would know that she has expressed her opinions about the concept of critical chloride threshold in several venues. The seeds of one of her most recent works on this subject were planted in a Gordon Research Conference (GRC) that took place in Ventura, California, in early 2020. Just before the entire world shut down because of the Covid-19 epidemic. The GRC meeting was mainly on cementitious materials, and there were few experts on reinforcement corrosion in attendance. During a session break, these experts came together in the sunny garden of the hotel where the meeting was taking place, and naturally, started talking about their

mixed feelings and opinions about the concept of critical chloride threshold. Figure 2 presents a photo of that exact gathering and shows Dr. Hansson with Dr. Ueli Angst, Dr. Mette Geiker, Dr. Burkan Isgor, and Dr. Alberto Sagues (the Ventura Team). The theme of the discussion was simple – everybody knew and agreed that the theoretical concept of critical chloride content was real, but there was also the question of its usefulness in predictive models of steel corrosion in concrete. Was it time to reconsider how we develop predictive models for chloride-induced steel corrosion in concrete? After a fruitful discussion, the group decided to work on a paper to express this opinion to provide guidance, and perhaps a framework, for future researchers. The decision led to two years of additional discussions, online and in-person meetings, and dozens of drafts of a paper, titled "Beyond the chloride threshold concept for predicting corrosion of steel in concrete," which was published in 2022 (34).

Figure 2: The Ventura Team - Gathering of experts on corrosion of steel in concrete in Ventura, California (2020). From left to right: Carolyn Hansson, Mette Geiker, Alberto Sagues, Burkan Isgor, and Ueli Angst.

One of the last questions the Ventura Team inquired was "is it time to abandon the concept of a CT with its associated, sharply defined, separation between initiation and propagation stages when developing predictive service life models?" The answer to that question is not straightforward. Tuutti's seminal work proposed the idea of the two-stage corrosion damage model in 1980 (108). In this definition, the initiation stage describes the period during which the chlorides penetrate concrete, and the subsequent propagation stage is when reinforcing steel corrosion initiates. The two stages are separated by a distinct point defined by the time chlorides at the steel surface level exceed the critical chloride threshold. As discussed in their paper, the Ventura Team presented that the transition from a passive state to active chloride-induced corrosion is a complex process, and not an instantaneous and uniform event across the large rebar surface. In fact, the breakdown of passivity occurs over an extended period and at different times for different locations, and de-passivated surfaces could passivate later depending on the chemical conditions and moisture/temperature state of concrete around the steel. Considering the challenges associated with the variability and predictability of critical chloride threshold (33, 34), they provided an alternative framework for predictive service life models for chloride-induced corrosion in concrete. In this approach, the focus is placed on the prediction of the steel corrosion rate starting from the day steel is placed in concrete. Steel experiences fluctuations in corrosion rate over time and space because of the changes in the environmental conditions and local chemical and microstructural variations at the steel-concrete interface (40-42). Therefore, once corrosion rates can be predicted at different locations on the steel surface over time, there would be no need for the two-stage corrosion damage model and the concept of a CT with its associated, sharply defined, separation between two stages. This new vision, of course, would require a sharp shift research focus to develop ways to predict and measure corrosion rate of reinforcing steel in concrete.

Unfortunately, the progress on on-site corrosion rate measurement techniques has been rather slow. The challenge associated with the determination of polarized area on the reinforcement is still an issue, particularly for large structures with highly dense and electrically connected reinforcement detailing (4, 109-114). The traditional current confinement techniques using guard ring methods have limitations for such structures; therefore, new research is definitely needed. The use of AC techniques has been suggested for addressing some of the issues; however, these laboratory-based electrochemical methods can be difficult to adapt in the field. Recent advances in model-assisted corrosion rate monitoring approaches (115) and using connectionless setups (that do not require an electrical connection to rebar) to produce alternative current (AC) pulses and analyzing the response through equivalent circuit modeling (116) have significant potential to overcome practical challenges while providing accurate predictions of corrosion rates. However, additional work is still needed. RILEM has recently established the Technical Committee ECS on the assessment of electrochemical methods to study corrosion of steel in concrete. Although TC ECS is mainly focused on the latest advances of electrochemical techniques for scientific studies, it is expected that practical outcomes will also be produced to make advances in on-site measurements.

Current trends toward reducing the cement/clinker content in concrete also brought a challenge with respect to reinforcement corrosion. These systems typically have a low pH buffer capacity due to reduced or eliminated calcium hydroxide in the hardened concrete. Cementitious reactions or pH-reducing reactions such carbonation in these systems can result in pore solution chemistries that can destabilize passivity of steel and increase corrosion rates. Furthermore, the ability of these low-clinker mixtures to bind aggressive species such as chlorides could be considerably different from the conventional ordinary Portland cement concrete. Physical binding of anions and cations from the pore solution by the hardened cementitious phases of these low-clinker mixtures could cause unforeseen pH, Cl^-/OH^- ratio, alkali content, and electrical resistivity. In the future, thermodynamic modeling, particularly when coupled with transport models, is expected to play a significant role in the low-carbon vision of the concrete industry which promotes the use of low-clinker binders with high limestone replacement, extensive use of traditional and alternative supplementary cementitious materials, and non-clinker based alternative cements or alkali activated binders (117-119).

Tepke and Mandy-Campbell (98) expand upon safety, sustainability and technology considerations that may impact corrosion control of existing structures in the near future. Some practice-related opportunities with respect to corrosion of reinforcing steel in concrete in new and existing structures may include the following.

- Integration of new technologies and approaches for measuring corrosion, improving corrosion performance and assessing new and existing concrete structures.
- Integration of durability provisions into projects, such as being developed by ACI Committees 201, 222 and 321 (Durability Code).
- Integration of machine learning and artificial intelligence with field data for analyzing and predicting corrosion performance
- More comprehensive integration of service-life modeling for better quantifying environmental impacts as part of sustainability initiatives.

CONCLUSION

Carolyn Hansson's work and vision on corrosion of steel in concrete mirrors the exponentially increasing interest on the subject since 1980s. During the time Dr. Hansson has been contributing to the scientific community, significant advancements have occurred in understanding and controlling corrosion of metals in concrete. Over the past six plus decades, a strong understanding was developed steel passivity and passive film breakdown; corrosion mitigation techniques including electrochemical chloride extraction, cathodic protection, and re-alkalization; corrosion resistant reinforcement; and corrosion measurement techniques. ACI 222 committee, among other committees in RILEM, AMPP (formerly NACE), and ECS have also made major contributions. Inconclusion, current trends in research and practice are discussed. This involved the need to improve corrosion rate measurement and modeling techniques and corrosion related challenges associated with reducing the cement/clinker content in concrete.

REFERENCES

1. Page CL, "Mechanism of Corrosion Protection in Reinforced-Concrete Marine Structures," Nature, V. 258, No. 5535. 1975, pp. 514-5.
2. Page CL, Treadaway KWJ, "Aspects of the Electrochemistry of Steel in Concrete," Nature, V. 297, No. 5862. 1982, pp. 109-15.
3. Hansson ILH, Hansson CM, "Electrical-Resistivity Measurements of Portland-Cement Based Materials," Cement and Concrete Research, V. 13, No. 5. 1983, pp. 675-83.
4. Hansson CM, "Comments on Electrochemical Measurements of the Rate of Corrosion of Steel in Concrete," Cement Concrete Res, V. 14, No. 4. 1984, pp. 574-84.
5. Hansson CM, Frolund T, Markussen JB, "The Effect of Chloride Cation Type on the Corrosion of Steel in Concrete by Chloride Salts," Cement and Concrete Research, V. 15, No. 1. 1985, pp. 65-73.
6. Byfors K, Hansson CM, Tritthart J, "Pore Solution Expression as a Method to Determine the Influence of Mineral Additives on Chloride Binding," Cement and Concrete Research, V. 16, No. 5, Sep. 1986, pp. 760-70.
7. Mammoliti LT, Brown LC, Hansson CM, Hope BB, "The influence of surface finish of reinforcing steel and pH of the test solution on the chloride threshold concentration for corrosion initiation in synthetic pore solutions," Cement and Concrete Research, V. 26, No. 4, Apr. 1996, pp. 545-50.
8. Trépanier SM, Hope BB, Hansson CM, "Corrosion inhibitors in concrete -: Part III.: Effect on time to chloride-induced corrosion initiation and subsequent corrosion rates of steel in mortar," Cement and Concrete Research, V. 31, No. 5, May. 2001, pp. 713-8.
9. Mammoliti L, Hansson CM, Hope BB, "Corrosion inhibitors in concrete - Part II: Effect on chloride threshold values for corrosion of steel in synthetic pore solutions," Cement and Concrete Research, V. 29, No. 10, Oct. 1999, pp. 1583-9.
10. Marcotte TD, Hansson CM, Hope BB, "The effect of the electrochemical chloride extraction treatment on steel-reinforced mortar - Part II: Microstructural characterization," Cement and Concrete Research, V. 29, No. 10, Oct. 1999, pp. 1561-8.
11. Marcotte TD, Hansson CM, Hope BB, "The effect of the electrochemical chloride extraction treatment on steel-reinforced mortar - Part I: Electrochemical measurements," Cement and Concrete Research, V. 29, No. 10, Oct. 1999, pp. 1555-60.
12. Hansson CM, Sorensen B, "The threshold concentration of chloride in concrete for the initiation of reinforcement corrosion," Book The threshold concentration of chloride in concrete for the initiation of reinforcement corrosion, Editor, ed.^eds., City, 1990, pp. 3-16.
13. Jaffer SJ, Hansson CM, "Chloride-induced corrosion products of steel in cracked-concrete subjected to different loading conditions," Cement and Concrete Research, V. 39, No. 2, Feb. 2009, pp. 116-25.
14. Jaffer SJ, Hansson CM, "The influence of cracks on chloride-induced corrosion of steel in ordinary Portland cement and high performance concretes subjected to different loading conditions," Corros Sci, V. 50, No. 12, Dec. 2008, pp. 3343-55.
15. Ogunsanya IG, Hansson CM, "The Influence of Coating Thickness and Composition on the Corrosion Propagation Rates of Galvanized Rebar in Cracked Concrete," Corrosion, V. 74, No. 1, Jan. 2018, pp. 134-43.
16. Ogunsanya IG, Strong V, Hansson CM, "Corrosion behavior of austenitic 304L and 316LN stainless steel clad reinforcing bars in cracked concrete," Materials and Corrosion-Werkstoffe Und Korrosion, V. 71, No. 7, Jul. 2020, pp. 1066-80.
17. Ogunsanya IG, Hansson CM, "The Critical Chloride Concentration of Austenitic and Duplex Stainless Steel Reinforcing Bars," Metallurgical and Materials Transactions a-Physical Metallurgy and Materials Science, V. 51, No. 9, Sep. 2020, pp. 4685-94.
18. Van Niejenhuis CB, Walbridge S, Hansson CM, "The performance of austenitic and duplex stainless steels in cracked concrete exposed to concentrated chloride brine," J Mater Sci, V. 51, No. 1, Jan. 2016, pp. 362-74.
19. Islam MA, Bergsma BP, Hansson CM, "Chloride-Induced Corrosion Behavior of Stainless Steel and Carbon Steel Reinforcing Bars in Sound and Cracked Concrete," Corrosion, V. 69, No. 3, Mar. 2013, pp. 303-12.
20. Thompson SE, "Report of Committee on Reinforced Concrete," ACI Journal Proceedings, V. 5. 1909, pp. 21 pp.
21. Davis C, "Concrete for Maritime Structures," ACI Journal Proceedings, V. 6, No. 2. 1910, pp. 120-57.
22. Friedland R, "Influence of the Quality of Mortar and Concrete upon Corrosion of Reinforcement (Title 47-8)," Journal of the American Concrete Institute, V. 22, No. 2. 1950, pp. 125-39.
23. Pletta DH, Massie, E.F., and Robins, H.S., "Corrosion Protection of Thin Precast Concrete Sections (Title 46-33)," J Am Concrete I, V. 21, No. 1. 1950, pp. 513-.

24. Broomfield JP, "A Historical Review of Impressed Current Cathodic Protection of Steel in Concrete," Construction Materials, V. 1, No. 1. 2020, pp. 1-21.
25. ICRI-Committee-510, "ICRI Guideline 510.1: Guide for Electrochemical Techniques to Mitigate the Corrosion of Steel for Reinforced Concrete Structures," Book ICRI Guideline 510.1: Guide for Electrochemical Techniques to Mitigate the Corrosion of Steel for Reinforced Concrete Structures, Editor, ed.^eds., International Concrete Repair Institute, City, 2013, pp. 26 pp.
26. Vrable JB, "Cathodic Protection for Reinforced Concrete Bridge Decks: Laboratory Phase," Book Cathodic Protection for Reinforced Concrete Bridge Decks: Laboratory Phase, Editor, ed.^eds., Transportation Research Board, City, 1977, pp. 145 pp.
27. Stratfull RF, "Experimental Cathodic Protection of a Bridge Deck," Book Experimental Cathodic Protection of a Bridge Deck, Editor, ed.^eds., City, 1974, pp. 15 pp.
28. Mozer JD, Bianchini, Albert C., and Kesler, Clyde E. (1965), , "Corrosion of Reinforcing Bars in Concrete (Title 62-54)," J Am Concrete I, V. 62, No. 8. 1965, pp. 909-30.
29. ACI-201-Committee, "Durability of Concrete in Service," J Am Concrete I, V. 59, No. 57. 1962, pp. 30 pp.
30. J.P. B, "Corrosion of steel in concrete: understanding investication and repair," Book Corrosion of steel in concrete: understanding investication and repair, Editor, ed.^eds., CRC Press, City, 1997, pp. 1-29.
31. Bohni H, "Corrosion in Concrete Structures ". New York: CRC Press; 2005.
32. Polder R, Andrade C, Elsener B, Vennesland O, Gulikers J, Weidert R, et al., "Rilem TC 154-EMC: Electrochemical techniques for measuring metallic corrosion - Test methods for on site measurement of resistivity of concrete," Mater Struct, V. 33, No. 234, Dec. 2000, pp. 603-11.
33. Angst U, Elsener B, Larsen CK, Vennesland O, "Critical chloride content in reinforced concrete - A review," Cement Concrete Res, V. 39, No. 12, Dec. 2009, pp. 1122-38.
34. Angst UM, Isgor OB, Hansson CM, Sagues A, Geiker MR, "Beyond the chloride threshold concept for predicting corrosion of steel in concrete," Appl Phys Rev, V. 9, No. 1, Mar. 2022.
35. Goni S, Andrade C, "Synthetic Concrete Pore Solution Chemistry and Rebar Corrosion Rate in the Presence of Chlorides," Cement Concrete Res, V. 20, No. 4, Jul. 1990, pp. 525-39.
36. Andrade C, Page CL, "Pore Solution Chemistry and Corrosion in Hydrated Cement Systems Containing Chloride Salts - a Study of Cation Specific Effects," Br Corros J, V. 21, No. 1. 1986, pp. 49-53.
37. Ghods P, Isgor OB, Mcrae G, Miller T, "The effect of concrete pore solution composition on the quality of passive oxide films on black steel reinforcement," Cement Concrete Comp, V. 31, No. 1, Jan. 2009, pp. 2-11.
38. Li L, Sagues AA, "Chloride corrosion threshold of reinforcing steel in alkaline solutions - Open-circuit immersion tests," Corrosion, V. 57, No. 1, Jan. 2001, pp. 19-28.
39. Pillai RG, Trejo D, "Surface condition effects on critical chloride threshold of steel reinforcement," Aci Mater J, V. 102, No. 2, Mar-Apr. 2005, pp. 103-9.
40. Ghods P, Isgor OB, McRae GA, Li J, Gu GP, "Microscopic investigation of mill scale and its proposed effect on the variability of chloride-induced depassivation of carbon steel rebar," Corros Sci, V. 53, No. 3, Mar. 2011, pp. 946-54.
41. Angst UM, Geiker MR, Michel A, Gehlen C, Wong H, Isgor OB, et al., "The steel-concrete interface," Mater Struct, V. 50, No. 2, Apr. 2017.
42. Angst UM, Geiker MR, Alonso MC, Polder R, Isgor OB, Elsener B, et al., "The effect of the steel-concrete interface on chloride-induced corrosion initiation in concrete: a critical review by RILEM TC 262-SCI," Mater Struct, V. 52, No. 4, Aug. 2019.
43. Wong HS, Angst UM, Geiker MR, Isgor OB, Elsener B, Michel A, et al., "Methods for characterising the steel–concrete interface to enhance understanding of reinforcement corrosion: a critical review by RILEM TC 262-SCI," Mater Struct, V. 55, No. 4. 2022.
44. Ghods P, Isgor O, Carpenter G, Li J, McRae G, Gu G, "Nano-scale study of passive films and chloride-induced depassivation of carbon steel rebar in simulated concrete pore solutions using FIB/TEM," Cement and Concrete Research, V. 47. 2013, pp. 55-68.
45. Gunay HB, Ghods P, Isgor OB, Carpenter GJC, Wu XH, "Characterization of atomic structure of oxide films on carbon steel in simulated concrete pore solutions using EELS," Appl Surf Sci, V. 274, Jun 1. 2013, pp. 195-202.
46. Ghods P, Isgor O, Brown J, Bensebaa F, Kingston D, "XPS depth profiling study on the passive oxide film of carbon steel in saturated calcium hydroxide solution and the effect of chloride on the film properties," Appl Surf Sci, V. 257, No. 10. 2011, pp. 4669-77.
47. Ghods P, Isgor OB, Bensebaa F, Kingston D, "Angle-resolved XPS study of carbon steel passivity and chloride-induced depassivation in simulated concrete pore solution," Corros Sci, V. 58, May. 2012, pp. 159-67.

48. Otieno MB, Beushausen HD, Alexander MG, "Modelling corrosion propagation in reinforced concrete structures–A critical review," Cement and Concrete Composites, V. 33, No. 2. 2011, pp. 240-5.
49. Jamali A, Angst U, Adey B, Elsener B, "Modeling of corrosion-induced concrete cover cracking: A critical analysis," Construction and Building Materials, V. 42. 2013, pp. 225-37.
50. Isgor OB, Weiss WJ, "A nearly self-sufficient framework for modelling reactive-transport processes in concrete," Materials and Structures, V. 52, No. 1. 2019, pp. 1-17.
51. Rossi E, Governo S, Shakoorioskooie M, Zhan Q, Mundra S, Mannes D, et al., "X-ray computed tomography to observe the presence of water in macropores of cementitious materials," RILEM Technical Letters, V. 8. 2023, pp. 165-75.
52. Albert CC, Mundra S, Ferreira Sanchez D, Furcas FE, Rajyaguru AD, Isgor OB, et al., "Microscale chemical imaging to characterize and quantify corrosion processes at the metal-electrolyte interface," npj Materials Degradation, V. 8, No. 1. 2024, pp. 116.
53. Mundra S, Rossi E, Malenica L, Pundir M, Angst UM, "Precipitation of corrosion products in macroscopic voids at the steel-concrete interface--observations, mechanisms and research needs," arXiv preprint arXiv:240805028. 2024.
54. Suda K, Misra S, Motohashi K, "Corrosion Products of Reinforcing Bars Embedded in Concrete," Corros Sci, V. 35, No. 5-8. 1993, pp. 1543-9.
55. Wang KJ, Monteiro P, " Corrosion Products of Reinforcing Steel and Their Effects on the Concrete Detenoration," Book Corrosion Products of Reinforcing Steel and Their Effects on the Concrete Detenoration, Editor, ed.^eds., City, 1996, pp.
56. Leek DS, "A Studv of the effects of Chloride and Sulphate in the Hvdration of Portland Cement and the Corrosion of Carbon Steel Reinforcemnt usina Electro-optical Techniques and Enerw Dis~enive X-rav Analvsis," Book A Studv of the effects of Chloride and Sulphate in the Hvdration of Portland Cement and the Corrosion of Carbon Steel Reinforcemnt usina Electro-optical Techniques and Enerw Dis~enive X-rav Analvsis, Ph.D., Editor, ed.^eds., University of London, City, 1997, pp.
57. Marcotte TD, Hansson CM, "Corrosion products that form on steel within cement paste," Mater Struct, V. 40, No. 3, Apr. 2007, pp. 325-40.
58. Marcotte TD, "Characterization of chloride-induced corrosion products that form in steel-reinforced cementitious materials," Book Characterization of chloride-induced corrosion products that form in steel-reinforced cementitious materials, Ph.D., Editor, ed.^eds., University of Waterloo, City, 2011, pp.
59. Otte K, Schmahl WW, Pentcheva R, "Density functional theory study of water adsorption on FeOOH surfaces," Surf Sci, V. 606. 2012, pp. 1623-33.
60. Nguyen MT, Seriani N, Gebauer R, "Water adsorption and dissociation on alpha-Fe2O3(0001): PBE+U calculations," J Chem Phys, V. 138. 2013, pp. 194709-1-8.
61. Pang Q, DorMohammadi H, Isgor OB, Árnadóttir L, "Density functional theory study on the effect of OH and Cl adsorption on the surface structure of α-Fe2O3," Comput Theor Chem, V. 1100. 2017, pp. 91-102.
62. Yin S, Ma X, Ellis DE, "Initial stages of H_2O adsorption and hydroxylation of Fe-terminateda-Fe_2O_3(0 0 0 1) surface," Surf Sci, V. 601. 2007, pp. 2426-38.
63. Soon A, RTodorova M, Delley B, Stampfl C, "Oxygen adsorption and stability ofsurface oxides on Cu(111): a first-principles investigation," Physical Review B - Condensed Matter and Materials Physics, V. 73. 2006, pp. 1-13.
64. Zhang CH, Liu M, Jin Y, Sun DB, "The corrosive influence of chloride ionspreference adsorption ona-Al_2O_3(0001) surface," Appl Surf Sci, V. 347. 2015, pp. 386-92.
65. A. C. T. van Duin, V. S. Bryantsev, M. S. Diallo, W. A. Goddard, O. Rahaman, D. J. Doren, et al., "Development and validation of a ReaxFF Reactive Force Field for Cu cation/water interactions and copper metal/metal oxide/metal hydroxide condensed phases," J Phys Chem A, V. 114. 2010, pp. 8.
66. O. Assowe, O. Politano, V. Vignal, P. Arnoux, B. Diawara, Verners O, et al., "Reactive molecular dynamics of the initial oxidation stages of Ni(111) in pure water: effect of an applied electric field " The Journal of Physical Chemistry A, V. 116. 2012.
67. C. Zou, Y. K. Shin, A. C.T. van Duin, Fangb H, Liu ZK, "Molecular dynamics simulations of the effects of vacancies on nickel self-diffusion, oxygen diffusion and oxidation initiation in nickel, using the ReaxFF reactive force field," Acta Mater, V. 83. 2015, pp. 11.
68. T. P. Senftle, S. Hong, M. M. Islam, S. B. Kylasa, Y. Zheng, Y. K. Shin, et al., "The ReaxFF reactive force-field: development, applications and future directions," npj Comput Mater, V. 2. 2016, pp. 14.
69. Lothenbach B, Damidot D, Matschei T, Marchand J, "Thermodynamic modelling: state of knowledge and challenges," Advances in Cement Research, V. 22, No. 4. 2010, pp. 211-23.

70. Damidot D, Lothenbach B, Herfort D, Glasser F, "Thermodynamics and cement science," Cement and Concrete Research, V. 41, No. 7. 2011, pp. 679-95.
71. Furcas FE, Lothenbach B, Isgor OB, Mundra S, Zhang ZD, Angst UM, "Solubility and speciation of iron in cementitious systems," Cement and Concrete Research, V. 151, Jan. 2022.
72. Furcas FE, Lothenbach B, Mundra S, Borca CN, Albert CC, Isgor OB, et al., "Transformation of 2-Line Ferrihydrite to Goethite at Alkaline pH," Environmental Science & Technology, V. 57, No. 42, 2023/10/24. 2023, pp. 16097-108.
73. Furcas FE, Mundra S, Lothenbach B, Angst UM, "Speciation Controls the Kinetics of Iron Hydroxide Precipitation and Transformation at Alkaline pH," Environmental Science & Technology, V. 58, No. 44, Oct 23. 2024, pp. 19851-60.
74. Azad VJ, Li C, Verba C, Ideker JH, Isgor OB, "A COMSOL-GEMS interface for modeling coupled reactive-transport geochemical processes," Comput Geosci-Uk, V. 92, Jul. 2016, pp. 79-89.
75. Isgor OB, Weiss WJ, "A nearly self-sufficient framework for modelling reactive-transport processes in concrete," Mater Struct, V. 52, No. 1, Feb. 2019.
76. Samson E, Marchand J, Beaudoin JJ, "Modeling the influence of chemical reactions on the mechanisms of ionic transport in porous materials - An overview," Cement and Concrete Research, V. 30, No. 12, Dec. 2000, pp. 1895-902.
77. Kranc SC, Sagues AA, "Detailed modeling of corrosion macrocells on steel reinforcing in concrete," Corros Sci, V. 43, No. 7, Jul. 2001, pp. 1355-72.
78. Isgor OB, Razaqpur AG, "Modelling steel corrosion in concrete structures," Mater Struct, V. 39, No. 3, Apr. 2006, pp. 291-302.
79. Bouteiller V, Tissier Y, Marie-Victoire E, Chaussadent T, Joiret S, "The application of electrochemical chloride extraction to reinforced concrete - A review," Constr Build Mater, V. 351, Oct 10. 2022.
80. Byrne A, Holmes N, Norton B, "State-of-the-art review of cathodic protection for reinforced concrete structures," Mag Concrete Res, V. 68, No. 13. 2016, pp. 664-77.
81. Glawe C, Raupach M, "Basics and new opportunities for chemical re-alkalisation of carbonated concrete, including alkali-activated binders," Mag Concrete Res, V. 76, No. 20. 2024, pp. 1185-97.
82. Andrade C, Alonso C, Gulikers J, Polder R, Cigna R, Vennesland O, et al., "Test methods for on-site corrosion rate measurement of steel reinforcement in concrete by means of the polarization resistance method," Mater Struct, V. 37, No. 273, Nov. 2004, pp. 623-43.
83. ACI-318-Committee, "ACI Committee 318 (1971), “Building Code Requirements for Reinforced Concrete," Book ACI Committee 318 (1971), “Building Code Requirements for Reinforced Concrete, Editor, ed.^eds., American Concrete Insitute, City, 1971, pp. 78.
84. ACI-201-Committtee, "Guide to Durable Concrete (ACI 201.2R-77)," ACI Journal, V. 74, No. 53. 1977, pp. 39 pp.
85. ACI-318-Committee, "ACI Committee 318 (1971), “Building Code Requirements for Reinforced Concrete," Book ACI Committee 318 (1971), “Building Code Requirements for Reinforced Concrete, Editor, ed.^eds., American Concrete Insitute, City, 1983, pp. 112.
86. ACI-222-Committee, "Corrosion of Metals in Concrete - Committee Report (ACI 222R-85)," ACI Journal, V. 82, No. 1. 1985, pp. 30.
87. ACI-222-Committee, "Corrosion of Metals in Concrete (ACI 222R-96)," Book Corrosion of Metals in Concrete (ACI 222R-96), Editor, ed.^eds., American Concrete Institute, City, 1996, pp. 34.
88. Isgor B, Halmen C, Trejo D, Tepke D, "Recent Initiatives of ACI Committee 222 on Corrosion of Metals in Concrete," Proceedings of the RILEM Spring Convention and Conference 2024, 2025, pp. 329-38.
89. Trejo D, Vaddey NP, Halmen C, "Standardizing Test to Quantify Chloride Threshold of Steel in Concrete," ACI Mater J, V. 118, No. 1, Jan. 2021, pp. 177-87.
90. Adil G, Halmen C, Vaddey P, Pacheco J, Trejo D, "Multi-Laboratory Validation Study of Critical Chloride Threshold Test Method," ACI Mater J, V. 119, No. 6, Nov. 2022, pp. 91-100.
91. Halmen C, Adil G, "A Collaborative Study for the Development of a Standard Critical Chloride Threshold Test Method," Book A Collaborative Study for the Development of a Standard Critical Chloride Threshold Test Method, Editor, ed.^eds., American Concrete Institute, City, 2020, pp.
92. Halmen C, "A Collaborative Study to Determine the Critical Chloride Threshold Test, OCcrit, Variability due to Material Sources," Book A Collaborative Study to Determine the Critical Chloride Threshold Test, OCcrit, Variability due to Material Sources, Editor, ed.^eds., American Concrete Institute, City, 2024, pp.

93. ACI-222-Committee, "222R: Guide to Design and Construction Practices to Mitigate Corrosion of Reinforcement in Concrete Structures," Book 222R: Guide to Design and Construction Practices to Mitigate Corrosion of Reinforcement in Concrete Structures, Editor, ed.^eds., American Concrete Institute, City, 2019, pp. 28.
94. Council NR, "Highway Deicing: Comparing Salt and Calcium Magnesium Acetate," Book Highway Deicing: Comparing Salt and Calcium Magnesium Acetate, Editor, ed.^eds., Transportation Research Board, City, 1991, pp.
95. ACI-501-Committee, "Building Regulations for Reinforced Concrete (ACI 501-36T)," Book Building Regulations for Reinforced Concrete (ACI 501-36T), Editor, ed.^eds., American Concrete Insitute, City, 1936, pp. 38.
96. ACI-318-Committee, "ACI Committee 318 (1963), “Building Code Requirements for Reinforced Concrete," Book ACI Committee 318 (1963), “Building Code Requirements for Reinforced Concrete, Editor, ed.^eds., American Concrete Insitute, City, 1963, pp. 148.
97. Tepke DG, "Looking Back to See Ahead: Using Historical Knowledge of Durability to Provide Clues for Concrete Repair”, ," Book Looking Back to See Ahead: Using Historical Knowledge of Durability to Provide Clues for Concrete Repair”, , Editor, ed.^eds., International Concrete Repair Institute, City, 2023, pp. 10-21.
98. Tepke DG, Mandry-Campbell J, "Historical Advancements in Corrosion Control of Existing Conventionally Reinforced Concrete Structures in the United States Towards a Sustainable and Viable Future," Concrete Repair Bulletin, International Concrete Repair Institute, V. 37, No. 2. 2024, pp. 21-30.
99. FHWA, "National Changes in Bridge Practices for Reinforcing Bars," Book National Changes in Bridge Practices for Reinforcing Bars, Editor, ed.^eds., USDOT Federal Highway Administration Research, Development, and Technology, City, 2016, pp. 12 pp.
100. Stratfull RF, "Progress Report on Inhibiting the Corrosion of Steel in a Reinforced Concrete Bridge," Corrosion (NACE), V. 15. 1959, pp. 331t–4t.
101. ACI-440-Committee, "ACI 440.1R: Guide for the design and construction of stuctural concrete reinfroced with fiber-reinforced polymer (FRP) bars," Book ACI 440.1R: Guide for the design and construction of stuctural concrete reinfroced with fiber-reinforced polymer (FRP) bars, Editor, ed.^eds., American Concrete Intitute, City, 2015, pp. 88.
102. ACI-212-Committee, "ACI 212.3R-16, Report on Chemical Admixtures for Concrete," Book ACI 212.3R-16, Report on Chemical Admixtures for Concrete, Editor, ed.^eds., American Concrete Insitute, City, 2016, pp. 76.
103. ACI-222-Committee, "222.3R: Guide to Protection of Metals in Concrete Against Corrosion," Book 222.3R: Guide to Protection of Metals in Concrete Against Corrosion, Editor, ed.^eds., American Concrete Institute, City, 2011, pp. 28.
104. ACI-318-Committee, "ACI 318-89: Building code requirements for structural concrete and commentary," Book ACI 318-89: Building code requirements for structural concrete and commentary, Editor, ed.^eds., American Concrete Insitute, City, 1989, pp. 356.
105. ACI-318-Committee, "ACI 318-99: Building code requirements for structural concrete and commentary," Book ACI 318-99: Building code requirements for structural concrete and commentary, Editor, ed.^eds., American Concrete Insitute, City, 1999, pp. 392.
106. ACI-318-Committee, "ACI 318-08: Building code requirements for structural concrete and commentary," Book ACI 318-08: Building code requirements for structural concrete and commentary, Editor, ed.^eds., American Concrete Insitute, City, 2008, pp. 471.
107. Abelev B, Adam J, Adamova D, Aggarwal MM, Rinella GA, Agnello M, et al., "Beauty production in pp collisions at root s=2.76 TeV measured via semi-electronic decays," Phys Lett B, V. 738, Nov 10. 2014, pp. 97-108.
108. Tuutti K, "Service Life of Structures with Regard to Corrosion of Embedded Steel," J Am Concrete I, V. 77, No. 5. 1980, pp. 380-1.
109. Fahim A, Ghods P, Isgor OB, Thomas MDA, "A critical examination of corrosion rate measurement techniques applied to reinforcing steel in concrete," Materials and Corrosion-Werkstoffe Und Korrosion, V. 69, No. 12, Dec. 2018, pp. 1784-99.
110. Feliu S, Gonzalez JA, Andrade C, "Effect of Current Distribution on Corrosion Rate Measurements in Reinforced-Concrete," Corrosion, V. 51, No. 1, Jan. 1995, pp. 79-86.
111. Gepraegs OK, Hansson CM, "A Comparative Evaluation of Three Commercial Instruments for Field Measurements of Reinforcing Steel Corrosion Rates," Journal of ASTM International V. 8, No. 2. 2005.
112. Gulikers J, "Theoretical considerations on the supposed linear relationship between concrete resistivity and corrosion rate of steel reinforcement," Mater Corros, V. 56, No. 6, Jun. 2005, pp. 393-403.
113. Poursaee A, Hansson CM, "Galvanostatic pulse technique with the current confinement guard ring: The laboratory and finite element analysis," Corros Sci, V. 50, No. 10, Oct. 2008, pp. 2739-46.

114. Wojtas H, "Determination of polarization resistance of reinforcement with a sensorized guard ring: Analysis of errors," Corrosion, V. 60, No. 4, Apr. 2004, pp. 414-20.
115. Marinier P, Isgor OB, "Refined half-cell potential mapping for corrosion detection using inverse modeling," Book Refined half-cell potential mapping for corrosion detection using inverse modeling, Editor, ed.^eds., City, 2012, pp. 105-25.
116. Fahim A, Ghods P, Alizadeh R, Salehi M, Decarufel S, "CEPRA: A New Test Method for Rebar Corrosion Rate Measurement," Book CEPRA: A New Test Method for Rebar Corrosion Rate Measurement, Editor, ed.^eds., ASTM International, City, 2019, pp. 59-80.
117. Bharadwaj K, Weiss WJ, Isgor OB, "Towards performance-based specifications for fly ash and natural pozzolans-Insights from a Monte-Carlo based thermodynamic modeling framework," Cement and Concrete Research, V. 172, Oct. 2023.
118. Mcalexander M, Bharadwaj K, Weiss WJ, Isgor OB, "Waterglass-based clinker-free cementitious systems," Constr Build Mater, V. 417, Feb 23. 2024.
119. Bharadwaj K, Isgor OB, Weiss WJ, "Optimizing the Carbon Footprint of Performance-Engineered Concrete Mixtures," Transp Res Record, V. 2678, No. 10, Oct. 2024, pp. 1422-40.

50 Shades of Deicers and Anti-icers

R. Douglas Hooton and Gustavo Julio-Betancourt

Synopsis: The increased use of alternative deicers to rock salt and introduction of anti-icing prior to winter events using concentrated brines has, in some cases, been associated with deterioration of concrete, especially at joints in pavements. While many commercial products are being used, most either are sodium, calcium, or magnesium chlorides, or mixtures of chlorides. In this study, the effects of different concentrations of calcium and magnesium chlorides on concrete are compared to that of sodium chloride. This study, completed in 2009, found that highly concentrated calcium and magnesium chloride brines caused damage to concrete exposed to low-temperature and freezing temperature cycles by formation of expansive oxychlorides. These results were confirmed by subsequent extensive research performed by others. This paper focusses on concrete performance when exposed to the different forms of chlorides.

Keywords: deicers, anti-icers; oxychlorides; concrete deterioration

ACI Honorary Member **R. Douglas Hooton** is Professor Emeritus in the Department of Civil & Mineral Engineering at University of Toronto. He Chairs ACI Committees 201 on Durability, 233 on Slag Cement, and 130A on Sustainability of Concrete Materials.

Gustavo Julio Betancourt is a Concrete Engineer in the Concrete Section, Transportation Infrastructure Management Division, Ontario Ministry of Transportation, Toronto. He obtained his PhD at University of Toronto in 2009.

INTRODUCTION

To better prevent winter accidents, highway agencies, and municipalities in cold climates have transitioned from mainly using applications of sodium chloride rock salt during or after a freezing event to use of other chlorides or acetates that are effective at lower temperatures (Fig. 1). In addition, anti-icing practices have been widely adopted which involves spraying of concentrated chloride brines onto pavements immediately prior to freezing events to inhibit ice formation. While some of the brines are mainly composed of sodium chloride, there are many commercially available brines composed of calcium or magnesium chlorides or combinations of chloride salts. In some cases, non-chloride materials are also used such as potassium acetate (KAc) and calcium-magnesium acetate (CMA) which, along with sodium formate, are also used on airport pavements. Therefore, ice prevention strategies involve a wide range of materials and concentrations. This paper presents one part of a much larger study [1] and mainly focusses on the durability of portland cement concrete from exposure to concentrated calcium chloride brines.

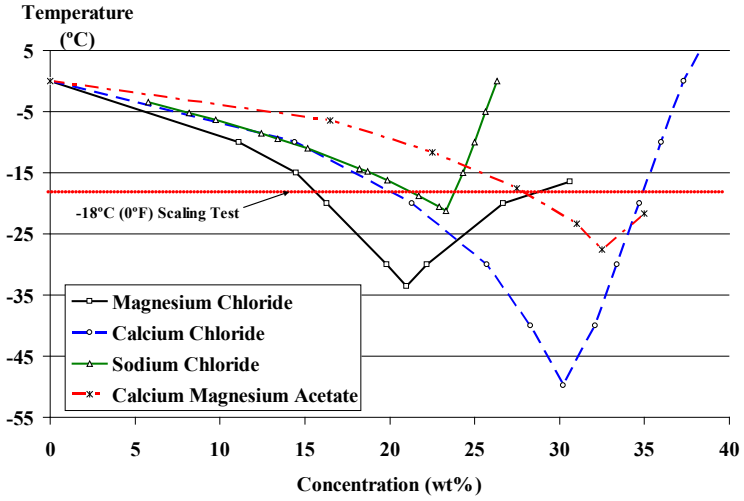

Fig. 1: Concentration-dependent freezing points of various de-icers.

Since the increased use of calcium and magnesium deicers on sidewalks and pavements and implementation of anti-icing practices using concentrated brines, there have been increased cases of so-called joint rot, often manifesting as progressive raveling of concrete adjacent to pavement joints. To address these concerns, this study was undertaken as a part of a Pooled Fund study for the South Dakota Department of Transportation led by Michigan Technological University between 2005 and 2008 [2].

Concentrations of calcium chloride brines as high as 30% by mass had been previously shown to be detrimental to cement-based materials; however, several prior research programs undertaken to determine the cause of the damage, were unable to or mis-identified the phase or phases responsible. For instance, Flint and Well (as cited in [3]) suspected that the formation of calcium chloroaluminate with considerable amounts of crystal water was the cause of the damage ($3CaO.Al_2O_3.CaCl_2.30\text{-}32H_2O$ or $3CaO.Al_2O_3.CaCl_2.8\text{-}12H_2O$). Chatterji and Jensen [4] could not identify the new compounds being formed and their further studies suggested that a complex salt was the cause of deterioration [5-7].

In other research, characteristic needle-like crystals that contained calcium and chloride as their main elements were found in cement paste specimens exposed to either 39.9% calcium chloride with corrosion inhibitor, or 37.9% calcium chloride without corrosion inhibitor [8]. However, because further analysis revealed the presence of phases containing calcium, chloride, aluminum, and sulphate, it was suggested that the crystallization and precipitation of the calcium aluminum chloride sulphate hydrate compound, $Ca_8Al_4O_{12}Cl_2SO_4.24H_2O$, was related to the damage [9]. However, Monosi and Collepardi [10, 11], after careful sample preparation, were able to identify the presence of calcium oxychloride, $3CaO.CaCl_2.15H_2O$, when mortars were exposed to 30% calcium chloride and linked its formation to the loss of mortar compressive strength of up 30% after just 1 month of exposure.

Testing performed as part of this study [1, 2, 12, 13, 14] also identified formation of oxychlorides and also found that these oxychloride phases were not stable and decomposed when exposed to typical lab drying procedures. In addition to $3CaO \cdot CaCl2 \cdot 15H_2O$, magnesium ($Mg3(OH)5Cl \cdot 4H_2O$) oxychloride was also identified as well as several forms of oxychlorides that contained different numbers of water molecules depending on both temperature and moisture conditions.

Other parts of this study [2, 14] indicated that damaging oxychloride formation could be mitigated by partial cement replacement by supplementary cementitious materials. This was found to be related to reductions in the amount of calcium hydroxide as had been previously found by Collepardi and Monosi [11], which is a component required in the formation of the oxychlorides. The role of SCMs in mitigating damaging oxychlorides was further studied and specific mitigation methods provided in subsequent work by others [15, 16].

EXPERIMENTAL

This contribution describes a series of tests was undertaken where in two different test series, a portland cement concrete mixture was exposed to concentrated sodium, calcium, and magnesium chlorides brines, prior to freezing and thawing or scaling tests.

Concrete Materials and Proportions:

Concrete mixtures were designed with a maximum water-cement ratio of 0.45, a compressive strength of 32 MPa [4640 psi] at 28 days and an air content of 5 to 8%. This meets the requirements of CSA A23.1 Class C-2 for non-reinforced concrete exposed to deicing and is similar to mixtures used in sidewalks and some pavements. Concrete mixtures were prepared with normal-density fine and coarse aggregates (either 10-mm or 20-mm nominal maximum size), CSA Type GU general use portland cement (ASTM Type I), tap water, and water-reducing and air-entraining admixtures with proprtions shown in Table 1.

Table 1−Concrete Mix Proportions - w/c = 0.45

Material	Mass (kg/m^3)
Cement (Type GU)	356.2
Water	160.3
Normal-density fine aggregate (sand)	672.7
Normal-density coarse aggregate (stone)	1116.5
Water-reducing admixture	250 mL/100 kg
Air-entraining admixture	70 mL/100 kg

Tests and Test Specimens

In addition to casting 100x200 mm [4x8 in] cylinders for strength, 75x75x300 mm [3x3x12 in] prisms for ASTM C666 Procedure A freezing and thawing tests and 300x300x75 mm [12x12x3 in] slabs for ASTM C672 scaling tests were cast. These tests were modified by using different types and concentration of deicer salt or anti-icing brines. Strength specimens as well as C666 and C672 specimens were moist cured to 28 days of age before exposure to concentrated brines.

Anti-icing Fluids

Eleven different commercially available anti-icing solutions were tested, with compositions obtained using Inductively Coupled Plasma (ICP) as shown in Table 2. Not all of these products were tested in the concrete test program. When used as a control solution, saturated lime water was labeled S0p.

Table 2−Composition of eleven commercially available anti-icing brines and fluids (major elements are **in bold**)

Solution Code	Elemental analysis (ppm)									pH
	Al	Ca	Fe	Mg	K	Na	Si	S	Cl	
S1p*	<0.5	<0.5	<0.5	11	**246,960**	721	64	5	0	10.5
S2p	<0.5	156	<0.5	**105,220**	2,230	2,240	<1	865	**206,094**	6.7
S3p	16	332	258	**63,840**	23,700	5,430	1,580	5,090	**130,954**	2.9
S5p	1	**138,330**	33	12,410	9,770	9,300	58	503	**211,955**	4
S7p	<0.5	20,780	13	2,050	3,240	**92,140**	4	502	**150,638**	5.1
S16p	7	**145,610**	32	666	10,045	3,199	13,900	500	**213,704**	3.9
S10p	106	6,364	1,258	2,653	166	>**222,600**	607	3,927	**537,789**	n.a.
S13p	370	6,149	2516	**116,379**	1,162	3,116	747	165	**329,289**	n.a.
S14p	4444	7,651	4,823	2,170	2,490	>**222,600**	33,204	2,409	**498,603**	n.a.
S12p	159	1,001	2,726	543	2,739	>**222,600**	701	363	**571,045**	n.a.
S11p**	1058	**77,792**	839	**98952**	664	43,481	2,755	561	0	n.a.

* potassium acetate; ** calcium magnesium acetate; n.a.= not measured

Exposure Test Series A.

Except for reference cylinders stored in saturated limewater, after curing, both strength cylinders and ASTM C666 prisms were immersed in undiluted commercial anti-icing solutions at 23°C [73°F] for 450 days, and strengths were measured at various intervals. It should be noted that when the undiluted deicing chemicals were used to immerse the C666 prisms, freezing did not occur at the lowest temperature (-18°C [0°F]) in the freezing cycles. In addition, 75 × 75 × 300 mm [3x3x12 in] concrete prisms were also immersed for 450 days in the undiluted chemicals at 23°C [73°F]. For the strength tests, both potassium and calcium-magnesium acetates were also included.

Exposure Test Series B.

Another group of concrete prisms and scaling slabs was ponded with sodium chloride-based, calcium chloride-based, and magnesium chloride-based brines. Solutions were prepared from each chemical based on the pessimum

concentration obtained in previous mortar experiments [1]. The concentrations used were 22% by mass for calcium chloride and 20% by mass for magnesium chloride. Because no pessimum concentration was established for sodium chloride products as no chemical attack of mortars had been observed, it was decided to prepare a solution of 23% by mass that had an equivalent chloride concentration to the other two chemicals. After 28-days curing, the concrete slabs were ponded with these solutions and placed inside refrigerators at 5±3°C [40±5°F] for 1 year. At the end of the 1-year ponding period, the slabs were removed from the ponding solutions and tested for salt scaling resistance following ASTM C 672/C 672M, "Test Method for Scaling Resistance of Concrete Surfaces Exposed to De-Icing Chemicals." During the 50 freezing and thawing cycles, the slabs were ponded with either 3% NaCl, 4% $CaCl_2$, or 4% $MgCl_2$, maintaining the same type of solution as the one previously used during the 1-year ponding period. These lower concentrations were used to allow freezing to occur at -18°C [0°F], because at the high salt concentrations of the undiluted deicers used for ponding prior to test, there would only be partial freezing of the ponded solutions.

TEST RESULTS

Test Program A

Strength changes when concrete cylinders were immersed at 23°C [73°F] in both limewater (labeled S0d) and in undiluted NaCl (S12d), $MgCL_2$ (S2p, S3p), $CaCl_2$ (S16p) potassium acetate (S1p) calcium magnesium acetate (S11d) are shown in Fig. 2.

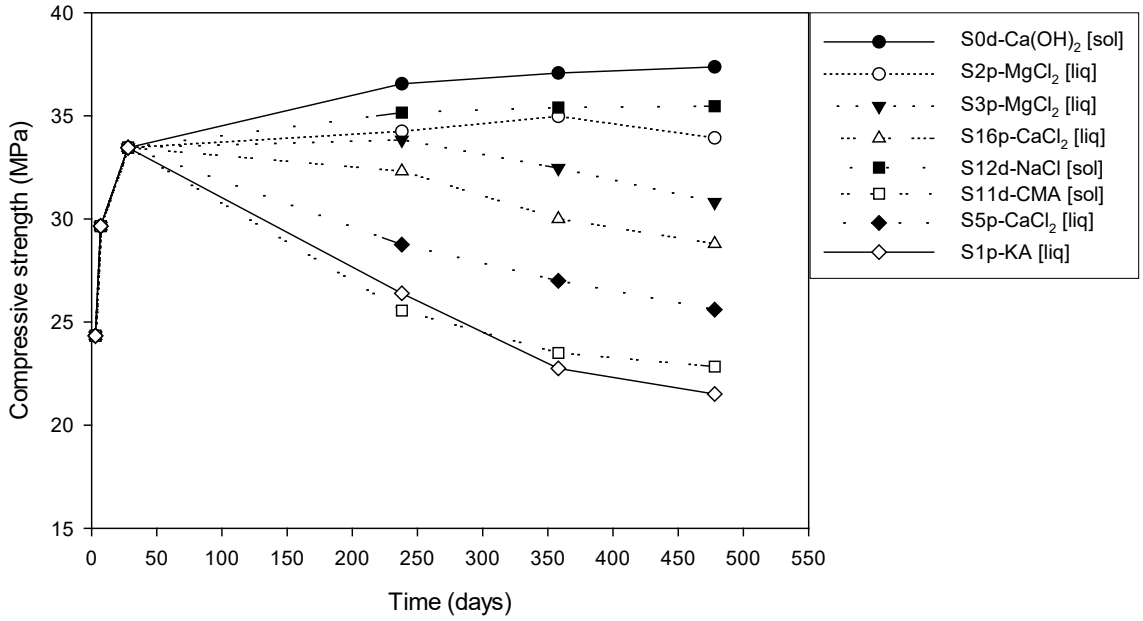

Fig. 2: Compressive strength evolution with time for concrete exposed to undiluted anti-icing chemicals for 450 days at 23°C[73°F].

Strengths continued to increase for cylinders stored in lime and NaCl solutions, but all other solutions resulted in strength losses, with the acetates exhibiting the highest losses.

The strength changes were also reflected in changes of similar magnitude to dynamic modulus elasticity, as shown in Fig. 3.

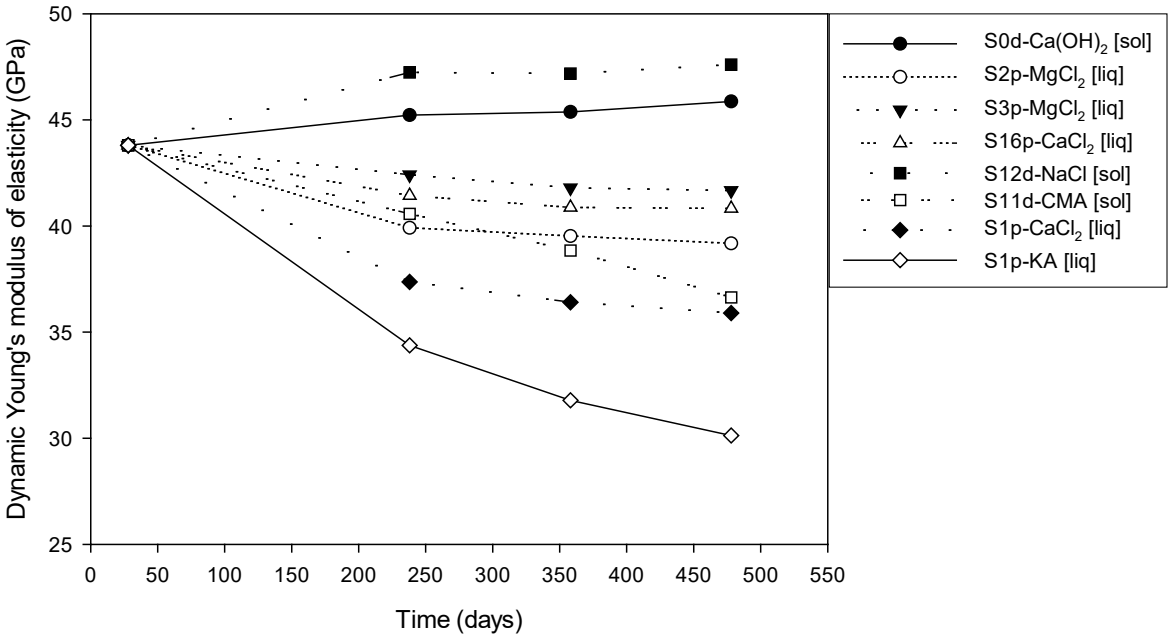

Fig.3: Calculated dynamic Young's modulus of elasticity evolution with time for concrete exposed to undiluted de-icer and anti-icing chemicals for 450 days at 23°C [73°F].

The changes in mass of the prisms during 450 days immersion in undiluted brines are shown in Fig. 4. The potassium acetate and the S5p $MgCL_2$ caused some minor scaling of the prism surfaces resulting in mass loss.

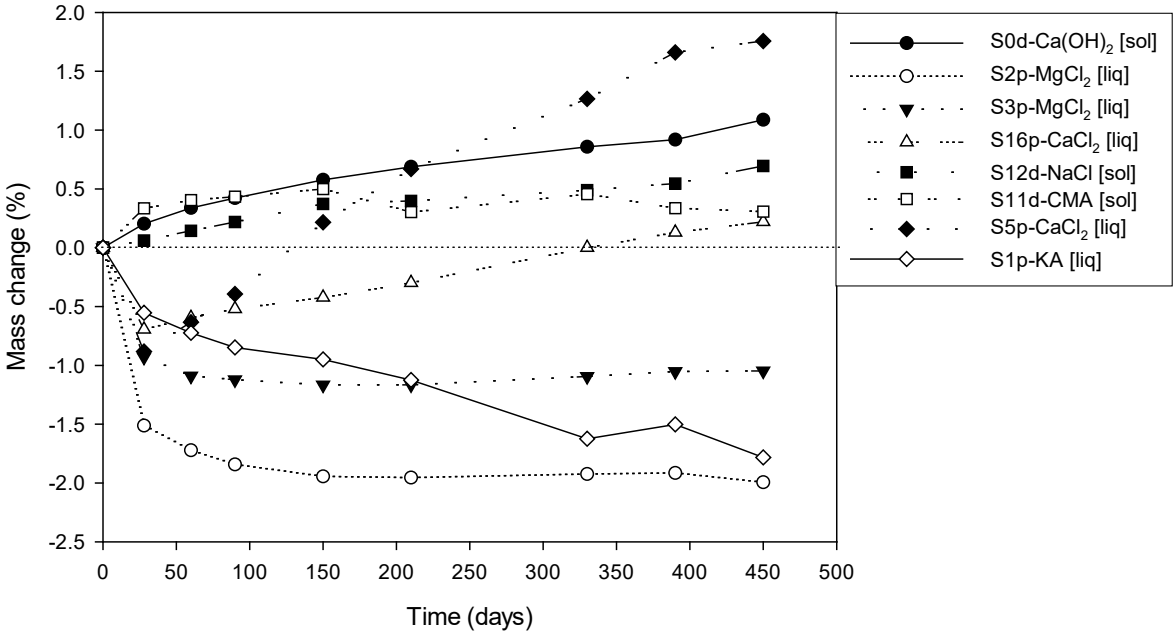

Fig. 4: Mass change with time for 75 × 75 × 308-mm concrete prisms immersed in undiluted de-icer and anti-icing chemicals for 450 days at 23°C [73°F].

The pH of the storage solutions was also monitored as shown in Fig. 5. High pH of at least 12 was only attained for $Ca(OH)_2$ and NaCl. The lower and in some cases, acidic pH of the other solutions may have contributed to the mass losses observed.

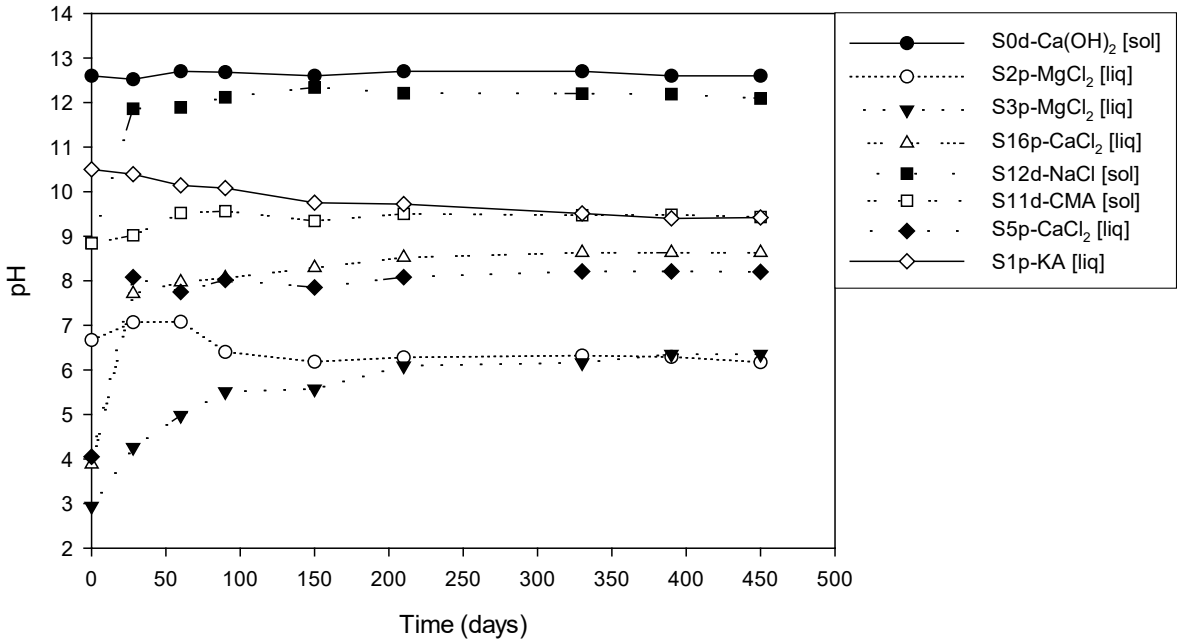

Fig. 5: pH changes with time for undiluted de-icer and anti-icer chemicals over 450 days of exposure at 23°C [73°F].

After immersion in the various solutions for 450 days at 23°C [73°F], concrete specimens from each exposure solution were tested for their resistance to freezing and thawing in the presence of diluted de-icers and anti-icing chemicals (3 molar chloride concentration, equivalent to 15±1% by mass) instead of water. The concentrations of the acetate chemicals were kept at 28% for CMA and at 50% for KAc. It was intended to use exposure solutions that would not freeze under the lowest temperature of the test so that if there were sufficient concentrations of deleterious ions were reached prior storage, the cold temperatures and pessimum concentrations would create favourable conditions for the formation of oxychlorides. In addition, any deterioration process would be related to the previous chemical attack during the immersing period instead of physical attack due to the formation of ice. The specimens were measured for length change, mass change, and pulse velocity, and the durability factor was calculated from fundamental transverse frequency measurements.

After just 33 freeze-thaw cycles as per ASTM C666, the concrete previously exposed to the undiluted calcium chloride-based brine and then subjected to freezing cycles while immersed in diluted $CaCl_2$, exhibited serious durability issues and cracking of the concrete prisms. Map-cracking was observed on all prism surfaces (Fig. 6).

After 67 cycles, the prisms were essentially destroyed as shown in Fig. 7.

Fig. 6: Condition of concrete prism exposed to the undiluted calcium chloride-based brine for 450 days, and then subjected to 33 freeze-thaw cycles in diluted $CaCl_2$, S16p.

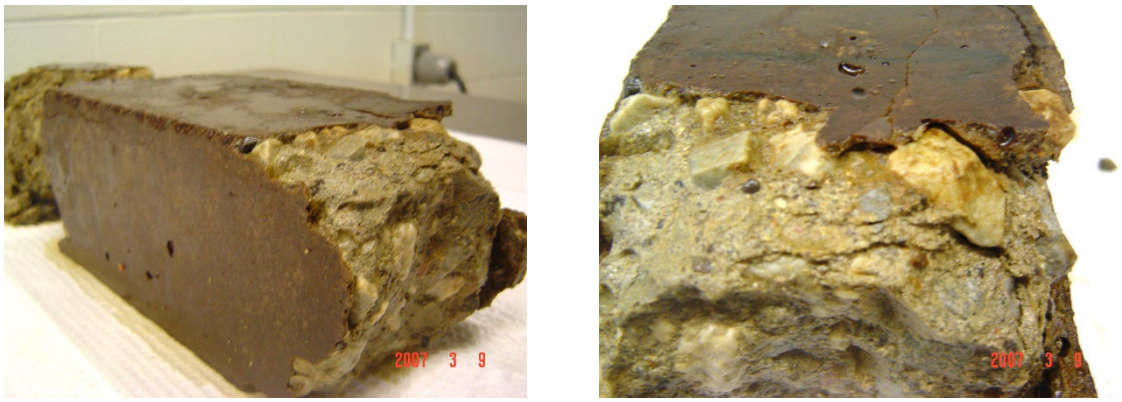

Fig.7: Condition of concrete prism exposed to the undiluted calcium chloride-based brine for 450 days, and then subjected to 67 freeze-thaw cycles in diluted $CaCl_2$, S16p.

Test Program B

ASTM C672 Scaling Tests: After the test surfaces of the slabs were ponded for one year with pessimum concentrations of chloride anti-icers (23% NaCl or 22% $CaCl_2$), ASTM C672 freezing and thawing cycles were initiated but ponded using normal salt concentrations (3% NaCl or 4% $CaCl_2$). Visually, the ponded slabs prior to C672 cycling were undamaged, as shown in Fig. 8. As well, small samples of the concrete surfaces were obtained and analysed by X-ray diffraction (XRD).

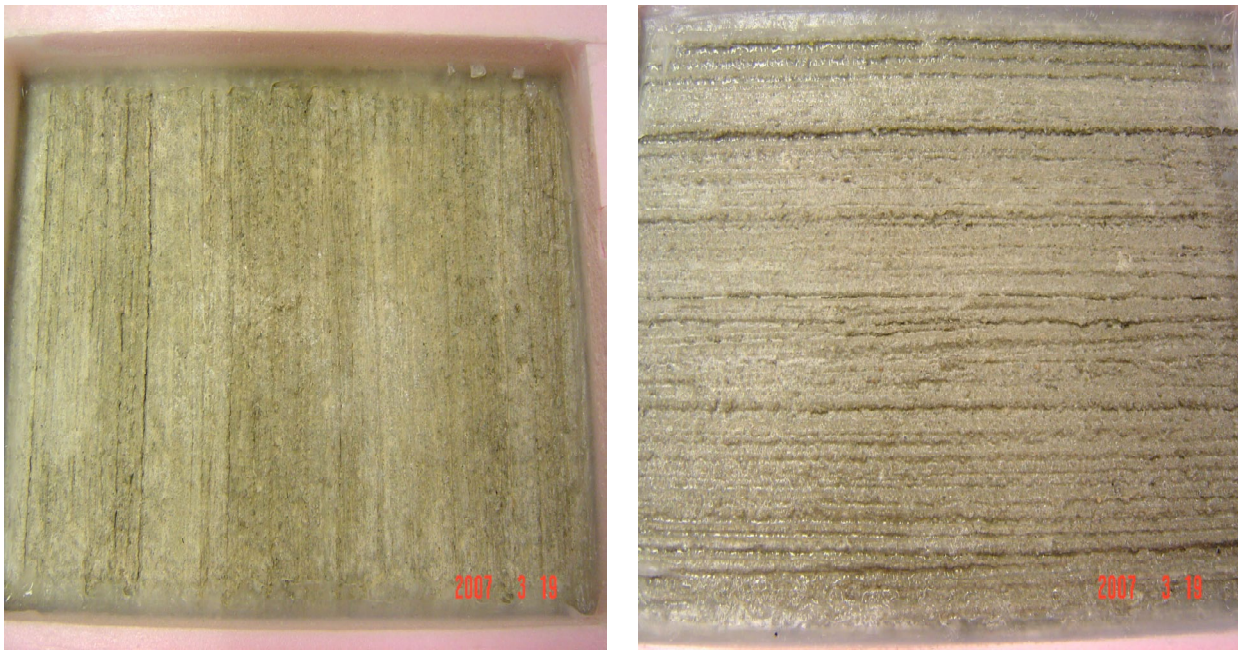

Fig. 8: Concrete slabs after 1-year ponding with concentrated salt solutions at 23°C (before freezing cycles): Left: 23% NaCl; Right: 22% $CaCl_2$

The XRD pattern of the concrete in the near-surface area that had been exposed to 22% $CaCl_2$ indicated the presence of calcium oxychloride.

The visual condition of slab surfaces after 50 and 100 cycles of freezing and thawing are shown in Figs. 9 and 10 respectively. The slabs exposed to NaCl showed no scaling after 50 cycles and very little after 100 cycles. The slabs exposed to $CaCl_2$ were severely scaled after 50 cycles, and after 100 cycles, all of the surface mortar had scaled off, and much of the mortar surrounding the coarse aggregate had also been removed.

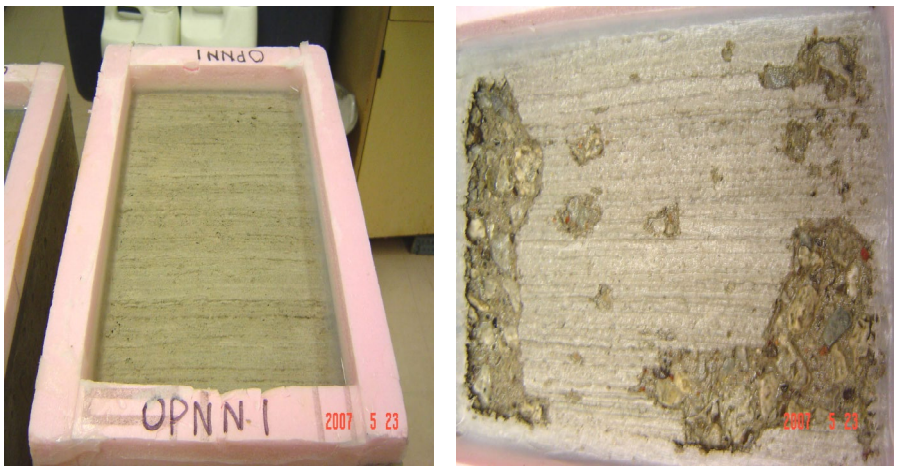

Fig. 9: Condition of slabs after 50 cycles of freezing and thawing: Left: 3% NaCl; Right 4% $CaCl_2$.

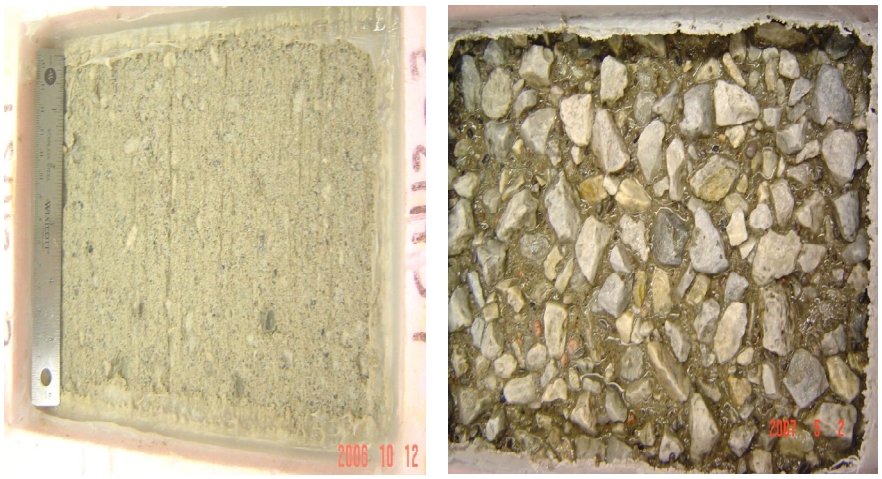

Fig. 10: Condition of slabs after 100 cycles of freezing and thawing: Left: 3% NaCl; Right 4% $CaCl_2$.

It was concluded that the initial exposure to concentrated $CaCl_2$ brine resulted in consumption of $Ca(OH)_2$ and formation of Ca-oxychloride in the surface layer, weakening it. Then the freezing and thawing cycles caused extensive scaling damage due to the weakened surface. This damage did not occur from exposure to concentrated NaCl brine. The scaling mass loss for $CaCl_2$ was at the maximum limit of 0.8 kg/m^2 [0.16 lb/sf] allowed by the Ontario Ministry of Transportation. Freezing cycles were continued and, after 100 cycles of freezing, the entire surface exposed to $CaCl_2$ had scaled off with a mass loss of 16.8 kg/m^2 [3.44 lb/sf] and XRD analysis of the scaled material indicated the presence of calcium oxychloride, while for NaCl the scaling mass was 0.6 kg/m^2 [0.12 lb/sf] after 100 cycles.

Similar conclusions were obtained from concrete slabs subjected to simulated field cycles [1] with a 23% sodium chloride, 22% calcium chloride or 20% $MgCl_2$, and then subjected to ASTM C672 scaling tests while ponded with 3% NaCl, 4% $CaCl_2$, or 4% $MgCl_2$ respectively. In this case the scaling damage after 50 cycles to the slab surfaces was 0.35 kg/m^2 [0.07 lb/sf] for NaCl, and 4.19 kg/m^2 [0.86 lb/sf] for $CaCl_2$.

Supplementary Cementitious Materials

In another limited series of tests, 35% slag cement and 15% fly ash replacement of portland cement were found to greatly improve resistance to damage from oxychloride formation [17]. SCMs consumed calcium hydroxide in the pozzolanic reaction thereby providing less calcium hydroxide in the cement paste to chemically react. The mitigation effects associated with the use of SCMs also results from a decrease in concrete permeability and much lower rate of absorption for these mixtures [2]. THe beneficial effect of lower rates of absorption was also examined by Ghantous et al in [19]. More extensive work was done elsewhere demonstrating the important role of SCMs in reducing calcium hydroxide contents to mitigate oxychloride formation [15,16,18].

DISCUSSION

In both test series, no strength loss or visible distress was observed when portland cement concrete specimens were exposed to concentrated NaCl solutions, nor when previously exposed specimens were subjected to cyclic freezing and thawing. However, when concretes were immersed in either concentrated calcium or magnesium chloride brines or potassium or calcium-magnesium acetates for 450 days at 23°C [73°F], concrete strengths were degraded by as much as 40% (KAc, CMA and one $MgCl_2$). The losses in strength were accompanied by similar reductions in dynamic modulus of elasticity, and either mass gains (1.8% for one $CaCl_2$) or losses (2% for one $MgCl_2$ and KAc).

CONCLUSIONS

- Portland cement concrete exposed to concentrated sodium chloride brines remained largely undamaged when later exposed to freezing and thawing using the ASTM C666 and C672 test regimes.
- Exposure to both concentrated $MgCl_2$ and $CaCl_2$ brines resulted in unacceptable expansion and change in dynamic modulus after ASTM C666 freeze-thaw testing indicating that temperature changes during cyclic freeze-thaw exposure exacerbates the damage caused by these deicers.
- Exposure to both concentrated $CaCl_2$ and $MgCl_2$ brines resulted in formation of oxychloride phases that caused damage, including severe scaling for $CaCl_2$.
- In all cases, the mechanism of failure was caused by the formation of oxychloride phases from the interaction between the deicer with calcium hydroxide in the hardened cement paste.
- Because these brines are more effective anti-icers at very low temperatures, they will continue to be used by highway agencies and municipalities. Additional testing undertaken as part of this study [1, 2, 14] showed that partial replacement of portland cement by slag cement or fly ash helped prevent damage from exposure to both calcium and magnesium chlorides, primarily by reducing calcium hydroxide contents in the concrete, as further shown in subsequent studies elsewhere as well as slowing that ingress of the brines.

REFERENCES

[1] G.A. Julio-Betancourt, Effect of de-icer and anti-icer chemicals on the durability, microstructure, and properties of cement-based materials, Ph.D. University of Toronto, 2009.

[2] L. Sutter, K. Peterson, G. Julio-Betancourt, D. Hooton, T.Van Dam, K. Smith, The Deleterious Chemical Effects of Concentrated Deicing Solutions on Portland Cement Concrete, Final Report for the South Dakota Department of Transportation, 2008. https://publications.iowa.gov/20043/1/IADOT_tr_480_Deleterious_Chemical_Effects_Deicing_Solutions_PCC_2008.pdf

[3] I. Biczók, Concrete corrosion and concrete protection (8th ed., Z. Szilvássy, Trans.), Budapest, Hungary, Akadémia Kiadó (Original work published 1956).

[4] S. Chatterji, A.D. Jensen, Studies of the mechanism of calcium chloride attack on portland concrete, Nordisk Betong, Journal of the Nordic Concrete Federation 5 (1975) 5-6.

[5] J. Bensted, A discussion of the paper: Mechanism of the $CaCl_2$ attack on portland cement concrete by S. Chatterji, Cement and Concrete Research, 9 (1) (1979) 139-140.

[6] U.A. Birnin-Yauri, F.P. Glasser, Chloruri nel cemento: Studi di fase del sistema $Ca(OH)_2$-$CaCl_2$-H_2O [Chlorides in cement: Phases studies of the $Ca(OH)_2$-$CaCl_2$-H_2O system], Il Cemento, 88 (3) (1991) 151-157.

[7] S. Chatterji, Mechanism of the $CaCl_2$ attack on portland cement concrete, Cement and Concrete Research, 8 (4) (1978) 461-468.

[8] K. Wang, D.E. Nelsen, W.A. Nixon, Damaging effect of deicing chemicals on concrete materials, Cement and Concrete Composites 28 (2006) pp. 173-188.

[9] K. Wang, D.E. Nelsen, W.A. Nixon, Damaging effect of deicing chemicals on concrete materials, Cement and Concrete Composites, 28 (2006) 173-188.

[10] S. Monosi, I. Alverà, M. Collepardi, L'attacco chimico del cloruro di calico sulla pasta de cemento portland [Chemical attack of calcium chloride on the portland cement paste], iL Cemento, 86 (2) (1989) pp. 97-104.

[11] M. Collepardi, S. Monosi, Effect of the carbonation process on the concrete deterioration by $CaCl_2$ aggression, Ninth International Congress on the Chemistry of Cement, New Delhi, India, 1992.

[12] K. Peterson, G. Julio-Betancourt, L. Sutter, R.D. Hooton, D. Johnston, Observations of chloride ingress and calcium oxychloride formation in laboratory concrete and mortar at 5°C, Cement and Concrete Research, 45 (2013) 79-90, http://dx.doi.org/10.1016/j.cemconres.2013.01.001.

[13] L. Sutter, K. Peterson, S. Touton, T. Van Dam, D. Johnston, Petrographic evidence of calcium oxychloride formation in mortars exposed to magnesium chloride solution, Cement and Concrete Research, 36 (8) (2006) 1533-1541, http://dx.doi.org/10.1016/j.cemconres.2006.05.022

[14] Sutter, L.L., K.R. Peterson, R.D. Hooton, and T.J. Van Dam, The Deleterious Chemical Effects of Concentrated Deicing Solutions on Portland Cement Concrete, Literature Review, Report SD2002-01, (2008). South Dakota Department of Transportation, Pierre, South Dakota. https://publications.iowa.gov/20357/1/TPF_5_042_Sutter_Delterious_Chemical_Effects_Literature_Review_SD2002-01_L_2008.pdf

[15] Y. Farnam, S. Dick, A. Wiese, J. Davis, D. Bentz, J. Weiss, The influence of calcium chloride deicing salt on phase changes and damage development in cementitious materials, Cement and Concrete Composites, 64, Nov. 2015, pp.1-15. https://doi.org/10.1016/j.cemconcomp.2015.09.006

[16] P. Suraneni, V.J. Azed, O.B. Isgor, J. Weiss, Role of Supplementary Cementitious Material Type in the Mitigation of Calcium Oxychloride Formation in Cementitious Pastes, Journal of Materials in Civil Engineering, ASCE, 30 (10), 2018, 10pp. https://doi.org/10.1061/(ASCE)MT.1943-5533.0002425

[17] Sutter, L.L., K.R. Peterson, G. Julio-Betancourt, R.D. Hooton, T.J. Van Dam, and D. Johnston, The Deleterious Chemical Effects of Concentrated Deicing Solutions on Portland Cement Concrete – Phase II Results, Transportation Research Board, TRB 09-3280, 2009, 18pp.

[18] Weiss, W J., Olek, J., Whiting, N. M., Panchmatia, P.,;Qiao, C., and Suraneni, P., Synthesis Report: Accelerating Implementation of Research Findings to Reduce Potential Concrete Pavement Joint Deterioration, Joint Transportation Research Program, Indiana Dept. of Transportation, 2018-12-01, FHWA/IN/JTRP-2018/24 DOI : https://doi.org/10.5703/1288284316869

[19] R. M. Ghantous, K. Zetterberg, H. Hall Becker, A. Behravan, M. T. Ley, O. B. Isgor, and W. J. Weiss, The influence of air voids and fluid absorption on salt-induced calcium oxychloride damage, Cement and Concrete Composites, 133, 2022, 104697, https://doi.org/10.1016/j.cemconcomp.2022.104697

Pitting Resistance Equivalent Number (PREN) Applicable to Stainless Steel Rebar in Concrete Environment

Mohaddeseh Abdolhosseini and Ibrahim G. Ogunsanya

Synopsis: To overcome the time- and resource-intensive electrochemical assessments used to evaluate the pitting corrosion resistance of stainless steel (SS) rebar alloys, a non-destructive assessment tool such as the Pitting Resistance Equivalent Number (PREN) index is important for decision-making involving building resilient engineering structures. By addressing the limitations of the existing PREN index, initially designed for SS alloys in high-temperature acidic or neutral environments, this study sought to develop a PREN index tailored for highly alkaline ambient-temperature concrete environments through a combination of electrochemical experimental analysis and machine learning modelling. This integrated approach and newly developed PREN index account for variations in SS alloying composition, concrete alkalinity, and environmental exposure conditions, addressing the growing demand for non-destructive, time- and cost-effective, and reliable alternatives for assessing SS rebar corrosion performance. Developed PREN will aid design of new and selection of existing SS alloys for reinforced concrete structures across diverse localities and applications. Two major formulas were reported, one for electrochemical parameters and the other for PREN related to these electrochemical parameters, each establishing their relationship with major SS alloying elements (i.e., Cr, Ni, Mo, Mn), concrete type (i.e. pH of testing solution), and concentration of deleterious species in exposure environment (i.e. chloride, sulphate). This study marks an initial step toward developing a non-destructive corrosion-performance assessment tool for civil engineering applications.

Keywords: Pitting Resistance Equivalent Number (PREN), Stainless Steel Rebar, Cement and Concrete, Pitting Corrosion, Non-Destructive Tools (NDT), Machine Learning, Regression Model

ACI member **Ibrahim G. Ogunsanya** is an Assistant Professor in the Department of Civil and Mineral Engineering at University of Toronto, Toronto, Canada. He is a member of the ACI 222 (Protection of Metals in Concrete Against Corrosion), 236 (Material Science of Concrete), 349A (Nuclear Structures-Materials) Committees and other Mineral, Metal and Materials Societies in North America (Canada and the United States) and Europe. His research focuses on the durability and sustainability of materials and structures, particularly reinforced concrete structures. As a metallurgist and material scientist, he studies the processing-structure-property-degradation relationship to develop new materials and improve existing ones, ranging from metal alloys to non-metals such as cement and concrete. His work emphasises selecting appropriate construction materials—reinforcing bars, cement, and concrete—to meet current and future demands for durable, sustainable, and economical structures.

ACI student member **Mohaddeseh Abdolhosseini** is a PhD candidate in the Department of Civil and Mineral Engineering at University of Toronto, Toronto, Canada. With a structural engineering background and current endeavour in the material science of construction materials, her research focuses on durability challenges of reinforced concrete structures with a view to apply experimental and modelling tools to understand the interaction between different reinforcing bars, concrete types, and field exposure conditions leading to corrosion damage.

INTRODUCTION

Reinforced concrete (RC) structures in regions with high exposure to de- and anti-icing salts and coastal areas suffer major corrosion durability and structural integrity challenges [1]. In these environments, chloride ions continue to diffuse through the porous concrete matrix until they reach the steel reinforcing bars (rebar) surface in sufficient quantity to break down their passive film and initiate active corrosion [2]. In response to this challenge, demand is high for corrosion-resistant alternatives, with stainless steel (SS) rebar being a prominent candidate. SS rebar offers increased corrosion resistance mainly due to their higher alloying composition resulting in a more stable passive film in higher chloride concentration [3]. The application of SS rebar can drastically reduce the need for frequent maintenance and extend the life span of RC structures, making it a cost-effective solution over the structure's life despite its higher initial cost.

SS alloys are prone to localised damage, known as pitting corrosion, which has since necessitated ongoing research [4]. Assessing pitting corrosion in SS rebar is typically achieved through accelerated testing involving high chloride exposures and a shift from a natural equilibrium state using electrochemical techniques such as potentio/galvano-static polarisation, potentio/galvano-dynamic polarisation, and electrochemical impedance spectroscopy tests [5]. Although these electrochemical assessments are invaluable for obtaining pitting corrosion parameters, they often require extensive time- and resource-consuming laboratory testing, such as the 15 weeks-long ASTM A955 "rapid" macrocell testing, which does not support timely decision-making by rebar manufacturers developing new alloy grades, geometry, or surface conditions, or bridge owners and transportation authorities searching for best-fit rebar grades for different regions [6]. These limitations make it important to develop a non-destructive, cost-effective, and reliable assessment tool for examining and pre-determining SS rebar corrosion performance. Such tool aids material selection for new RC structures to be erected in different localities and applications.

Pitting Resistance Equivalent Number (PREN) index [7] is a widely recognised non-destructive tool (NDT) for quantifying the pitting resistance of SS alloys. In 1969, Lorenz and Medawar introduced the first PREN equation by studying a variety of austenitic SSs in boiling nitric acid, boiling magnesium chloride, and artificial seawater to define the effect of alloying composition on critical pitting temperature and pitting and stress corrosion cracking resistance [7]. Their findings on the breakdown potential in seawater were a function of 1% Chromium (Cr) and 3% Molybdenum (Mo), which introduced the first PREN = %Cr + 3.3% Mo. This formula suggests that critical pitting temperature, pitting, and stress corrosion resistance of SS used in similar environments, as examined by Lorenz and Medawar, will increase with the increase in Cr and Mo content. Subsequent work by Renner et al. [8] and others [9,10] demonstrated the benefit of Nitrogen (N) additions in improving resistance of SS alloys to corrosion-related damage in this environment, resulting in the most common expression of PREN formula – stated by ISO 21457 [11] – as $PREN_{16}$ = %Cr + 3.3%Mo + 16%N (for austenitic SS) or $PREN_{30}$ = %Cr + 3.3%Mo + 30%N (for duplex SS). A high PREN value represents high pitting corrosion resistance [3,7].

Since its development, the PREN formula has been used for decision-making related to SS alloys used by several engineering fields. However, there are several factors limiting the applicability of the existing PREN index to RC structures. Firstly, the existing PREN formula was initially developed for SS alloys in acidic or neutral environments

at elevated temperatures (300 – 400˚ C) [12], limiting its applicability to highly alkaline concrete environments, which are typically at ambient or low temperatures. Secondly, to develop cost-effective SS grades, the concentration of expensive alloying elements such as Ni and Mo is often reduced, with elements such as Manganese (Mn) being substituted for Ni [13]. The existing PREN equation does not account for these compositional changes and resulting performance variations in different concrete mixes and exposure conditions, further complicating their applicability [14]. Thirdly, the traditional PREN index was developed based on the critical pitting temperature, which is not an appropriate criterion for assessing the corrosion durability of rebar in concrete structures. Instead, parameters such as corrosion potential (E_{corr}), pitting potential (E_{pit}), corrosion current density (i_{corr}), and current density at passivity before pitting corrosion initiation (i_{pit}) from chloride- or carbonation-induced rebar corrosion provide a more meaningful basis for developing a PREN index specific to these environments. These limitations are often overlooked, resulting in the misapplication of existing PREN in the civil/structural engineering field [12].

This study addresses a critical research gap by developing a PREN index tailored for SS rebar alloys used in high pH, ambient-temperature concrete environments exposed to chloride ions. Experimental testing of different grades of SS rebar alloys was conducted to gather key electrochemical parameters such as E_{corr}, E_{pit}, i_{corr}, and i_{pit} from different commercial austenitic and duplex SS rebar alloys. Afterwards, different regression models, including Linear, Ridge, Lasso, and Exponential Regression, were developed, using parameters from experimental testing, to construct a predictive and easily applicable PREN formula based on E_{corr}, E_{pit}, i_{corr}, or i_{pit}. Unlike existing formula, this approach and developed formula: (i) enables ranking of SS rebar grades (following their varying alloy composition) based on various commonly used electrochemical criteria; (ii) indicates the basis and limitation of the PREN formula, allowing thermodynamic-based $PREN_{Ecorr}$, kinetic-based $PREN_{icorr}$, and polarisation-based $PREN_{Epit}$ and $PREN_{ipit}$ formula to be used for elucidating corrosion performance under free/natural and induced conditions; (iii) accounts for varying concrete mixes and the exposure environment through incorporation of pH and Cl. Overall, this initial effort to model the applicable PREN formula supports the development of new and selection of existing SS alloys, offering guidance on the required composition to achieve target corrosion resistance levels for specific concrete types and exposure conditions.

MATERIALS AND METHODS

Electrochemical Test and Experimental Data Collection

16 mm nominal diameter SS bars, with the composition presented in Table 1, were cut to a length of 127 mm. One end was drilled and soldered with a solid copper wire to establish a reliable electrical connection and masked on both ends with electroplating Stop-Off lacquer to leave an exposed length of 76 mm for testing. After washing and cleaning with alcohol to degrease the bars, they were placed as working electrodes in their respective testing solutions with a saturated calomel electrode (SCE) as the reference electrode and a titanium mesh as the counter electrode in the set-up shown in Figure 1.

Table 1— Grades and compositions of the SS bars from the mill certificate provided by the manufacturer. Note that 304 = 304L and 316 = 316L.

Class	Rebar grade (ASTM)	In text as	Composition (wt.%)							
			Cr	Ni	Mo	Mn	C	N	Si	Cu
Austenitic	UNS S31603	316	16.6	9.5	2	1.6	0.03	0.14	0.7	0.4
	UNS S30403	304	17.4	8.2	0.5	1.3	0.03	0.1	1	0.6
	UNS S24100	24100	17.1	0.9	0.19	12.7	0.04	0.34	0.9	0.14
Duplex	UNS S32205	2205	22.7	4.4	3	1.4	0.02	0.14	0.6	0.3
	UNS S32304	2304	22.4	3.2	0.3	1.8	0.02	0.14	0.7	0.3

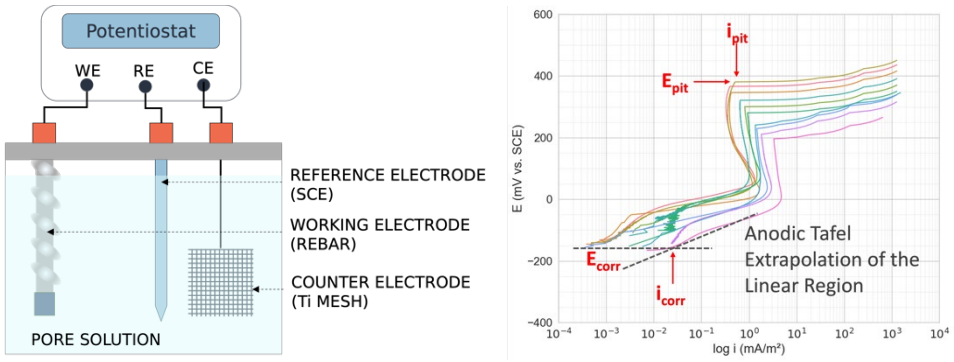

Figure 1— Test setup for corrosion testing (left) and sample polarisation curves obtained from different SS bars in their testing solution (right) [15]

Prepared rebar specimens were examined in three testing solutions: (i) saturated $Ca(OH)_2$, referred to as CHS, (ii) synthetic concrete pore solution corresponding to that obtained from pore solution expression of 75% Portland cement and 25% blast furnace slag paste (w/c = 0.4), referred to as SPS, and (iii) synthetic pore solution, same as mix design in (ii) but with corresponding sulphate increment at every chloride increase (as advised by result from pore expression of paste with admixed chloride), referred to as SPSS. Each solution was stirred to ensure complete dissolution of all the salt compounds shown in Table 2, allowed to rest for 48 hours, and pH measurements were taken afterwards. For each SS rebar grade, three replicates were examined per solution.

Table 2— Testing solutions' chemical compositions (in mol/L) and their corresponding average pH

Testing solution (text denotations)	Composition (M)				pH
	$Ca(OH)_2$	KOH	NaOH	$CaSO_4.2H_2O$	
Calcium hydroxide solution (CHS)	Saturated	-	-	-	~12.5
Synthetic pore solution (SPS)	0.0014	0.48	0.13	-	~13.6
Synthetic pore solution plus sulphate (SPSS)	0.0014	0.48	0.13	0.002	~13.5

To commence the electrochemical assessment, each rebar was placed in desired testing solution for two weeks to ensure they reached equilibrium in that environment and attained passivity, determined by monitoring E_{corr} throughout this duration. Following this phase, further electrochemical assessment commenced with bars in their testing solution without chloride and then with chloride and sulphate (in SPSS) addition to the solution, following Table 3. Chloride and sulphate additions were based on the amount reported by Ogunsanya and Hansson [3]. When chlorides and sulphates were added to a solution where rebar had been passivated, E_{corr} was monitored for one hour (observed to be the optimal time) to ensure the bars were equilibrated again before further testing. The electrochemical assessment involved a potentiodynamic polarisation scan from the samples E_{corr} to the anodic potential of 500mV$_{SCE}$ (or until pitting potential is reached) with a scan rate of 0.01 mV/s using the BioLogic Model VSP potentiostat. The values of E_{corr}, E_{pit}, i_{corr}, and i_{pit} were extracted from each polarisation curve (an example is shown in Figure 1 (right)) for every distinct rebar specimen, resulting in a total of 225 data points corresponding to E_{corr} and i_{corr}, and 180 data point corresponding to E_{pit}, and i_{pit}.

Table 3— Chloride and sulphate additions to testing solutions (in mol/L). Chlorides were added as NaCl, and sulphates were added as $CaSO_4.2H_2O$

	Chloride (Sulphate) concentration					
Salt, wt.%	0%Cl^- (0%SO_4)	5% - 6% Cl^- (1.9-2%SO_4)	10% - 12% Cl^- (3.8-4%SO_4)	18% - 20% Cl^- (4.8-5%SO_4)	24% - 25% Cl^- (6.3-6.5%SO_4)	30% Cl^- (9%SO_4)
Cl^-, M	0	0.70-0.85	1.41-1.69	2.29-2.54	3.24-3.38	5.07
SO_4^{2-} (only in SPSS), M	0.002	0.13-0.14	0.17-0.18	0.23-0.24	0.34-0.35	0.48

Histogram plots in Figure 2 depict the distribution of major alloying elements in the examined SS rebars (i.e., Cr, Ni, Mo, and Mn) in plots A to D, key properties of the testing solution they were examined (i.e. pH, Cl^-) in plot E to F,

and the electrochemical parameters obtained from them (i.e. E_{corr}, E_{pit}, i_{corr}, and i_{pit}) in plot G to J. Notable peaks in specific ranges shown in plot A to F reflect the predominant values for each key input factor, indicating the typical compositional ranges for alloying elements. The variability in corrosion-related parameters from the potentiodynamic polarisation test is shown in plots G to J. For instance, when comparing plots H and J, which correspond to i_{corr} and i_{pit} values, respectively, it is observed that i_{corr} shows a high frequency between 0.001 and 0.5 mA/m^2, whereas i_{pit} demonstrates a high frequency at values above 1-3 mA/m^2. Also, the shape of the distribution can be observed across different input parameters. For example, some of the inputs, such as alloying elements (Cr, Ni, etc.), show a more uniform distribution with distinct groups, while others, such as i_{corr} and $i_{pit,}$ show skewed distributions with data concentrated at lower values.

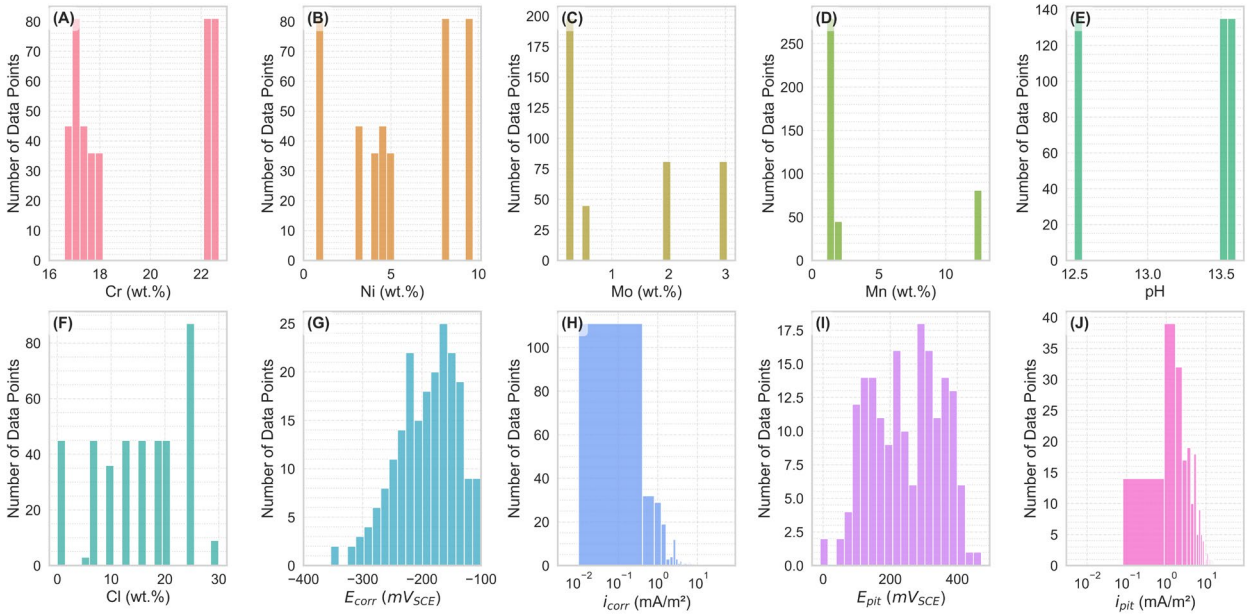

Figure 2— Histograms distribution graphs of key input factors (Cr, Ni, Mo, Mn, pH, and Cl^-) in A – F and electrochemical parameters (E_{corr}, i_{corr}, E_{pit}, and i_{pit}) in G – J from experimental testing of various SS rebar

Regression Models Development Using Machine Learning Techniques

Machine learning models

The machine learning techniques used in this study are categorized as supervised learning, where models are trained on experimental electrochemical data to establish mathematical relationships between input parameters (i.e., Cr, Ni, Mo, Mn, pH and Cl^-) and corrosion performance indicators (i.e., E_{corr}, i_{corr}, E_{pit}, and i_{pit}). The primary objective is to identify patterns and predict corrosion behaviour by analysing how these factors influence the electrochemical response of SS alloys [16]. Since the target variables are continuous numerical values, this study treats the problem as a regression task, utilizing multiple regression techniques – Linear, Ridge, Lasso, and Exponential regression – to evaluate predictive accuracy and model interpretability [17]. While more complex advanced machine learning techniques such as K-nearest neighbours, support vector machines, decision trees and random forest, could be explored, they fall short in generating simple predictive equations compared to the regression techniques chosen for the present work. Although these models have been widely applied in other fields, a brief summary of their relevance to this study is presented.

Linear regression – Multivariable linear regression establishes a direct linear relationship between input variables and the target output, assuming a linear dependency. Although it provides a simple equation, it may not fully capture complex interactions and non-linear dependencies in corrosion behaviour among variables. Models developed with this technique determine the coefficients of independent variables by minimising the mean square error (MSE) between predicted and actual output values [18].

Ridge regression – This technique estimates the coefficients of multiple-regression models in scenarios where the independent variables are highly correlated [19]. This technique extends the linear regression model by incorporating a regularization term (called L2) representing the sum of squares of the model's coefficients [20] . This term adds a penalty to the loss function – used to quantify the difference between predicted and actual target values – thereby guiding the learning process by minimising error. The addition of this penalty helps to reduce multicollinearity – a situation where the predictors in a regression model are linearly dependent – and prevents overfitting [21]. This method is practically useful when predictor (i.e., input) variables, such as Cr, Ni, Mo and Mn, exhibit high correlations, as commonly observed in SS alloys. By constraining the magnitude of the coefficients, Ridge regression improves model stability and generalizability [22]. However, unlike Lasso regression, ridge regression does not perform variable selection, allowing all inputs to remain in the models. The regression coefficients are obtained by minimising the sum of squared errors and adding a penalty term that controls the degree of regularisation.

Lasso regression – This technique, similar to Ridge regression, incorporates a regularisation term. However, instead of L2 regularization, it employs an alternative regularization method (called L1), which adds the absolute value of each model coefficient as a penalty term to the loss function, thereby facilitating automatic feature selection [23]. By applying this penalty, Lasso regression forces some coefficients to become exactly zero, effectively eliminating less influential variables from the model. This makes Lasso regression models practically useful in corrosion performance studies where certain elements may dominate corrosion properties and resistance while others contribute minimally. However, for highly correlated features, Lasso tends to select only one of them while shrinking others towards zero, which may lead to biased coefficient estimation [24].

Exponential regression – This regression technique is used when the relationship between variables follows a non-linear trend, as commonly observed in electrochemical reactions and corrosion current values, where small environmental changes can lead to considerable variations in the electrochemical measurements. Models developed with this technique are particularly relevant when analysing i_{corr} and i_{pit}, as corrosion current densities tend to increase exponentially with chloride concentration or changes in alloy composition [25]. Unlike linear models, exponential regression allows for a better representation of aggressive corrosion behaviours.

These models were selected and implemented to evaluate their effectiveness in predicting corrosion behaviour and developing corresponding PREN indices while balancing accuracy, interpretability, and practical usability in civil engineering applications. Polynomial regression was initially considered due to its ability to capture complex, non-linear relationships, but its model outcome resulted in high complexity and an extensive number of terms and coefficients in the equation (50+), making its interpretation and practical application challenging.

Performance Evaluation Metrics

The predictive performance of the developed models was evaluated with different statistical metrics widely used in deterministic and probabilistic models, such as the root mean square error (RMSE) and coefficient of determination (R^2) given as [26]:

$$RMSE = \sqrt{\frac{1}{m}\sum_{i=1}^{m}(Y_i - \hat{Y}_i)^2} \quad (1)$$

$$R^2 = 1 - \frac{\sum_{i=1}^{m}(Y_i - \hat{Y}_i)^2}{\sum_{i=1}^{m}(Y_i - \bar{Y}_i)^2} \quad (2)$$

where Y_i and $\hat{Y}_i$ are actual and predicted outputs, respectively, and m is the number of total observations. MSE indicates the average root squared difference between the observed and predicted values across all observations, therefore, lower RMSE values represent more accurate predictions. R^2 is a widely used statistical indicator that measures how accurately the observed outputs are predicted by the developed model. R^2 close to 1 indicates that the better fit of the predictions of the regression model to actual data observations.

Developing PREN Indices Based on Electrochemical Metrics

To develop PREN indices corresponding to each corrosion performance-related values (i.e., E_{corr}, i_{corr}, E_{pit}, and i_{pit}), the coefficients from the normalized best-performing regression models were used. For E_{corr} and E_{pit}, the positive correlation with resistance was preserved. For i_{corr} and $_{ipit,}$ an inversion step was applied to ensure that higher corrosion

rates result in lower PREN values, maintaining consistency across all newly developed indices. More details are presented in the subsequent sections.

Dataset Partitioning and Model Development

To ensure robust model development and evaluation, the dataset underwent a series of preprocessing, training and validation steps, as outlined below:

(i) Dataset partitioning – Dataset, comprising 225 records for E_{corr} and i_{corr} and 180 records for E_{pit} and i_{pit}, was divided using an 80:20 split. 80% was randomly allocated for model training and validation of trained model, while the remaining 20% was held out for final testing. This approach maintained statistical consistency across subsets and supported a reliable assessment of model generalizability [27].

(ii) Data preprocessing – Dataset was assessed for completeness and consistency; neither missing values nor significant outliers were detected since they were obtained under uniform laboratory conditions, and thus, no additional cleaning was necessary. To ensure consistent scaling across all variables and avoid dominance of features with larger magnitude, feature scaling using a standardization method was applied to both the input (called feature) and output (called target) variables. This transformation converted the data into a standard normal distribution by subtracting the mean and dividing by the standard deviation for each variable, supporting numerical stability and optimal model performance [28].

(iii) Hyperparameter tuning – To optimize the model performance by tunning its hyperparameters (i.e. parameters initially assigned to some functions/settings in the ML algorithm), the training set (i.e. 80% of total dataset) was further subdivided into 10 folds to undergo a 10-fold cross-validation iteration process where each iteration involved using 9 folds for training and remaining 1 for validation. The validation fold was changed during repeated iterations until 10 iterations that yielded unique hyperparameters were complete. Grid search was employed to explore different hyperparameters and select one that yielded the lowest validation RMSE and R^2 score across folds, thereby identifying the optimal settings that support the development of 4 intended regression models [29].

(iv) Final model evaluation and selection – Each of the developed regression models was then tested on the 20% reserved testing set to evaluate their performance (using earlier mentioned metrics, R^2 and RMSE) on unseen data. Based on these evaluation results, the best-performing model was selected for each target electrochemical output variable (E_{corr}, E_{pit}, i_{corr}, and i_{pit}), ensuring both accuracy and reliability of the final predictive equations.

RESULTS AND DISCUSSION

Electrochemical Outputs from Potentiodynamic Polarization Test

Figures 3 and 4 elucidate the performance of the SS bars in different testing conditions (i.e. testing solution type, pH, chloride concentration), depicting the relationship between E_{corr} and i_{corr}, as well as the relationship between E_{pit} and i_{pit}. The severity level of corrosion damage is also included in the figures, where $i_{corr} > 10$ mA/m^2, $5 < i_{corr} < 10$ mA/m^2, $1 < i_{corr} < 5$ mA/m^2, and $i_{corr} < 1$ mA/m^2, indicates high corrosion, moderate, low, and passive corrosion regions, respectively. Aligning with decades of research findings on both carbon and SS rebar, decreasing pH (similar to reinforced concrete increasingly exposed to carbonation) and increasing chloride concentration decreases corrosion resistance due to passive film destabilization or localized passivity damage from chloride ions, respectively. Figures 3A to E, corresponding to CHS and pH ~12.5, reveal that Cl^- concentration increase results in a more negative E_{corr} value, indicating the increasing probability of active corrosion, which is supported by their i_{corr} values that shows transitioning from negligible/passive corrosion to low or high corrosion zones. A similar trend is observed in E_{pit} and i_{pit} plots shown in Figure 4A to E, where increasing Cl^- content resulted in lower E_{pit} and higher i_{pit} values, indicating decreasing potential value to be reached before pitting corrosion begins and an increasing current at passivity resulting in pitting corrosion. Although bars in SPSS (Figure 3F to J and 4F to J) and SPS (Figure 3K to O and 4K to O) solution also showed a similar trend, their E_{corr} and E_{pit} values were higher (more positive), and their i_{corr} and i_{pit} were lower than bars in CHS solution, indicating the better corrosion resistance in SPS and SPSS solutions. It should be noted that only 2205 SS grade was tested at 30% chloride concentration, as it was the only rebar type that demonstrated great pitting resistance at 25% chloride addition.

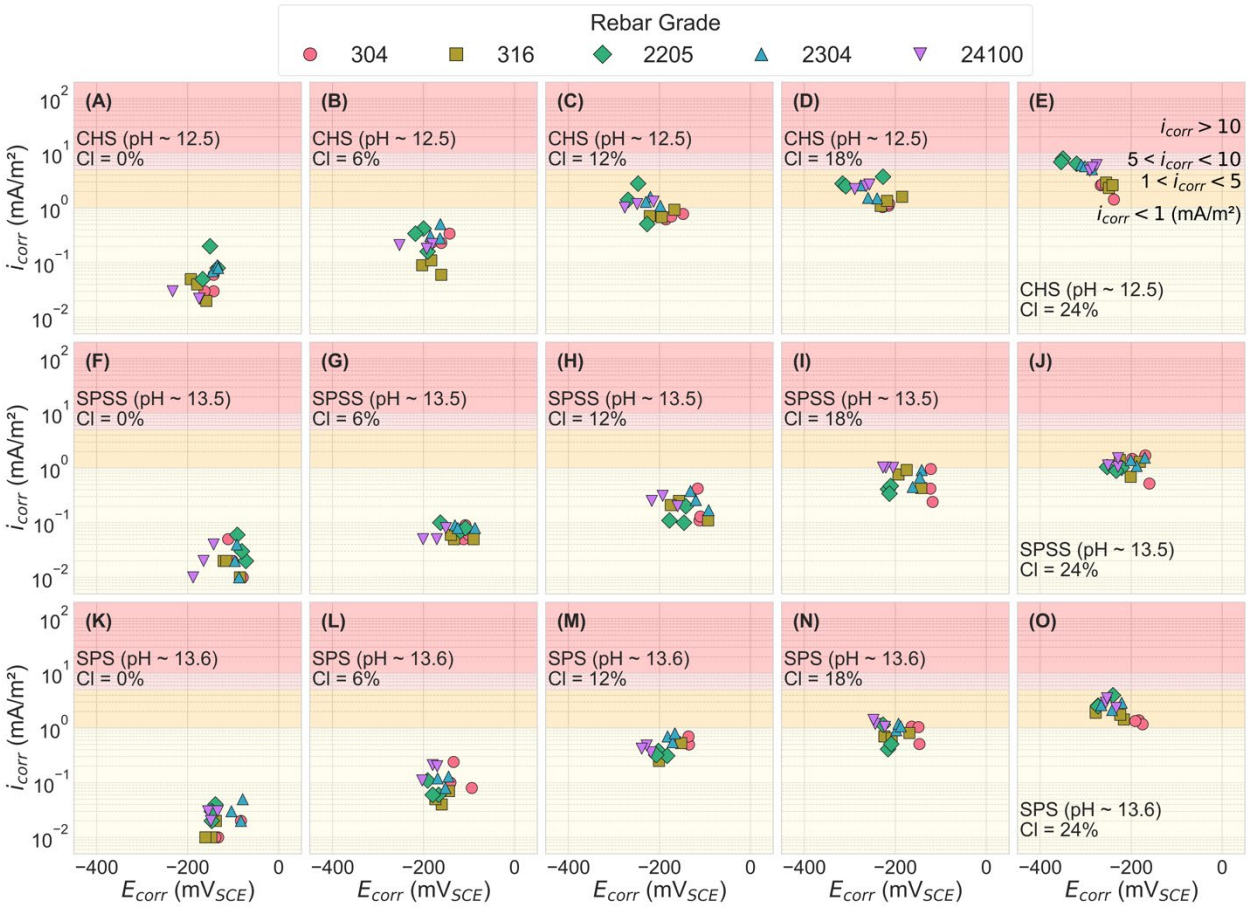

Figure 3— i_{corr} versus E_{corr} values for SS grades in different test solutions (CHS – A to E, SPSS – F to J, and SPS – K to O) under varying pH and Cl^- concentrations. Shaded regions represent distinct corrosion activity level: $i_{corr} > 10$ mA/m^2 (high corrosion), $5 < i_{corr} < 10$ mA/m^2 (moderate corrosion), $1 < i_{corr} < 5$ mA/m^2 (low corrosion), and $i_{corr} < 1$ mA/m^2 (passive corrosion)

Figure 4— i_{pit} versus E_{pit} values for SS grades in different test solutions (CHS – A to E, SPSS – F to J, and SPS– K to O) under varying pH and Cl^- concentrations. Shaded regions represent distinct corrosion activity level: i_{corr} > 10 mA/m^2 (high corrosion), 5 < i_{corr} < 10 mA/m^2 (moderate corrosion), 1 < i_{corr} < 5 mA/m^2 (low corrosion), and i_{corr} < 1 mA/m^2 (passive corrosion)

Influence of Input Variables on Corrosion Behaviour

Electrochemical data from Figures 5 and 6 were further elucidated to better understand the corrosion performance of the SS alloys as a function of alloying composition, pH, and chloride concentrations. Figures 5 and 6 show the variation of E_{corr}, i_{corr}, $E_{pit,}$ and i_{pit} as a function of key input variables for different SS grades (304, 316, 2205, 2304, and 24100). These scatter plots present individual data points for each SS alloy sample, with dashed lines representing the mean trendlines and shaded regions indicating the range between the minimum and maximum values for each input variable. For E_{corr} and i_{corr} values plotted versus input variables, as shown in Figure 5A – L, varying trends can be observed.

Alloys with <18% Cr (i.e. austenitic 304, 316, and 24100) possessed E_{corr} between -80 and -300mV$_{SCE}$ across all testing solutions (values near the higher end are from low chloride solution and values near the lower end are from high chloride CH/SPS/SPSS solution), whereas alloys with >22% Cr (i.e. duplex 2205 and 2304) possess a wider E_{corr} range between -80 and -380 mV$_{SCE}$ across all testing solution. This trend indicates that increasing Cr content in SS rebar alloys, at least in the duplex SS grades, decreases (i.e. more negative) E_{corr} of the alloy, which loosely interprets as a higher probability of active corrosion. It is essential to point out that only six samples (i.e. datapoints) of the 2205 and 2304 exist at potentials below -300mV$_{SCE}$, which may be outliers (shown by broken grey cilrcles), and it is possible that the effect of increasing Cr from 16.6 to 22.6 wt.% is negligible on measured E_{corr} value. Figure 5G shows the corresponding i_{corr} values of these alloys. Following their more negative E_{corr} value, the duplex alloys with higher Cr content possess higher mean i_{corr} values, indicating greater severity to corrosion. Increasing Cr in the alloy was expected to increase the Cr_2O_3 layer in the passive oxide film, resulting in better protection against corrosion, but such beneficial effect was not observed beyond 18 wt.% on alloys examined in the present work.

The effect of Ni beyond 3.3 wt.% on corrosion resistance is inconclusive. Increasing Ni content yielded a more positive mean E_{corr} value, suggesting a lower susceptibility to corrosion, Figure 5B. However, if the earlier mentioned six samples of the duplex grade existing below -300mV are considered outliers, the mean and maximum (representing passive corrosion) and minimum (representing active corrosion) range of the E_{corr} plot is similar beyond 3.3 wt.% Ni content, suggesting that Ni addition beyond 3.3 wt.% may not be beneficial to corrosion resistance. This observation is supported by the slight decrease in mean i_{corr} values (shown in Figure 5H) as Ni increases beyond 3.3 wt.%. Despite a slight decrease in mean i_{corr} values, the similarity in min-max i_{corr} range above 3.3 wt.% Ni content further supports the absence of Ni benefits beyond that addition. Past works on SS examined in high pH environments also observed the contribution of Ni to passivity and protection against corrosion to be limited. Unlike Cr, that forms its own oxide and participates in the formation of different oxide spinels with Fe across the passive film layers, Ni mainly forms oxide spinel with Fe and stabilizes the outer layer of the oxide film [15].

Increasing Mo beyond 0.5 wt.% did not improve corrosion resistance of SS rebar. Alloys with 0.2-0.5 wt.% Mo (i.e. trace amounts) showed more positive mean E_{corr} values than grades with higher Mo content as shown Figure 5C, suggesting increasing susceptibility to corrosion as Mo content increases. If the 2304 and 2205 samples with E_{corr} values below -300 mV_{SCE} are considered outliers, then the min-max E_{corr} range is similar at low and high Mo content. The corresponding i_{corr} values shown in Figure 5I also supports the similar or negative influence of increasing Mo content. Some authors have also reported similar minimal or negative impact of increasing Mo content in SS rebar alloys examined in high pH concrete environment [4].

Mn addition to SS rebar, in replacement of Ni, resulted in similar passive corrosion resistance but may lower active corrosion resistance, which is attributed to the presence of several Mn oxide species, whose defect density are higher than Ni oxides, in the passive film [15]. As Mn content increases beyond trace amount (<2 wt.%), a decrease (more negative) in mean E_{corr} value is observed in Figure 5D, suggesting an increasing probability of corrosion with Mn increment. However, the min-max E_{corr} range observed on high-Mn 24100 SS rebar grade (also possessing low Ni, Cr, and Mo) are narrower (between -125 and -300 mV_{SCE}) than the low-Mn austenitic and duplex SS alloys (304, 316, 2304, 2205). This suggests that when E_{corr} values are monitored over time to determine the corrosion durability of field reinforced concrete, the high-Mn SS rebar alloys in concrete exposed to the chloride-laden environment may not show large/wide transition from the passive (i.e. more positive E_{corr}) to active (i.e. more negative E_{corr}) corrosion, which is consistent with past findings [30]. In particular, the minimum (i.e. active E_{corr}) range of both Ni-rich and Mn-rich alloys is similar when the outliers are not considered, while the maximum range (i.e. passive E_{corr}) of the Mn-rich alloys are more negative. Figure 5J shows the corresponding i_{corr} values of these alloys and slight increase in mean and a negligible difference in min-max i_{corr} is observed between the Ni-rich and Mn-rich alloys, indicating little beneficial or detrimental effect to Mn increment in SS rebar alloys.

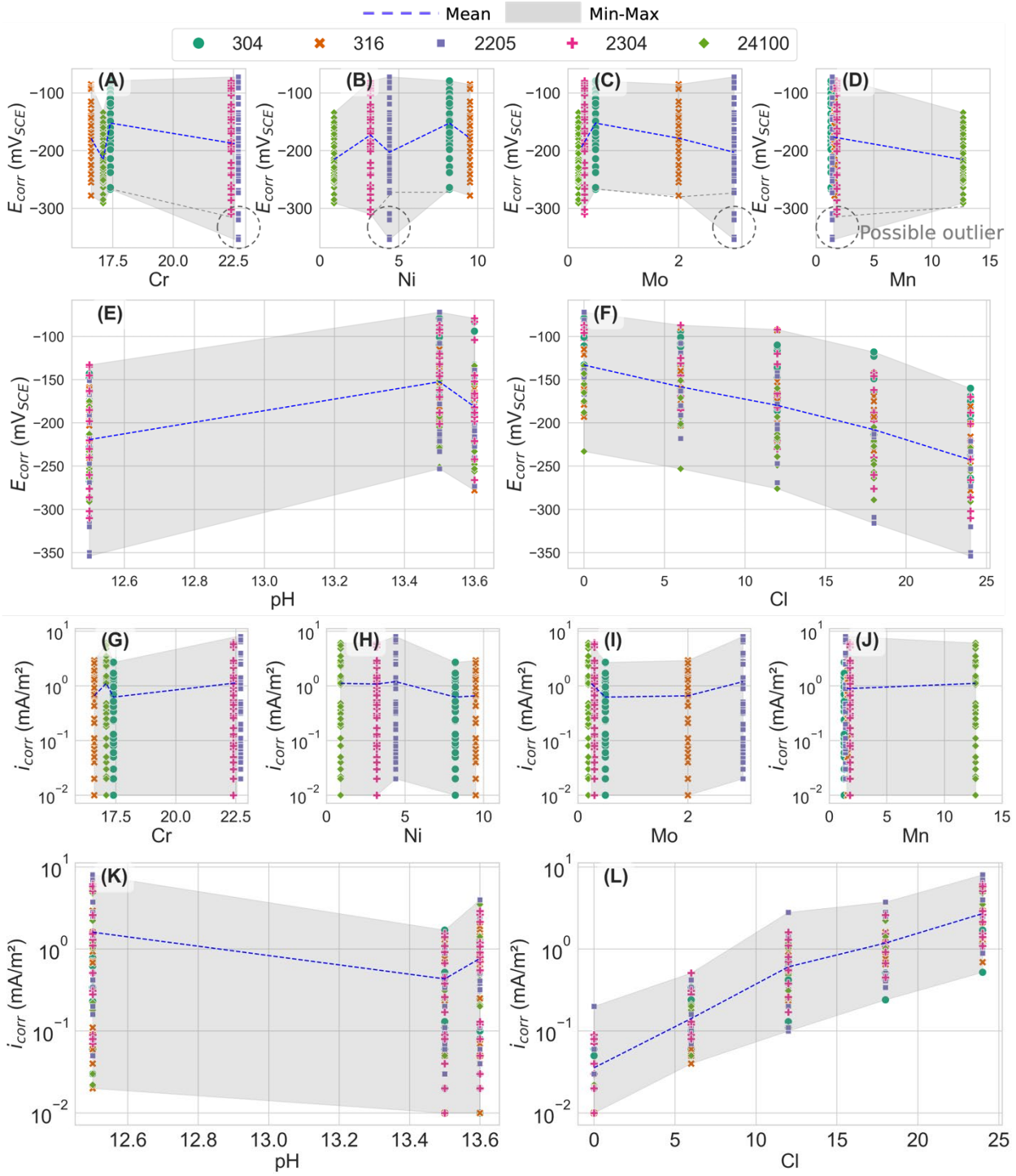

Figure 5— Variation of E_{corr} (A – F) and i_{corr} (G – L) as a function of input variables for different SS grades with dashed lines for mean trendlines and shaded regions representing the Min-Max range of the data points

While Figure 5 considers the corrosion properties of the SS alloys under non-induced conditions (i.e. E_{corr} and i_{corr}, from the natural state of the bars with their naturally formed passive film before application of polarization potential beyond the Tafel linear region), Figure 6 presents the corrosion properties obtained after significant polarisation level (i.e. E_{pit} and i_{pit}). For E_{pit} and i_{pit} values plotted versus input variables shown in Figure 6A - L, varying behaviour can be observed. In Figure 6A, the mean E_{pit} slightly increased with increasing Cr content, while the min-max range

(excluding noted outliers) are similar (existing between 80-420 mV_{SCE}) for all samples, suggesting negligible effect of Cr addition beyond the 16.6 wt.% observed earlier in Figure 5. The corresponding i_{pit} values in Figure 6G also indicate slight increase to ~17.5 wt.%Cr and a negligible change in mean i_{pit} with increasing Cr content, as well as a similar min-max range (excluding possible outlier). In Figure 6B, the mean E_{pit} value fluctuates with increasing Ni content, with the average change remaining negligible beyond the earlier observed 3.3 wt.% Ni, and the outlier-free min-max E_{pit} range are also similar. Their corresponding i_{pit} values in Figure 6H also indicate negligible change beyond 3.3wt.%Ni and a slight increase in i_{pit} value up to that point. In Figures 6C and 6I, increasing Mo content beyond trace amount did not benefit E_{pit} (decreasing value) and i_{pit} (increasing value). However, Mo-containing alloys possess much narrower E_{pit} and i_{pit} min-max range. In Figure 6D, increasing Mn content slightly decreases mean E_{pit}, suggesting a negligible overall effect. Specifically, while an increase in Mn content resulted in a slight decrease in E_{corr} and E_{pit}, the overall variations is within 20-50 mV, which may be considered negligible as they are present in the typical linear polarisation value range. This is supported by negligible mean i_{pit} change shown in Figure 6J as Mn content increases. In Figures 6E and 6K, the potential and current values that must be reached before pitting corrosion is experienced increases and decreases, respectively, with increasing pH, whereas the trend is opposite with increasing chloride concentration, as shown in Figures 6F and 6L. It should be noted that only the 24100 SS grades showed pitting corrosion at lower 5% Cl^- and only the 2205 SS grades showed pitting properties beyond 25% Cl^-. The absence of a conclusive increasing or decreasing E_{pit} or i_{pit} trend in Figure 6 A-D and G-J indicates the challenge associated with determining the contribution of SS alloying composition to pitting corrosion through the use of commercial SS alloys containing multi and interdependent elemental components.

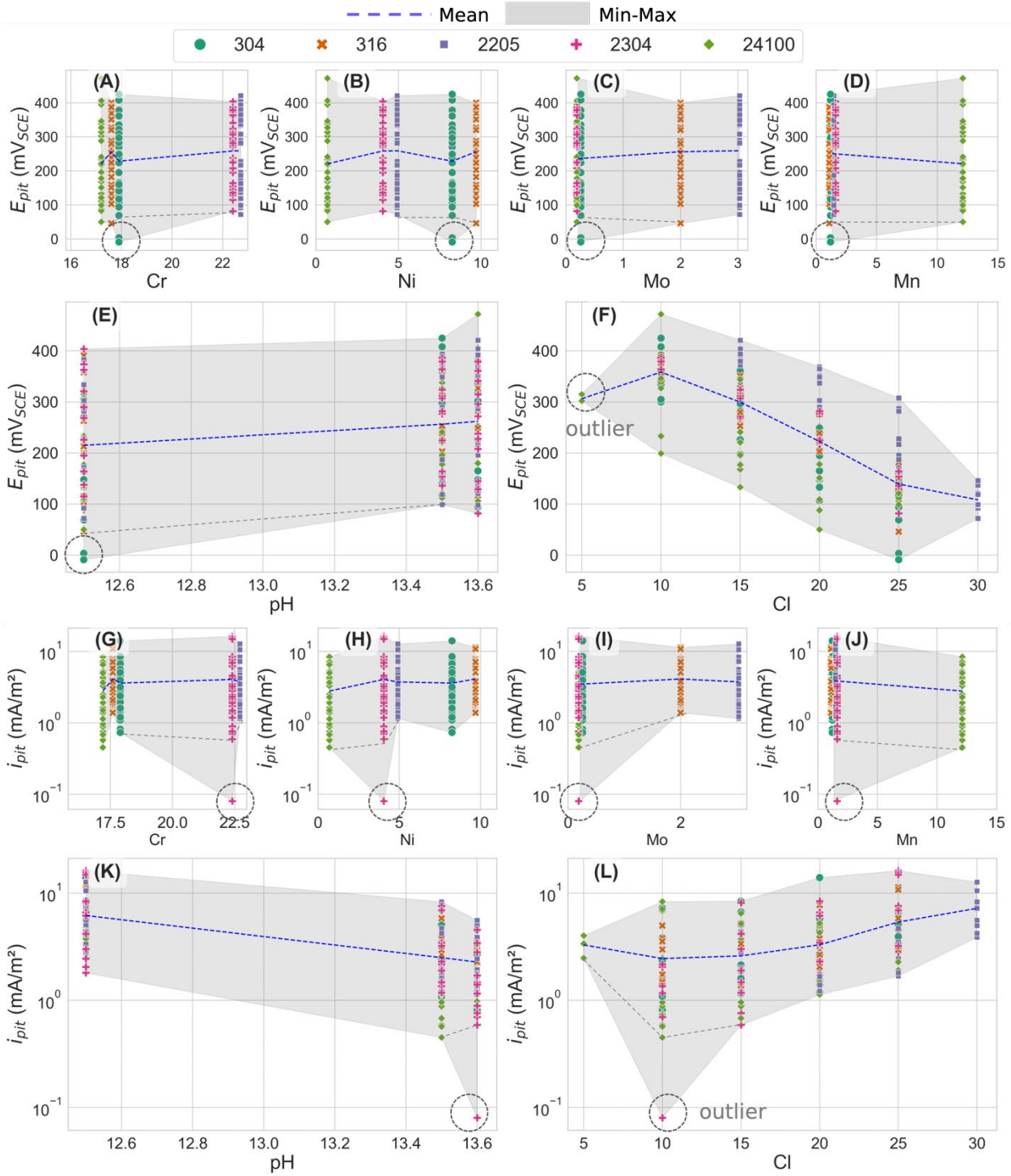

Figure 6— Variation of E_{pit} (A – F) and i_{pit} (G – L) as a function of input variables for different SS grades with dashed lines for mean trendlines and shaded regions representing the Min-Max range of the data points

Machine Learning-Based Regression Models

Four different models developed and trained with 80% of the experimental dataset were used to predict corrosion performance indicators (i.e. target electrochemical output variables) and compared with the reserved 20%

experimental dataset to test accuracy with unseen data. Figure 7 presents the model's outcome, including the best-performing models per target output, where each model was evaluated on the testing dataset, and the predicted target values were compared to the actual experimental ones for both training and testing datasets corresponding to each target output. The results from two statistical evaluation metrics (R^2 and RMSE) used to assess the performance of each of the 4 models are presented in Table 4. As shown in Figure 7 and Table 4, considering the desired target output value, each developed model was able to predict the corrosion property with variable accuracy. Based on combined RMSE and R^2 metric, the best-performing model for E_{corr}, i_{corr}, E_{pit} and i_{pit} is Linear, Exponential, Ridge and Ridge, respectively, as shown by a broken green border. Furthermore, the results of the best-performing regression models for each electrochemical measure are summarised in the form of predictive equations shown in Equations 3-6.

In the case of E_{corr} and E_{pit} equations, the more negative the coefficients indicate that the corresponding input variable contributes to a lower (more negative) corrosion or pitting potential, thereby increasing susceptibility to corrosion. Among variables, only Mo and pH exhibit a consistently positive influence on potential-related equations, suggesting a reduction in corrosion risk – although their overall impact remains limited due to their relatively small coefficients. Ni and Mn appear to exert the strongest negative influence on potential values, as reflected by their highly negative coefficients. This suggests that increased compositions of these elements shift the corrosion and pitting potentials towards more negative values, thereby indicating higher susceptibility to corrosion. In the case of i_{corr} and i_{pit}, more negative coefficients generally indicate that the corresponding input variables contribute to lower corrosion and pitting current densities, which are associated with a reduced corrosion rate and improved corrosion resistance. Consistent with potential-related equations, Mo and pH – both exhibiting negative coefficients – contribute to reducing current densities, indicating their beneficial role. In contrast, Cr and Ni contribute to increased current densities, suggesting a detrimental effect compared to Mo and pH. Mn, Cr, Ni and chloride concentration contribute to increased corrosion rates having a negative effect on corrosion resistance. In general, the sign-associated effect of each coefficient on corrosion resistance was consistent across potential-related and current-related equations, reinforcing the agreement in their contribution to overall corrosion performance.

$$E_{corr} = -3.98(Cr\%) - 4.81(Ni\%) + 0.50(Mo\%) - 4.97(Mn\%) + 0.41(pH) - 0.64(Cl^-) \quad (3)$$

$$i_{corr} = \exp(0.94(Cr\%) + 0.92(Ni\%) - 0.16(Mo\%) + 1.03(Mn\%) - 0.49(pH) + 1.50(Cl^-) - 1.10) \quad (4)$$

$$E_{pit} = -0.48(Cr\%) - 1.00(Ni\%) + 0.43(Mo\%) - 1.10(Mn\%) + 0.27(pH) - 0.98(Cl^-) \quad (5)$$

$$i_{pit} = 2.23(Cr\%) + 3.33(Ni\%) - 0.71(Mo\%) + 3.31(Mn\%) - 0.63(pH) + 0.53(Cl^-) \quad (6)$$

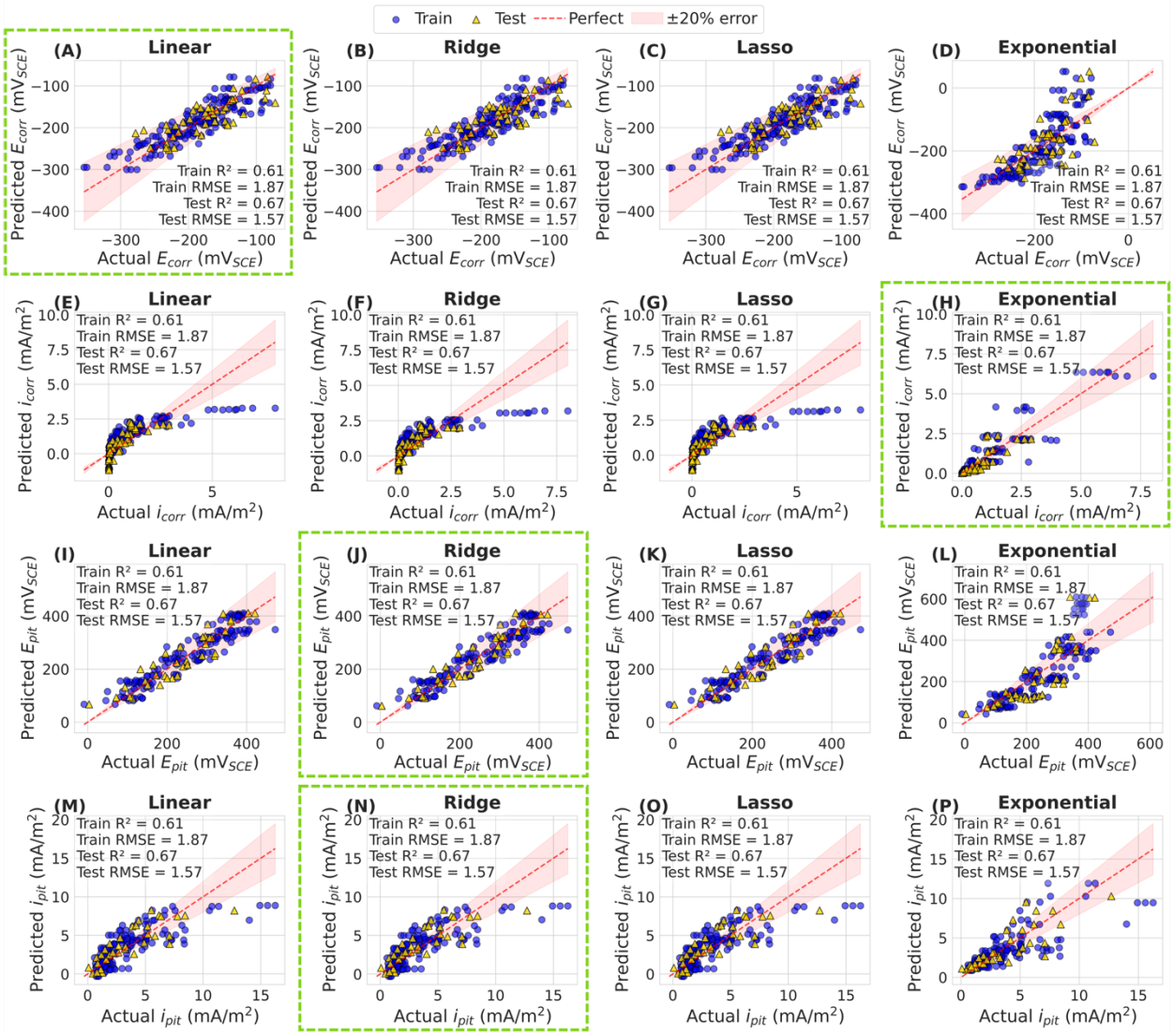

Figure 7— Comparison of predicted versus actual experimental values for E_{corr}, i_{corr}, E_{pit} and i_{pit} using the corresponding regression model across the experimental dataset. Best-performing model per target is specified by a broken green border.

Table 4— Developed models performance metrics calculated for both training and testing data corresponding to each target output.

Target output	Model	Training		Testing		Best-performance
		RMSE	R^2	RMSE	R^2	
E_{corr}	Linear Regression	25.59	0.79	30.08	0.63	Linear Regression
	Ridge Regression	26.67	0.79	30.33	0.63	
	Lasso Regression	26.67	0.79	30.34	0.63	
	Exponential Regression	52.77	0.18	56.65	-0.30	
i_{corr}	Linear Regression	0.92	0.60	0.60	0.31	Exponential Regression
	Ridge Regression	0.93	0.60	0.56	0.39	
	Lasso Regression	0.93	0.60	0.36	0.36	
	Exponential Regression	0.58	0.84	0.40	0.69	
E_{pit}	Linear Regression	36.31	0.88	38.33	0.84	Ridge Regression
	Ridge Regression	36.64	0.88	36.42	0.86	
	Lasso Regression	36.32	0.87	37.97	0.85	
	Exponential Regression	82.37	0.39	90.72	0.12	

i_{pit}	Linear Regression	1.88	0.60	1.55	0.68	Ridge Regression
	Ridge Regression	1.88	0.60	1.55	0.68	
	Lasso Regression	1.88	0.60	1.55	0.68	
	Exponential Regression	1.87	0.61	1.57	0.67	

To avoid relying solely on sign conventions and coefficient weights associated with Equations 3-6, SHAP (Shapley Additive exPlanations)-based feature importance was employed to evaluate the influence of alloy composition and environmental factors as input variables on the predicted corrosion performance-related outputs. SHAP assigns an interpretable contribution value to each feature, offering a model-agnostic and comprehensive approach for understanding feature relevance and interactions [31]. Figure 8 presents each feature's mean absolute SHAP values across four electrochemical targets. Ni and Mn exhibited the greatest influence on E_{corr} and i_{pit}, while Cl^- and pH were dominant for i_{corr}. Cr showed moderate importance to i_{corr} and i_{pit} and it has lowest impact on E_{pit} predictions. Mo also contributed the least across all targets. These results underscore the distinct role of individual variables and the multifactorial nature of SS corrosion resistance in chloride-laden alkaline environments.

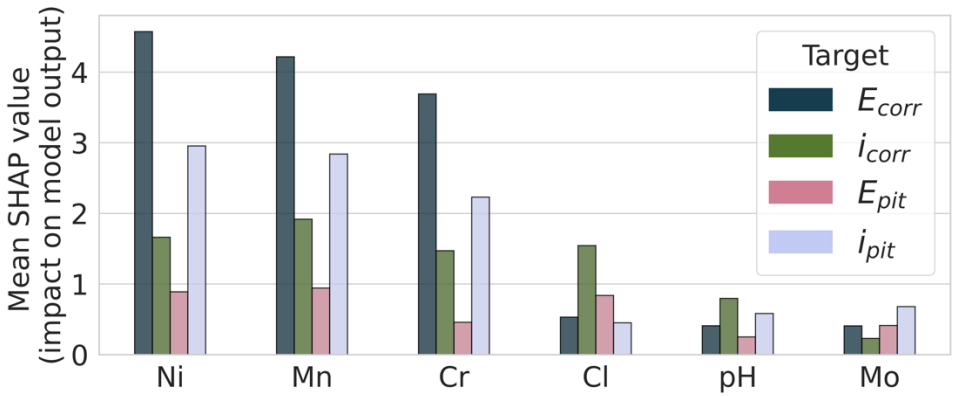

Figure 8— SHAP-based feature importance values for each input variable across all target output parameters.

Figure 9 summarizes the relationship between the predicted (filled marks) and actual (non-filled marks) electrochemical parameters – E_{corr} (9A), i_{corr} (9B), E_{pit} (9C), and i_{pit} (9D) – across varying Cl^- concentrations (wt.%) for different SS grades. The close clustering of predicted and actual data points in most regions, mainly for E_{corr} and E_{pit}, suggests high model accuracy. However, as expected, the scatter at higher Cl^- percentages (mainly >24% Cl^-) in i_{corr} and i_{pit} areas indicates areas where the model may have limitations in adequately capturing the corrosion behaviour of SS grades. The graphs also illustrate the behaviour of various SS grades across different Cl^- content and elucidate how each grade responds to the evaluated electrochemical parameter. For instance, grades such as 304 and 316 generally exhibit "better performance" based on E_{corr} compared to other grades, while the 2205 grade was the least performing using this parameter. Conversely, SS grades 2205 and 2304 demonstrate better performance based on E_{pit}. When using i_{corr} as a criterion, grades 304 and 316 show the best performance, while 2205 and 24100 performed optimally when i_{pit} is used as a criterion. Overall, Figure 9 shows the variation in conclusion that can exist when different electrochemical parameters are used in determining and ranking the corrosion performance of SS rebar alloys in a concrete environment.

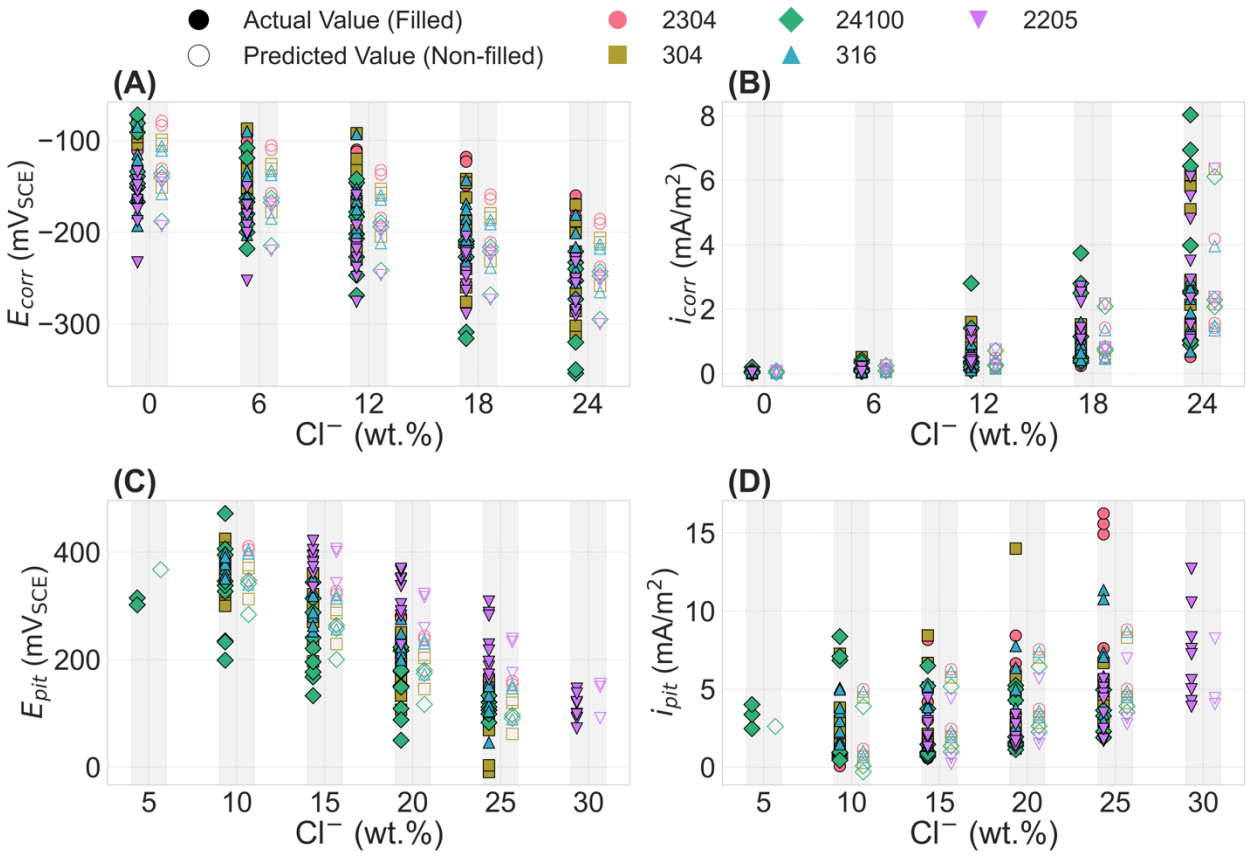

Figure 9— Comparison of predicted and actual electrochemical parameters: (A) E_{corr}, (B) i_{corr}, (C) E_{pit} and (D) i_{pit}, obtained from best-performing regression models for various SS grades across different chloride concentrations.

Using standardised coefficients obtained from best-performing regression modes corresponding to each target value, PREN formula was generated and presented in Equations 7-10. It should be noted that for E_{corr} and E_{pit}, the values calculated from scaled equations exhibit a positive correlation with the actual E_{corr} and E_{pit} values. As such, their corresponding PREN indices remain consistent with original regression-based equations, where higher PREN values indicate improved corrosion performance through more positive corrosion or pitting potentials. Conversely, for i_{corr} and i_{pit}, the best-performing regression models showed a positive correlation with the actual current densities – meaning that higher i_{corr} or i_{pit} values (indicating less corrosion resistance) yield higher outputs from the scaled equations. To maintain consistency in the interpretation of PREN indices across all targets and also with the existing PREN concept (i.e. the higher the PREN index, the better the corrosion performance), the scaled equations for i_{corr} and i_{pit} were inverted by subtracting the predicted values from its maximum, thus reversing the relationship. This adjustment ensures that increasing corrosion or pitting current densities corresponds to lower PREN values, aligning with the conventional understanding that higher corrosion currents indicate poorer corrosion resistance.

$$PREN_{E_{corr}} = -3.98(Cr\%) - 4.81(Ni\%) + 0.50(Mo\%) - 4.97(Mn\%) + 0.41(pH) - 0.64(Cl^-) \quad (7)$$

$$PREN_{i_{corr}} = 10 - (\exp(0.94(Cr\%) + 0.92(Ni\%) - 0.16(Mo\%) + 1.03(Mn\%) - 0.49(pH) + 1.50(Cl^-) - 1.10)) \quad (8)$$

$$PREN_{E_{pit}} = -0.48(Cr\%) - 1.00(Ni\%) + 0.43(Mo\%) - 1.10(Mn\%) + 0.27(pH) - 0.98(Cl^-) \quad (9)$$

$$PREN_{i_{pit}} = 15 - (2.23(Cr\%) + 3.33(Ni\%) - 0.71(Mo\%) + 3.31(Mn\%) - 0.63(pH) + 0.53(Cl^-)) \quad (10)$$

Figure 10 illustrate the relationship between developed parameter-based PREN index (presented in Equations 7-10) and their corresponding experimental electrochemical parameters (i.e. E_{corr}, i_{corr}, E_{pit}, and i_{pit}) to understand the accuracy of the models used and developed formula and demonstrate how these variables influence the corrosion

behaviour of SS alloys. Figures 10A and 10C show a clear positive correlation between E_{corr}/E_{pit} and their corresponding PREN indices, indicating that higher corrosion and pitting potentials – markers of better corrosion resistance – translate into higher potential-based PREN values. Conversely, Figures 10B and 10D demonstrate a negative correlation between the PREN index and i_{corr}/i_{pit}, where increasing current densities (i.e., higher corrosion rates) correspond to lower PREN values, as expected for reduced corrosion resistance.

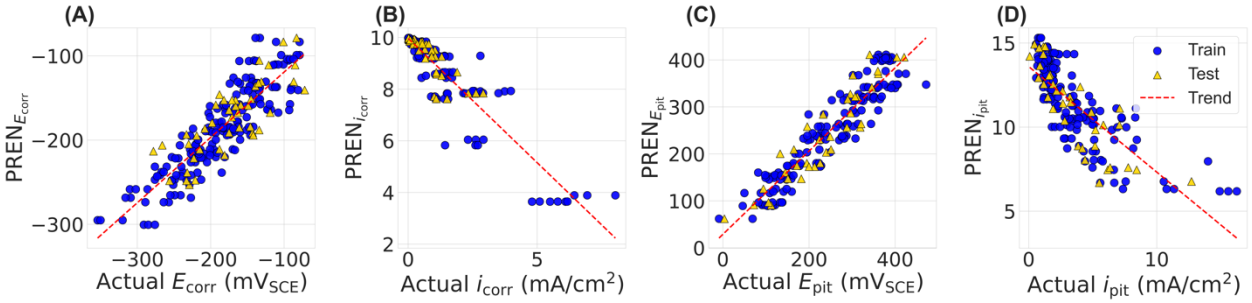

Figure 10— Relationship between developed PREN index and the target electrochemical outputs based on experimental data.

Comparison, Implications, and Recommendations

An overall ranking was obtained by using PREN index formulas to predict the corrosion performance of commercial SS grades exposed to SPS (pH ~ 13.6) containing 24 wt.% Cl^- concentration is also presented in Table 5. SPS was chosen as the test solution because it is one of the most common environments analogous to the alkaline conditions found in concrete and the 24 wt.% Cl^- concentration was selected as a worst-case scenario to assess the alloys' performance in highly chloride-laden environments. To calculate the overall ranking of alloys, two multi-criteria decision-making methods were applied: Analytic Hierarchy Process (AHP) and Weighted Sum Method (WSM). Both methods consider 4 key criteria related to alloy ranking, including predicted $E_{corr,}$ i_{corr}, E_{pit}, and i_{pit} values and corresponding PREN indexes developed based on them (i.e. $PREN_{Ecorr}$, $PREN_{icorr}$, $PREN_{Epit}$, $PREN_{ipit}$). The AHP method involves normalizing the data by dividing each value by the sum of its corresponding column (criterion) to account for the relative importance of each criterion. The final scores for each alloy were obtained by averaging the normalized values across all criteria. Alloys with lower scores are considered to perform better overall. In contrast, the WSM method assumes equal importance for all criteria and sums the ranks across all categories, where a lower total score indicates better overall performance.

As shown in Table 5, both methods produced consistent rankings, with 2205 SS alloy emerging as the top performer due to its consistently low scores across the criteria. The next best performance was 304, containing higher Ni and lower Cr content than 2205. Both Ni-rich alloys outperformed the Mn-rich 24100 alloy which ranked lowest in both metrics and existing PREN index, indicating relatively poor pitting corrosion resistance and less beneficial effect of its Mn component than Ni. It should be noted that some variation in ranking may occur depending on the relative importance or weighting of pH and Cl^- content in different predictive and PREN-related equations. In other words, depending on electrochemical test used to examine these SS grades, such as linear polarization resistance to record E_{corr} and i_{corr} measurement over time, their ranking may fit more with the parameter-based PREN rather than overall ranking. For instance, alloys with higher Mo content, such as 2205 (22.7 wt.% Cr) tend to perform better in terms of pitting corrosion resistance under polarized conditions, as indicated by their ranking in $PREN_{Epit/ipit}$ criteria, but ranked lower under natural or linearly polarized conditions. In contrast, the enrichment of Ni in 304 (8.2 wt.% Ni) induces better corrosion resistance under free or linearly polarized conditions than at large/high polarisation conditions, as indicated by their $PREN_{Ecorr/icorr}$. Additionally, Mn-rich alloys such as 24100 SS (~12 wt.%) may also show high pitting corrosion resistance if i_{pit} was recorded, as indicated by the 2nd place ranking in $PREN_{ipit}$. Furthermore, the variation in the ranking of SS grades when using the existing PREN compared to the developed PREN index underscores the limitations of the existing PREN for structural applications characterized by high alkalinity, low temperatures, and the presence of deleterious ions such as chloride.

Table 5—Summary of the overall ranking of SS grades based on the developed PREN index for various electrochemical criteria and existing PREN index in SPS testing solution containing 24 wt.% Cl^-

Criteria	Rebar's ranking

	304	316	2205	2304	24100
$PREN_{Ecorr}$	1	3	4	2	5
$PREN_{icorr}$	2	1	3	4	5
$PREN_{Epit}$	4	3	1	2	5
$PREN_{ipit}$	3	4	1	5	2
Overall ranking using developed model – WSM (lower score is better)	2	3	1	4	5
Overall ranking using developed model – AHP (lower score is better)	2	3	1	4	5
Ranking using existing PREN index	4	2	1	3	5

Several refinements can be considered to enhance the accuracy of the PREN index and regression models. Although regularization methods, such as Lasso or Ridge regression used in current work, helped mitigate overfitting and capture more complex relationships, particularly in heterogeneous datasets, advanced machine learning models, such as random forests, support vector machines, or neural networks, can further improve the model's ability to capture non-linear interactions and underlying patterns in large, complex datasets. Additionally, robust regression techniques and ensemble modelling approaches could improve the model's resilience to outliers, enhancing overall predictive performance. Incorporating more advanced data preprocessing and feature engineering, as well as accounting for environmental and temporal variables (e.g., humidity, exposure time, cyclic wetting and drying, etc.), could better reflect the real-world corrosion behaviour of SS. Finally, considering uncertainty quantification would ensure that the model remains reliable across various datasets, addressing the inherent variability in material properties and corrosion phenomena. Nevertheless, it is important to emphasize that one of the key objectives of this work was to develop a simple, interpretable, and straightforward PREN equation that can be used to estimate corrosion resistance based on input variables. This approach ensures usability by rebar manufacturers, engineers, and decision-makers (e.g. bridge owners and transportation ministries) without the need for advanced computational tools or specialized programming skills while maintaining a balance between accuracy and accessibility.

SUMMARY AND CONCLUSION

This study introduced a PREN index applicable to evaluate the corrosion resistance of SS rebar alloys in high alkaline concrete environments, which differs significantly from traditional PREN developed for applications of SS in high-temperature, acidic or neutral exposure conditions. The developed PREN index, based on four common electrochemical parameters in rebar corrosion studies, offers a new assessment tool for ranking commercially existing SS grades to be used in different concrete mixtures and exposure environments. Key findings from the study are summarised as follows:

- PREN index equations, derived using the standardized coefficients obtained from the regression models based on literature data in this study are as follows:

$$PREN_{E_{corr}} = -3.98(Cr\%) - 4.81(Ni\%) + 0.50(Mo\%) - 4.97(Mn\%) + 0.41(pH) - 0.64(Cl^-)$$

$$PREN_{i_{corr}} = 10 - (\exp(0.94(Cr\%) + 0.92(Ni\%) - 0.16(Mo\%) + 1.03(Mn\%) - 0.49(pH) + 1.50(Cl^-) - 1.10))$$

$$PREN_{E_{pit}} = -0.48(Cr\%) - 1.00(Ni\%) + 0.43(Mo\%) - 1.10(Mn\%) + 0.27(pH) - 0.98(Cl^-)$$

$$PREN_{i_{pit}} = 15 - (2.23(Cr\%) + 3.33(Ni\%) - 0.71(Mo\%) + 3.31(Mn\%) - 0.63(pH) + 0.53(Cl^-))$$

- The overall ranking of the SS grades, from best to worst, based on different applied criteria, using SPS testing solution at pH 13.6 and containing 24 wt.% Cl^-, follows: 2205, 304, 316, 2304, and 24100, while ranking based on most accurate PREN index (i.e. $PREN_{Epit}$) follows: 2205, 24100, 304, 316, and 2304.
- The contribution of individual alloying elements to corrosion resistance in concrete environments varies, and not all elements beyond a certain amount provide significant benefits. For instance, SS 2205 containing ~4 wt.% Ni and 3 wt.% Mo ranked highest overall, suggesting that a balanced combination of these elements enhances

corrosion resistance in chloride-rich concrete environments. SS 304, with 8 wt.% Ni and no Mo, ranked second, while SS 316, with the highest Ni content (9 wt.%) and 2 wt.% Mo, ranked third. These results suggest that increasing Ni beyond ~3-4 wt.% may not yield additional corrosion resistance benefits in these conditions. The role of Mn appears less conclusive; although Mn-rich alloys like 24100 showed strong performance for certain electrochemical parameters (e.g., i_{pit}), their overall ranking remained low. This may be due to the substantial replacement of Ni with Mn, implying that maintaining a minimum Ni content (e.g. ~4 wt.%) may be necessary for balanced corrosion resistance. Similarly, increasing Cr content beyond ~17 wt.% did not consistently improve performance, as alloys with higher Cr sometimes exhibited lower electrochemical values and PREN rankings. These findings highlight the importance of optimising—not simply maximising—the content of individual alloying elements for corrosion performance in concrete environments.

- SHAP-based feature importance analysis revealed that Ni and Mn most strongly influenced E_{corr} and $i_{pit,}$ while Cl^- and pH were dominant for i_{corr} predictions. These findings highlight the multifactorial nature of SS corrosion resistance and the distinct roles of individual alloying and environmental variables in chloride-rich alkaline environments.
- Conventional PREN index, originally developed for high-temperature, acidic or neutral environments, does not adequately reflect the conditions found in concrete structures. The new-developed PREN indices proposed in this study account for key environmental factors such as high pH and chloride exposure, leading to a more meaningful ranking of SS grades for civil engineering applications. The significant differences observed between the new and existing PREN rankings underscore the necessity of this tailored approach for civil engineering usage.
- Although the regression models used to develop the PREN indices were enhanced with application of advanced regression techniques (such as Ridge, Lasso and Exponential), data tunning and rigorous preprocessing to allow better handling of non-linearity and variable interactions, and strengthening model performance and physical relevance of using PREN indices for corrosion prediction, applying advanced machine learning models could further enhance model accuracy and predictive performance. However, these methods do not yield simple analytical expressions, which limits their ease of use for practical engineering applications.
- While pH and chloride concentration were used as the primary differentiators of environmental conditions, other concrete-specific factors—such as ionic composition, chloride binding capacity related to specific cement types, and porosity—as well as the influence of surrounding testing conditions (e.g., pore solution vs. mortar vs. concrete) also play critical roles. Future work will aim to incorporate these variables, including cathode current densities, to better link electrochemical measurements with actual durability performance.
- Finally, the developed PREN formula aids quantitative ranking of SS grades using various corrosion criteria and provides a non-destructive tool for performance assessment in concrete environments. The developed PREN indices support alloy optimization by accounting for pH variability and chloride exposure—factors often overlooked in conventional indices. Overall, this work lays the foundation for a corrosion-performance-driven alloy design strategy, with promising applications in material selection, durability assessment, and future SS innovation in civil infrastructure.

REFERENCES

[1] I.G. Ogunsanya, C.M. Hansson, Detection of the critical chloride threshold of carbon steel rebar in synthetic concrete pore solutions, RILEM Technical Letters 3 (2018) 75–83. https://doi.org/10.21809/rilemtechlett.2018.70.

[2] I.G. Ogunsanya, C.M. Hansson, Influence of chloride and sulphate anions on the electronic and electrochemical properties of passive films formed on steel reinforcing bars, Materialia (Oxf) 8 (2019). https://doi.org/10.1016/j.mtla.2019.100491.

[3] I. Ogunsanya, Influence of alloying elements, testing solution and surface roughness on corrosion behaviour of stainless steel reinforcing bars, 2019.

[4] I.G. Ogunsanya, C.M. Hansson, Reproducibility of the corrosion resistance of UNS S32205 and UNS S32304 stainless steel reinforcing bars, Corrosion 76 (2020) 114–130. https://doi.org/10.5006/3360.

[5] F. Lollini, M. Carsana, M. Gastaldi, E. Redaelli, Corrosion behaviour of stainless steel reinforcement in concrete, Corrosion Reviews 37 (2019) 3–19. https://doi.org/10.1515/CORRREV-2017-0088/MACHINEREADABLECITATION/RIS.

[6] D. Coelho, O.A.C. Linares, A.L.S. Oliveira, M.A.S. Andrade, L.H. Mascaro, J.E.S. Batista Neto, O.M. Bruno, E.C. Pereira, Introducing a low-cost tool for 3D characterization of pitting corrosion in stainless steel, Journal of Solid State Electrochemistry 24 (2020) 1909–1919. https://doi.org/10.1007/s10008-020-04586-2.

[7] K. Lorenz, G. Medawar, Über das Korrosionsverhalten austenitischer Chrom-Nickel-(Molybdän-) Stähle mit und ohne Stickstoffzusatz unter besonderer Berücksichtigung ihrer Beanspruchbarkeit in chloridhaltigen Lösungen, Thyssenforschung 1 (1969) 97–108.

[8] M. Renner, U. Heubner, M. 6 Rockel, E. Wallis, Temperature as a pitting and crevice corrosion criterion in the FeCI, test*, Werkstoffe Und Korrosion 37 (1986) 183–190.

[9] Werkst. G. Herbselb, -, Korros. 33 (1982) 334–340.

[10] R.F.A. Jargelius-Pettersson, Application of the Pitting Resistance Equivalent Concept to Some Highly Alloyed Austenitic Stainless Steels, Corrosion 54 (1998) 162–168. https://doi.org/10.5006/1.3284840.

[11] Petroleum, petrochemical and natural gas industries-Materials selection and corrosion control for oil and gas production systems Industries du pétrole, de la pétrochimie et du gaz naturel-Choix des matériaux et contrôle de la corrosion pour les systèmes de production de pétrole et de gaz COPYRIGHT PROTECTED DOCUMENT from IHS, 2145.

[12] B. Craig, Clarifying the Applicability of PREN Equations: A Short Focused Review, Corrosion 77 (2021) 382–385. https://doi.org/10.5006/3723.

[13] E.B. Haugan, M. Næss, C.T. Rodriguez, R. Johnsen, M. Lannuzzi, Effect of Tungsten on the Pitting and Crevice Corrosion Resistance of Type 25Cr Super Duplex Stainless, (2016). https://doi.org/10.5006/2185.

[14] R.F.A. Jargelius-Pettersson, CORROSION-FEBRUARY 1998 CORROSION ENGINEERING SECTION Application of the Pitting Resistance Equivalent Concept to Some Highly Alloyed Austenitic Stainless Steels, 1998.

[15] I.G. Ogunsanya, C.M. Hansson, The semiconductor properties of passive films and corrosion behavior of stainless steel reinforcing bars in simulated concrete pore solution, Materialia (Oxf) 6 (2019). https://doi.org/10.1016/j.mtla.2019.100321.

[16] P. Cunningham, M. Cord, S.J. Delany, Supervised Learning, Cognitive Technologies (2008) 21–49. https://doi.org/10.1007/978-3-540-75171-7_2.

[17] V. Nasteski, An overview of the supervised machine learning methods, Horizons 4 (2017) 51–62. https://doi.org/10.20544/HORIZONS.B.04.1.17.P05.

[18] J. Han, M. Kamber, J. Pei, Data Preprocessing, Data Mining (2012) 83–124. https://doi.org/10.1016/B978-0-12-381479-1.00003-4.

[19] D.E. Hilt, D.E. Hilt, D.W., Seegrist, U. States., Pa.) Northeastern Forest Experiment Station (Radnor, Ridge, a computer program for calculating ridge regression estimates, Dept. of Agriculture, Forest Service, Northeastern Forest Experiment Station, Upper Darby, Pa, 1977. https://doi.org/10.5962/bhl.title.68934.

[20] Regression, (n.d.).

[21] A.E. Hoerl, R.W. Kennard, Ridge Regression: Biased Estimation for Nonorthogonal Problems, Technometrics 12 (1970) 55. https://doi.org/10.2307/1267351.

[22] N. Van Kinh, N. Van Kinh, Regularization Methods to Approximate Solutions of Variational Inequalities, Open Journal of Optimization 12 (2023) 34–60. https://doi.org/10.4236/OJOP.2023.122004.

[23] R. Tibshirani, Regression Shrinkage and Selection Via the Lasso, J R Stat Soc Series B Stat Methodol 58 (1996) 267–288. https://doi.org/10.1111/J.2517-6161.1996.TB02080.X.

[24] H. Zou, T. Hastie, Regularization and variable selection via the elastic net, J. R. Statist. Soc. B 67 (2005) 301–320. https://academic.oup.com/jrsssb/article/67/2/301/7109482 (accessed March 25, 2025).

[25] CORROSION Fundamentals of Mechanisms, Causes, and Preventative Methods, (n.d.).

[26] A. Marani, T. Oyinkanola, D.K. Panesar, Probabilistic deep learning prediction of natural carbonation of low-carbon concrete incorporating SCMs, Cem Concr Compos 152 (2024) 105635. https://doi.org/10.1016/J.CEMCONCOMP.2024.105635.

[27] K.K. Dobbin, R.M. Simon, Optimally splitting cases for training and testing high dimensional classifiers, BMC Med Genomics 4 (2011) 1–8. https://doi.org/10.1186/1755-8794-4-31/TABLES/3.

[28] F. Pedregosa FABIANPEDREGOSA, V. Michel, O. Grisel OLIVIERGRISEL, M. Blondel, P. Prettenhofer, R. Weiss, J. Vanderplas, D. Cournapeau, F. Pedregosa, G. Varoquaux, A. Gramfort, B. Thirion, O. Grisel, V. Dubourg, A. Passos, M. Brucher, M. Perrot andÉdouardand, andÉdouard Duchesnay, Fré. Duchesnay EDOUARDDUCHESNAY, Scikit-learn: Machine Learning in Python Gaël Varoquaux Bertrand Thirion Vincent Dubourg Alexandre Passos PEDREGOSA, VAROQUAUX, GRAMFORT ET AL. Matthieu Perrot, Journal of Machine Learning Research 12 (2011) 2825–2830. http://scikit-learn.sourceforge.net. (accessed March 25, 2025).

[29] S.M. Malakouti, M.B. Menhaj, A.A. Suratgar, The usage of 10-fold cross-validation and grid search to enhance ML methods performance in solar farm power generation prediction, Clean Eng Technol 15 (2023) 100664. https://doi.org/10.1016/J.CLET.2023.100664.

[30] C.B. Van Niejenhuis, S. Walbridge, C.M. Hansson, The performance of austenitic and duplex stainless steels in cracked concrete exposed to concentrated chloride brine, J Mater Sci 51 (2016) 362–374. https://doi.org/10.1007/S10853-015-9387-0/FIGURES/10.

[31] S.M. Lundberg, P.G. Allen, S.-I. Lee, A Unified Approach to Interpreting Model Predictions, Adv Neural Inf Process Syst 30 (2017). https://github.com/slundberg/shap (accessed March 26, 2025).

Design Specification For Service Life Evaluation: Technical Implications

Jose Pacheco and Kyle Stanish

Synopsis: ACI Committee 365 published a new Design Specification in 2024. The Design Specification was developed to provide requirements to the Service Life Engineer, a specialty engineer focused on durability, for performing service life predictions of new structures. The Service Life Engineer is responsible for predicting the service life performance of concrete elements and developing requirements for the verification of the service life prediction during construction. The Service Life Report, developed during or prior to construction, and a Service Life Record Report, delivered at the completion of construction, are deliverables prepared by the Service Life Engineer at the completion of the project. The requirements of the Design Specification aim to provide consistency to the practice of service life prediction of new concrete structures. The technical requirements for performing service life predictions following the Design Specification are discussed in this paper.

Keywords: service life prediction, design specification, corrosion, durability

Jose Pacheco, Ph.D., P.E., P.Eng., is an Associate Principal of MJ2 Consulting. He received his PhD from Delft University of Technology. He is the current chair of ACI 365-Service Life Prediction and a member of 222-Corrosion, 357-Offshore & Marine, and 563-Repair Specifications.

Kyle Stanish, FACI, Ph.D., S.E., P.E., is Vice President of Engineering at Tourney Consulting Group. He received his PhD from the University of Toronto. He is the immediate past chair of ACI 365-Service Life Prediction and a member of 364-Rehabilitation, 562-Repair Code, 563-Repair Specifications, and 321-Durability Code.

INTRODUCTION

The American Concrete Institute Committee 365 "Service Life Prediction" initiated the work for developing a Design Specification in 2017 and the Design Specification was published in 2024 [1]. Service life predictions of new structures have become a performance requirement adopted for new construction. For example, the American Association of State Highway and Transportation Officials (AASHTO) Service Life Design Reference Guide published in 2022 recommends a service life of 75 years for new interstate highway bridges [2]. Other public infrastructure projects with requirements of 100 years or greater have been initiated in North America, demonstrating the interest and need for service life prediction requirements in the industry.

Design Specifications are documents written in mandatory language as Codes and Specifications that can be part of the Contract Documents of a project. The Design Specifications differ from codes and other specifications in that it does not need to be adopted by Code Officials. This allows the Design Specification to be used for projects with service life requirements without being an onus on projects where service life is not considered.

The Design Specification defines the role of the Service Life Engineer as the technical lead for performing the service life prediction, developing verification requirements for validation, and producing deliverables for the prediction. This paper describes the technical implications of the selection of durability strategies and modeling approaches by the Service Life Engineer.

RESEARCH SIGNIFICANCE

During the past two decades [3,4], service life prediction was predominantly limited to specific projects where the long-term performance of the structure was considered. In most cases in North America, this was particularly focused on new bridges. With the development of the Design Specification, performance requirements for new structures long past their construction can be set forth by Owners. The Design Specification developed the role of Service Life Engineers, who are responsible for developing the approach to achieve the required service life and indicating the requirements for the validation of the predictions to provide clarity in the roles and responsibilities of the project. This paper expands on the decisions that the Service Life Engineer must make when performing service life predictions, which include selecting the modeling approach, identifying the limitations of the modeling, and documentation of the service life modeling methodology and verification during construction.

SERVICE LIFE ENGINEER

The Design Specification defines the Service Life Engineer as follows:

> *"(an) individual who is licensed to practice engineering as defined by the statutory requirements of the professional licensing laws of the state or jurisdiction in which the structure is to be constructed, and who is responsible for the service life prediction. The individual shall be qualified by training and experience to perform service life prediction."*

This requirement establishes that the Service Life Engineer is an individual with competence in the industry available service life prediction methodologies and is licensed to practice engineering. Performing service life predictions involves using engineering knowledge and judgment, which, therefore, requires the Service Life Engineer to follow the bylaws of engineering practice. In North America, these are essential for defining the role of the Service Life Engineer within the engineering field.

An individual fulfilling the role of the Service Life Engineer must be competent in performing a service life prediction. Although there is no currently available certification body for the knowledge requirements of the Service Life Engineer, the Design Specification requires the Service Life Engineer to be able to identify and be knowledgeable in the following tasks:

1. Identification of the concrete deterioration mechanisms applicable to the project
2. Selecting and understanding the modeling approach to be used and its limitations

3. Developing a strategy to achieve the requested service life
4. Providing specification requirements for the qualification and verification of acceptance of the materials used in all construction phases of the project
5. Performing the service life prediction using well-defined parameters that can be reproduced by others
6. Documenting the service life prediction and Service Life Report at the end of the project

The following sections provide guidance to Service Life Engineers with regard to the fundamental requirements for each of the tasks described above.

PERFORMING SERVICE LIFE PREDICTIONS

Identification of Deterioration Mechanisms

The Service Life Engineer should be able to identify the deterioration mechanisms applicable to the project at hand. For concrete, typical deterioration mechanisms can be found in ACI PRC 201.2 [5], ACI PRC 222 [6], and ACI PRC 365.1 [7], among others. A review of service life modeling approaches used outside of North America was recently published [8].

ACI CODE 318 [9] provides exposure categories and classes based on the expected conditions for structural concrete. The exposure categories are broad in definition, and the Service Life Engineer should know that the ACI 318 exposure classes and categories are unlikely to cover all scenarios and may not be sufficiently stringent for extended service life requirements.

As other materials are expected to be part of the service life prediction, the Service Life Engineer should be able to identify the appropriate guidelines and requirements for such materials, i.e., reinforcing steel, structural steel, aluminum, asphalt, wood, etc. Representative service life predictions rely on the compatibility of the selected materials and the prediction of material behavior and performance.

Selection of Service Life Prediction Methodology

Historically, most service life prediction documents in the industry focus on selecting the service life prediction methodology. The ACI 365.1 guide summarizes the initial to the most recent prediction methodologies for concrete materials in the industry, but modeling tools are expected to change and improve over time. The Service Life Engineer should be capable of keeping up with the advances in material behavior and modeling.
Service life models are typically focused on modeling the transport of single ions (most frequently chlorides) [10-14], but models addressing multi-ionic transport are available [15,16]. The Service Life Engineer should be able to discern which type of modeling tool is appropriate for the specific project and be able to identify and indicate the limitations of the selected modeling tool. Additionally, the Service Life Engineer must define if deterministic or probabilistic modeling [17] is necessary based on the project service life requirements.

The current development of modeling tools is mature for modeling the ingress of chlorides and reinforcement corrosion [18-23]. Models for sulfate deterioration and alkali-aggregate reactions are available but used less frequently [24-28]. Models for other deterioration mechanisms do exist but have remained in a research phase with little adoption in the industry [29-31]. In most cases, this is caused by the limited number of field studies necessary for the validation of the models.

DETERIORATION MECHANISMS

Chloride Ingress and Reinforcing Steel Corrosion

Due to its frequency and body of research, the prediction of chloride ingress and reinforcing steel corrosion has developed more extensively than other deterioration mechanisms. The transport of chlorides through a concrete system has been studied extensively, and diffusion-based transport models have been used for decades. Due to the time-dependent characteristics of the concrete pore structure and variations in internal moisture content, diffusion-based modeling has adopted correction factors addressing the aging coefficient [32-36] and the convection or partial saturation conditions on the transport of chlorides.

The number of publications identifying reinforcement corrosion parameters such as the critical chloride content [37-40], chloride ion and cation [41-43], and reinforcing steel corrosion [44-50] is overwhelmingly large. The body of research has concluded that chloride transport in concrete is controlled by the exposure conditions, the

characteristics of the concrete system, and the steel-concrete interface [51,52]. These parameters play a critical role in the long-term prediction of the structure behavior and should be considered by the Service Life Engineer.

Sulfate-Induced Deterioration

Deterioration from exposure to external sulfates in soil and water is relevant for buried and submerged concrete elements such as drilled shafts, footings, mat foundations, and marine infrastructure [53]. Mass concrete elements can be vulnerable to internal sulfate deterioration due to delayed ettringite formation (DEF), when elevated temperatures and combinations of DEF-susceptible cementitious materials are used [54]. Approaches for mitigating sulfate-induced deterioration have been focused on selecting sulfate-resistant cementitious materials and proportions (for internal or external sulfate deterioration). For external sulfates, additional mitigating measures, such as increasing the thickness of the concrete cover or selecting sulfate-resistant concrete mixtures, are frequently adopted. For aggressive exposure conditions with high sulfate concentrations, service life modeling, including sulfate ingress, is often necessary for buried and submerged concrete elements. [55,56]. Finally, thermal control plans are required to control and mitigate the temperature rise of concrete to prevent internal sulfate deterioration during the service life of the structure.

Alkali-Aggregate Reactions and Other Mechanisms

Due to its complexity and severity, current service life modeling of alkali-aggregate reactions is of limited use in the industry. Prevention strategies are routinely adopted to minimize the risk of expansion, with modeling of the degradation mechanism as an option for special cases or research purposes. New modeling approaches are being developed and is anticipated that they could be used in the industry in the future [57].

Prevention strategies are often used for abrasion, chemical attack, freezing and thawing, and physical salt attack. The Service Life Engineer should be able to discern which prevention strategies are appropriate to address deterioration mechanisms that do not have established modeling approaches for the project.

Developing a Strategy

Requirements for service life are often indicated in the number of years before major repair or rehabilitation is required. In most cases, the definition of “major repair or rehabilitation” is vague or incomplete, leaving the Service Life Engineer with the task of defining the acceptable condition of the structure at the end of the specified service life. It should be noted that achieving the specified service life of the structure does not mean an “end-of-use”, but rather that the performance of the structure has achieved the specified requirement. A frequent misconception is that maintenance and minor repairs mean that the structure or its elements have failed to achieve its service life, when, in fact, maintenance and minor repairs are often necessary and expected to achieve the specified service life. The Service Life Engineer should clearly identify how maintenance, repair, and major rehabilitation are defined in the project.

Achieving the specified service life can often include different strategies. For projects where accessibility is available, a reasonable approach could be to accept the replacement of non-critical components of the structure. For example, barriers and other auxiliary elements of a bridge can be replaced periodically. In contrast, the bridge deck may be anticipated to be refurbished or replaced in a specific time frame, which is shorter than the overall service life of the structure. This type of strategy should be agreed upon between the Owner and the Service Life Engineer to avoid conflicts in the interpretation of the requirements.

Specification Requirements for Qualification and Verification

Developing the requirements for the qualification and verification of materials in the project is a crucial task that must be executed by the Service Life Engineer. In most cases, project-specific specifications indicate the applicable environmental conditions and material requirements assumed by the Service Life Engineer for performing the predictions. The Service Life Engineer should be familiar with industry-available specifications, such as ACI 301 [58], and identify the areas where additional requirements are necessary for the project. A concise qualification verification requires identifying the appropriate means of validation, most frequently as documentation of composition, laboratory or field testing, and accreditation requirements for testing, manufacturing, and handling tasks associated with the project.

The Service Life Engineer should be aware of variations in performance or material substitutions during construction. The methods of validation and qualification for alternative material sources or for addressing non-

compliant performance, i.e., low compressive strength, among others, are vital for reducing the time and cost of addressing the non-compliance.

DELIVERABLES

Service Life Report

Once the strategy has been developed for the project, the Design Specification requires the Service Life Engineer to develop and produce a Service Life Report. The Service Life Report is developed before or during the early stages of the project using the assumptions defined in the selected strategy, the results of qualification testing of the applicable concrete and other materials, and the defined exposure conditions. For this task, the Service Life Engineer should clearly identify the prevention strategies and modeling approaches for achieving the specified service life. When deviations or user-defined changes to the model or input parameter are used, the Service Life Engineer should be concise in documenting the deviation and the reasoning for the change, as well as interpret the results of the prediction within the limitations of the modeling approach. Since service life predictions can be sensitive to relatively minor changes to the input parameters and modeling, clarification by the Service Life Engineer is necessary for third-party verification, if necessary. Although not typically necessary, documentation of the user-defined changes is useful when independent reviews are conducted or when the service life report is reviewed many years after construction. An example of a common user-defined change is the duration of the effect of concrete aging on transport properties. Some models consider aging, the reduction of the rate of transport of ions in concrete, for a fixed period of time (i.e., 25 years), while other models consider the entire service life.

Another critical decision by the Service Life Engineer that must be included in the Service Life Report relates to the effect of cracking on the service life predictions. Cracks allow for the fast ingress of water, often containing chlorides or other deleterious ions, and usually lead to premature deterioration of the concrete element. Because crack-free concrete cannot be guaranteed, specifiers and Service Life Engineers often define a crack width threshold for crack repair. When silent on the effect of cracks in the modeling approach, this means that cracks with a width less than the specified value are considered to be insignificant for the service life predictions. Approaches to consider the effect of cracks are available in the literature [59-62]. The appropriateness of this consideration is to be determined by the Service Life Engineer.

Service Life Record Report

The final task required for Service Life Engineers is to produce detailed documentation of the strategies, modeling approaches, user-defined changes, and relevant considerations for performing a service life prediction. Requirements for conducting an as-built assessment of the structure after completion of its construction are provided with the aim of producing a Service Life Report (also know as Birth Certificate). This report is intended to be a recompilation of the verification of compliance of the in-place structure as a means to verify fulfilment of the project requirements. As a recommendation, the Service Life Report should also include suggestions for extending the service life of the structure past its specified requirement. This requirement focuses on having a detailed record of the tasks described above, which should remain accessible to the Service Life Engineer and the Owner for the specified duration of the document record keeping.

SUMMARY

The Design Specification developed by ACI Committee 365 and published in 2024 was established to provide homogeneous requirements for performing service life predictions in the industry. The Design Specification covers the requirements for the Service Life Engineer, the individual responsible for performing the service life prediction, and for documentation of the strategies and modeling approaches adopted for the project.

Although currently performed for special projects, service life prediction tools can be applied to any construction project when adopted by the Contract Documents. The selection of the strategies and modeling is the responsibility of the Service Life Engineer. Compliance with the requirements of the Design Specification is aimed at providing documented evidence of the service life prediction and as-built conditions of the structure for further reference.

ACKNOWLEDGEMENTS

The authors acknowledge the contributions of Dr. Carolyn Hansson for the development of the Design Specification. Dr. Hansson has been a long-time member of ACI Committee 365 and other durability-focused committees in ACI, and her work has been cited in many of the Institute guides and reports.

REFERENCES

[1] ACI Code-365 (2024). Service Life Evaluation—Design Specification, American Concrete Institute.

[2] Hopper, T., Langlois, A. M., Murphy, T., & America, C. N. (2022). *Reference Guide for Service Life Design of Bridges* (No. FHWA-HIF-22-052). United States. Federal Highway Administration. Office of Bridges and Structures.

[3] S. Rostam (2005). Service life design of concrete structures-a challenge to designers as well as to owners, Asian Journal Civil Engineering, vol. 6, no. 5, pp. 423–445

[4] P. Hovde and K. Moser (2004). Performance-Based Methods for Service Life Prediction, CIB W080 / RILEM 175-SLM Service Life Methodologies, Tech. Rep.

[5] ACI PRC-201.2 (2023). Durable Concrete—Guide, American Concrete Institute.

[6] ACI PRC-222 (2019). Guide to Protection of Metals in Concrete Against Corrosion. American Concrete Institute.

[7] ACI PRC-365.1 (2017). Report on Service Life Prediction. American Concrete Institute.

[8] Kesner, K., Klein, J., Marcotte, T., & Poston, R. (2020). Literature Review of Concrete Durability & Service Life Requirements in Global Codes and Standards. American Concrete Institute Foundation.

[9] ACI CODE-318 (2022). Building Code Requirements for Structural Concrete and Commentary. American Concrete Institute

[10] Collepardi, M., Marcialis, A., & Turriziani, R. (1972). Penetration of chloride ions into cement pastes and concretes. *Journal of the American Ceramic Society*, *55*(10), 534-535.

[11] Thomas, M. D., & Bamforth, P. B. (1999). Modelling chloride diffusion in concrete: Effect of fly ash and slag. Cement and concrete research, 29(4), 487-495.

[12] Stanish, K., & Thomas, M. (2003). The use of bulk diffusion tests to establish time-dependent concrete chloride diffusion coefficients. *Cement and concrete research*, *33*(1), 55-62.

[13] Andrade, C., Prieto, M., Tanner, P., Tavares, F., & d'Andrea, R. (2013). Testing and modelling chloride penetration into concrete. *Construction and Building Materials*, *39*, 9-18.

[14] Jensen, O. M., Hansen, P. F., Coats, A. M., & Glasser, F. P. (1999). Chloride ingress in cement paste and mortar. *Cement and Concrete Research*, *29*(9), 1497-1504.

[15] Samson, E., & Marchand, J. (2007). Modeling the transport of ions in unsaturated cement-based materials. *Computers & Structures*, *85*(23-24), 1740-1756.

[16] Johannesson, B., Yamada, K., Nilsson, L. O., & Hosokawa, Y. (2007). Multi-species ionic diffusion in concrete with account to interaction between ions in the pore solution and the cement hydrates. *Materials and structures*, *40*, 651-665.

[17] Fib Bulletin 34 (2006), Model Code for Service Life Design, FIB, Tech. Rep. 34.

[18] Tuutti, K. (1982). Corrosion of steel in concrete.

[19] Glass, G. K., & Buenfeld, N. R. (2000). The influence of chloride binding on the chloride induced corrosion risk in reinforced concrete. *Corrosion Science*, *42*(2), 329-344.

[20] Khan, M. U., Ahmad, S., & Al-Gahtani, H. J. (2017). Chloride-Induced Corrosion of Steel in Concrete: An Overview on Chloride Diffusion and Prediction of Corrosion Initiation Time. *International journal of corrosion*, *2017*(1), 5819202.

[21] Glass, G. K., & Buenfeld, N. R. (2000). Chloride-induced corrosion of steel in concrete. *Progress in Structural Engineering and Materials*, *2*(4), 448-458.

[22] Šavija, B., Pacheco, J., & Schlangen, E. (2013). Lattice modeling of chloride diffusion in sound and cracked concrete. *Cement and Concrete Composites*, *42*, 30-40.

[23] Ji, Y., Pel, L., Zhang, X., & Sun, Z. (2021). Cl-and Na+ ions binding in slag and fly ash cement paste during early hydration as studied by 1H, 35Cl and 23Na NMR. *Construction and Building Materials*, *266*, 121606.

[24] Sarkar, S., Mahadevan, S., Meeussen, J. C. L., Van der Sloot, H., & Kosson, D. S. (2010). Numerical simulation of cementitious materials degradation under external sulfate attack. *Cement and Concrete Composites*, *32*(3), 241-252.

[25] Marchand, J., Samson, E., Maltais, Y., & Beaudoin, J. J. (2002). Theoretical analysis of the effect of weak sodium sulfate solutions on the durability of concrete. *Cement and Concrete Composites*, *24*(3-4), 317-329.

[26] Esposito, R., & Hendriks, M. A. N. (2019). Literature review of modelling approaches for ASR in concrete: a new perspective. *European Journal of Environmental and Civil Engineering*, *23*(11), 1311-1331.

[27] Iskhakov, T., Timothy, J. J., & Meschke, G. (2019). Expansion and deterioration of concrete due to ASR: Micromechanical modeling and analysis. *Cement and Concrete Research*, *115*, 507-518.
[28] Alnaggar, M., Cusatis, G., & Di Luzio, G. (2013). Lattice discrete particle modeling (LDPM) of alkali silica reaction (ASR) deterioration of concrete structures. *Cement and Concrete Composites*, *41*, 45-59.
[29] Çopuroğlu, O., & Schlangen, E. (2008). Modeling of frost salt scaling. *Cement and Concrete Research*, *38*(1), 27-39.
[30] Liu, Q., Andersen, L. V., & Wu, M. (2024). Prediction of concrete abrasion depth and computational design optimization of concrete mixtures. *Cement and Concrete Composites*, *148*, 105431.
[31] Rong, X. L., Li, L., Zheng, S. S., Wang, F., Huang, W. Y., Zhang, Y. X., & Lu, D. (2023). Freeze–thaw damage model for concrete considering a nonuniform temperature field. *Journal of Building Engineering*, *72*, 106747.
[32] Andrade, C., Prieto, M., Tanner, P., Tavares, F., & d'Andrea, R. (2013). Testing and modelling chloride penetration into concrete. *Construction and Building Materials*, *39*, 9-18.
[33] Thomas, M. (2016). The durability of concrete for marine construction: Materials and properties. In *Marine Concrete Structures* (pp. 151-170). Woodhead Publishing.
[34] Petcherdchoo, A., & Chindaprasirt, P. (2019). Exponentially aging functions coupled with time-dependent chloride transport model for predicting service life of surface-treated concrete in tidal zone. *Cement and Concrete Research*, *120*, 1-12.
[35] Polder, R. B., & De Rooij, M. R. (2005). Durability of marine concrete structures-Field investigations and modelling. *HERON*, *50*(3), 133.
[36] Baroghel-Bouny, V., Dierkens, M., Wang, X., Soive, A., Saillio, M., Thiery, M., & Thauvin, B. (2013). Ageing and durability of concrete in lab and in field conditions: investigation of chloride penetration. *Journal of Sustainable Cement-Based Materials*, *2*(2), 67-110.
[37] Angst, U., Elsener, B., Larsen, C. K., & Vennesland, Ø. (2009). Critical chloride content in reinforced concrete—A review. *Cement and concrete research*, *39*(12), 1122-1138.
[38] Markeset, G. (2009). Critical chloride content and its influence on service life predictions. *Materials and Corrosion*, *60*(8), 593-596.
[39] Pacheco, J., & Polder, R. B. (2016). Critical chloride concentrations in reinforced concrete specimens with ordinary Portland and blast furnace slag cement. *Heron*, *61*(2), 99-119.
[40] Adil, G., Halmen, C., Vaddey, P., Pacheco, J., & Trejo, D. (2022). Multi-Laboratory Validation Study of Critical Chloride Threshold Test Method. *ACI Materials Journal*, *119*(6), 91-100.
[41] Hansson, C. M., Frølund, T., & Markussen, J. B. (1985). The effect of chloride cation type on the corrosion of steel in concrete by chloride salts. *Cement and Concrete Research*, *15*(1), 65-73.
[42] Song, Z., Jiang, L., Liu, J., & Liu, J. (2015). Influence of cation type on diffusion behavior of chloride ions in concrete. *Construction and Building Materials*, *99*, 150-158.
[43] Zhu, Q., Jiang, L., Chen, Y., Xu, J., & Mo, L. (2012). Effect of chloride salt type on chloride binding behavior of concrete. *Construction and Building Materials*, *37*, 512-517.
[44] Andrade, C. (2019). Propagation of reinforcement corrosion: principles, testing and modelling. *Materials and Structures*, *52*(1), 2.
[45] Bertolini, L., Elsener, B., Pedeferri, P., Redaelli, E., & Polder, R. B. (2013). *Corrosion of steel in concrete: prevention, diagnosis, repair*. John Wiley & Sons.
[46] Broomfield, J. P. (2023). *Corrosion of steel in concrete: understanding, investigation and repair*. Crc Press.
[47] Otieno, M. B., Beushausen, H. D., & Alexander, M. G. (2011). Modelling corrosion propagation in reinforced concrete structures–A critical review. *Cement and Concrete composites*, *33*(2), 240-245.
[48] Isgor, O. B., & Razaqpur, A. G. (2006). Modelling steel corrosion in concrete structures. *Materials and Structures*, *39*, 291-302.
[49] Raupach, M. (2006). Models for the propagation phase of reinforcement corrosion–an overview. *Materials and Corrosion*, *57*(8), 605-613.
[50] Sagüés, A. A. (2003). Modeling the effects of corrosion on the lifetime of extended reinforced concrete structures. *Corrosion*, *59*(10)
[51] Angst, U. M., Geiker, M. R., Michel, A., Gehlen, C., Wong, H., Isgor, O. B., ... & Buenfeld, N. (2017). The steel–concrete interface. *Materials and Structures*, *50*, 1-24.
[52] Angst, Ueli M., Mette R. Geiker, Maria Cruz Alonso, Rob Polder, O. Burkan Isgor, Bernhard Elsener, Hong Wong et al. "The effect of the steel–concrete interface on chloride-induced corrosion initiation in concrete: a critical review by RILEM TC 262-SCI." *Materials and Structures* 52 (2019): 1-25.
[53] Marchand, J., Odler, I., & Skalny, J. P. (2001). *Sulfate attack on concrete*. CRC Press.

[54] ACI PRC-207.1 (2021). Mass Concrete—Guide. American Concrete Institute.
[55] Samson, E., & Marchand, J. (2007). Modeling the transport of ions in unsaturated cement-based materials. *Computers & Structures*, *85*(23-24), 1740-1756.
[56] Ikumi, T., & Segura, I. (2019). Numerical assessment of external sulfate attack in concrete structures. A review. *Cement and Concrete Research*, *121*, 91-105.
[57] Nguyen, T. N., Sanchez, L. F., Li, J., Fournier, B., & Sirivivatnanon, V. (2022). Correlating alkali-silica reaction (ASR) induced expansion from short-term laboratory testings to long-term field performance: A semi-empirical model. *Cement and Concrete Composites*, *134*, 104817.
[58] ACI SPEC-301 (2020) Specifications for Structural Concrete. American Concrete Institute.
[59] Pacheco, J. (2019). Incorporating Cracks in Chloride Ingress Modeling and Service Life Predictions. *ACI Materials Journal*, *116*(5).
[60] Cui, Z., & Alipour, A. (2018). Concrete cover cracking and service life prediction of reinforced concrete structures in corrosive environments. *Construction and Building Materials*, *159*, 652-671.
[61] Audenaert, K., Marsavina, L., & De Schutter, G. (2009). Influence of cracks on the service life of concrete structures in a marine environment. *Key Engineering Materials*, *399*, 153-160.
[62] Alexander, M., & Beushausen, H. (2019). Durability, service life prediction, and modelling for reinforced concrete structures–review and critique. *Cement and Concrete Research*, *122*, 17-29.

High-Throughput Analysis of the Kinetics of Chloride-Induced Passive Layer Breakdown in Different Carbon Steel Microstructures within Simulated Concrete Pore Solution

Gisoo Daviran and Amir Poursaee

Synopsis: Carbon steel bars are critical in steel-reinforced concrete structures and their corrosion leads to significant deterioration. Using a high-throughput approach, this study explored the kinetics of passive layer breakdown on different microstructures within a carbon steel reinforcing bar. Thermomechanically treated steel bars with three distinct microstructures (martensite in the outer layer, bainite in the middle, and pearlite in the center) were vertically cut and immersed in the simulated concrete pore solution. After 24 hours of immersion, the solution was contaminated with 0.8M chloride ions. Scanning Electrochemical Microscopy (SECM) was employed to study the kinetics of the passive layer breakdown on each microstructure. The results showed that the breakdown of the passive layer was a time-dependent process and that the microstructure influenced its kinetics.

Keywords: Concrete, Corrosion, Martensite, Pearlite, Pore solution, SECM.

ACI student member **Gisoo Daviran** is a Graduate Student in the Department of Civil Engineering at Clemson University

Amir Poursaee is a professor at the Glenn Department of Civil Engineering at Clemson University. His research interests include corrosion, NDT, and concrete materials.

INTRODUCTION

The corrosion of steel bars immersed in concrete significantly impacts the durability of steel-reinforced concrete structures, resulting in substantial economic losses due to the corrosion (Poursaee and Angst 2023). In a highly alkaline environment such as concrete, a thin protective (passive) layer forms on the steel surface. The formation of passive layers on carbon steel involves the development of thin layers of iron-oxides/hydroxides on the steel surface, which act as a protective barrier against corrosive agents (Poursaee and Angst 2023). The existence of chloride ions (Cl^-) in the same environments as the steel leads to the breakdown of the passive layer and corrosion of the steel bars (Glass and Buenfeld 1997, Koleva et al. 2007). Steel's microstructure influences steel's corrosion behavior (Torbati-Sarraf and Poursaee 2018, Torbati-Sarraf and Poursaee 2018), and it is imperative to study this influence on the breakdown of the passive layer, which is the objective of this study.

Thermomechanically Treated (TMT) steel is simultaneously produced by heat and mechanical treatment at the same time. This process forms steel with distinct microstructures (martensite in the outer region and bainite and pearlite in the inner regions, respectively). Owing to its unique characteristics, TMT steel was used in this study. This study focused on two of the three phases of TMT steel: martensite and pearlite.

Traditional methods to study the kinetics of the breakdown of the passive layer and the subsequent corrosion of steel are time-consuming, costly, and mostly insufficient (Chambers et al. 2005, Rojhirunsakool et al. 2022). High-throughput methodology simplifies the prototyping process while many samples can be rapidly analyzed to identify their behavior (Wang et al. 2022). To study the corrosion behavior of different steel microstructures locally and microscopically, this study used a Scanning Electrochemical Microscope (SECM) as a high-throughput technique to investigate the kinetics of the breakdown of the passive layer and corrosion of each microstructure within the TMT steel in a concrete pore solution contaminated with chloride ions. SECM is a scanning probe technique with an ultramicroelectrode (UME), scanning the sample of interest to record the current generated by the substrate (Bard et al. 1989, Polcari et al. 2016). SECM allows for the characterization of chemical processes and heterogeneous interfaces with high resolution, offering valuable insights into electrochemical reactions (Mirkin 1999). SECM is a highly effective tool for investigating corrosion processes, offering high spatial resolution and the capability to monitor electrochemical activities at the micrometer scale. SECM allows in-situ monitoring of corrosion phenomena by detecting electrochemically active species with high resolution (Vega et al. 2023).

EXPERIMENTAL

Materials

Three samples with a length of 100 mm (3.93 in.) from a #4 TMT reinforcing steel bar were cut and mounted in two-part cold epoxy at room temperature. All tests were conducted on these three identical samples. The chemical composition of the TMT steel is listed in Table 1.

Table 1— Chemical composition of the TMT steel used in this study

Alloying elements (%)									
C	Mn	Si	P	S	Cu	Ni	V	Mo	Fe
0.31	1.23	0.29	0.018	0.024	0.23	0.08	0.002	0.016	Balance

The samples were ground with SiC sandpapers of 240#, 400#, 600#, 800#, and 1200# grids, and then polished using a 1μm (0.000039 in.) alumina slurry.

Figure 1 shows a cross-section and optical micrograph of the microstructures of one of the samples.

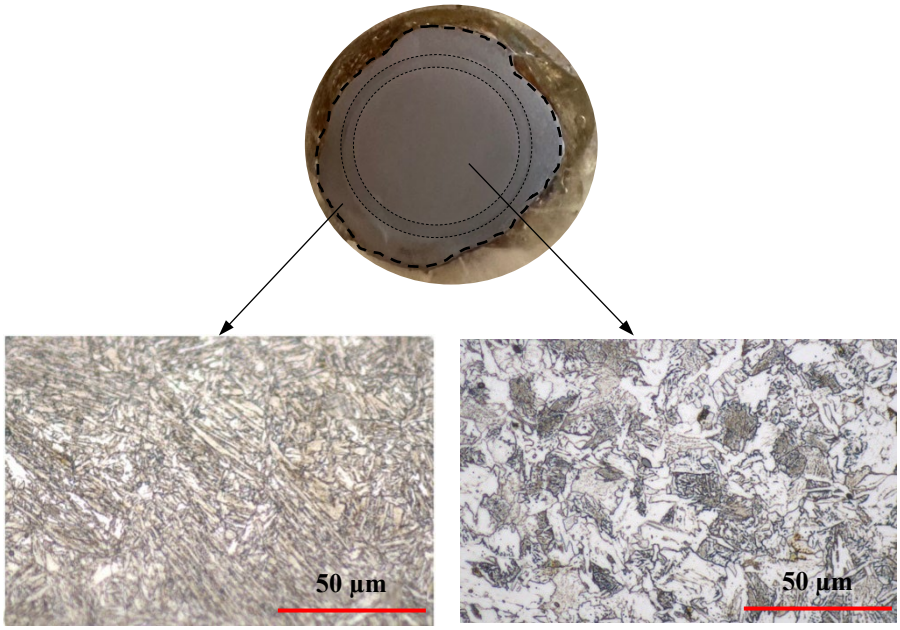

Fig. 1: Cross-section of TMT steel and micrographs of tempered martensite (left) and pearlite (right) phases. Dashed line highlights the boundaries of the steel bar

A copper wire was attached to the samples for electrical connection. The mounted samples were immersed in a simulated concrete pore solution with the composition listed in Table 2.

Table 2— Composition of simulated concrete pore solution.

Compound	mol/L (mol/in.^{3})
KOH	0.3 (0.00492)
NaOH	0.1 (0.00164)
Ca $(OH)_2$	0.03 (0.000492)
CaSO4.2H2O (gypsum)	0.003 (0.000492)
$K_3[Fe(CN)_6]$ (Mediator)	0.0005 (0.00000819)

The samples remained in the chloride-free solution for 24 hours, which was then contaminated with 0.8 M NaCl. Potassium ferricyanide (K_3 $[Fe(CN)_6]$) was also added to the solution with NaCl. In SECM, a mediator is used to facilitate the detection of electrochemical activities at the sample surface. It contains redox-active species that transfer electrons between the SECM tip and the sample surface, thus amplifying the electrochemical signals. This process improves the sensitivity of the measurements, making it easier to detect and quantify the reactivity of the sample. Detecting the current using the SECM tip is nearly impossible without a mediator. With its reversible redox couple (Fe^{3+}/Fe^{2+}), potassium ferricyanide can easily alternate between oxidized and reduced states, making it an effective choice to facilitate the electrochemical processes, and it is required for the SECM experiment (Zhang et al. 2020, Mena-Morcillo et al. 2024, Steimecke et al. 2024).

SECM setup

The 10 µm (0.00039 in.) diameter UME with an RG ratio of 10 was used as the scanning probe. RG ratio is the ratio of the radius of the insulating cover of the probe to the active area of the electrode. The SECM probe was calibrated using a standard ferro/ferricyanide redox couple to ensure accurate measurement of the feedback current. Additionally, its functionality has been validated against a gold-mounted sample, with well-known characterization. Before each experiment, the UME was polished smoothly with the 1200 grid sandpaper and rinsed with deionized water. A 5 × 15 mm platinum steet and an Ag/AgCl were used as the counter and reference electrodes, respectively. All the measurements were conducted at room temperature.

The sample was placed in the SECM sample holder, and the concrete pore solution was added to the top surface of the sample in the sample holder. Figure 2 shows a schematic illustration of the scanning process and the actual SECM setup.

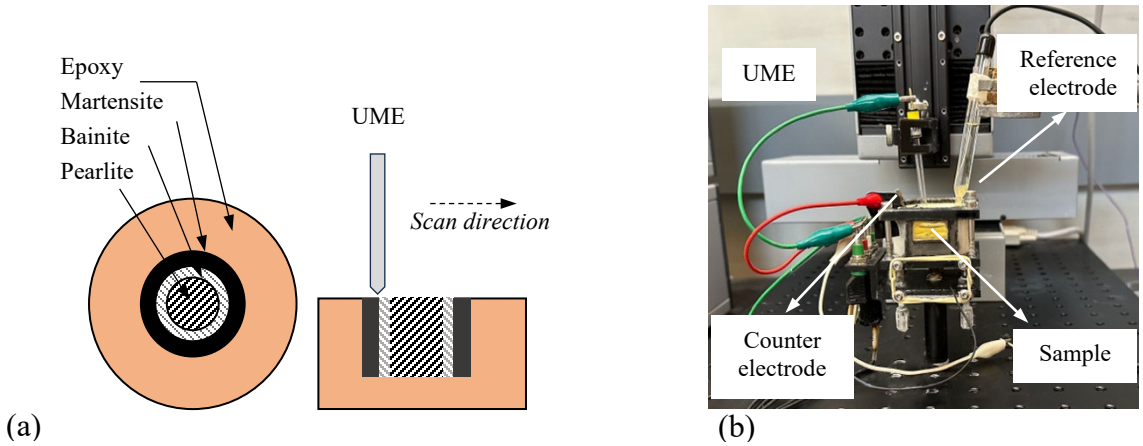

Fig. 2 (a) Schematic illustration of scanning process and (b) SECM setup.

Z- Approach Curves

The approach curves demonstrate the changes in the current recorded by the UME as it approaches the surface. Numerical analysis of the approach curve data provides kinetic constants, which are used for characterizing the activity of the substrates (Steimecke et al. 2024). To conduct the approach curve experiment, the UME was positioned above a single microstructure within the steel sample and gradually lowered until it contacted the sample's surface. It was then retracted to +10 µm (0.00039 in.) above the surface of the sample. The UME was further moved to +150µm (0.0059 in.) from its last position for the approach curve measurement. The UME was biased by applying a +650mV potential versus the reference electrode, while the sample remained unbiased. Biasing the UME tip helps detect the concentrations of reactants or products near the surface of the substrate. The UME approached the surface at a speed of 1 µm/s (0.000039 in./s) for all the measurements, and the process was repeated three times. Approach curve measurements were taken 72 hours after adding the salt.

Cyclic Voltammetry and the k_{eff}

Cyclic voltammetry (CV) in SECM is a powerful tool for studying the redox processes, surface interactions, and kinetics of electron transfer reactions. CV was conducted on each microstructure after 24, 48, and 72 hours of contaminating the solution with salt with scan rates of 20, 40, 60, 80, 100, and 200 mV/s. The results obtained from the experiment were used to calculate the diffusion coefficients of the electroactive species, providing insight into their movement through the solution. Moreover, these findings allowed for the estimation of the effective rate coefficient (k_{eff}), which serves as a key parameter in evaluating the kinetics of the electrochemical reactions occurring at the electrode surface (Liu and Bard 2002, Neufeld and O'Mullane 2006). k_{eff} is a measure of how quickly the

reactants are converted into products on the surface of a metal. It is influenced by the reaction and how quickly the reactants move to that site. As the UME approached the sample surface, the collected current influenced by the distance, L, which is the distance between the sample and the tip. The current at L distance, $I_T(L)$, is determined as:

$$I_T(L) = \left[I_T^{ins}(L) + I_S(L) \left(1 - \frac{I_T^{ins}(L)}{I_T^{con}(L)} \right) \right] \quad (1)$$

where $I_T^{ins}(L)$ and $I_T^{con}(L)$ are tip currents corresponding to diffusion-controlled regeneration of a redox mediator and an insulating substrate (no mediator regeneration), respectively. For RG ~ 10 $I_T^{ins}(L)$ and $I_T^{con}(L)$ can be written as:

$$I_T^{con} = 0.7449932 + \frac{0.7582943}{L} + 0.2353042 \cdot e^{-\frac{1.683087}{L}} \quad (2)$$

$$I_T^{ins}(L) = \frac{1}{0.4571825 + \frac{1.4604238}{L} + 0.4312735 \cdot e^{-\frac{2.350667}{L}}} + \frac{-0.145437 \cdot L}{5.5768952 + L} \quad (3)$$

$I_S(L)$ can be written as the normalized first-order rate constant κ:

$$I_s(L,\kappa) = \frac{0.78377}{L\left(1+\frac{1}{\kappa L}\right)} + \frac{0.68 + 0.3315e^{\frac{-1.0672}{L}}}{1 + \frac{\frac{11}{\kappa L} + 7.3}{110 - 40L}} \quad (4)$$

k_{eff} can be written as:

$$k_{eff} = \kappa \cdot \frac{D}{r} \quad (5)$$

where D is the diffusion coefficient of the mediator, r is the radius of the UME tip, and κ is the dimensionless first-order rate constant. Cyclic voltammetry experiments were conducted with different scan rates to calculate D, as described before. Based on the Randles-Sevcik method (Ngamchuea et al. 2014):

$$i_p = 0.446nFCA\sqrt{\frac{nFvD}{RT}} \quad (6)$$

The slope of the i_p- $\sqrt{v}$ plots (v is the scan rate) is $0.446nFCA\sqrt{\frac{nFD}{RT}}$. In equation 6 i_p is peak current values obtained from cyclic voltammograms, n is the number of electrons involved in the redox reaction ($Fe(CN)_6^{3-} + 1e^- \leftrightarrow Fe(CN)^{-4}_6$), F is Faraday constant (96500 $C.mol^{-1}$), C represents the concentration of the electroactive species (0.5 mM (0.00819 mmol/in.^{3})), in this study), A is the surface area of the working electrode (113.1 mm^2 (0.175 in.^{2}) in this case), T indicates the temperature (the experiment was conducted at ambient temperature, i.e., 24ºC (~75ºF, 297K), R denotes for the gas constant, and D is the diffusion coefficient. Knowing the slopes of the i_p- $\sqrt{v}$ plots allow for the calculation of the diffusion coefficient (D) of species on the different microstructures.

RESULTS AND DISCUSSION

Approach curves for martensite and pearlite 24 and 72 hours after immersion in chloride-contaminated solution are shown in Figure 3. Approach curves, i.e., decreasing the distance between the UME tip and sample, are usually plotted as normalized current versus the distance. The tip current is normalized by its value in the bulk.

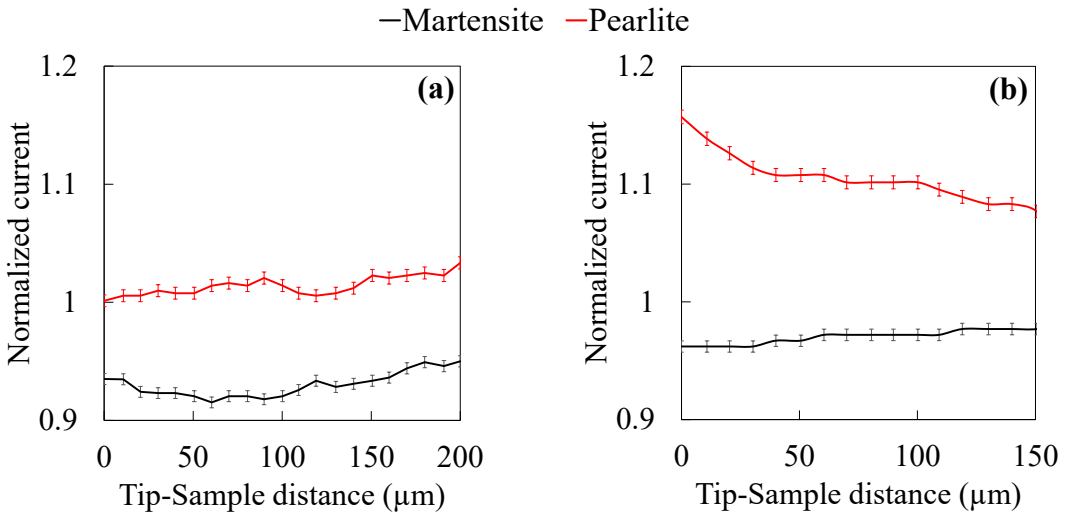

Fig. 3: Z-approach curves for martensite and pearlite microstructures after (a) 24-hour and (b) 72-hour immersion in the chloride-contaminated solution

The normalized current of the approach curves for both times indicated that martensite exhibited a lower collected current than pearlite. However, over time, the current for both phases increased. This increase is more substantial for pearlite compared to the martensite. This observation implied that martensite demonstrated superior corrosion resistance after adding salt to the solution compared to pearlite.

Cyclic voltammetry was performed at different scan rates, as described previously. The i_p- $\sqrt{\upsilon}$ plots for martensite and pearlite are shown in Figure 4.

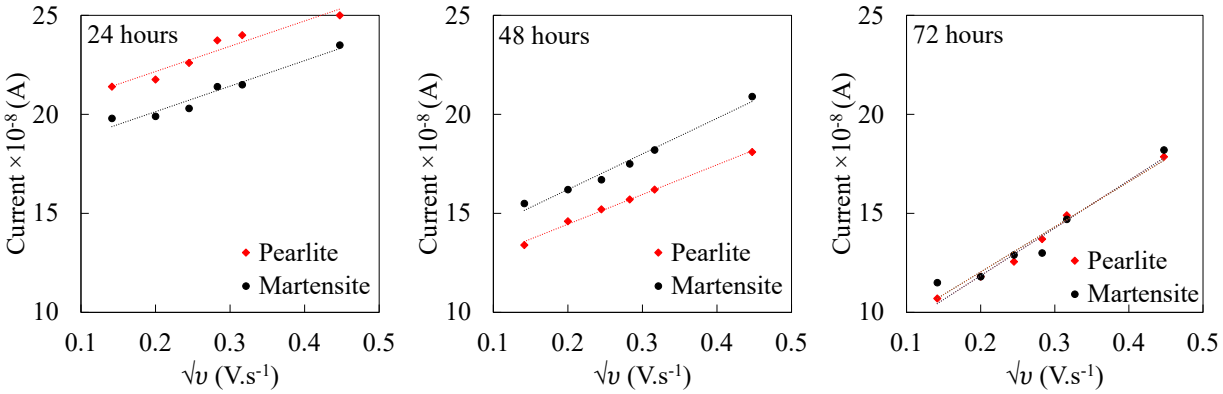

Fig. 4: i_p- $\sqrt{\upsilon}$ plots for martensite and pearlite at different times after immersion in the chloride-contaminated solution

Using the slope of the plots in Figure 4 and equation (6), the diffusion coefficient values were calculated and are shown in Table 3.

Table 3 —Diffusion coefficient values on martensite and pearlite phases.

Time hours after the addition of chlorides	Diffusion Coefficient, cm^2/s ($in.^2/s$)	
	Martensite	Pearlite
24	0.000243 (0.0000377)	0.000203 (0.0000315)
48	0.000771 (0.0001197)	0.00071 (0.00011)
72	0.00213 (0.00033)	0.0028 (0.000434)

The effective kinetic parameter, k_{eff} , of the mediator was determined using approach curves and cyclic voltammetry data, which are shown in Figure 5.

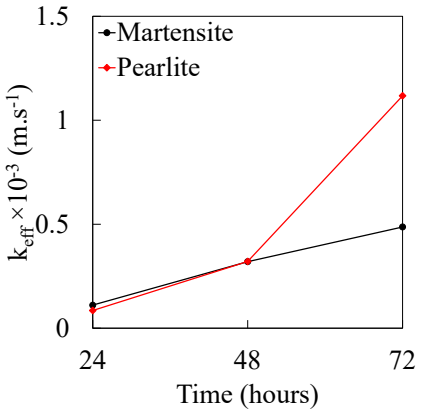

Fig. 5: k_{eff} values for martensite and pearlite in chloride-contaminated solution at different immersion times.

An increase in k_{eff} indicates an increase in surface activity. As can be seen, k_{eff} generally increased with time for both phases, indicating increasing activity, i.e., corrosion, on the surface of both phases. Up to 48 hours of immersion, both phases showed relatively similar activity. However, at 72 hours of immersion in the salt solution, the pearlite showed considerably more activity, i.e., ~130%, than the martensite.

It is hypothesized that the lamellar structure of pearlite, consisting of ferrite and cementite, is the reason for such observation. Rojhirunsakool et al. (Rojhirunsakool et al. 2022) demonstrated that in pearlitic structures, the ferrite phase can act as an anode relative to the cementite, leading to accelerated dissolution of the ferrite. This galvanic effect becomes especially prominent in an alkaline environment where pitting corrosion occurs (Cui et al. 2000). The superior corrosion resistance of the martensite phase can be attributed to its microstructure. In steel with ~0.3% carbon, the martensite typically forms a lath martensite structure. Lath martensite consists of thin, parallel plates or laths grouped in packets. The laths are primarily composed of a body-centered tetragonal (BCT) structure of iron that is supersaturated with carbon. The microstructure is characterized by a high density of dislocations and a lack of carbide precipitates, differentiating it from other phases like pearlite. This arrangement can provide a unique configuration that makes the anodic and cathodic reactions difficult while the potential differences between laths are negligible. However, corrosion may occur later since this microstructure is not homogenous, and corrosion can initiate at weak points within the microstructure. If this occurs, it may lead to very localized corrosion.

SUMMARY AND CONCLUDING REMARKS

This research examines the kinetics of passive layer breakdown induced by chloride on martensite and pearlite phases in TMT carbon steel using a high-throughput method with SECM. It was shown that SECM is a powerful method for studying surface electrochemical activities. The samples were immersed in a simulated concrete pore solution. After the formation of a passive layer, chloride ions were introduced to break down the passive layer and initiate corrosion. The results revealed that the microstructure of the steel significantly influences the breakdown of the passive layer.

After 72 hours of immersion in a chloride-contaminated solution, martensite showed superior corrosion resistance compared to pearlite. The research further highlighted that the kinetic of the corrosion is a time-dependent process. Nonetheless, further research is needed to fully understand the nuances of microstructure-corrosion relationships and the long-term performance of different phases in carbon steel.

ACKNOWLEDGMENTS

This work was conducted in the Corrosion Research Laboratory (CorRLab) at Clemson University. This study is funded by National Science Foundation Grant No. 2221098, which is greatly acknowledged. Any opinions, findings, conclusions, or recommendations expressed in this material are those of the authors and do not necessarily reflect the views of the National Science Foundation.

REFERENCES

Bard, A. J., Fan, F. R. F., Kwak, J. and Lev, O. (1989). "Scanning Electrochemical Microscopy. Introduction and Principles." Analytical Chemistry **61**(2): 132-138.

Chambers, B. D., Taylor, S. R. and Kendig, M. W. (2005). "Rapid Discovery of Corrosion Inhibitors and Synergistic Combinations Using High-Throughput Screening Methods." CORROSION **61**(5): 480-489.

Cui, N., Qiao, L. J., Luo, J. L. and Chiovelli, S. (2000). "Pitting of Carbon Steel with Banded Microstructures in Chloride Solutions." British Corrosion Journal **35**(3): 210-215.

Glass, G. K. and Buenfeld, N. R. (1997). "The Presentation of the Chloride Threshold Level for Corrosion of Steel in Concrete." Corrosion Science **39**(5): 1001-1013.

Koleva, D. A., van Breugel, K., de Wit, J. H. W., van Westing, E., Boshkov, N. and Fraaij, A. L. A. (2007). "Electrochemical Behavior, Microstructural Analysis, and Morphological Observations in Reinforced Mortar Subjected to Chloride Ingress." Journal of The Electrochemical Society **154**(3): E45.

Liu, B. and Bard, A. J. (2002). "Scanning Electrochemical Microscopy. 45. Study of the Kinetics of Oxygen Reduction on Platinum with Potential Programming of the Tip." The Journal of Physical Chemistry B **106**(49): 12801-12806.

Mena-Morcillo, E., Ebrahimzadeh Pilehrood, A., Moshrefi, R., Shafiee, G., Keech, P. G., Behazin, M. and Gateman, S. M. (2024). "Effect of Redox Mediators on Corrosion Behavior and Scanning Electrochemical Microscopy Response." Analytical Chemistry **96**(22): 9122-9131.

Mirkin, M. V. (1999). "High Resolution Studies of Heterogeneous Processes with the Scanning Electrochemical Microscope." Mikrochimica Acta **130**(3): 127-153.

Neufeld, A. K. and O'Mullane, A. P. (2006). "Effect of the Mediator in Feedback Mode-Based Secm Interrogation of Indium Tin-Oxide and Boron-Doped Diamond Electrodes." Journal of Solid State Electrochemistry **10**(10): 808-816.

Ngamchuea, K., Eloul, S., Tschulik, K. and Compton, R. G. (2014). "Planar Diffusion to Macro Disc Electrodes—What Electrode Size Is Required for the Cottrell and Randles-Sevcik Equations to Apply Quantitatively?" Journal of Solid State Electrochemistry **18**(12): 3251-3257.

Polcari, D., Dauphin-Ducharme, P. and Mauzeroll, J. (2016). "Scanning Electrochemical Microscopy: A Comprehensive Review of Experimental Parameters from 1989 to 2015." Chemical Reviews **116**(22): 13234-13278.

Poursaee, A. and Angst, U. (2023). Principles of Corrosion of Steel in Concrete Structures. Corrosion of Steel in Concrete Structures, Elsevier**:** 17-34.

Rojhirunsakool, T., Thublaor, T., Shirani Bidabadi, M. H., Chandra-ambhorn, S., Yang, Z. and Gao, G. (2022). "Corrosion Behavior of Multiphase Bainitic Rail Steels." Metals **12**(4): 694.

Steimecke, M., Carthäuser, J., Fiedler, L., Dieterich, E. and Bron, M. (2024). "Probing Carbon Materials Towards the Vanadium(Iv)/(V) Reaction by Scanning Electrochemical Microscopy." ChemElectroChem.

Torbati-Sarraf, H. and Poursaee, A. (2018). "Corrosion of Coupled Steels with Different Microstructures in Concrete Environment." Construction and Building Materials **167**: 680-687.

Torbati-Sarraf, H. and Poursaee, A. (2018). "Study of the Passivation of Carbon Steel in Simulated Concrete Pore Solution Using Scanning Electrochemical Microscope (Secm)." Materialia **2**: 19-22.

Vega, J. M., Ganborena, L., Gonzalez-Garcia, Y., Özkaya, B., Grande, H.-J. and García-Lecina, E. (2023). "Exploring the Effect of the Ph on the Corrosion of Multilayer Nickel-Chromium Coatings." Corrosion Science **210**: 110819.

Wang, Y., Goh, B., Moorehead, M., Hattrick-Simpers, J. and Couet, A. (2022). "High-Throughput Electrochemistry to Study Materials Degradation in Extreme Environments." Analytical Chemistry **94**(48): 16528-16537.

Zhang, H., Du, N., Wang, S., Zhao, Q. and Zhou, W. (2020). "Determination of Iron Valence States around Pits and the Influence of Fe(3+) on the Pitting Corrosion of 304 Stainless Steel." Materials (Basel, Switzerland) **13**(3): 726.

How concrete corrosion macrocells affect assessment and forecasting

Alberto A. Sagüés and Christopher L. Alexander

Synopsis: Corrosion of steel in concrete involves interactions between net anodic and cathodic regions that may extend into the cm, m or multi-m range. Such broad macrocells conveniently help corrosion detection methods based on half-cell potential surveys. However, the macrocells can also complicate the interpretation of polarization measurements of corrosion rates, leading to over or under estimates depending on the chosen placement of the sensor electrodes. Corrosion macrocells can also make interdependent the corrosion initiation and propagation stages of contiguous parts of a structure, by mutually affecting chloride threshold values and corrosion rates. Damage evolution forecasts change considerably when interdependence is taken into consideration, an issue of importance in creating next generation models. This paper addresses understanding by the corrosion in concrete community in a selection of these issues, and anticipates challenges to be resolved next.

Keywords: corrosion, localized, macrocells, steel, rebar, concrete, measurement, polarization, impedance, modeling

ACI member **Alberto A. Sagüés** is a Distinguished University Professor Emeritus in the Department of Civil and Environmental Engineering at the University of South Florida in Tampa, FL. His research interests are corrosion of engineering Materials, concrete, materials for Infrastructure, materials for energy systems, durability forecasting, physical metallurgy and nuclear waste disposal. He is a licensed Professional Engineer in Florida.

ACI member **Christopher L. Alexander** is an Assistant Professor, and Susan and William Bracken Junior Faculty Fellow in the Department of Civil and Environmental Engineering at the University of South Florida in Tampa, FL. His research interests are corrosion of civil infrastructure and critical systems, electrochemical impedance spectroscopy, and modeling of electrochemical systems.

INTRODUCTION

Corrosion of steel reinforcement (e.g., rebar) in concrete has long been recognized as an electrochemical process ruled by the general laws of aqueous corrosion. However, because of the typically large size of reinforced concrete components and the range of conductivity values of concrete, there is often distinct and sustained separation of net anodic and net cathodic regions on the steel surface, sometimes over appreciable distances. Such configuration is commonly named a corrosion macrocell. If there is corrosion but with no appreciable separation with common instrumentation of net anodic and cathodic regions, the case is variously named a local cell configuration, or a microcell [1]. Those terms are somewhat relative as there could actually be harder to detect but still strong separation of regions at the microscopic level, with the separation being either stable as may happen in pitting of stainless steel reinforcement [2], or rapidly varying with time but with a neutral average. Thus, it may be necessary to preface the term macrocell with modifying terms such as microscale, as in the example just given (separations in the order of um), mesoscale (~mm- cm) or macroscale (m) if a distinction is to be made.

Understanding of the electrochemical processes at work in concrete macrocells has made significant progress during the last decades [1-13], but some issues persist and merit revisiting. Among those, we selected for review two avenues of particular interest. In Part 1 we address some critical aspects on how the presence of meso- and macro- scale macrocells can affect the results and interpretation of nondestructive transient electrochemical measurements of corrosion rates, first in systems where the corrosion macrocell components can be separated, and then in impedance tests on complete macrocells. In Part 2, we review how consideration of corrosion macrocells is emerging as a necessary component next generation models for forecasting corrosion in reinforced concrete.

PART 1 - CORROSION MEASUREMENTS WITH MACROCELLS PRESENT.

Basic Considerations

In an idealized macrocell-free situation, one may consider an electrically continuous but otherwise isolated metallic component that is corroding uniformly and having uniform polarization properties. The metallic body then develops, with respect to the surrounding electrolyte, a uniform electric potential that is variously named the open circuit potential (OCP) , the corrosion potential (E_{corr}) or the mixed potential (E_{mix}). At that potential, the rate of electron release by the anodic reaction equals the rate of electron consumption by the cathodic reaction both locally and globally. Such system then exists on a state that is steady as long as the factors that control the dependence of anodic and cathodic reaction rates on electrode potential remain unaltered. Under the above circumstances measurement of the uniform

corrosion rate on the metal surface by polarization methods can be understood in relatively straightforward terms, if the polarization functions for both corrosion and interfacial charge storage processes are known, and the excitation current is uniformly applied to the entire surface. The problem then is equivalent to the kind of analysis used for a small discrete electrode sample in the laboratory. Measurement complications in macrocell-free cases do occur, notably stemming from the practical need of having to use a finite size counter electrode (CE) that is usually much smaller than the reinforcement assembly is. While the amount of current delivered by the CE is well defined by the electronic instrumentation, the size of the portion of the rebar assembly receiving that current (and the corresponding, usually non-uniform current density distribution on that area) is not. The issue is addressed by devices such as guard-ring CEs, which confine [14] – more or less successfully [15]- the excitation current to a known area portion of the assembly. Alternatively, an unconfined finite CE could be used, combined with modeling approaches implemented to estimate some effective equivalent excited rebar assembly area. Recently, a mathematical relation between the measured apparent polarization resistance and the true value was proposed that incorporates a transmission line model to account for the current spread beyond the CE edge.[16]

The corrosion rate measurement becomes significantly more complicated if a pronounced corrosion macrocell is present. That is partly because the corrosion current density (and its associated polarization admittance) on the rebar assembly is non-uniform to start with, thus resulting in a non-uniform excitation current distribution even if a potentiostated CE were to ideally cover the entire rebar assembly. But even if the excitation current distribution were known, interpretation of the results per the approaches commonly used for macrocell-free cases could lead to completely erroneous results, such as estimating significantly high corrosion rates for regions that are still in the passive state. Further complications arise from disproportionate effects of the macrocell configuration on the distribution of the charge-storage admittance (e.g., from interfacial capacitance) associated with the cathodic and anodic regions, which introduce errors in the ohmic resistance that must be subtracted for calculating polarization resistance in models. Examples of the associated challenges and interpretation approaches are given next.

For the following discussion, consider the case of an extended structural component subject to chloride exposure such that some parts of the assembly have already reached an active corroding condition while the rest are still on the passive condition. An idealized and highly simplified system has been chosen, as it is sufficient to reveal the key issues of concern that are inherent to the macrocell problem, which would remain, likely aggravated, in more sophisticated representations. The system provisions are (see Table 1 for nomenclature):

1) the anodic reaction is of the form $Fe \rightarrow Fe^{+2} + 2e$ while the cathodic reaction is oxygen reduction as $O_2+H_2O + 4e \rightarrow 4\ OH^-$. The potentials developed in the system are assumed to be removed far enough from the respective equilibrium potentials to result in negligible reverse reaction rates.

2) the anodic reaction on the actively corroding portions of the assembly is activation-polarized with current density $i_a=i_{0a}\ 10\text{^}[(E-E_{0a})/\beta_a]$. On the passive portions of the assembly, the rate is small and potential independent, $i_a=i_p$

3) the cathodic reaction on both active and passive regions is subject to mixed activation and concentration polarization per $i_c=ic_0\ (C_o/C_{0o})\ 10\text{^}[(E_{0c}-E)/\beta_c]$. As a rough approximation, the cathodic kinetic constants are assumed to be the same whether the surface is active or passive.

4) in addition to the above noted corrosion processes, both active and passive steel surfaces have charge storage behavior in the form of a simple and uniformly distributed interfacial capacitance, C_i, that results in an additional electrode current density component $i_C = C_i\, dE/dt$

5) the concrete is treated as a homogeneous medium with finite uniform homogenized electric resistivity and oxygen diffusivity.

Polarization Measurements in Separable Macrocell Components

We look first at idealized polarization measurements performed at very low scan rates, where the interfacial charge storage contributions to the excitation current are negligible compared to those of the corrosion process – conditions resembling those in a simple, notional polarization resistance method (PRM) experiment [17]. Consider initially a macrocell-free situation with ideally uniform corrosion and a CE arrangement that delivers uniform excitation current density, and assume for the moment absence of concentration polarization (that is, $C_o \sim C_{0o}$). Those conditions meet the classic treatment by Stern and Geary [13]. There $i_{as}=i_{cs}=i_{corr}$ (the subscript s means the steady state value) and $E=E_{corr}$. In such system an applied potential[A] change from E to $E+\Delta E$ [B] results, when $\Delta E \rightarrow 0$, in partial current density changes $\Delta i_a \sim \Delta E\, i_{as}\, 2.3 / \beta_a$ and $\Delta_{ic} \sim -\Delta E\, i_{cs}\, 2.3 / \beta_c$, as a consequence of the properties of the assumed exponential nature of the polarization functions upon small variations. Thus in that small amplitude limit the total applied (excitation) current density $i_x = \Delta_{ia} - \Delta_{ic}$ associated with the applied potential change is nearly linearly related to the potential change. That linear limit behavior is expressed in the familiar form of a polarization resistance, defined as $R_p = \Delta E / i_x$.

For the present case, R_p can be easily calculated from the experimental data, and by simple derivation from the above expressions [17, 18] it is readily seen that R_p is inversely related to i_{corr} by

$$R_p = B / i_{corr} \qquad \text{(Eq. A)}$$

where $B = \beta_a \beta_c / [2.3(\beta_a + \beta_c)]$.

Thus, with previous knowledge - or judicious estimates - of the polarization slope values β_a and β_c, the results of a small amplitude polarization measurement can provide a useful estimate of the ongoing corrosion rate in this simple activation-polarized macrocell-free system.

It is emphasized that Eq.(A) is not the general definition of R_p ($R_p$is the potential/current density ratio stated earlier), but rather it indicates the value of R_p is for the specific case considered. With appropriate working assumptions, the treatment can be extended to obtain estimates, or at least bounding values, of i_{corr} for cases having mixed activation-concentration polarization of the corrosion reactions. For such cases a different, more complicated expression for the value of R_p applies and other descriptors, such as the charge transfer resistance R_{ct} are more convenient in lieu of R_p to relate to the corrosion rate [19]. For the following discussion, unless otherwise indicated it will suffice to consider only systems with simple

[A] The term “applying” (or imposing) a potential change is shorthand for using an auxiliary electrode and electric power source to create an electric field across parts of the system, that cause in ionic or electronic rearrangement until a certain desired interfacial potential value is achieved – a form of potentiostatic control. Conceptually the process can be equivalently expressed with the same results in impressed current, galvanostatic terms. Either expression will be used subsequently when convenient.

[B] Potential measurements are idealized as being conducted with a reference electrode having the sensing tip placed in the concrete immediately next to the metal surface at the location being assessed.

activation polarization, with the understanding that the arguments could be readily extended to more general cases.

The above analysis for the macrocell-free system remains at least approximately valid if the CE is engineered to confine efficiently a known and nearly uniform excitation current density to only a small region of the rebar assembly. A confined impressed potential or impressed current experiment to determine R_p can be readily conducted when a macrocell is present as well. However, the R_p value thus obtained is no longer simply related to the corrosion rate as it was above. Consider for example the case where a small portion of the rebar assembly, assessed via a confined excitation current, has steady state uniform values of i_a and i_c but with $i_c > i_a$, that is, exhibiting a net cathodic behavior. That means that there is a net steady state macrocell current density $i_m = i_c - i_a$ flowing across that selected portion of the metal-concrete interface. Because of the current imbalance associated with the macrocell the corrosion current density i_{corr} is no longer equal to both i_{as} and i_{cs}, but rather only to i_{as}, which under the working assumptions is the only descriptor for the steady state metal dissolution process.

To examine the consequences, notice that regardless of whether there is a macrocell or not, the small potential change ΔE in the confined region of interest still causes changes in the anodic and cathodic densities equal respectively to $\Delta i_a \sim \Delta E\ i_{as}\ 2.3 / \beta_a$ and $\Delta i_c \sim -\Delta E\ i_{cs}\ 2.3 / \beta_c$. However, since in this case i_{as} and ics are no longer equal, the ratio $R_p = \Delta E / (\Delta i_a - \Delta i_c)$ is no longer simply related to i_{corr} ($=i_{as}$) but rather given by

$$R_p = B / [i_{corr}\ \beta_c/(\beta_a+\beta_c) + i_{cs}\ \beta_a/(\beta_a+\beta_c)] \qquad \text{(Eq. B)}$$

where B is the same as before.

Individual situations can now be examined. If $i_{corr} = i_{cs}$, Eq.(B) reduces to Eq(A) as it should, since that is the macrocell-free case. In an extreme macrocell case where the portion being assessed is a pure anode ($i_{cs}=0$), R_p is simply related to corrosion rate by

$$R_p = B_a / i_{corr} \qquad \text{(Eq. C)}$$

where $B_a = \beta_a / 2.3$

Although the proportionality constant B_a is somewhat different from B (by a factor of 2 if $\beta_a = \beta_c$), Eq, (C) indicates as in the macrocell-free case that a finite, low value of R_p signals the presence of appreciable corrosion activity. Thus, in both situations just considered a finite value of R_p is indicative of ongoing, (and if R_p is small, strong) corrosion.

However, generalization of the above association to all macrocell cases could be highly misleading. That becomes evident when considering the opposite extreme macrocell case where the local behavior is purely cathodic. Then locally $i_{corr}=0$, but the polarization of the cathodic reaction still yields a finite, and depending on location (especially near anodic regions) possibly small, value of R_p:

$$R_p = B_c / i_{cs} \qquad \text{(Eq. D)}$$

where $B_c = \beta_c / 2.3$

Thus, uncritical interpretation of the observed finite polarization resistance measurement could erroneously diagnose ongoing corrosion (possibly even strong) where there is none. In less extreme, but still predominantly cathodic conditions, various degrees of exaggerated indication of ongoing corrosion may occur. This caveat is important especially if corrosion surveys are conducted with automatic

instrumentation that may display results based on interpretative algorithms or AI methods not transparent to the operator. Advice by a specialist should be considered when planning assessments of this type.

Another issue of caution applies to assessments, usually in laboratory studies, where parts of the rebar assembly in a macrocell assembly can be connected or disconnected at will from the rest of the reinforcement. Those systems offer the opportunity to make well delimited measurements of polarization conditions in individual rebar segments that are parts of a wider macrocell. Thus, issues such as uncertain current confinement by the CE system are avoided. An early example of such configuration, comparable to that used in numerous other concrete macrocell investigations [6, 12, 13] is shown in Figure 1 [5].

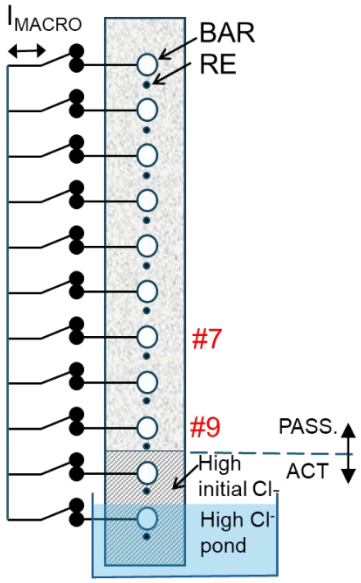

Figure 1 - Multiple rebar column with the lowest two segments in Cl^--rich concrete (lowest level ponded as well), causing active steel behavior. The rest of the segments were in the passive condition. The segments (No. 1 -11 from top to bottom) were all normally interconnected. Each segment could be temporarily disconnected from the rest for measurement of the segment's macrocell current I_m and other polarization tests. Further details in Ref. [5].

While the arrangement can be very useful, proper control of the steady state and differential polarization conditions during measurements of a separable segment is essential for the results to be meaningful. For example, simply disconnecting a segment and attempting to conduct on it a PRM or EIS test, as if it were a steady state open circuit system, can lead to erroneous information. That is because the steady state condition includes a segment bias current I_m applied through the segment connecting wire. I_m is the integral of i_m over the surface of the segment, or ~i_m A_s if conditions are approximately uniform over the surface area A_s. When the segment is disconnected without any other provision, I_m becomes zero, and the potential of the segment with respect to the surrounding concrete starts to drift (initially quite fast, but then slowly over possibly many hours) toward some new terminal steady state value consistent with I_m=0. That new terminal potential can be markedly different from that present before the disconnection, and with accordingly different values of i_{as} and i_{cs}. That situation can seriously complicate the execution and

interpretation of corrosion measurements. For example, if typically available PRM or EIS equipment were set to conduct an open circuit test upon disconnection, the device may start the test only at some uncertainly controlled time after disconnection, when the potential drift rate had reached below some instrumentation-set criterion to decide when conditions are stable for the requested test. The equipment software may cancel the test anyway if the persistent drift produces unmanageable data, but even if the test were completed conditions at that time will likely correspond to some potential quite different from that of the initial or the new terminal steady state, and results would be accordingly uninformative.

Correct evaluation of a separable segment needs the premises for developing Eqs. B to D to remain valid. To achieve that, the segment to be assessed needs to remain current-biased at the original steady state conditions, and yet subject to additional excitation current that is precisely differentially polarizing that segment. For example, if a PRM is to be made using a potentiostatic device, the starting potential for the test should be pre-specified ahead of the test, to a value equal to the previous undisturbed steady state potential value, measured before disconnecting the segment. WE, CE and RE connections of the potentiostat should be respectively to the rebar segment, an external electrode (preferably the rest of the rebar assembly), and a suitably operational reference electrode placed ideally next to the rebar segment surface. In the Fig. 1 example, the REs were metal/metal oxide bars embedded in the concrete [5]. The test can then proceed by first disconnecting the segment from the rest of the assembly and simultaneously transferring the connection to the controlling potentiostat. A brief conditioning period should be specified for the system to stabilize from any transients that might have taken place during disconnection and subsequent takeover by the potentiostat to deliver the current I_m that was formerly provided by the rest of the assembly. After that period, that may be as short as a few seconds, the polarization experiment proper can begin. The processing software should be programmed to calculate R_p as the ratio of the potential changes, to the variations in current around the value of I_m. That current can be scaled per the value of A_s if it is desired to express the results in nominal area-specific terms under the approximating assumption that conditions are uniform over the surface of the segment. Alternatively, if the test is to be done with a galvanostatic device (with electrode connections same as above), then the value of the current I_m flowing to the segment should be measured prior to the polarization experiment using a Zero Resistance Ammeter (ZRA). Next, a direct-current current source[C], set to deliver I_m, should be inserted between the segment and the rest of the rebar assembly. The galvanostatic PRM device can then be connected to deliver the excitation current, additional to I_m, between the CE and the segment, with comparable operation stability caveats to those indicated above.

EIS tests either under potentiostatic or galvanostatic operation can be addressed with generally the same provisions as those above for PRM operations. It is noted that for EIS the current source for galvanostatic tests should approximate ideal behavior (infinite impedance) at all frequencies tested, so any capacitor that might have been added in parallel with the source to reduce high frequency noise [5, 20] should be removed.

Adequate implementation of those approaches can provide valuable and accurate information, as demonstrated in experiments with the columns described in Figure 1. There an extended macrocell existed, with the passive upper segments (No.1 to 9) experiencing net cathodic current of decreasing value as the distance from the active lower segments (and therefore the intervening concrete path resistance)

[C] An ideal current source is a two-terminal device that drives a current, of a preset value, across an electric load placed across the terminals regardless of the resistance or native potential difference across the terminals of the load. Practical current sources suitable for the present purpose are readily implemented with off the shelf electronic devices

increased. The individual cathodic segment currents could be accurately measured, as well as cathodic polarization curves using slow scan rate measurements where the macrocell current was manipulated as needed. Those tests yielded well-defined cathodic polarization slope values (on average β_c = 137 mV/decade for the period of interest, consistent with values normally observed for steel in concrete). That was confirmed by separate steady state potential-current correlations that indicated also that those segments had only very small anodic current values, consistent with passive dissolution conditions, so conditions approximated pure cathodic behavior. Galvanostatic EIS experiments conducted in selected segments of multiple columns were then conducted using the current biasing procedure indicated earlier. Results were evaluated using suitable equivalent circuits for separating the (non-ideal) interfacial charge storage contribution from that of the cathodic reaction, and precisely estimating the R_p values. The EIS-determined cathodic reduction current for selected segments at various system ages were then calculated per Eq. (C). Those EIS-determined values showed excellent agreement with the independently, directly ZRA- measured cathodic currents for the same segments at the same times, as demonstrated by the 1:1 plot in Figure 2. Note that values shown in that Figure are whole segment currents. Based on the system geometry and for cathodic segments, current densities were anticipated to be approximately uniform in each segment. The resulting nominal area-specific current densities, typically ~<1 uA/cm^2, were in the order of those observed in comparable macrocell situations in concrete [11].

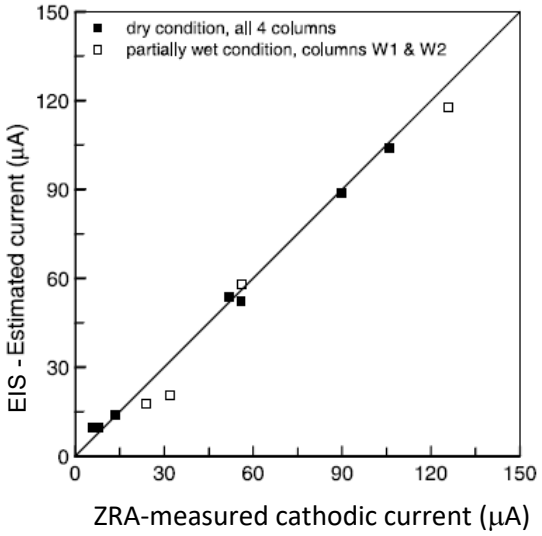

Figure 2 –Cathodic current for the system show in Figure 1 estimated from EIS measurements vs. direct ZRA measurements for segments No. 7 and 9. Surface area of each segment in contact with concrete: 166 cm^2. (From Ref. [5]).

Macrocell-induced error in EIS corrosion rate determination

In the simplified treatment of differential polarization measurements of the previous section, it was assumed that the reference electrode had its sensing tip placed in the concrete ideally immediately next to the metal surface at the location being assessed. Except for rare conditions, that provision is not satisfied; for practical reasons the sensing point needs to be located often at the external surface of the concrete or in general, at some distance from

the interface of interest. In a simple system with otherwise uniform conditions, the effect of that separation may be largely remediated by an ohmic compensation of the measured potential change:

$$\Delta E_{comp} = \Delta E_{meas} - i_x R_{ohm} \qquad \text{Eq. (E)}$$

There R_{ohm} is the surface-specific resistance of the intervening concrete between the interface point of interest and the RE sensing tip. ΔE_{comp}, approximates what would have been observed if the sensing tip had been placed directly at the interface, so ΔE_{comp} is used in lieu of ΔE for polarization resistance and related calculations.

Under very simple conditions, for example excitation current flowing uniformly out of the interface of interest, and RE tip a short distance x_r away, and if the resistivity ρ of the concrete in that region had been previously determined by independent measurement, Rohm could be reasonably estimated by $R_{ohm} = \rho\, x_r$. If ρ and/or x_r were not known beforehand, an EIS measurement could be used to obtain R_{ohm}. It can be approximated by the real value of the impedance at the intermediate high frequency impedance arrest, that in concrete may effectively occur at frequencies in the audio range or even as low as ~1Hz [21]). There the impedance has nearly no imaginary component, as the excitation current flows mainly through the ohmic path of the concrete pore network since the frequency is too low to significantly sense the dielectric capacitive path within the concrete. Concurrently, the current is also shorted across the interfacial capacitance of the interface since, in contrast with the case of the concrete dielectric capacitance, frequency, is high enough to make the interfacial capacitance path have negligible impedance compared to that of the reaction polarizations.

While the above approach is reasonably accurate for conditions of some corrosion uniformity, as it will be shown next it can lead to considerable underestimation of the corrosion rate in the presence of corrosion macrocells, especially in the micro- and meso-scale. Consider for example the modeled system shown in Figure 3 [22].

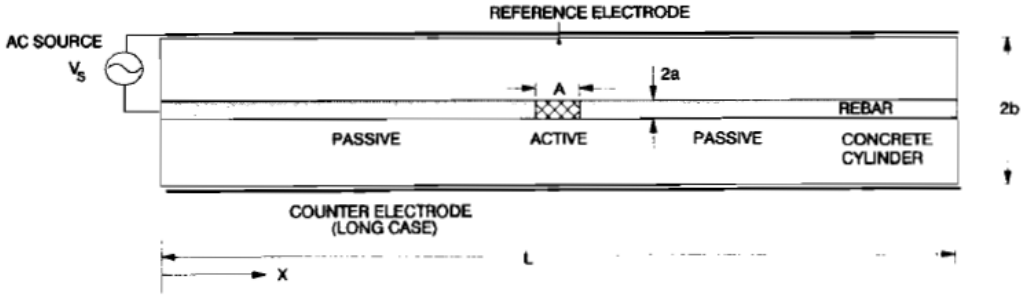

Figure 3 – Reinforced concrete cylinder with central rebar having a short active region near the center and the rest in the passive condition. For EIS measurements, a CE covers the entire lateral external surface. RE tip is placed center on the external concrete surface just beneath the CE. From Ref. [16].

The CE covers the entire length of the rebar so it might be thought at first glance that excitation current distribution would not deviate much from uniformity. However, quantitative modeling of the system shows that such result applies only to the high end of the impedance spectrum.

As shown in Figure 4 (top) at sufficiently high frequencies (in this case already at 1 Hz), representative interfacial capacitance values of steel in concrete (e.g. in the order of 100 $\mu F/cm^2$ when considered as the equivalent value of a usually non-ideal charge storage process at the frequencies of interest [21]) have impedance values much smaller than those of typical surface-specific polarization resistances under corrosion conditions , as well as of those associated with the resistivity of the concrete. Thus the rebar surface represents a comparatively near-zero

impedance boundary, and the current distribution approaches that which would result from the applied excitation potential at the CE and a cylindrical space of uniform resistivity ρ. The resulting value of R_{ohm} is comparatively low.

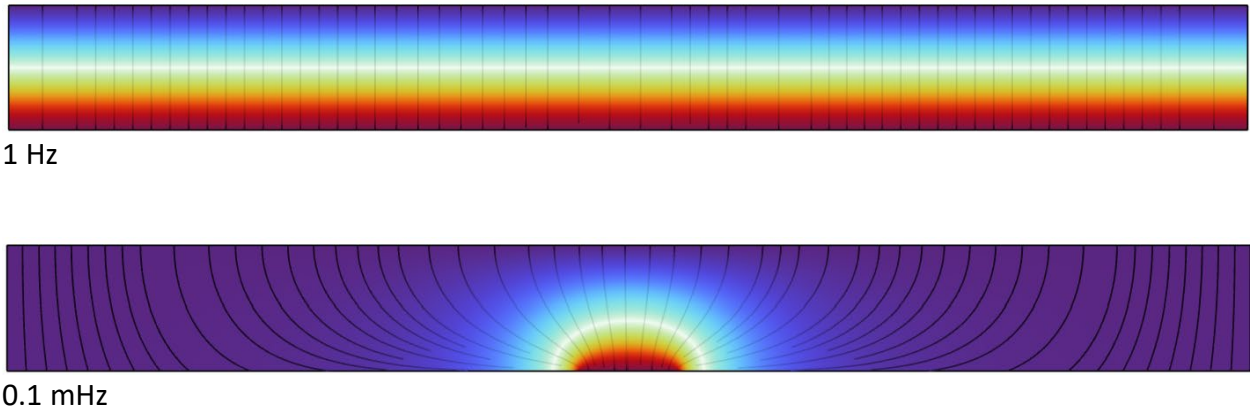

Figure 4 – Differences between the ac signal distribution pattern at high (1 Hz) and low (0.1 mHz) frequencies for the half-space of the cylindrical geometry system in Figure 1. Upper and lower edges in each diagram correspond to CE and rebar surfaces respectively. Blue-to-red color scheme correspond to respectively highest and lowest effective ac voltage values. Simulation created to correspond to results in Ref. [22].

At the low frequency end of the spectrum (e.g, 0.1 mHz, several orders of magnitude less than before) the current distribution is markedly less uniform, as shown in figure 4, bottom. The admittance of the interfacial capacitance is now negligible compared with that for polarization of the corrosion reactions. Of those, surface-specific admittance for the passive portions of the rebar is in turn much smaller than for the small, net anodic active portion. As a result, most of the excitation current from the large CE is now sinking in the small anode region, resulting in a markedly non-uniform current distribution pattern. That concentration of excitation current density near the anode at the low frequencies causes an accordingly substantial increase in ohmic potential drop between the concrete at the steel interface and the location of the RE tip.

Duly noting that the enhanced potential drop at low frequencies is not uniform along the bar, the overall result (now expressed in terms of non-surface specific amounts, superscript ') would resemble that of a discrete system where the solution resistance is frequency dependent, with greater values at low frequencies. In a simple, activation limited discrete system the Nyquist diagram corresponds to a semicircle horizontally offset from the origin by a fixed value R'_{ohm}, and the value of R'_p is given by the semicircle diameter. Discrete systems with more complex polarization cases, for example involving diffusional components and needing charge transfer resistance (R'_{ct}) computations in lieu of R'_p, would still involve a fixed offset. Instead, the macrocell system behaves as if having a diagram shift that increases with decreasing frequency. As shown in Refs. [22-24] the result is a semicircle that is elongated in the real axis direction. Thus, if that pattern is subject to the circuit fit analysis normally used for discrete systems, the calculations would yield an apparent value of R'_p (or of R'_{ct} if that is the case) significantly greater than the one representative of actual conditions. The corresponding measured value of I_{corr} would then accordingly underestimate the actual value. It is noted that while the analysis is treated as that for EIS experiments, its general meaning applies too to PRM, pulse tests, or similar methods when viewed via frequency to time-domain transformations [15, 25, 26]

Such underestimation of corrosion activity could be quite severe, especially in the case of a scattering of small active spots on a mostly passive field, as it may occur during the early stages of corrosion, or in the increasingly important

case of use of stainless or other newly implemented corrosion resistance rebar materials [2, 27]. Analysis of a number of representative cases was conducted in a previous study [24], as shown in Figure 5.

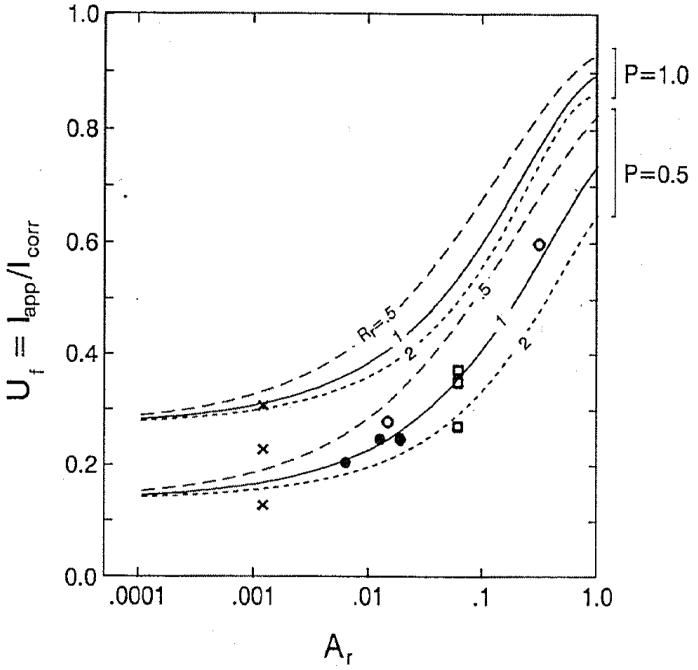

Figure 5 – Theoretical model forecast for various degrees of corrosion localization. See text for parameter definitions. From Ref. [18].

Based on the results and the underlying principles a theoretical predictive model (not a regression fit) was formulated that projected the ratio U_f of apparent integrated corrosion current (I_{app}) obtained by EIS analysis, to actual corrosion current $I_{corr.}$ Projection parameters where the area ratio Ar= total area of net anodic regions / total area of net cathodic regions, the extent P= I_m/I_{corr} to which the corroding spots had purely anodic behavior, and the ohmic effect importance ratio $R_r=R_s/R_p$, where R_s is the value of the apparent solution resistance (high frequency impedance limit) , to the value of polarization resistance that would have been measured without ohmic drops in the measurement process. The individual symbols in Fig. 5 show the result of numerical model calculations for various individual CE, WE and RE configurations ranging from cylindrical systems as that in Figure 1, to a circular ring electrode centered on a disk-shape corroding spot [16-18]. Those systems had P values ranging from 1 to 0.62 and R^r from 0.16 to 46, but in most instances $0.75<R_r<5.04$. The results show that the theoretical model, without parameter adjustment, reasonably captured the main behavior trends. Of particular interest are model predictions for P=0.5, that is roughly representative of many actual concrete macrocells where I_m is an appreciable fraction of I_{corr} [10]. There the results suggest that there could be severe – approaching one order of magnitude - underestimation of I_{corr} in the aforementioned situations where A_r is very small. Thus, careful evaluation of measurement findings should be exercised in macrocell configurations like these, to understand the potential sources of error and lead to adequate corrosion control decisions.

Variations of effective solution resistance with frequency, leading also to inaccurate estimates of corrosion rate, may occur from other sources as well. Current work using modern FEM treatments [27] examines the added effect of elevated specific interfacial capacitance at the anodic zone, which was not included in the previous analysis. Because of the corresponding frequency-dependent differences in ohmic paths to each zones, different time constants occur in the impedance spectrum corresponding to the primarily anodic and cathodic regions respectively. The result is an added frequency-dependent "ohmic" impedance (with both real and complex components) with associated underestimation of the corrosion rate if not take into account. It is noted that an "ohmic" resistance – and associated

inaccuracies in corrosion measurement- can also result from the non-uniform current distribution imposed by the specimen geometry and electrode configuration [16].

Data analysis to either directly calculate accurate corrosion rates, or to obtain correction factors to apply to apparent results is in theory possible. However, it may not be feasible without precise information on the actual damage morphology, or on accurate system dimensions and configuration. Even with that information, accurate analysis may require unaffordable computational support. At present, the best path to a practical outcome with reasonable estimates of corrosion rates may involve some incremental steps. A first is to increase awareness of the pitfalls that may be involved in this type of measurements, as it is hoped reviews like this will contribute. Another is to increase the experimental knowledge base of comparisons between electrochemical and direct measurements of corrosion rates, as exemplified by recent work in techniques ranging from EIS to accelerated pulse measurements [28, 29]. Furthermore, for field studies, it is recommended that R_p measurements be coupled with half-cell potential mapping (HCP). That mapping can provide indication of macrocell activity and help distinguish locations between primarily anodic and cathodic zones. If such information is available, it may be assumed that corrosion rate estimates corresponding to locally anodic regions will likely be underestimated and corrosion rates estimated in locally cathodic regions that are near anodic regions would be overestimated. Compilation of the information derived from the above approaches together with modeling to cover an anticipated range of conditions encountered in actual systems may then lay the foundation for establishing more accurate correction factors to apply to measured apparent corrosion current values for a set of likely scenarios.

PART 2: INCORPORATING MACROCELL EFFECTS IN CORROSION FORECASTING

The forecasting task

There is general recognition that the corrosion localization associated with the presence of corrosion macrocells merits treatment when evaluating service life. Modeling approaches have been developed accordingly. However, the macrocell presence creates electrochemical interactions between the zones of the assembly were active corrosion has started and those where it had not yet started. Such interactions can substantially delay the time of new events of corrosion initiation, while aggravating the extent of active corrosion in the regions that are already corroding. Interactions of this type are often ignored in present generation forecasting models, with consequent sometimes overly conservative or un-conservative projections of future damage and associated inadequacy for design or maintenance decisions. Illustrations of ongoing attempts to incorporate macrocell effects in next generation modeling are presented subsequently.

Forecasting models for corrosion of steel in concrete may be viewed as the ultimate intended outcome of the effort to measure and understand corrosion in that system. A rational predictive model allows the designer to make critical choices in selection of materials and structural configuration, to achieve a service life goal in the most economical and safe manner. Rational modeling started in the 1970s with the proposition that the corrosion process could be divided into distinct corrosion evolution stages [31]. In the first or initiation stage, the external aggressive agent penetrates the concrete and builds up at the reinforcement surface until triggering the transition from passive to active corrosion. In the second or propagation stage, the active corrosion consumes steel, weakening the rebar, and at the same time accumulates expansive corrosion products that locally crack the concrete and weaken the mechanical steel/concrete bond. The propagation stage is declared complete when the rebar and concrete integrated damage exceeds some previously defined serviceability limit stage, for example appearance of cracks on the surface, or reduction of bar size or bond strength to some structurally unacceptable level. The duration

of each stage is calculated based on the aforementioned understanding, together with knowledge of the functional relationships between design parameter choices and the corrosion and deterioration consequences. For example, if the main controlling factor during the initiation stage is how fast aggressive chloride ions can build up in the concrete next to the steel, then parameters describing chloride transport (e.g diffusion rate values) combined with dimensional information (e.g., rebar cover thickness) and critical chloride corrosion threshold (C_T) information provide a theoretical basis using well established diffusion equations for calculating the duration of the initiation stage. A service life projection is finally obtained as the added duration of both stages. Clearly, this binary approach is a sweeping abstraction of a more complicated reality. More nuanced treatments have been proposed for future treatment [32, 33], and indeed the present discussion sets the basis for one such advancement.

Early in the development of predictive models, it was understood that the values of the parameters used in those calculations would experience natural scatter from point to point on the structure; so the projected durability would vary spatially. That led to implementation of statistical components in the predictive models, starting with treatment of the effect of rebar cover fluctuations via a standard deviation description [34] and then of a number of other influencing variables for both the initiation and propagation stages [35-38].

Interdependence and corrosion macrocells

The statistical treatments have progressed to this day, but with most approaches explicitly or implicitly sharing a common limitation: in spatially extended systems, effects of statistical variation of adjacent portions were not interdependent. Such assumption may be justified if there is little electrochemical interaction between the various regions, for example if the resistivity of the concrete is relatively high so lateral conductive coupling in a concrete slab structure may not be important. On the other hand, interactions could be quite strong in a marine substructure system. There concrete submerged in seawater or subject to extensive pore water chloride contamination elsewhere can be highly conductive, and extended corrosion macrocells be maintained over relatively large distances. Thus, if a region of the steel assembly is actively corroding, due to the efficient conductive coupling it may strongly depress the potential of nearby regions compared to the open circuit value they had otherwise developed. If both regions in such coupled pair were already in an active condition but at different degrees, the region with the highest corrosion rate could be provide some degree of cathodic protection to the other, extending the duration of the corrosion propagation stage of the latter and shortening it for the former.

The interdependence effect could be even more consequential if the macrocell coupling were between an already actively corroding region, and another that is still in the passive condition. The C_T of passive steel has been shown to depend on the potential that it has with respect to the immediately adjacent concrete, becoming greater as the steel is polarized cathodically. This phenomenon of a potential-dependent-threshold (PDT) is due in part to the cathodically impressed electric field within the passive film, which acts in a direction that opposes passivity breakdown - an “intrinsic” effect. Concurrently, due to reaction products from the cathodic polarization and ionic migration in the concrete, there is induced elevation of pH and decrease of chloride content at the concrete-steel interface, both beneficial local environment changes that deter passivity breakdown - an “extrinsic” effect. Increasing evidence shows that the resulting effective increase in the C_T is strong, with a PDT relationship of the type

$$C_T=C_{T0}\ 10^{[(E_{CT0}-E)]/\ \beta_{CT}]} \qquad \text{Eq. (F)}$$

where C_{T0} and E_{CT0} are respectively the threshold and the open circuit potential values typically encountered in OCP atmospheric exposure conditions, and β_{CT} an exponential cathodic prevention slope

somewhere between ~200 mV [39] to ~500 mV [40, 41], so relatively modest changes in steel potential could result in an order of magnitude increase in C_T.

Per the above, regional interdependence could significantly affect the evolution of the corroding system, not only by affecting the propagation stage as indicated earlier, but also by delaying –or even suppressing- the completion of the corrosion initiation stage in the parts of the structure that had not yet experienced passivity breakdown. To illustrate how that would work, consider a chloride-exposed reinforced concrete structure that when put in service has a reinforcing steel assembly entirely in the passive condition. The steel has then a spatial potential distribution consistent with the passive condition – relatively noble values- and a corresponding distribution of comparatively low C_T values. As chloride intrusion progresses with time that initial C_T value distribution would be exceeded at some point of most severe exposure. Consequently, some of the steel surface in that location would transition to the active condition, forming a corrosion macrocell where a central anode is polarized to a markedly more negative potential than earlier, and a surrounding cathodic region with strong negative polarization near the anode and gradually decaying with distance. The newly established potential pattern in the surrounding passive steel would have as consequence an equally new C_T distribution, with values greater than before, especially in the region immediately surrounding the newly created anode. As time progresses and chloride levels at the steel assembly continue to grow overall, the next activation events will again occur where C_T is exceeded next. However, unless the chloride penetration pattern is highly non uniform, such condition is now less likely in the region immediately surrounding the first activation place, as the threshold there has increased significantly over the previous values. Therefore, the pattern of corrosion initiation progression is more likely to consist of separate regions with in-between, passive regions, compared with wide incidence of corrosion at earlier times in a forecast without zonal interdependence.

Implementation and present status

Recognition of the potential importance of these factors lead to early modeling attempts to assess how strong of an effect could be expected on the damage forecast of a notional marine substructure element. That work [42], while simplified and of moderate computing scope, confirmed the expectation of strongly delayed long-term damage projection. The work also highlighted some important challenges to incorporation of the concept in practical predictive models. Notably, in models not considering interdependence the development of conditions within each region can be computed independently and the results for the whole tallied by simple addition, a fast and efficient computational task. In an interdependent treatment, the computation must evaluate the consequences of each steel activation event to establish how it will affect the subsequent evolution of the system. That involves a number of steps following determination that a newly activated zone has been created. Even for a basic implementation scheme, the process is quite involved. For example, based in the size and position of that zone, the corresponding newly established potential distribution over the entire steel assembly must be calculated based on the electrochemical reaction polarization and species transport laws in the model. Then, the corresponding newly prevalent C_T distribution on the assembly is calculated using the threshold potential dependence law assumed for the model. Next, the time evolution of the chloride penetration is calculated based on the assumed external contamination sources and chloride transport laws. The model needs subsequently to compare the increasing chloride distribution values with the calculated new prevalent C_T, until such moment in which it is exceeded and a newly activated region is declared, at which time the process begins again. Implementation of those steps is highly computationally intensive so present applications have focused on explorations of feasibility with increasing degrees of model complexity.

A practical model implementation of the above approach was conducted in follow up work [43], in which a rotationally symmetric, quasi-2D finite different formulation was used to simulate conditions in a reinforced steel column partially submerged in seawater. The results confirmed the direction of the expected behavior and importantly, showed that incorporating PDT had a very strong effect on the amount of projected damage as the structure aged. This is illustrated in Figure 6 where the damage projection is shown as a fraction of the external surface of the concrete exhibiting cracks as function of service time.

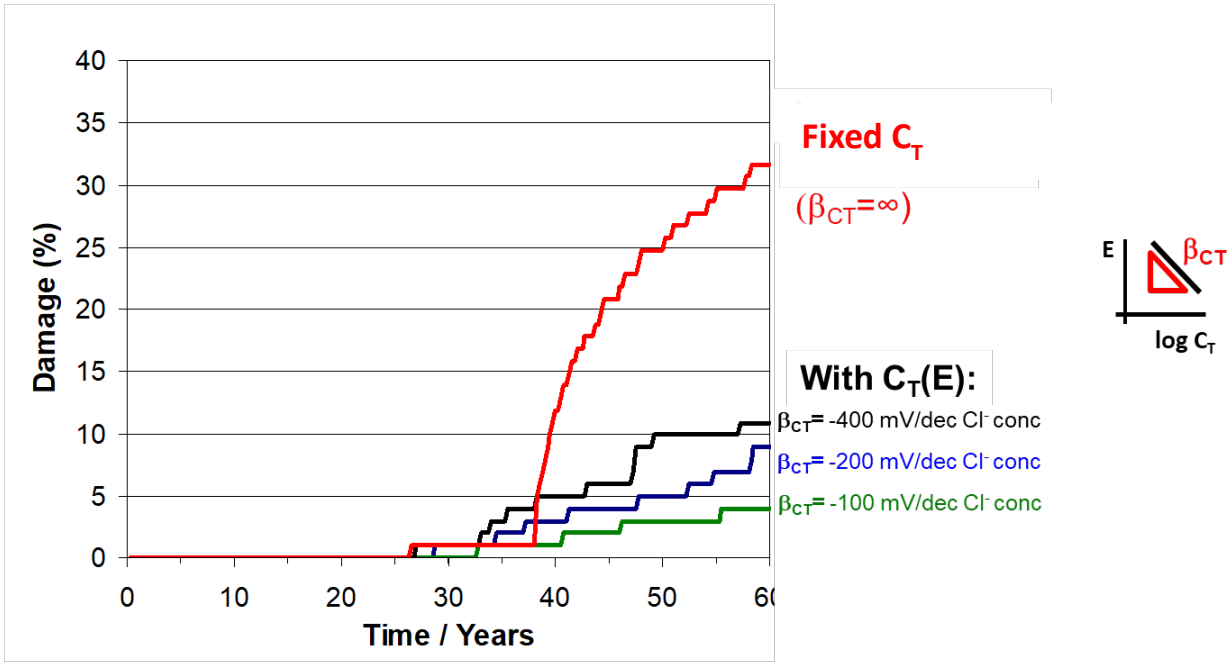

Figure 6 – Damage evolution projections assuming fixed C_T, and C_T that depends on polarization of passive steel, which changes as macrocells develop between various parts of the structure as it ages. The effect on the forecast is increasingly stronger when the dependence is more marked (smaller β_{CT}) in selected cases. Adapted from Ref [43]

There, if the PDT behavior has been turned off (by specifying $\beta_{CT} = \infty$, effectively fixing C_T as C_{T0}), corrosion induced damage of the structure approaches a large terminal value after some 4 or 5 decades of service. However, if PDT is enabled by specifying β_{CT} values in or around the order of the data cited earlier [43], the damage projection for long service times becomes markedly reduced, to values that can be only a small fraction of those for the traditional, non-interdependent modeling approaches. Analysis of the results indicates that this long-term effect is primarily related to the initiation stage delay or suppression resulting from macrocell-induced C_T elevation. On the other hand, close examination of the results shows that at low service times an opposite situation exists, where the interdependent model shows somewhat earlier appearance of the first, small indications of damage. Unlike the long-term effects, this occurrence is related to the aforementioned influence of the macrocell on the propagation stage behavior. Since new activation events are slower to develop, the corrosion rate of the initial active spots is increased and maintained in the interdependent approach due a sustained small anode, large cathode configuration. That configuration is relatively short-lived in the traditional, non-interdependent model approach as new activation events proceed unhindered.

Development of models that incorporated these macrocell effects continued later with development of rotationally symmetric true 2D formulations, implemented with an up to date Multiphysics FEM platform. Those models were used successfully to develop corrosion forecasts and design recommendations for marine substructure with partially submerged components [44-45].

Proof of the concept with more realistic 3D models is important, as in 2D configurations the anodic regions are unlimited in one direction (the perimeter for the rotational case) which unrealistically enlarges the anodic spots and their zone of influence compared with what might be expected in a natural 3D situation without bias for one dimension. Implementation of true 3D models however is daunting, because the additional dimension multiplies the already severe computational burden mentioned above. Exploratory simplified 3D modeling efforts have nevertheless been recently conducted with promising results, as illustrated in Figure 7 [46]. In that system a highly permeable concrete slab with reinforcement near the bottom surface is subject to chloride penetrating from the upper surface, which has uneven contamination with maxima near the center of each quadrant. As anticipated, the effect of newly created anodic region was found to be proportionally more restricted than in the 2D simulations. Nevertheless, the 3D model results continued to show both the strongly reduced long term forecast, as well as the short-term propagation stage enhancement, when the macrocell effect is incorporated.

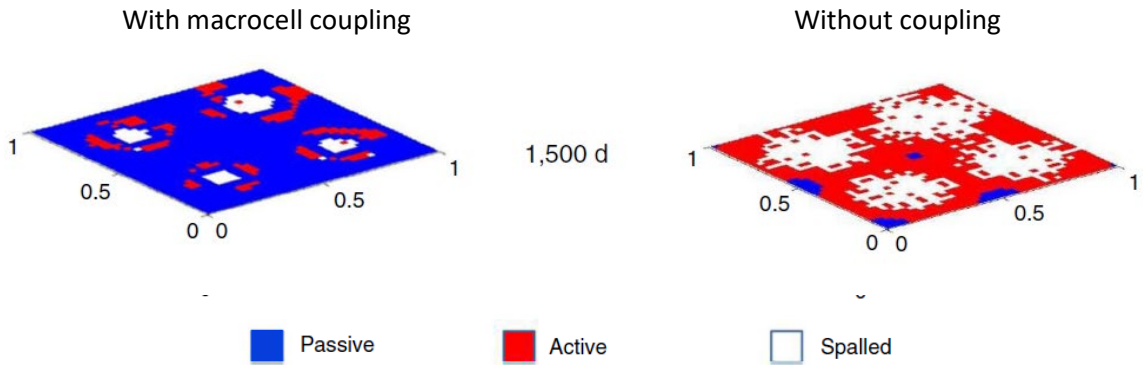

Figure 7 – Illustration of results from exploratory 3D modeling of a reinforced concrete slab (1 m on the side) with macrocell-induced interdepending behavior (left side) and traditional independent behavior treatment (right side). Color-coding indicates local conditions after 1,500 days of service under highly aggressive, uneven chloride exposure of the upper surface of the slab. Blue and Red: initiation and propagation stages respectively still in progress. White: propagation stage completed, resulting in damage visible on upper surface. Adapted from Ref. [46].

The interdependent modeling effort described above were for simplicity all limited to treating the C_T variations as intrinsic effects, ignoring the ionic migration consequences of the macrocell electric fields on the redistribution of the species as the system ages. Moreover, the computational scheme of the models introduced an arbitrary variable, the size of the activation zone, as a means to make viable the calculations of damage progression. Attempts at obviating those shortages and arbitrary choices are presently in progress, starting with a quasi-2D formulation on a Multiphysics FEM platform [47]. There a Nernst-Plank formulation introduces ionic migration rearrangement of both Cl^- and OH^- species, with C_T retaining its intrinsic potential dependence but including proportionality to the OH^- concentration at the interface, as in a chloride-to-hydroxide concentration ratio criterion [30]. Importantly, the scheme does not include

activation area size as a model parameter, but rather lets it evolve as part of the time-dependent solution of the entire coupled electrochemical and transport system of equations. That solution is arrived to without the artifice of predetermined alternating steps for each calculation, and the time step is not pre-fixed for the entire calculation as in the previous models, but rather automatically customized for stability. The initial results demonstrated viability of the approach, and were consistent with the most important features identified earlier concerning the relative effect of introducing interdependent behavior on damage projections. With migration terms in place, the models still produced forecasts where activation events were delayed at some distance from a previously active region. However, the new models forecast also some degree of lateral growth of the size of the previous active region. Initial analysis suggests that this lateral growth is a result of concurrent acidification of the existing active interface, decreasing OH^- content at the adjacent passive region to an extent that exceeds the benefits of cathodic polarization there. Examination of the adequacy of this hypothesis and progress toward a multidimensional implementation of a migration-featured model are the subject of current work in progress.

The incorporation of macrocell related PDT features in forecasting models still faces practical challenges to ensure computational viability, as well as to limit realistically the number of mechanistic features to include. Nevertheless, the results of the exploratory studies shown above indicate that ignoring this type of macrocell-induce interdependence could at various stages seriously under- or over-estimate the forecast amount of damage that the structure will experience as it ages, with possibly costly consequences if design or maintenance decisions were made accordingly. These findings are a strong incentive for follow up efforts to include corrosion macrocell features in next generation predictive models.

CONCLUSIONS

Corrosion macrocells are an integral feature of many reinforcement corrosion situations and represent important challenges and opportunities is controlling this form of infrastructure deterioration. On the issues selected for review here:

1- Corrosion rate measurements with polarization techniques can be easily performed on a system with an extended macrocell but interpretation of the results requires caution and may not be possible without additional information. For example, uncritical processing of results could yield a finite corrosion rate where the only important process is a cathodic reaction. Measurements in systems where rebar segment can be disconnected from the rest can give highly useful information, but the state of polarization of the segment needs careful control.

2-Polarization-based corrosion rate measurements of systems with macrocells from highly localized corrosion could yield seriously underestimated values, if the measurements rely on compensation of effective reference/working electrode ohmic resistance. The problem is traced to variations in excitation current pattern between behavior at the high frequencies used for solution resistance determination, and the low frequency or dc pattern relevant to the polarization of the corrosion reactions.

3-Corrosion macrocells reflect electrochemical interactions between various parts of the rebar assembly of a structure, which become interdependent as corrosion evolves with structure age. This mutual reaction can result in corrosion of one part being enhanced or decreased at the expense of another part, with resulting mutual effects on corrosion rates as well as timing of depassivation events. Corrosion models built accounting for this interdependence showed that ignoring it could seriously under- or over-estimate the forecast amount of damage that the structure will experience as it ages; next generation models should address this issue.

ACKNOWLEDGMENT

Support for this investigation was provided by the University of South Florida and the Florida Department of Transportation. The opinions and findings in this work are those of the authors and not necessarily those of the supporting organizations.

TABLES

Table 1 – List of symbols and notation

Symbols

A_r	Area ratio = total area of net anodic regions / total area of net cathodic regions
A_s	Surface area of a rebar segment
C_o	Homogenized O2 concentration in the concrete
C_{0o}	Homogenized O2 concentration at concrete surface in contact with air
C_T	Chloride corrosion threshold
C_{T0}	CT value typically encountered under atmospheric OCP conditions
C_i	Surface-specific interfacial capacitance
E	Electric potential in the concrete at the bulk or at interface points under consideration
E_{0a}	Nominal equilibrium potential for the Fe redox reaction
E_{0c}	Nominal equilibrium potential for the O2 redox reaction
E_{corr}	(also Emix and OCP) Steady state potential achieved under macrocell-free conditions
E_{comp}	Value of E after ohmic potential drop has been subtracted from E_{meas}
E_{meas}	Measured value of E
E_{CT0}	Typical OCP encountered under atmospheric conditions
i_{0a}	Nominal exchange current density for the Fe redox reaction
i_{0c}	Nominal exchange current density for the Fe redox reaction when Co=C0o
$i_{a(s)}$	Current density of iron oxidation reaction (steady state value if subscripted s)
$i_{c(s)}$	Current density of oxygen reduction reaction (steady state value if subscripted s)
i_C	Current density resulting from changes in interfacial capacitance charge
i_{corr}	Corrosion current density
I_{corr}	Integrated corrosion current density over a given area.
i_{appl}	Applied current density
I_{app}	Apparent integrated corrosion current
i_p	Anodic current density under passive conditions
i_m	Macrocell current density
I_m	Integral if i_m over a given surface area
P	I_m/I_{corr}
R_{ct}	Surface-specific charge transfer resistance (e.g., ohm-cm^2)
R_{ohm}	Surface-specific resistance of concrete between steel surface and RE tip
R_p	Surface-specific polarization resistance
R_r	R_s/R_p, ohmic effect importance ratio
R_s	Apparent surface-specific solution resistance
x_r	Separation between steel surface and RE
‘	Superscript indicating non-surface-specific quantity (e.g., ohm)

Greek characters

β_a Polarization slope of iron oxidation reaction (Tafel slope in simple activation-limited cases)
β_a Polarization slope of oxygen reduction reaction (ditto)
β_{CT} Cathodic prevention slope
PDT Potential-dependent chloride threshold
ρ Homogenized concrete electric resistivity
σ Homogenized concrete electric conductivity

Abbreviations

CE Counter Electrode
EIS Electrochemical Impedance Spectroscopy
FEM Finite Element Modeling
RE Reference Electrode
PRM Polarization Resistance Method
WE Working Electrode
ZRA Zero-resistance ammeter

REFERENCES

[1] A. B. Revert, K. Hornbostel, K. De Weerdt, and M. Geiker (2019). Macrocell corrosion in carbonated Portland and Portland-fly ash concrete - Contribution and mechanism. Cement and Concrete Research, 116, 273–283. doi:10.1016/j.cemconres.2018.12.005

[2] J. Saire-Yanez, C. Alexander and A. Sagüés, "The Corrosion Propagation Stage of Stainless-Steel Reinforced Concrete: A Review", Corrosion, Vol. 77, pp.812-828 (2021) https://doi.org/10.5006/3811

[3] "Detailed Modeling of Corrosion Macrocells on Steel Reinforcing in Concrete", S.C Kranc and A.A. Sagüés, Corrosion Science, Vol. 43, p. 1355, (2001). DOI: 10.1016/S0010-938X(00)00158-X

[4] S.C. Kranc and A.A. Sagüés, "Computation of Reinforcing Steel Corrosion Distribution in Concrete Marine Bridge Substructures", Corrosion, Vol. 50, p.50, (1994). https://doi.org/10.5006/1.3293494

[5] A.A. Sagüés, M.A. Pech-Canul and A.K.M. Shahid Al-Mansur, "Corrosion macrocell behavior of reinforcing steel in partially submerged concrete columns" , Corrosion Science 45 (2003) 7–32 https://doi.org/10.1016/S0010-938X(02)00087-2

[6] J. Lliso-Ferrando, J. Soto, I. Gaschand M. Valcuende, (2023). Significance of macrocell currents in reinforced concrete columns partially immersed in seawater. Construction and Building Materials, 389 (131739), 131739. doi:10.1016/j.conbuildmat.2023.131739

[7] K.Maekawa, Y. Okano and F. Gong, Space-Averaged Non-Local Analysis of Electric Potential for Polarization Reactions of Reinforcing Bars in Electrolytes, Journal of Advanced Concrete Technology Vol. 17, 616-627 (2019) https://doi.org/10.3151/jact.17.616

[8] L. Bertolini, B. Elsener, P. Pedeferri, R. Polder, Corrosion of Steel in Concrete, WILEY-VCH Verlag GmbH & Co. KGaA, Weinheim, (2004)

[9] H. Boehni, Ed., Corrosion in reinforced concrete structures, CRC Press, Boca Raton, (2005)

[10] C.M. Hansson, A. Poursaee, A. Laurent, Macrocell and microcell corrosion of steel in ordinary Portland cement and high performance concretes, Cement and Concrete Research 36 (2006) 2098–2102 https://doi.org/10.1016/j.cemconres.2006.07.005

[11] C. Andrade, Propagation of reinforcement corrosion: principles, testing and modelling, Materials and Structures (2019) 52:2 https://doi.org/10.1617/s11527-018-1301-1

[12] G. Li, M. Boulfiza, R. Evitts, On the subtilities of rebar corrosion behaviour in cracked concrete, in press at Cement and Concrete Composites (2025), https://doi.org/10.1016/j.cemconcomp.2025.106038.

[13] J. Li, J. Xiong, Z. Fan,Z. Gu, M. Chen, L. Sun, H. Zheng and W. Li, Macrocell Effect on Chloride Threshold Value and Corrosion Rate of Steel Bar in Simulated Concrete Pore Solution, J. Mater. Civ. Eng., (2023), 35(12): 04023436 , DOI: 10.1061/JMCEE7.MTENG-15509

[14] S. Feliu, J. Gonzalez, S. Feliu Jr. and M. C. Andrade, Confinement of the Electrical Signal for in Situ Measurement of Polarization Resistance in Reinforced Concrete, ACI Mater. J. 87,457 (1990). DOI: 10.14359/1830

[15] S.Kranc and A. Sagüés,"Polarization Current Distribution and Electrochemical Impedance Response of Reinforced Concrete When Using Guard Ring Electrodes", Electrochimica Acta, Vol 38, p. 2055, (1993). https://doi.org/10.1016/0013-4686(93)80340-6

[16] C. Alexander, Christopher, S. Agbakansi, and WVDC Bezerra. "Addressing geometric influences on electrochemical impedance spectroscopy for accurate corrosion assessment in steel-reinforced concrete beams." Corrosion Science 247 (2025): 112703. https://doi.org/10.1016/j.corsci.2025.112703
Get rights and content

[17] [F. Mansfeld, The polarization resistance technique, in Advances in Corrosion Science and Technology, Vol. 6, M. Fontana and R. Staehle, Eds., Plenum Press, New York, 1976

[18] M. Stern and A.L. Geary, Electrochemical Polarization –I. A Theoretical Analysis of the Shape of Polarization Curves, J. Electrochem. Soc.Vol 104, 56-63 (1957). DOI 10.1149/1.2428496

[19] Epelboin, I., Gabrielli, C., Keddam, M. and Takenouti, H., “AC Impedance Applied to Corrosion Studies”, in Electrochemical Corrosion Testing, p. 150, ASTM STP 727, F. Mansfeld and U. Bertocci, Eds., ASTM, Philadelphia (1981). DOI: 10.1520/STP28031S

[20] A.A. Sagüés , Electrochemical Impedance of Corrosion Macrocells on Reinforcing Steel in Concrete, Corrosion 90 Conference, paper no. 132, NACE International, Houston (1990). http://www.eng.usf.edu/~sagues/Documents/NACE90-132%20Macro.pdf

[21] A.A. Sagüés, S.C. Kranc, E.I. Moreno, The time-domain response of a corroding system with constant phase angle interfacial component: Application to steel in concrete, Corros. Sci. 37 (7) (1995) 1097-1113. https://doi.org/10.1016/0010-938X(95)00017-E

[22] S. Kranc, A. Sagüés, "Calculation of Extended Counter Electrode Polarization Effects on the Electrochemical Impedance Response of Steel in Concrete," in Electrochemical Impedance: Analysis and Interpretation, ed. M. Kendig West Conshohocken, PA: ASTM International, (1993), 365–383, https://doi.org/10.1520/STP18080S.

[23 S. C. Kranc and A. A. Sagüés, "Computation of Corrosion Macrocell Current Distribution and Electrochemical Impedance of Reinforcing Steel In Concrete", ASTM STP 1154, Computer Modeling in Corrosion, R. Munn, Ed., p. 95, American Society for Testing and Materials, Philadelphia (1992). https://doi.org/10.1520/STP24689S

[24] A. Sagüés, S. Kranc, "Computer Modeling of Effect of Corrosion Macrocells on Measurement of Corrosion Rate of Reinforcing Steel in Concrete," in Techniques to Assess the Corrosion Activity of Steel Reinforced Concrete Structures, ed. E. Escalante, C. Nmai, D. Whiting ,West Conshohocken, PA: ASTM International (1996), 58–73, https://doi.org/10.1520/STP16967”

[25] A.A. Sagüés, S.C. Kranc and E.I. Moreno, "Evaluation of Electrochemical Impedance with Constant Phase Angle Component from the Galvanostatic Step Response of Steel in Concrete" Electrochimica Acta, Vol 41, p.1239, 1996. https://doi.org/10.1016/0013-4686(95)00476-9

[26] A.A. Sagüés, S.C. Kranc and E.I. Moreno, "An Improved Method for Polarization Resistance from Small Amplitude Potentiodynamic Scans in Concrete" Corrosion, Vol. 54, p.20(1998). https://doi.org/10.5006/1.3284824

[27] C. L. Alexander. The influence of localized forms of corrosion on the impedance of steel in concrete. In preparation (2024).

[28] Fahim A, Ghods P, Isgor OB, Thomas MD. A critical examination of corrosion rate measurement techniques applied to reinforcing steel in concrete. Materials and Corrosion. (2018) 69:1784–1799. https://doi.org/10.1002/maco.201810263

[29] Ueli Angst and Markus Büchler, A new perspective on measuring the corrosion rate of localized corrosion, Materials and Corrosion, 71, 1–16 (2020). https://doi.org/10.1002/maco.201911467

[31] K. Tuutti, Corrosion of Steel in Concrete (ISSN 0346-6906) (Stockholm, Sweden: Swedish Cement and Concrete Research Institute, 1982).

[32] U.M. Angst, O. B. Isgor, C. M. Hansson, A. Sagüés, and M. R. Geiker, “Beyond the chloride threshold concept for predicting corrosion of steel in concrete”, Appl. Phys. Rev (2022) 9: p.011321

[33] N. Maamary amd O. Ogunsanya, Chloride threshold level determination: Call for test standardization to limit variations in experimental methodology and resolve inherent experimental and modelling detection challenges, Case Studies in Construction Materials 22 (2025) e04167, doi.org/10.1016/j.cscm.2024.e04167

[34] P.D. Cady, R.E. Weyers, Deterioration Rates of Concrete Bridge Decks, J. Transp. Eng. 110, 1 (1984): p. 35-44. https://doi.org/10.1061/(ASCE)0733-947X(1984)110:1(34)

[35] M.D.A. Thomas, E.C. Bentz, (2002), “Life-365 Service Life Prediction Model™ and Computer Program for Predicting the Service Life and Life-Cycle Costs of Reinforced Concrete Exposed to Chlorides” (Lovettsville, VA: Silica Fume Association [SFA], 2008), p. 12-56.

[36] E.C. Bentz, Probabilistic Modeling of Service Life for Structures Subjected to Chlorides, ACI Mater. J. 100, 5 (2003). DOI: 10.14359/12814

[37] EN 1990 (2002), Eurocode—Basis of Structural Design (The European Union Per Regulation 305/2011, Directive 98/34/EC, Directive 2004/18/EC).

[38] A.A. Sagüés, “Modeling the Effects of Corrosion on the Lifetime of Extended Reinforced Concrete Structures”, Corrosion, Vol. 59, p.854 (2003). https://doi.org/10.5006/1.3287706

[39] Fache, K., Keßler, S., & Harnisch, J. (2024). On the impact of cathodic polarization on the chloride threshold of carbon steel in alkaline solutions. Materials and Corrosion. doi:10.1002/maco.202414601

[40] "Steel Activation in Concrete Following Interruption of Long Term Cathodic Polarization", F. J. Presuel-Moreno, A. A. Sagüés, S.C. Kranc, Corrosion, Vol. 61, p.428 (2005) https://doi.org/10.5006/1.3280642

[41] Alonso, M. Castellote, C. Andrade, “Chloride threshold dependence of pitting potential of reinforcements”, Electrochim. Acta 47, 21 (2002): p. 3469-3481. DOI: 10.1016/S0013-4686(02)00283-9

[42] A.A. Sagüés and S.C. Kranc, “Model for a Quantitative Corrosion Damage Function for Reinforced Concrete Marine Substructure” (Summary Paper), in Rehabilitation of Corrosion Damaged Infrastructure, p.268, Proceedings, Symposium 3, 3rd. NACE Latin-American Region Corrosion Congress, P.Castro, O.Troconis and C. Andrade, Eds., ISBN 970-92095-0-7, NACE International, Houston (1998). http://www.eng.usf.edu/~sagues/Documents/1998%20CancunDamageFunction.pdf

[43] “Service Life Forecasting For Reinforced Concrete Incorporating Potential-Dependent Chloride Threshold”, A.A. Sagüés, A.N. Sánchez, K. Lau and S.C. Kranc, Corrosion, Vol. 70, pp. 942-957 (2014). https://doi.org/10.5006/1286

[44] M.T. Walsh and A.A. Sagüés, “Steel Corrosion in Submerged Concrete Structures - Part 2: Modeling of Corrosion Evolution and Control”, Corrosion 72 (2016): pp. 665-678 https://doi.org/10.5006/1944

[45] M.T. Walsh and A.A. Sagüés, “Steel Corrosion in Submerged Concrete Structures - Part 1: Field Observations and Corrosion Distribution Modeling,” Corrosion 72 (2016): pp. 518-533 https://doi.org/10.5006/1945

[46] A.A Sagüés and C.L. Alexander; “Exploration of Next-Generation Reinforced Concrete Corrosion Modeling with Interdependent Initiation and Propagation Stages”, Corrosion 79, 3 (2023): pp.350-362. https://doi.org/10.5006/4193

[47] A.A. Sagüés and C. L. Alexander, “Concrete Reinforcement Corrosion Forecasting With Potential-Dependent Threshold: Migration Effects”, Paper Number. AMPP-2024-20744, AMPP Annual Conference 2024, 15 pp., AMPP, Houston, TX, (2024). https://onepetro.org/amppcorr/proceedings-abstract/AMPP24/AMPP24/AMPP-2024-20744/556729

The Effects of Cations on Chloride Ingress and Hydroxide Levels in Concrete

Neal Berke, Kyle Stanish, and Ali Inceefe

Synopsis: This paper demonstrates how a model that includes the chemical reactions in concrete, as well as the tortuosity of the concrete, can be used to predict the effects of cations on the ingress of chloride and changes in the hydroxide levels. Scenarios using low and high C_3A cements exposed to NaCl, KCl, $CaCl_2$, and $MgCl_2$ are modeled. The predictions are compared to test data presented several years ago by Professor Hansson. The modeling provides a rapid means that can be used to assess both the salt and cement type on the corrosion susceptibility of embedded steel reinforcement in concrete.

Keywords: chlorides, modeling, deicing salts, seawater, corrosion, concrete

ACI Fellow **Neal S. Berke**, is Vice President, Research at Tourney Consulting Group in Kalamazoo, MI. He is a member of ACI Committees 212, 222, 224, and 365. He has extensive experience in the development and application of concrete admixtures and materials as well as corrosion and the durability of concrete. He is a recipient of the J.C. Roumain Innovation in Concrete Award. He has a Ph.D. from the University of Illinois, Urbana.

Kyle Stanish, Ph.D., S.E., P.E., F.ACI, has over twenty years of experience working as a consulting engineer. His work has included durability design, the existing structure evaluation, and rehabilitation design. His PhD is from the University of Toronto and he is a licensed professional engineer in 17 jurisdictions. He is the former chair of the ACI's Committee 365 on Service Life Prediction, current chair of the Durability Subcommittee for the Repair Code (ACI 562), and a member of various ACI committees.

Ali N. Inceefe, M.Sc., P.E., is an engineer with Tourney Consulting Group in Kalamazoo, MI. He is a licensed professional engineer in Michigan and an AMPP-certified Cathodic Protection Technician (CP2). He has over five years of experience as a consulting engineer specializing in materials engineering services, construction materials development and optimization, and service life analysis of new and existing structures. He is a member of ACI Committees 329, 353, and 365. He received his MS from Western Michigan University.

INTRODUCTION

The ingress of chloride into concrete is the major cause for reinforcing steel corrosion in environments subjected to deicing or marine salts. Modeling often does not distinguish between the type of chloride salt (assuming NaCl) or the chemistry of the concrete. This could be significant for determining the service life if an alternative deicing salt is used or the cementitious binder has low chloride binding properties.

There are numerous combinations of salts available as well as binder compositions. In this paper, to demonstrate the effects on chloride ingress, four cations – Na, K, Ca, and Mg – for the chloride salts, and two concrete mixtures with an ordinary Type I portland cement and a Type V portland cement with a C_3A content under 5% are studied. One example using artificial seawater with additional ions is performed.

STADIUM® is used to model the chloride and cation ingress into the concrete. The pore-water and total concentrations are calculated. STADIUM is an acronym that stands for *Software for Transport and Degradation In Unsaturated Materials*. STADIUM predicts the transport of ions in cement-based materials and the chemical modifications occurring to the material as a result of these ionic movements [1-3]. The transport equation is based on the extended Nernst-Planck model, and the chemical reactions such as precipitation, salt formation, and binding are calculated by multiple modules. The references provide the details as to how the calculations are performed, which are too involved to include in this paper. The modeling results were found to have a good correlation to the actual ingress of chloride and other ions.

This work ties into experimental work performed by Carolyn Hansson that looked at the effects of the different cations on the pore-water composition and chloride ingress [4-7].

MODELING

Material and Mix Properties

Transport and other concrete properties are determined for similar concrete mixes in the STADIUM database to be used in the modeling. The chemical compositions of the two cements used in the modeling are in Table 1. Table 2 shows the concrete mixture proportions and fresh concrete properties. Table 3 and Table 4 show the strength values and the transport properties, respectively.

Comparing the strengths in Table 3 to the transport properties in Table 4 shows that even though the strengths are higher for the Type V cement mixture, the transport properties show higher diffusion and permeability for the Type V mixture versus the Type I/II mixture. The porosity is slightly lower for the Type V mixture and the saturation at 50% relative humidity (RH) is lower. This indicates that the capillary pores are finer for the Type I/II, which is consistent with the lower diffusion and permeability values.

Table 1—Cement Chemistries

Chemistry	Cement Type	
	Type I/II	Type V
Oxides (%)		
SiO_2	20.4	21.6
Al_2O_3	4.82	3.6
Fe_3O_4	3.48	3.07
CaO	63.7	65.3
MgO	1.25	1.83
SO_3	2.75	2.1
K_2O	0.4	0.22
Na_2O	0.11	0.14
Loss on Ignition	1.9	1.3
Pore Solution (mM/L)		
OH	194.4	129.1
Na	66.3	71.8
K	133.1	62.3
Bogue Composition (%)		
C_2S	13.96	11.35
C_3S	59.04	67.06
C_3A	6.89	4.35

Table 2—Concrete Mixtures

Material	Type I/II	Type V
Cement, lb/yd^3 (kg/m^3)	632 (375)	632 (375)
Coarse Aggregate, lb/yd^3 (kg/m^3)	1559 (925)	1559 (925)
Fine Aggregate, lb/yd^3 (kg/m^3)	1374 (815)	1374 (815)
Air Entrainer, fl oz/yd^3 (ml/m^3)	0.92 (35.6)	0.92 (35.6)
Superplasticizer, fl oz/yd^3 (ml/m^3)	28.44 (1100.0)	18.1 (700.0)
Paste Volume (%)	28.8	28.8
Plastic Air (%)	7.6	6.0
Slump, in (mm)	4.5 (115)	3.9 (100)
Water-to-cement ratio (w/c)	0.45	0.45

Table 3—Compressive Strengths

Age (days)	Type I/II, psi (MPa)	Type V, psi (MPa)
7	4020 (27.7)	5160 (35.6)
28	5540 (38.2)	6000 (41.4)
91	7600 (52.4)	7640 (52.7)

Table 4—Transport Properties

Transport Property	Type I/II	Type V
Volume of Permeable Voids (%)	11.80	11.04
[OH^-] Diffusion Coefficient (m^2/s)	9.71×10^{-11}	1.12×10^{-10}
[Cl^-] Eff. Diffusion Coefficient (m^2/s)	4.42×10^{-12}	4.77×10^{-12}
Permeability (m^2)	1.14×10^{-21}	1.89×10^{-21}
Saturation at 50% R.H.	0.52	0.49
Aging Function-a	1	1
Aging Function-α (1/day)	0	0
ASTM C1202-28 days (Coulombs)	3431	3750
ASTM C1202-91 days (Coulombs)	2450	3087

Environmental Exposure

A large concrete wall exposed to chloride on one side is used for the modeling. The temperature is a constant 68°F (the model, however, can address temperature changing as a function of time), the water is at pH 8, and the relative humidity is 100%. The chloride exposure for the four chloride salts evaluated is at 500 mM/L chloride at the surface. For Na and K, the concentration at the surface is 500 mM/L, and for Ca and Mg, the concentration is 250 mM/L as they are divalent. Table 5 shows the composition used for the artificial seawater. Some of the trace ions are noted in ASTM D1141. It should be noted that STADIUM balances the composition for ionic neutrality as seen in the table.

Table 5 —Composition of the Artificial Seawater

Chemical	User	Balanced	
	(ppm)	(ppm)	mM/L
Na	10973.1	11056.13	480.92
K	31.3	31.54	0.81
SO_4	2708.9	2688.40	27.99
Ca	400.8	403.83	10.08
Mg	1215.5	1224.70	50.39
Cl	19447.5	19300.35	544.39
HCO_3	140.3	139.24	2.28
TDS	34917.4	34844.19	NA

USGS Classification: Saline Water

Modeling Results

Fifty-year depth profiles are determined for the ion distributions for the five scenarios. These are shown in Figure 1 through Figure 5. The figures clearly show that chloride ingress is higher for the Type V cement mixture. Since the modeled mixtures do not have very low water-to-cement ratios and the ambient temperature is 68 °F, the chloride ingress is relatively quick.

There appears to be little effect of sodium or seawater at higher depths on the hydroxide content. Potassium, however, increases the pH deeper into the concrete. Both $CaCl_2$ and $MgCl_2$ decrease the pH (lower OH) significantly compared to NaCl, indicating that they facilitate the leaching of Na(OH). This is observed in Figure 1 through Figure 5.

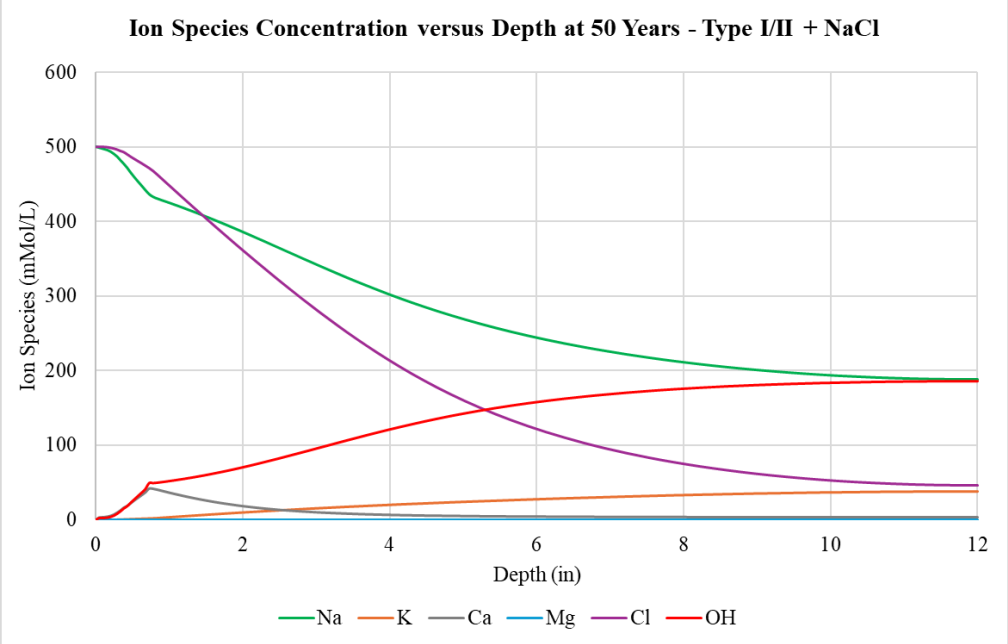

(a)

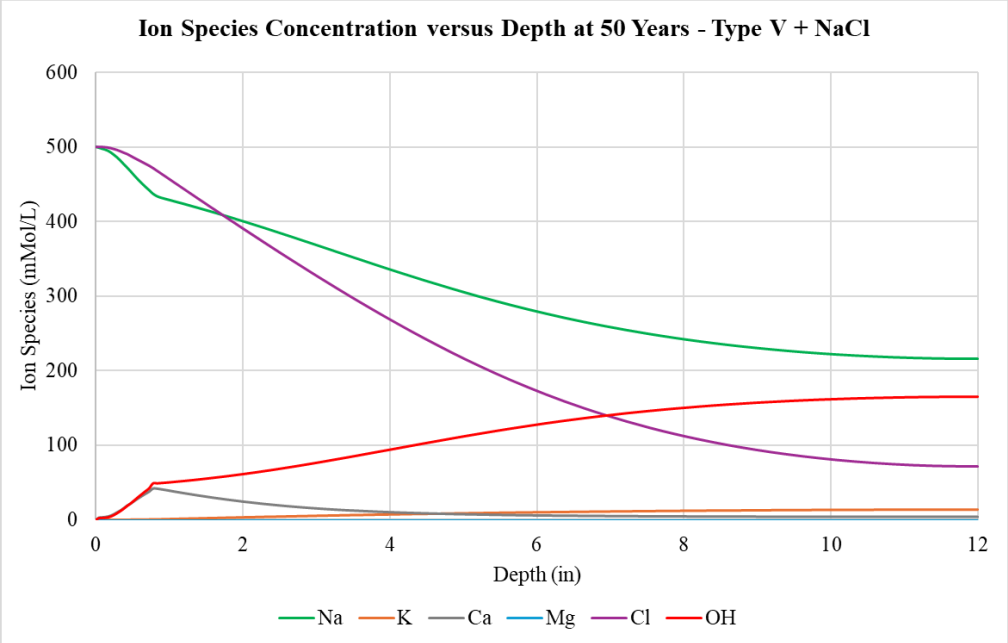

(b)

Figure 1: Pore-water ion concentrations for NaCl exposure. (a) Type I/II mixture. (b) Type V mixture.

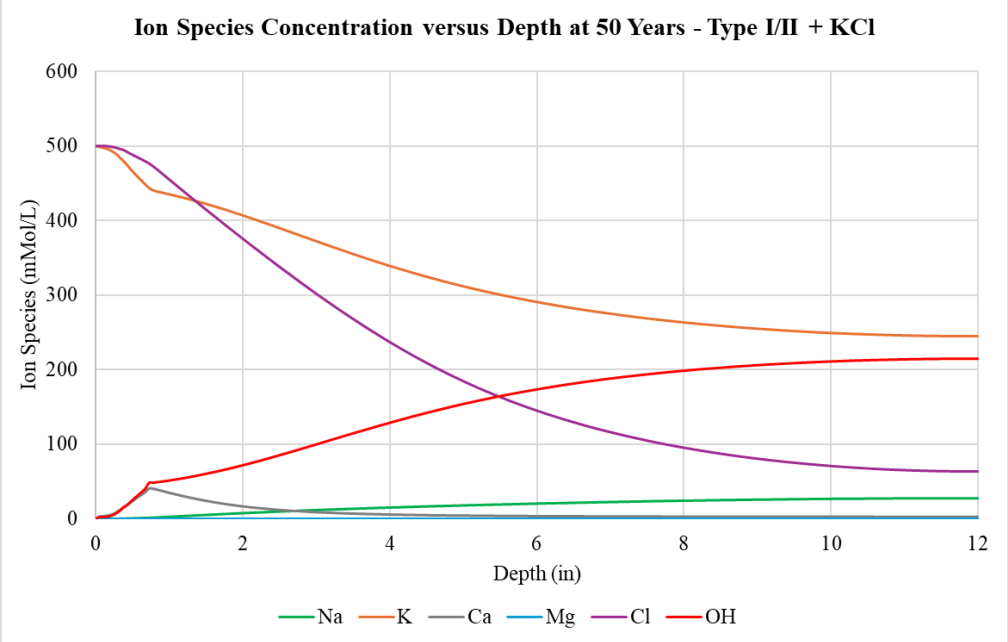

(a)

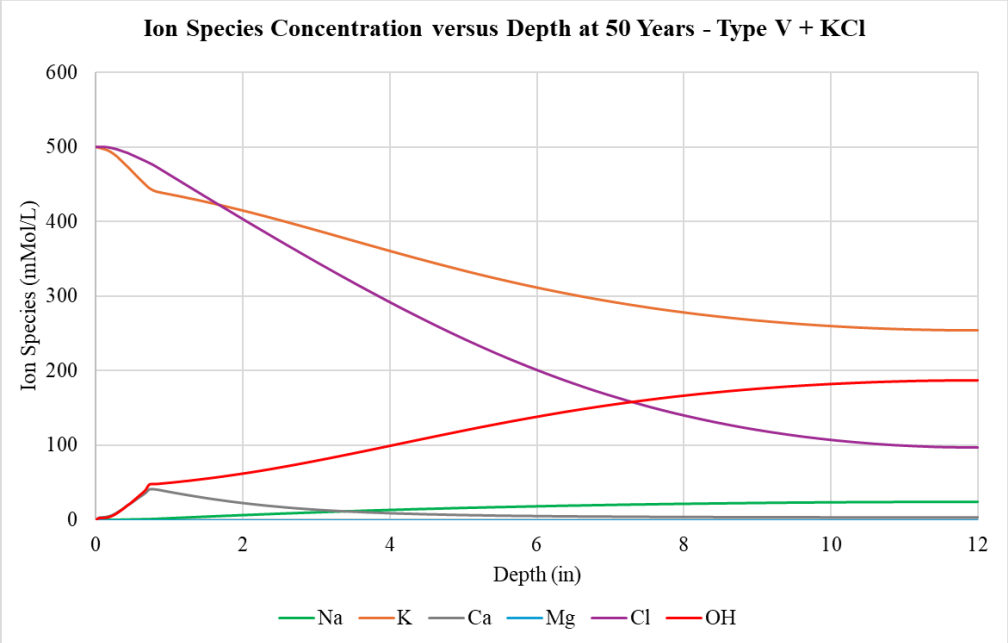

(b)

Figure 2: Pore-water ion concentrations for KCl exposure. (a) Type I/II mixture. (b) Type V mixture.

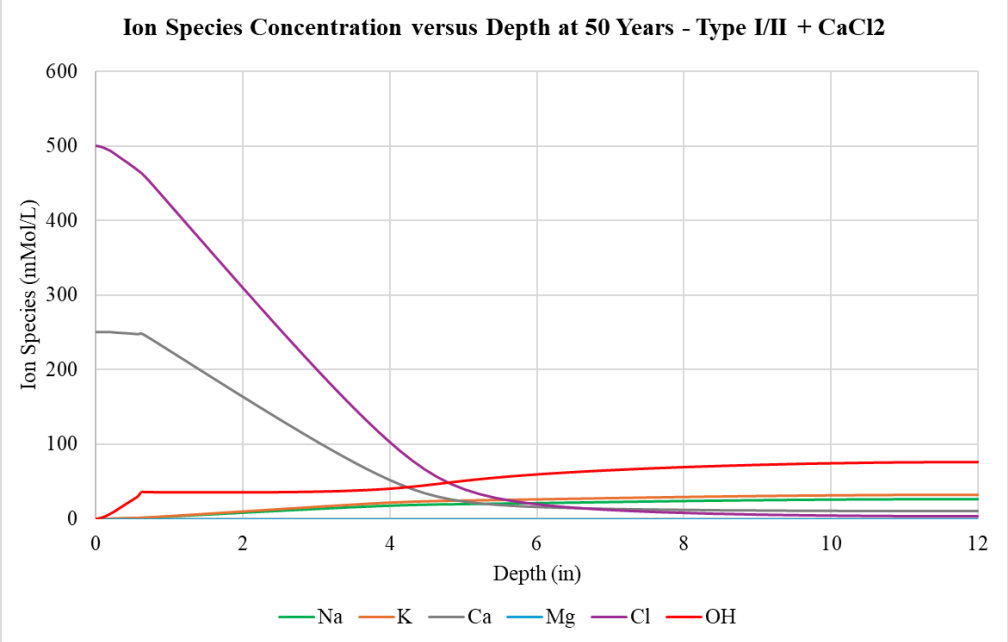

(a)

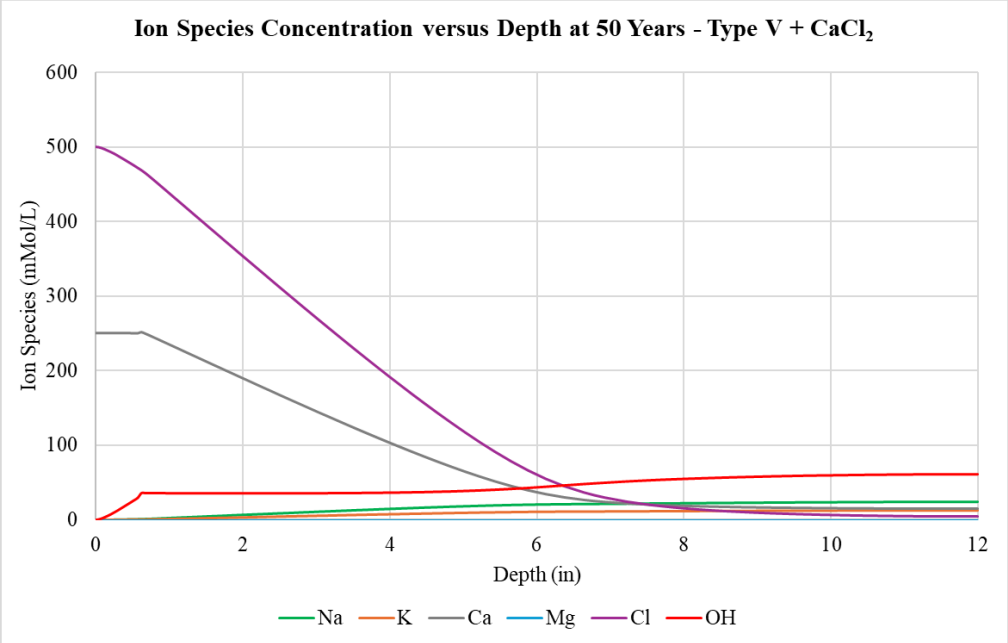

(b)

Figure 3: Pore-water ion concentrations for $CaCl_2$ exposure. (a) Type I/II mixture. (b) Type V mixture.

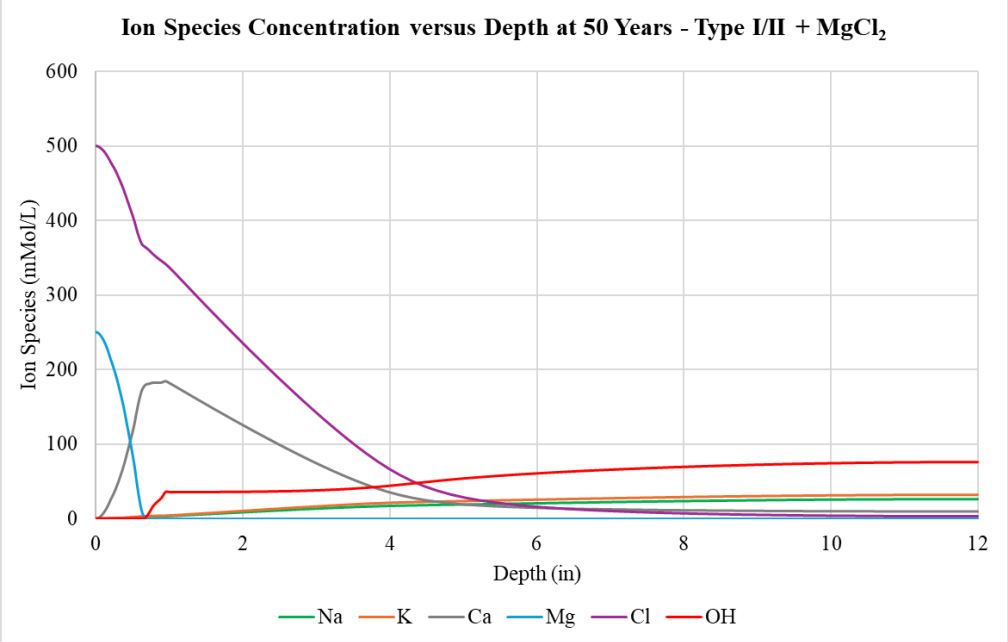

(a)

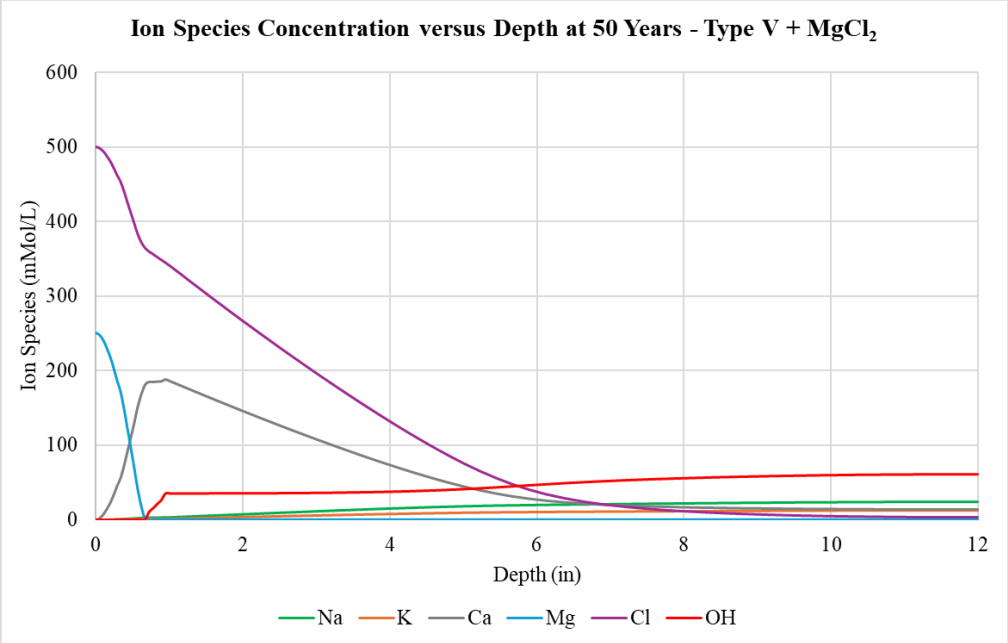

(b)

Figure 4: Pore-water ion concentrations for $MgCl_2$ exposure. (a) Type I/II mixture. (b) Type V mixture.

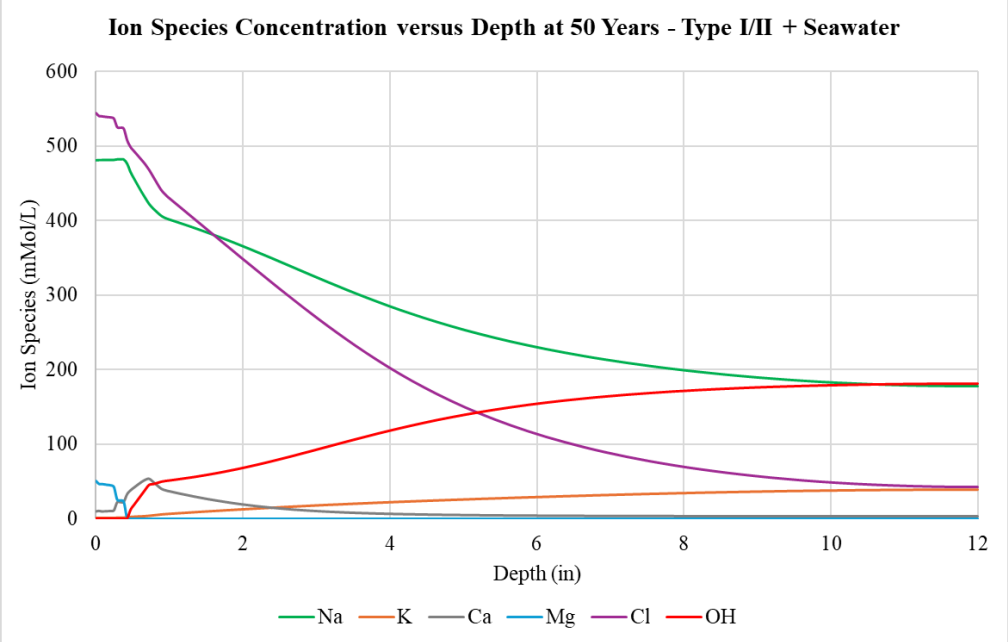

(a)

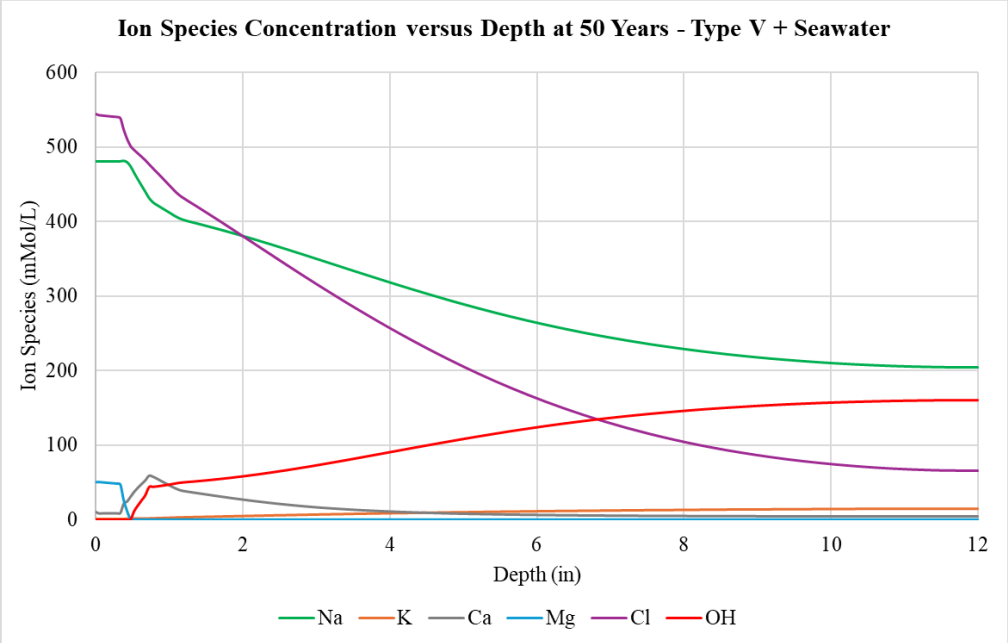

(b)

Figure 5: Pore-water ion concentrations for seawater. (a) Type I/II mixture. (b) Type V mixture.

Comparing the chloride ingress for the exposures, the modeling predicts that K will have a higher chloride ingress than Na. Chloride ingress with Ca and Mg is less than that for Na. Seawater is primarily NaCl at a concentration close to the NaCl exposure, so it is similar to NaCl. These are shown in Figure 6.

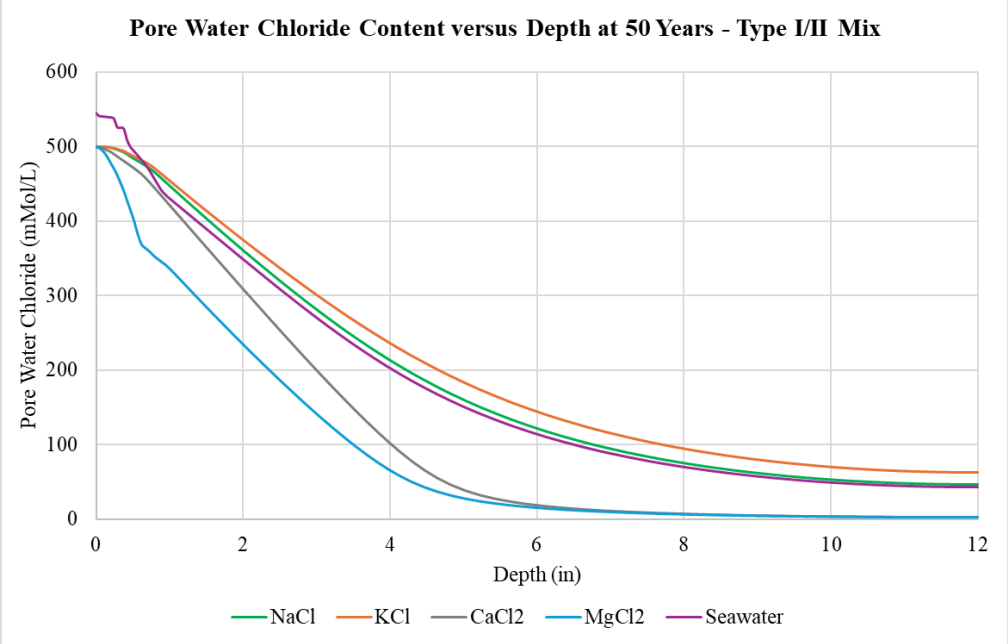

(a)

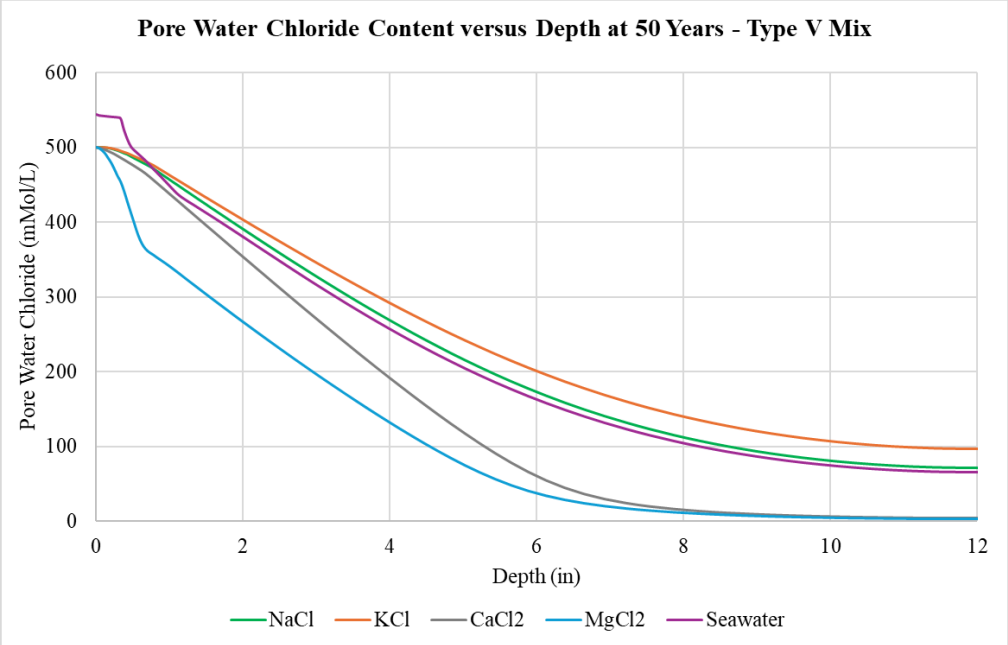

(b)

Figure 6: Comparison of pore-water chlorides for the different cations. (a) Type I/II mixture. (b) Type V mixture.

The total chloride including chloride that reacts with the cement is higher at the surface for Type I/II than Type V cement mixtures, which could account for the lower pore-water contents for Type I/II versus the Type V mixtures. Figure 7 shows this for a comparison of NaCl to $CaCl_2$. The overall amount of total chloride is higher for the Type I/II mixture, indicating that it is reacting with the chloride at a greater rate than the Type V mixture.

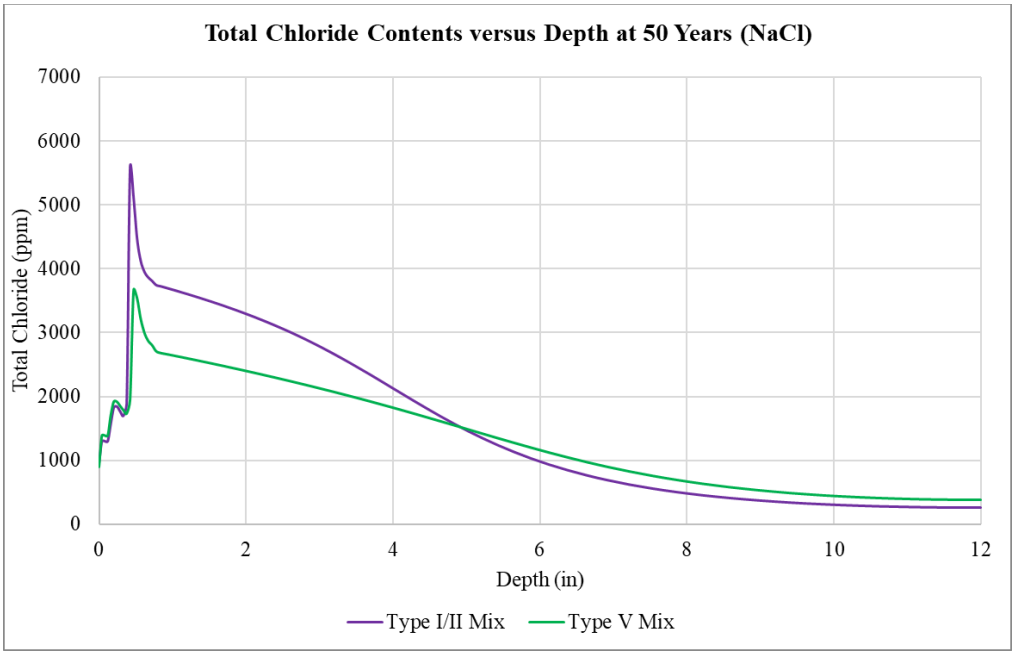

(a)

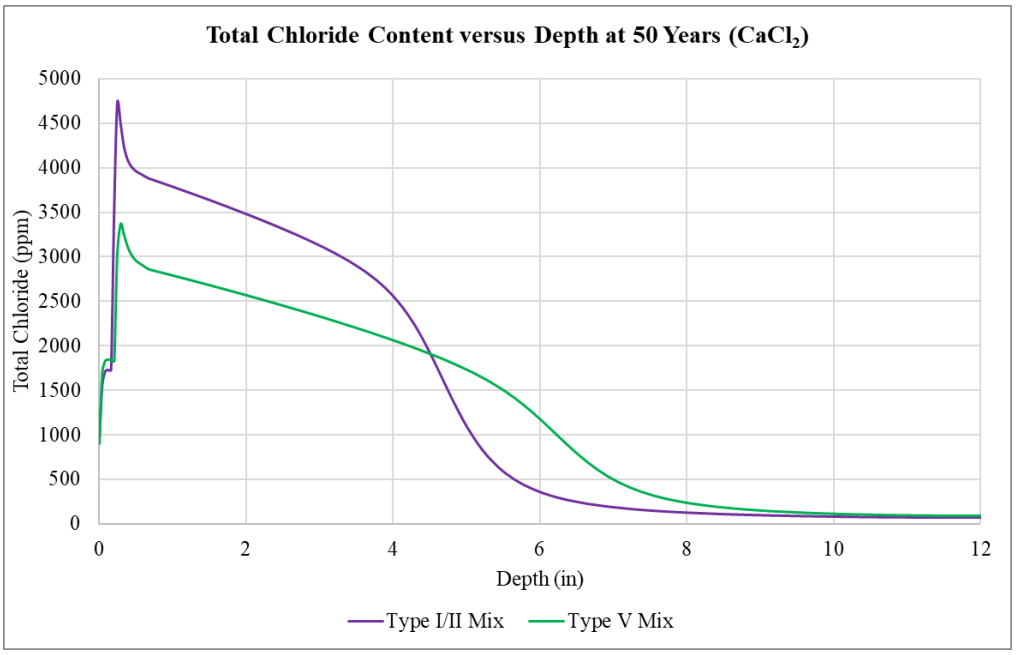

(b)

Figure 7: Comparison of total chloride contents for (a) NaCl and (b) $CaCl_2$.

The modeling predicts that chloride ingress into Type I/II cement concrete will be less than that for Type V cement. This indicates that corrosion of reinforcing bars would be expected to occur quicker for the Type V mixture. The chloride-to-hydroxide ratio ($[Cl^-]:[OH^-]$) is typically used as an indicator as to when corrosion will initiate with a typical value of 0.6 used as the threshold [8].

Figure 8 shows the $[Cl^-]:[OH^-]$ as a function of depth at 50 years comparing the salts for both Type I/II and Type V mixtures. The $[Cl^-]:[OH^-]$ is higher for the Type V mixture as expected, however, it is also higher for the non-divalent cation chloride salts as it approaches 0.6, indicating that the depth at which corrosion will initiate will be lower for the

non-divalent salts. Figure 8 indicates for these cases that the chloride threshold level will affect embedded steel several inches from the surface.

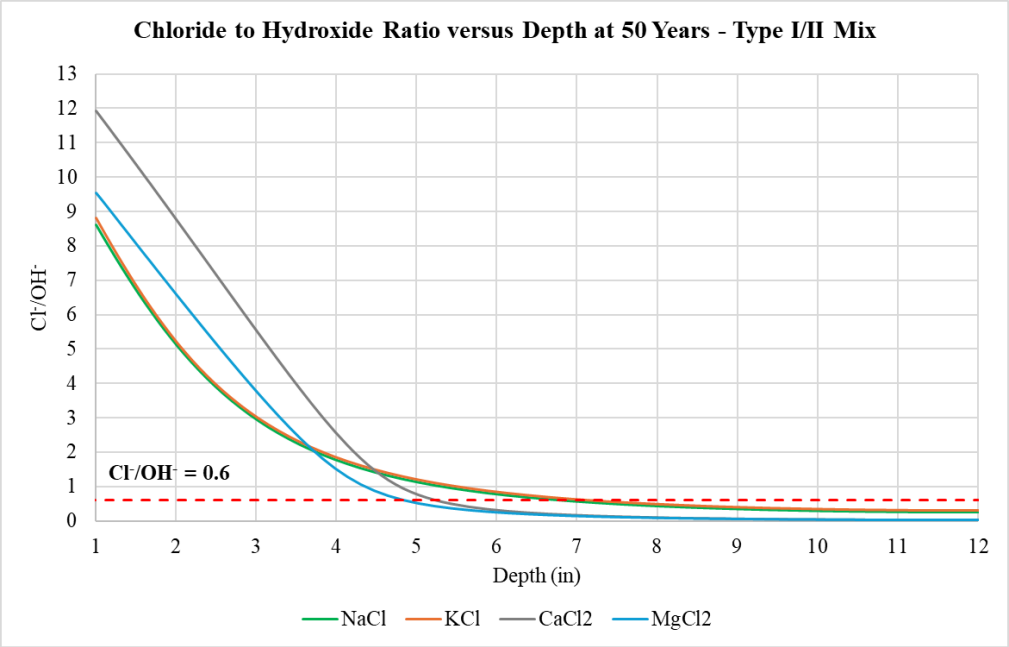

(a)

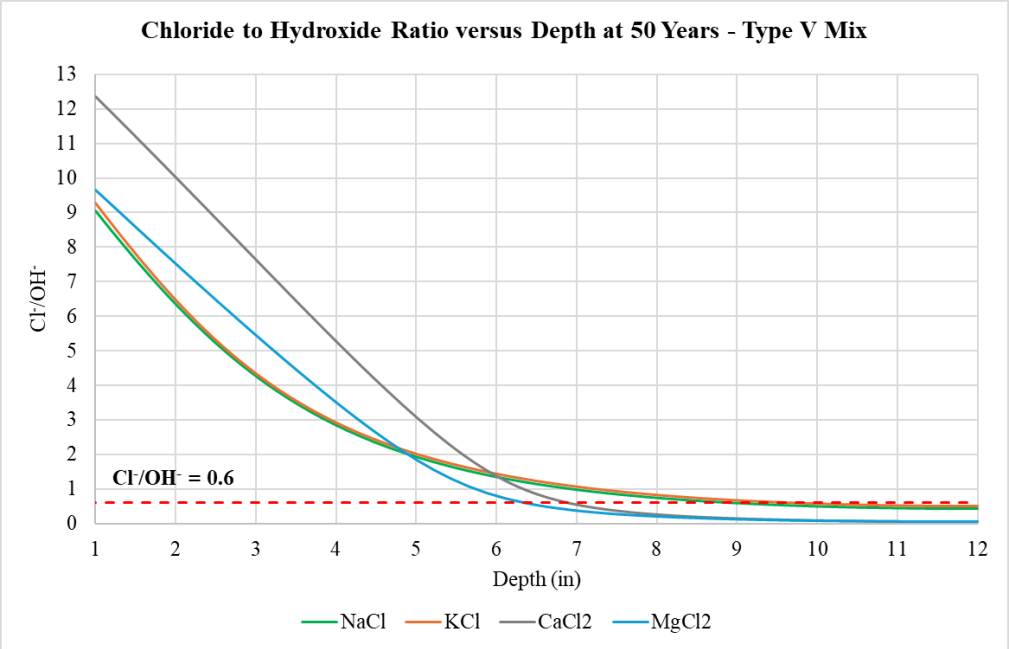

(b)

Figure 8: Chloride-to-hydroxide ratios for different cations in (a) Type I/II and (b)Type V mixtures.

As expected, the time to reach the $[Cl^-]:[OH^-]$ of 0.6 is shorter for Type V cement mixture. The time to the predicted initiation is lower for the non-divalent cation salts. Figure 9 shows a comparison of the $[Cl^-]:[OH^-]$ at two inches of cover, for NaCl and $MgCl_2$.

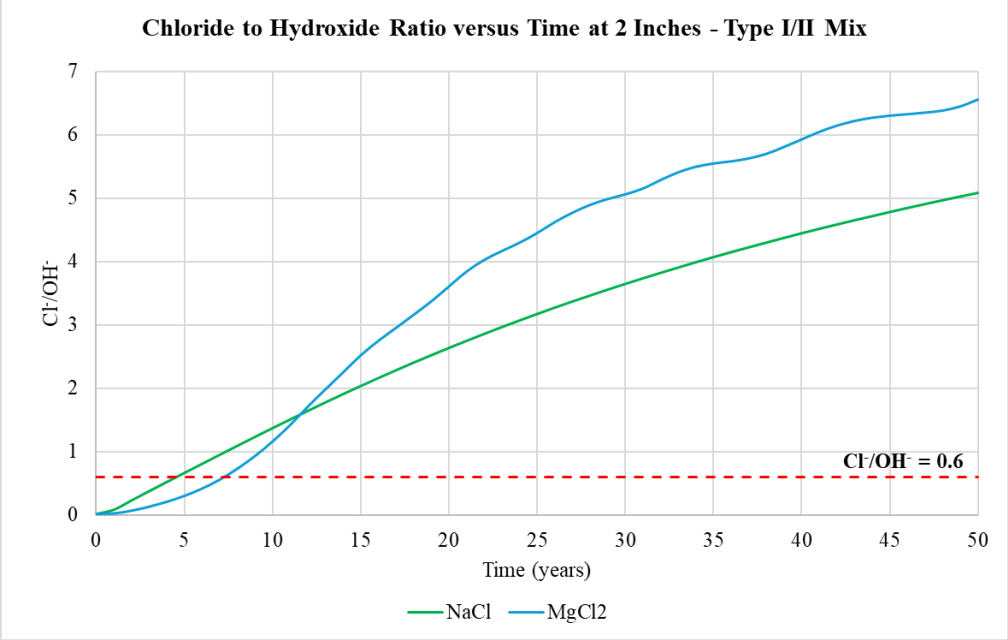

(a)

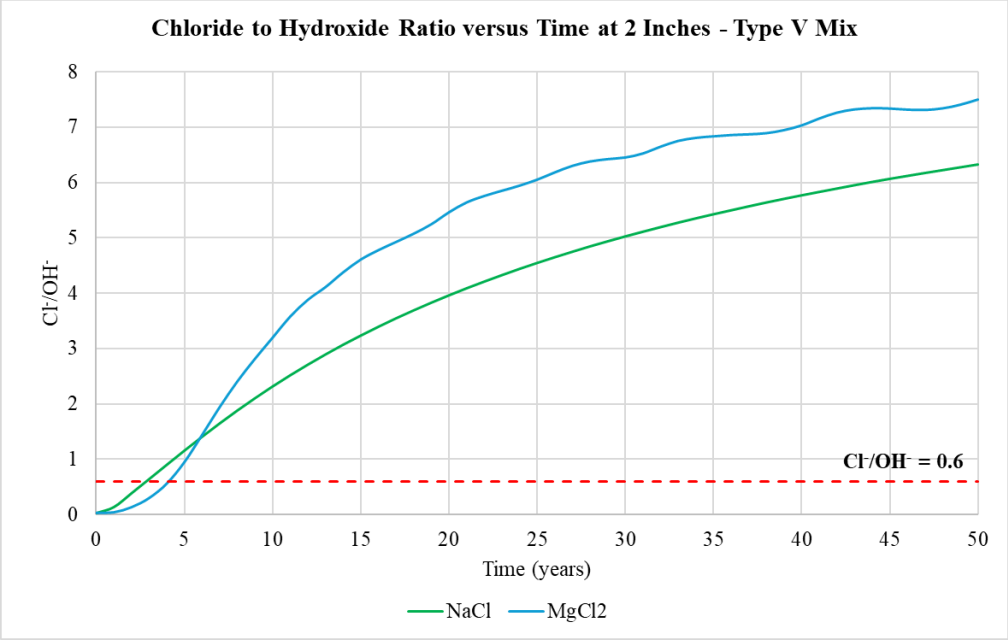

(b)

Figure 9: Chloride-to-hydroxide ratios at 2-inch depth over time for NaCl and $MgCl_2$ in (a) Type I/II and (b) Type V mixtures.

DISCUSSION

The modeling conducted predicts that there will be more chloride ingress into a concrete with a low C_3A cement (Type V) compared to one at a higher C_3A cement (Type I/II) at the same mixture proportions. Then, $[Cl^-]$:$[OH^-]$ for the Type I/II mixture is predicted to be lower than for the Type V, indicating that at the same reinforcing cover and environmental exposure, corrosion would initiate early for the concrete with the Type V cement.

These results are in agreement with what Hansson found [7]. Others such as Rasheeduzzafar et al. also found corrosion initiating earlier in concretes with Type V cement vs. Type I cement for chloride exposures [9].

Hansson found that the diffusion coefficients are higher for $CaCl_2$ versus NaCl [7]. This is indicated by the total chloride contents as a function of depth being higher for the $CaCl_2$ versus NaCl in Figure 7. However, there is less chloride in the pore-water for $CaCl_2$ exposure, and the hydroxide content is also lower for $CaCl_2$ as shown in Figure 1 and Figure 3. This is in agreement with Hansson [7].

What is somewhat surprising is that the predicted chloride-to-hydroxide levels are lower for the divalent chlorides near the surface early in time but larger at later times, as seen in Figure 9. This results in a slight increase in time to exceed the $[Cl^-]:[OH^-]$ of 0.6 for the divalent chlorides. The times to exceed the 0.6 criterion are always higher for Type I/II versus Type V cement mixtures.

CONCLUSIONS

Modeling predicts that chloride ingress will be increased for a Type V versus a Type I/II cement mixture. It is also predicted that chloride initiated corrosion will occur earlier based upon $[Cl^-]:[OH^-]$. For the cases modeled here, the difference in time to corrosion initiation was approximately two to three years, however, the time difference would be expected to be greater for a lower permeability concrete.

The cation types affect the predicted pore-water pH and chloride contents in the pore-water. In general, OH^- is higher for sodium and especially for potassium and lower for calcium and magnesium salts.

The chloride and hydroxide profiles were similar for NaCl and simulated sea water, indicating that laboratory testing in NaCl is a reasonable substitute sea water, when chloride induced corrosion is the main concern.

The model used considers both ionic mobilities and chemical reactions of cations. This is observed to cause differences between pore-water and total chloride ratios for given salt exposure. This could change for different cement and SCM combinations.

The differences noted between the different cations are of importance in selecting potential deicing salts. These results are for ordinary portland cement concrete. The effects of supplementary cementitious materials should be evaluated to determine how they might affect the predictions, as should changing temperature conditions in future studies.

REFERENCES

[1] Samson E., Marchand J., Robert J.-L., Bournazel J.-P., *Modelling Ion Diffusion Mechanisms in Porous Media*, Int. J. for Num. Methods in Engineering, vol.46, pp.2043-2060 (1999).

[2] Samson E., Marchand J., Beaudoin J.J., *Describing Ion Diffusion Mechanisms in Cement-Based Materials Using the Homogenisation Technique*, Cement and Concrete Research, vol.29, no.8, pp.1341-1345 (1999).

[3] Samson E., Marchand J., Henocq P., Beausejour P., Recent Advances in the Determination of Ionic Diffusion Coefficients Using Migration Test Results, in RILEM Proceedings 58 – CONMOD 2008 (Delft, The Netherlands), E. Schlangen and G de Schutter eds., pp.65-78 (2008).

[4] Byfors, K., Hansson, C.M., and Tritthart, Cement and Concrete Research, 16, pp. 760-770 (1986).

[5] Hansson, C.M., Froelund,Th., and Markussen, J.B., Cement and Concrete Research, 15. pp. 65-73 (1985).

[6] Tuutti, K., Nordic Concrete Research, No. 1 Paper 25 (1982).

[7] Hansson, C.M. and Berke, N.S., Materials Research Society Symposium, 137, pp. 253-270 (1989).

[8] Hausman, D.A., *Steel Corrosion in Concrete,* Materials Protection, 6(11) (1967).

[9] Rasheeduzzafar, Dakhil, F.H., Saad Al-Gahtani,A., Al-Saadoun, S.S., and Bader, M.A., ACI Materials Journal, 87, pp. 114-122 (1990).

The steel-concrete interface and its impact on corrosion – an updated review and research perspectives

Ueli M. Angst and Mette R. Geiker

Synopsis: It is well known that the steel–concrete interface (SCI) influences corrosion of steel in concrete. Numerous factors related to the SCI have been hypothesized to affect the mechanism of corrosion initiation and propagation, including steel surface characteristics, interfacial concrete properties (voids, cracks, etc.), and conditions related to the exposure (e.g., SCI moisture state). This contribution offers an overview of current knowledge on these aspects. Additionally, recent advances toward a fundamental understanding of corrosion-related processes occurring at the SCI are highlighted, including a novel experimental methodology for studying the steel surface behavior, imaging of the SCI moisture state, and the impact of macroscopic voids. Finally, perspectives for future research are given.

Keywords: concrete, durability, reinforcement corrosion, steel-concrete interface, cracks

Ueli M. Angst is associate professor at ETH Zurich, Switzerland. He obtained his degrees in civil engineering from ETH Zurich in Switzerland (MSc, 2000) and from the Norwegian University of Science and Technology, NTNU, in Trondheim, Norway (PhD, 2011). Since January 2017, Ueli Angst chairs the research group on Durability of Engineering Materials at ETH Zurich, Switzerland. Before this, Ueli Angst spent several years in industry, working as consulting engineer. He uses experimental and computational methods covering corrosion science, electrochemistry, materials science, porous media and reactive mass transport, and civil engineering. Prof. Angst is a member of ACI, *fib,* and of RILEM.

Mette R. Geiker is a professor at the Norwegian University of Science and Technology (NTNU), Department of Structural Engineering, Norway. She studied chemical engineering at the Technical University of Denmark (DTU) and has worked 15 years in the industry and 25 years in academia. Her research interests include the structure-property relationship of cementitious materials in their fresh, hardening and hardened state, durability, service life prediction, and sustainability. Prof. Geiker is a member of ACI, *fib* and RILEM, and fellow of both ACI and RILEM.

INTRODUCTION

Reinforced concrete (RC) plays a crucial role in the construction of a wide range of civil infrastructure, including bridges, tunnels, marine structures, office and housing buildings, and sewer systems. Many of these structures are essential for societies' function and economic competitiveness. While there are numerous examples of RC structures exhibiting durability, even in harsh exposure environments, different deterioration mechanisms can reduce their service lives. The most prevalent cause of damage for RC structures is the corrosion of reinforcing steel. This leads to high maintenance and repair costs and additional adverse impacts on society, as described by C.M. Hansson (Hansson 2011).

Understanding corrosion of steel in concrete has thus been a priority in research for at least the last 50 years. Recognizing that in chloride exposure environments, the concentration of chlorides reaching the steel influences the probability for triggering steel corrosion, concepts such as the chloride threshold have been suggested. Over recent decades, numerous studies reported attempts to measure threshold values, under consideration of various aspects, such as cement type or parameters related to concrete mix proportions, or the chloride salt cation, for example (Hansson, Frølund et al. 1985, Hansson and Sørensen 1990). C.M. Hansson was among the first researchers recognizing the importance of the steel surface properties (Mammoliti, Brown et al. 1996) as well as the moisture condition in the concrete (Enevoldsen, Hansson et al. 1994). As will be shown and discussed later in this contribution, these two factors remain highly relevant and require further research. Another aspect of similar importance in ensuring the durability of RC structures is the influence of concrete cracks (Jaffer and Hansson 2008).

With time, it became increasingly clear that the conditions at the steel-concrete interface (SCI) fundamentally affect corrosion of steel embedded in concrete, especially in the case of localized corrosion such as for chloride-exposed RC structures. However, literature often refer to "weaknesses" at the SCI and remain relatively vague in terms of terminology describing the conditions at the SCI. Over the last decades, many studies have shed light on different aspects, with some aspects being investigated more comprehensively and repeatedly than others. Nevertheless, it remained unclear which of all the factors related to the SCI are the dominant ones in controlling the susceptibility of RC to corrosion. Thus, in 2015, a technical committee (TC) of RILEM (www.rilem.org), TC 262-SCI, started working on these questions. The aim was to bring together experts and to compile knowledge about the SCI: how it influences corrosion of reinforcing steel, and how the SCI can be characterized experimentally. The following section summarizes the work carried out by RILEM TC 262-SCI. Subsequently, more recent developments – some of them triggered by RILEM TC 262-SCI – are briefly described. The authors believe that these advancements, including the development of novel experimental methodologies, can contribute to a fundamental understanding of the corrosion-related processes occurring at the SCI. We hope this will inspire further research in the spirit of RILEM TC 262-SCI, where C.M. Hansson played an active and influential role.

STATE-OF-THE-ART

This section provides a summary of the work of RILEM technical committee (TC) 262-SCI, that was active between 2015 and 2020. When the RILEM TC started its work, a systematic documentation of the numerous aspects and properties of the SCI was lacking in the literature. Thus, first a review of local characteristics of the SCI reported in the literature was compiled, considering their properties and occurrences in both engineering structures and laboratory specimens (Angst, Geiker et al. 2017). A systematic approach was proposed to describe the SCI, distinguishing between features related to the steel side of the SCI and the concrete side of the SCI. This included

properties such as metallurgy and steel surface condition (rust scales, mill scales, etc.) on the one hand, and concrete composition, macroscopic voids (cracks, bleed water zones, entrapped / entrained interfacial air voids, etc.) and moisture state on the other hand. It became apparent that there is significant spatial inhomogeneity at the SCI, both along and around the reinforcing steel. An important finding was that this heterogeneity was observed to vary notably across different engineering structures and even within individual structures. From this, it was inferred that a "generic SCI", representing on-site conditions does not exist. Additionally, considerable differences in SCI characteristics exist between laboratory-made specimens and engineering structures. Accordingly, it was concluded that specimens manufactured in the laboratory are generally not representative for site conditions, and as a consequence, it was recommended that laboratory findings should be applied to engineering structures with caution.

In a second step, RILEM TC 262-SCI investigated the effect of the SCI on chloride-induced corrosion (Angst, Geiker et al. 2019). To this aim, a method was developed to quantify and normalize the influence of individual SCI characteristics as reported in different literature studies. This allowed for summarizing the findings from different studies, in which obviously very different experimental approaches were used, in a comprehensive overview. From this, it was observed that research attention was uneven for different SCI characteristics. While factors such as the water-to-binder (w/b) ratio and cement type had received significant research focus, aspects such as the metallurgy of the steel, the presence of mill scale or rust layers, and the interfacial concrete moisture state had been investigated in a few studies (Figure 1). Interestingly, the reviewed literature consistently indicated that factors such as w/b and cement type only had a moderate impact on the chloride threshold value, that is, the chloride content at which corrosion starts. On the other hand, despite limited literature available, the steel surface properties, especially spatial variability, and the interfacial moisture state were identified to play major roles in chloride-induced corrosion. It was thus recommended that future research in the area of predicting chloride-induced corrosion initiation within concrete should consider these factors in more detail. A particularly important research question left for further consideration seemed to be the complex mechanisms related to moisture conditions within voids – both microscopic and macroscopic – at the SCI.

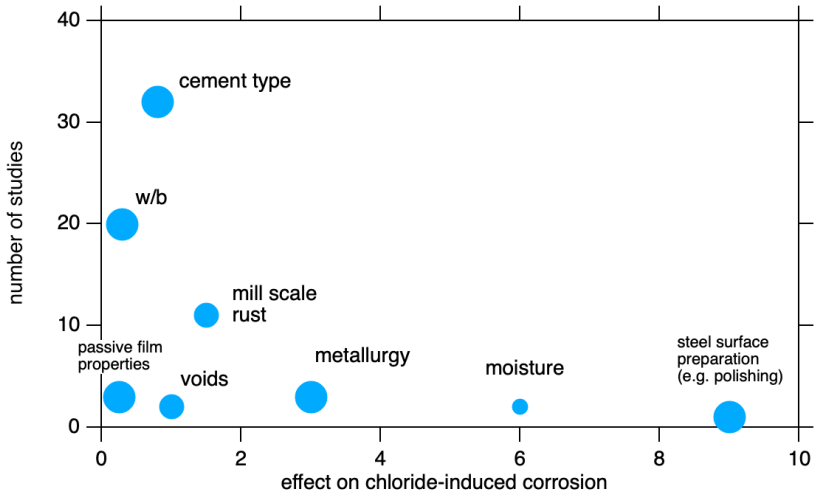

Figure 1: Summary of important findings of RILEM TC 262-SCI, illustrating that features identified to have a pronounced effect on chloride-induced corrosion initiation (abscissa) received comparatively little attention in the literature (ordinate), based on (Angst, Geiker et al. 2019). The symbol size qualitatively represents the number of experimental techniques available to characterize these features, based on (Wong, Angst et al. 2022). Small = virtually no established technique available; intermediate = different proven techniques available, but generally ex-situ techniques; large = numerous techniques available, including in-situ techniques (or irrelevance of in-situ determinations, e.g., for cement type).

Finally, RILEM TC 262-SCI provided a summary on experimental techniques available to characterize the different features related to the SCI and potentially relevant for steel corrosion (Wong, Angst et al. 2022). Over 20 methods were reviewed and their advantages and limitations as well as their applicability to study certain questions were addressed. It was concluded that there is a lack of well-established, non-destructive techniques suitable for directly monitoring various of the important features of the SCI with sufficiently high spatial and temporal resolution. In particular, a lack of techniques to study the moisture content and distribution at the SCI, such as in the interfacial cementitious matrix and in interfacial macroscopic voids, was recognized (Figure 1). However, different promising techniques were identified and their potential for further development and application was discussed. Since the moisture content at the SCI, within pores and macroscopic voids, was previously found to play a major role, it was

recommended that future research should attempt to provide better insight into the moisture state and distribution at the pore scale. The identified promising approaches to study interfacial moisture included computed tomography, namely based on X-ray and neutron radiation, and potentially nuclear magnetic resonance (NMR) despite various challenges inherent to the application of NMR to the SCI. Further work on this was encouraged and as the next sections will show, such work has in the meantime proven to be a research avenue worth following.

RECENT PROGRESS RELATED TO STUDYING THE STEEL-CONCRETE INTERFACE

Characterization of variability in electrochemical steel surface behavior

Recently, a novel technique to study the spatial variability in electrochemical behavior of reinforcing steel surfaces was developed (Michel and Angst 2018, Michel and Angst 2022). This technique termed "Automated local electrochemical characterization" (ALEC) was specifically developed for application to surfaces representative for practice, that is, having complex shape (e.g. ribbed steel) and possibly mill scales or rust scales on the surface. This is considered important because for existing electrochemical surface characterization techniques (e.g., Scanning Vibrating Electrode Technique (SVET) or Scanning Reference Electrode Technique (SRET)), the need for extensive sample preparation to ensure smooth surfaces can limit the applicability of experimental findings to engineering conditions.

In the ALEC technique, a probe with a soft, porous diaphragm establishes an electrolytic connection with the metal. A setup was developed on the basis of an industrial articulated-arm robot with five degrees of freedom, capable of moving the mentioned probe and positioning on the sample (Figure 2a). Together with an additional specimen holder, designed to hold close-to-cylindrical specimens such as rebar segments, capable of rotating the rebar around its axis, it is ensured that the probe can be positioned on any point of the cylindrical specimen. This positioning is additionally force-controlled. By adjusting the force applied to the soft probe, the contact area can be modified and controlled (in the range of approx. 0.5 – 2.5 mm^2 with the probe tips used so far). The probe is further linked to an electrochemical cell (including a reference and a counter electrode) that allows to perform various electrochemical measurements (e.g. cyclic voltammetry, electrochemical impedance spectroscopy) and thus characterization of the metal point by point. Thanks to automation of both the positioning and the electrochemical measurement procedures, automated mapping is possible, which enables high-throughput local electrochemical characterization of the metal surface, generating data suitable for statistical and spatial analysis. Since with the use of specimens exhibiting surface scales (mill scale, corrosion products), the porous probe diaphragm may be contaminated during successive measurements (by iron oxides/hydroxides), an automated cleaning procedure was implemented. This was found effective to avoid contamination-related drifts in the experimental results over the course of mapping.

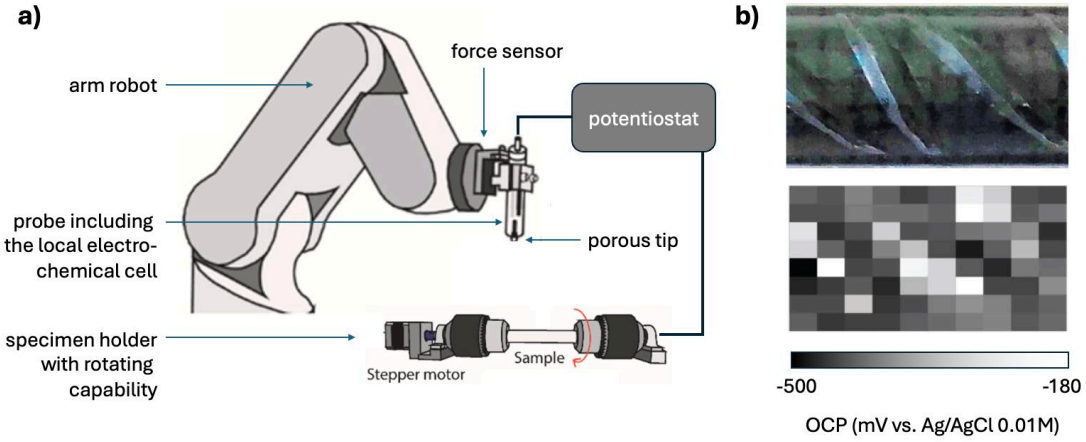

Figure 2: Automated local electrochemical characterization (ALEC), a new technique to study the variability in terms of the electrochemical behaviour of practice-related, complex shaped metal surfaces such as reinforcing steel bars; a) schematic illustration of the most important components of the setup, b) example of experimental data (top: image of a rebar, bottom: corresponding map of open circuit potentials (OCP) (Michel and Angst 2018)).

While a wide range of electrochemical techniques can be applied at each point, Figure 2b shows a simple example of open circuit potential measurements at different points. The corresponding optical image (top) reveals that the electrochemical behavior appeared to have a relationship with the surface shape, that is, on ribs the OCP tended to

be more negative, while it was more positive between the ribs. In later corrosion tests in chloride exposure solutions, indeed the localized corrosion was found to preferentially initiate on/at the ribs. For more details about this particular experiment, the reader is referred to (Michel and Angst 2018) and for the technique in general to (Michel and Angst 2022). It is expected that this novel experimental technique can provide further insight into metallurgical and steel-surface related aspects and their role in initiation of chloride-induced steel corrosion in concrete.

Imaging moisture with X-ray computed microtomography

A recent study (Rossi, Governo et al. 2023) addressed the question of whether the presence of electrolyte within macroscopic concrete voids, including voids at the SCI, can be observed by X-ray computed microtomography (XCT). A potential limitation in detecting aqueous solution within cementitious matrices is generally attributed to the low sensitivity of X-rays to low-density elements (such as hydrogen and oxygen). For this reason, water transport in concrete or mortar is generally investigated with other techniques, including X-ray radiography (2D) and neutron imaging, including neutron tomography. Nevertheless, the findings by Rossi et al. (Rossi, Governo et al. 2023) suggest that the detection of aqueous solution in macropores such as air voids is more constrained by the pore size under investigation and the limitations in XCT spatial resolution, rather than by the low attenuation coefficient of the electrolyte. Figure 3 shows an example of a cylindrical mortar specimen (20 mm diameter) produced from ordinary portland cement, water/cement ratio = 0.45, and sand with 2 mm max. particle size. A carbon steel bar (smooth, 6 mm diameter) was centrally embedded. The specimen was cured at >95% relative humidity and room temperature for 28 days, upon which an initial XCT acquisition was recorded (Figures 3a and b). All XCT acquisitions were carried out at the ICON beamline at Paul Scherrer Institute (PSI) in Villigen, Switzerland, using an acceleration voltage of 150 keV, with 1125 projections over 360°, with 20 s exposure time per projection. The final voxel size was 13.8 µm. It can be seen that coarse air voids can well be identified inside the cementitious matrix due to the comparatively low X-ray attenuation coefficient of dry air. Upon immersion in chloride containing water, these voids start filling up, as shown in Figures. 3c and d, which clearly reveal the meniscus of the water accumulating inside the void. The possibility to observe free solution in air, as done here, depends on the signal-to-noise ratio (SNR) of the XCT images as well as other parameters. While it is outside the scope of this manuscript to discuss these experimental parameters in detail (the reader is referred to (Rossi, Governo et al. 2023)), Figure 3 demonstrates that adequate experimental settings can lead to XCT images that allow reserachers to study, in-situ and in an undisturbed state, the ingress of moisture in concrete voids at the SCI. This possibility opens up new avenues to explore the role of moisture at the SCI in corrosion initiation. Additionally, such approaches may be useful in studying other degradation mechanisms, including freeze-thaw damage.

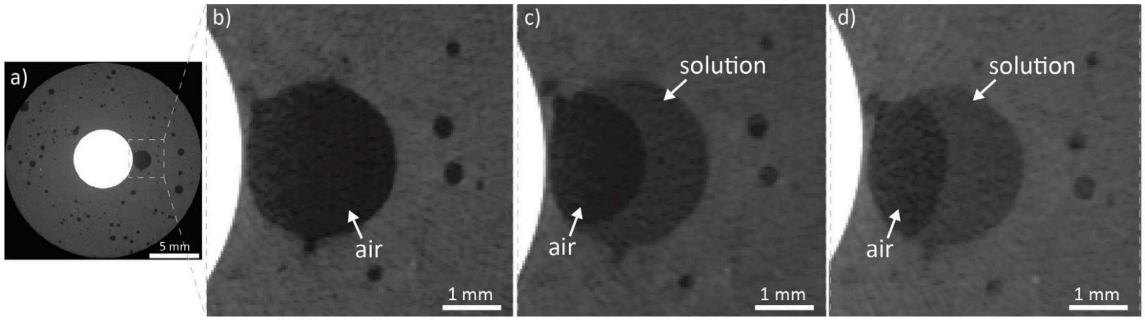

Figure 3: X-ray computed microtomography (XCT) cross-sections of a reinforced mortar cylindrical specimen showing water ingress in macroscopic interfacial concrete voids over time. a) specimen section perpendicular to the steel (white area in the center) in dry conditions; b) closeup of interfacial air void in dry conditions; c) and d) same interfacial air void showing increasing presence of aqueous solution upon immersion in NaCl solution for 8 and 12 weeks, respectively. Figures reproduced from (Rossi, Governo et al. 2023), https://doi.org/10.21809/rilemtechlett.2023.190, licensed under Creative Commons Attribution 4.0 International License (CC BY 4.0), https://creativecommons.org/licenses/by/4.0/.

Cracks and spacers

As part of the work in RILEM TC SCI, characteristics of the SCI were described, among others including macroscopic voids as listed in Table 1 (Angst, Geiker et al. 2017). Depending on other local characteristics, such macroscopic voids have been observed to strongly influence the initiation of chloride-induced corrosion (Angst, Geiker et al. 2019). The moisture conditions at the interface - and the potential interaction with the exterior causing

moisture variation - especially affect the impact of macroscopic voids (Angst, Geiker et al. 2019, Angst, Isgor et al. 2022).

Table 1 — List of macroscopic voids at the steel-concrete interface (SCI). (Angst, Geiker et al. 2017).

Macroscopic voids at the SCI	Length scale	
	perpendicular to steel surface	along steel surface
Entrapped/entrained air voids	µm – mm	µm – mm
Bleed-water zones, depending on rebar orientation	µm – mm	µm – mm
Cracks (including slip/separation)	µm – mm	µm – cm
Honeycombs	mm – cm	mm – cm

Cracks and interconnected voids in the concrete cover facilitate exchange of matter (fluids, gases) with the exterior. Such macroscopic voids affecting the SCI have been reported often to cause premature corrosion initiation, as e.g., reviewed in (Boschmann, Angst et al. 2017, Robuschi, Ivanov et al. 2022). Treating the available (and unfortunately biased) literature data statistically, Robuschi et al. (Robuschi, Ivanov et al. 2022) found that the corrosion rate of pits increased in the proximity of cracks, but also that with time the number of pits increased while the corrosion rate of the individual pits decreased, and that there was no clear correlation between surface crack width and corrosion damage.

Despite increased chloride content at cracks, corrosion might not initiate or be sustained. This was demonstrated by Marcos-Meson et al. (Marcos-Meson, Geiker et al. 2020), who investigated the combined impact of chloride and hydroxyl ions for steel fibre corrosion. In an other study, a sustained high hydroxyl ion concentration was hypothesized as the reason for not observing reinforcement corrosion in any significant amounts in cracked concrete panels after 9 years of marine exposure (Geiker, Robuschi et al. 2023). The high pH was explained by the combination of the crack type and location, the large cover, and the binder composition (portland cement) (Geiker, Robuschi et al. 2023).

Boschmann Käthler et al. (Boschmann Käthler, Angst et al. 2021) highlighted the importance of wetness for corrosion propagation of steel in cracked concrete. Insignificant corrosion rates were observed in the event of drying of the SCI to a relative humidity (RH) below a critical level. That is, in case of wetting-drying cycles, the overall corrosion development depended on the duration of the wetting and drying periods and the RH during drying. Based on the observations, Boschmann Käthler et al. (Boschmann Käthler, Angst et al. 2021) proposed a model to estimate corrosion rates in cracked concrete exposed to cyclic wetting-drying cycles, adopting the concept of "time of wetness".

Several types of macroscopic voids may be present in the same concrete element, and the possible chloride-induced corrosion initiation at a macroscopic void appears, among other factors, to depend on the presence of active corrosion within a certain distance. An example supporting this is the observed combined impact of spacers (reinforcement chairs) and cracks on the performance of marine exposed pre-cracked concrete beams (Geiker, Danner et al. 2021). The spacers used were made from plastic resulting in an imperfect bond between spacer and concrete. In addition, the compaction of the concrete in the vicinity of the spacers was insufficient, probably due to the geometry of the spacers. After 25 years of exposure, no or very limited corrosion was observed outside the location of a few of the inadequate plastic spacers, see Figure 4. In addition, the distance between corroding areas (pits) appeared to depend on the concrete resistivity. In line with the description of potential-dependent chloride thresholds described by Sagüés et al. (Sagüés, Sánchez et al. 2014), these observations caused Geiker et al. (Geiker, Danner et al. 2021) to suggest that ongoing corrosion (at weak spots, in the present case at spacers) may protect the adjacent reinforcement from corrosion through the cathodic polarisation. This hypothesis of "mutual protection" calls for great care in the application and generalization of data on the possible impact of macroscopic voids on reinforcement corrosion. It should be mentioned that early corrosion initiation is not necessarily connected to macroscopic voids. Using bimodal X-ray and neutron imaging to study very early corrosion, Angst et al. (Angst et al. 2024) found only half of the corrosion sites to be in close proximitry to macroscopic voids. Moreover, some of these corrosion initiation sites were found in very close proximity, suggesting that the "mutual protection" effect is limited for small anodic sites and early-stage corrosion. Furthermore, when applying results from small-scale laboratory specimens to dimensions representative of structural members, the lower likelihood of weak spots in small specimens – causing a size-dependent value of chloride thresholds (Angst and Elsener 2017) – should be kept in mind.

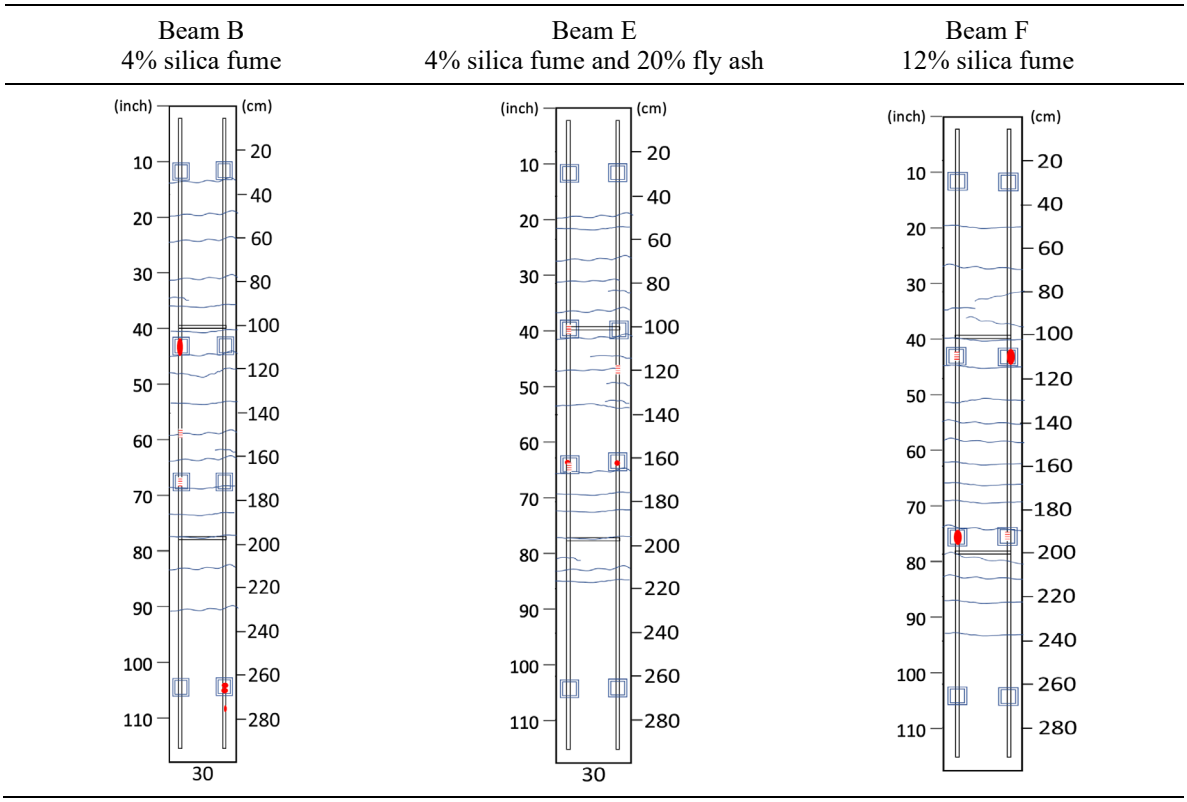

Figure 4: Extent of corrosion (marked in red) observed on reinforcement in three different pre-cracked concrete beams after 25 years marine exposure (from top to bottom: atmospheric, tidal, and submerged). Corrosion was observed after removal of the concrete and cleaning the rebars. Double lines indicate reinforcement, squares indicate location of plastic spacers, and horizontal lines indicate cracks. Length from top measured in cm and inch, respectively. Figures modified from (Geiker, Danner et al. 2021).

CONCLUDING REMARKS

RILEM technical committee 262-SCI – which was active between 2015 and 2020 – provided an extensive state-of-the-art documentation of the steel-concrete interface (SCI), including a systematic classification and compilation of the various features that can be expected at the SCI. Furthermore, the effect of the various features on chloride-induced corrosion initiation was assessed based on reported literature data. A quantitative statistical analysis allowed comparing the relevance of these features and thus identifying the most important ones: steel metallurgy and surface properties, interfacial macroscopic voids and especially their moisture state as well as the moisture distribution at the SCI. The work of RILEM TC 262-SCI further revealed that unfortunately, limited suitable experimental techniques were available to address some of these important scientific questions, namely there was a lack of in-situ techniques to study the moisture at the SCI and how it impacts corrosion.

Following the suggestions of RILEM TC 262-SCI, recent work has made progress in addressing the questions raised. First, a novel technique – "Automated local electrochemical characterization" (ALEC) – allows the study of the spatial variability in electrochemical behavior of reinforcing steel surfaces. This technique is suitable for application to surfaces representative for practice, that is, having complex shape and surface conditions, e.g. rust scales and mill-scales. Second, further progress has been made in XCT in-situ imaging, which allows researchers to monitor in an undisturbed state, the movement of moisture in concrete, and in particular its presence in macroscopic voids at the SCI. These advancements in experimental techniques create new opportunities to study the roles of spatially variable rebar surface properties and moisture at the SCI in corrosion initiation.

Laboratory and field studies have brought additional understanding of the detrimental conditions for corrosion initiation and propagation at macroscopic voids. The importance of moisture for corrosion to propagate was further highlighted and a model was proposed for the prediction of corrosion during wetting and drying cycles. Also, the detrimental impact of combinations of chlorides and reduced pH on steel corrosion was shown for the example of

steel fibres. Finally, field observations indicated that corrosion at weak spots may, under some conditions, protect the remaining reinforcement despite possible other macroscopic voids. This possible interaction among different defects within a structural member calls for great care in the application and generalization of data on the impact of macroscopic voids on reinforcement corrosion.

ACKNOWLEDGEMENTS

The first author is grateful to the Swiss National Science Foundation for the financial support (projects PP00P2_163675, PP00P2_194812, and CRSII5_205883). The second author acknowledges support from the Research Council Norway (project number 340843: Green Management of Structures for Infrastructure, known as EXCON and project number 262644: PoreLab – Centre of Excellence). Both authors are grateful for the support provided by RILEM in running the technical committee and for the active contributions of all committee members.

REFERENCES

Angst, U. M. and B. Elsener (2017). "The size effect in corrosion greatly influences the predicted life span of concrete infrastructures." Science Advances **3**(8).

Angst, U. M., M. R. Geiker, M. C. Alonso, R. Polder, B. Elsener, O. B. Isgor, H. Wong, A. Michel, K. Hornbostel, C. Gehlen, R. François, M. Sanchez, M. Criado, H. Sørensen, C. Hansson, R. Pillai, S. Mundra, J. Gulikers, M. Raupach, J. Pacheco and A. Sagüés (2019). "The effect of the steel-concrete interface on chloride-induced corrosion initiation in concrete – a critical review by RILEM TC 262-SCI." Materials and Structures **52**: 88.

Angst, U. M., M. R. Geiker, A. Michel, C. Gehlen, H. Wong, O. B. Isgor, B. Elsener, C. M. Hansson, R. Francois, K. Hornbostel, R. Polder, M. C. Alonso, M. Sanchez, M. J. Correia, M. Criado, A. Sagues and N. Buenfeld (2017). "The steel-concrete interface." Materials and Structures **50**(2): 143.

Angst, U. M., B. Isgor, C. M. Hansson, A. A. Sagüés and M. R. Geiker (2022). "Beyond the chloride threshold concept for predicting corrosion of steel in concrete." Applied Physics Reviews **9**: 011321.

Angst, U. M., E. Rossi, C. Boschmann Käthler, D. Mannes, P. Trtik, B. Elsener, Z. Zhou and M. Strobl (2024). "Chloride-induced corrosion of steel in concrete—insights from bimodal neutron and X-ray microtomography combined with ex-situ microscopy." Materials and Structures **57**(4): 56.

Boschmann, C., U. M. Angst, M. Wagner, C. K. Larsen and B. Elsener (2017). Effect of cracks on chloride-induced corrosion of steel in concrete - a review (NPRA report no. 454)**:** 37.

Boschmann Käthler, C., U. M. Angst, G. Ebell and B. Elsener (2021). "Chloride-induced reinforcement corrosion in cracked concrete: The influence of time of wetness on corrosion propagation." Corrosion Engineering, Science and Technology **56**(1): 1-10.

Enevoldsen, J., C. Hansson and B. Hope (1994). "The Influence of Internal Relative Humidity on the Rate of Corrosion of Steel Embedded in Concrete and Mortar." Cement and Concrete Research **24**: 1373-1382.

Geiker, M., T. Danner, A. Michel, A. Belda Revert, O. Linderoth and K. Hornbostel (2021). "25 years of field exposure of pre-cracked concrete beams; combined impact of spacers and cracks on reinforcement corrosion." Construction and Building Materials **286**: 122801.

Geiker, M., S. Robuschi, K. Lundgren, C. Paraskevoulakos, C. Gundlach, T. Danner, U. H. Jakobsen and A. Michel (2023). "Concluding destructive investigation of a nine-year-old marine-exposed cracked concrete panel." Cement and Concrete Research **165**: 107070.

Hansson, C. M. (2011). "The impact of corrosion on society." Metallurgical and Materials Transactions A **42**(10): 2952-2962.

Hansson, C. M., T. Frølund and J. B. Markussen (1985). "The effect of chloride cation type on the corrosion of steel in concrete by chloride salts." Cement and Concrete Research **15**(1): 65-73.

Hansson, C. M. and B. Sørensen (1990). The threshold concentration of chloride in concrete for the initiation of reinforcement corrosion. Corrosion rates of steel in concrete. N. S. Berke, V. Chaker and D. Whiting, ASTM STP 1065**:** 3-16.

Jaffer, S. J. and C. M. Hansson (2008). "The influence of cracks on chloride-induced corrosion of steel in ordinary Portland cement and high performance concretes subjected to different loading conditions." Corrosion Science **50**(12): 3343-3355.

Mammoliti, L. T., L. C. Brown, C. M. Hansson and B. B. Hope (1996). "The influence of surface finish of reinforcing steel and pH of the test solution on the chloride threshold concentration for corrosion initiation in synthetic pore solutions." Cement and Concrete Research **26**(4): 545-550.

Marcos-Meson, V., M. Geiker, G. Fischer, A. Solgaard, U. H. Jakobsen, T. Danner, C. Edvardsen, T. L. Skovhus and A. Michel (2020). "Durability of cracked SFRC exposed to wet-dry cycles of chlorides and carbon dioxide – Multiscale deterioration phenomena." Cement and Concrete Research **135**: 106120.

Michel, L. and U. M. Angst (2018). Towards understanding corrosion initiation in concrete – Influence of local electrochemical properties of reinforcing steel. 5th Int. Conf. Concrete Repair, Rehabilitation and Retrofitting - ICCRRR, 2018. M. G. Alexander, H.-D. Beushausen, F. Dehn and P. Moyo. Cape Town, South Africa, CRC Press.
Michel, L. and U. M. Angst (2022). "Automated local electrochemical characterization on metals with complex shape and practice-related surface state." Measurement **201**: 111713.
Robuschi, S., O. L. Ivanov, M. Geiker, I. Fernandez and K. Lundgren (2022). "Impact of cracks on distribution of chloride-induced reinforcement corrosion." Materials and Structures **56**(1): 7.
Rossi, E., S. Governo, M. Shakoorioskooie, Q. Zhan, S. Mundra, D. Mannes, A. Kaestner and U. Angst (2023). "X-ray computed tomography to observe the presence of water in macropores of cementitious materials." RILEM Technical Letters **8**: 165-175.
Sagüés, A. A., A. N. Sánchez, K. Lau and S. C. Kranc (2014). "Service Life Forecasting for Reinforced Concrete Incorporating Potential-Dependent Chloride Threshold." CORROSION **70**(9): 942-957.
Wong, H. S., U. M. Angst, M. R. Geiker, O. B. Isgor, B. Elsener, A. Michel, M. C. Alonso, M. J. Correia, J. Pacheco, J. Gulikers, Y. X. Zhao, M. Criado, M. Raupach, H. Sorensen, R. Francois, S. Mundra, M. Rasol and R. Polder (2022). "Methods for characterising the steel-concrete interface to enhance understanding of reinforcement corrosion: a critical review by RILEM TC 262-SCI." Materials and Structures **55**(4).

Electrical Resistivity in Air-Entrained, Partially Saturated Industrial Concretes

Timothy J. Barrett and W. Jason Weiss

Synopsis: The electrical properties of concrete are being increasingly used to assess concrete resistance to fluid transport. Electrical measurements are strongly dependent on sample conditioning, which includes the degree of saturation. This paper presents an analytical approach for interpreting electrical measurements in partially saturated concrete. Previous approaches have used a power law to describe the influence of saturation. This paper proposes a saturation function that accounts for the contributions of the entrained air voids, the capillary pores, and the gel pores (the GCA function). The proposed approach is demonstrated for high performance, internally cured concrete mixtures tested between the ages of 30 d and 120 d. The power function had a greater measured uncertainty than the GCA function, which performed better at both high and low degrees of saturation. The resistivity of specimens submersed in simulated pore solution was measured as was the resistivity of sealed specimens. The sealed specimens have a degree of saturation that is similar to those at the nick point (matrix saturation), with an offset consistently only due to the self-desiccation of the binder.

Keywords: conductivity, electrical properties, resistivity, saturation

Timothy J. Barrett, ACI member, Research Civil Engineer in the Office of Infrastructure Research and Development at the Federal Highway Administration Turner-Fairbank Highway Research Center. He earned a BS, MS, and Ph.D. in civil engineering from Purdue University, West Lafayette, IN.

W. Jason Weiss, FACI, Edwards Distinguished Professor of Engineering at Oregon State University. He earned a BAE in architectural engineering from the Pennsylvania State University, University Park, PA, and a MS and Ph.D. in civil engineering from Northwestern University, Evanston, IL. He is currently a member of the ACI Technical Activities Committee, a former ACI Board Member and the former editor of the *ACI Materials Journal*.

INTRODUCTION

The desire to rapidly evaluate the potential durability or service life of concrete has led to the development of several test methods that rely on applying an electrical potential across a sample. Common methods include the rapid chloride permeability (RCP) test (ASTM C1202/AASHTO T277),[1] the Nordtest non-steady-state migration approach,[2] and a proprietary modified migration test,[3] among others. More recently, electrical resistivity (AASHTO T358, AASHTO T402, ASTM C1876)[4–6] has gained significant interest due to its ability to measure rapidly and economically.

Each of the aforementioned testing approaches relies on the measurement of the electrical properties of concrete. Electrical properties have been utilized in the study of concrete for more than a century.[7,8] While the electrical resistivity method has been a research subject in laboratories for decades[9,10] and has been expanded upon significantly in recent years,[11–27] the focus of this paper is on the practical application of this method to industrially produced concretes containing entrained air. Special attention will be given to the testing procedure itself and the effect of changes in the degree of saturation (DOS) in concrete samples on the measured electrical resistivity. The relationship between DOS and the measured electrical resistivity will be presented and the role of the choice of sample conditioning method will be addressed as this choice is of critical consideration in practice.[28] A comparison of two AASTHO T402 conditioning procedures (submersion in a simulated pore solution and sealed samples) will be given.

BACKGROUND ON THE MEASUREMENT OF ELECTRICAL PROPERTIES

The electrical resistivity of concrete is described by Eq. (1a).

$$\rho = R \cdot k \tag{1a}$$

$$\rho = R \cdot \left(\frac{A}{L}\right) \tag{1b}$$

where the measured resistance (R) of a specimen is multiplied by a geometry factor (k). The geometry factor for a uniaxial cylindrical specimen (AASHTO 402, ASTM C1876) is provided in Eq. (1b) as the cross-sectional area (A) divided by its length (L). A separate geometry factor is needed for the application of surface resistivity meters or embedded probe type measurements and can be taken from literature,[22,29] numerically estimated, or measured experimentally.[30]

Eq. (2a) illustrates electrical conductivity as a measure of the material's structure, which can be defined as the formation factor (F). The equivalent and more common form using resistivity (the numerical inverse of conductivity) is provided in Eq. (2b).

$$\frac{\sigma_c^o}{\sigma_p^o} = (\phi\beta)|_{S=1} \equiv \frac{1}{F} \tag{2a}$$

$$\frac{\rho_p^o}{\rho_c^o} = (\phi\beta)^{-1}|_{S=1} \equiv F \tag{2b}$$

where the formation factor is defined as the inverse of the product of the pore volume (ϕ) and the pore connectivity (β), assuming the pores are filled with conductive fluid, which would be consistent with a degree of saturation (S)

equal to one. The formation factor is measured by dividing the conductivity of saturated concrete (σ_c^o) (hereafter the superscript (^{o}) will designate a measurement in the saturated state ($S = 1$)) by the conductivity of the pore solution in the concrete at saturation (σ_p^o). The formation factor (F) can then be related to the diffusion of any ionic species using the Nernst-Einstein relationship, as shown in Eq. (3).[31]

$$\frac{1}{F} = \frac{D}{D_0} \tag{3}$$

where (D) is the intrinsic diffusion coefficient of the concrete and (D_0) is the self-diffusion coefficient of an ionic species and is taken here as 1.9 x 10^{-9} m^2/s for chloride ions.[32]

This relationship shows that the measurement of electrical resistivity may be used to obtain the formation factor and corresponding concrete diffusion coefficient for use in an appropriate model to evaluate the potential service life of a given mixture,[33] where the boundary conditions and the effects of chloride binding are included.[34] Strictly speaking, Eq. (3) is defined at saturation. While the previous equations appear to be simple and their application seemingly straight forward, careful consideration must be given to factors that may influence testing to determine resistivity as shown in Eq. (4).[29]

$$\left(\frac{\sigma_c}{\sigma_p^o}\right)_{T_{ref}} = \frac{1}{F} \cdot f(S) \cdot f(T) \cdot f(L) \cdot f(M) \tag{4}$$

where ($f(S)$) is the effect of specimen saturation, ($f(T)$) is the effect of temperature on the electrical measurement, ($f(L)$) is the effect of alkali leaching during curing, and ($f(M)$) is the effect of curing choices on the microstructural development for a given reference temperature (T_{ref}). Historically, curing concrete samples in lime-water tanks has been common,[4,35] however significant alkali leaching may occur. Leaching may result in changes in measured pore solution conductivities of up to 80 % when compared with the original solution conductivity.[19] Further, storing specimens submerged under water does not result in a state of 100 % saturation as it is very difficult to saturate the air voids, rather the specimens are most closely associated with the nick point degree of saturation where the gel and capillary pores are full while the air voids remain empty.[36–38] These experimental errors introduce both known and unknown uncertainties, which limit the applicability of the resistivity method for chloride diffusion measurement and service life modeling if not measured and understood.

Two standard methods have been used to minimize the influence of leaching and saturation. The first is the so-called bucket test method in which the samples may be submerged in a simulated pore solution matching the estimated or measured ionic concentrations of the pore solution of the test specimen.[5,39] It is possible to closely match the ionic composition of a concrete pore solution by matching only the most electrically conductive components of the solution (namely the K^+, Na^+, OH^-, and Ca^{2+}), which minimizes the effects of the leaching process.[19] In the AASHTO T358 and T402 standards, the solution has been fixed to a single composition at the request of state highway agencies for ease of use in practice; however, this introduces experimental error. While this offers a method to minimize leaching effects, the approach remains limited to measuring the electrical properties of concrete containing fluid that can be absorbed easily. As such, the concrete is not completely saturated and remains near the nick point degree of saturation. The use of submerged curing with simulated pore solution may also be challenging on an industrial scale.[40]

The second testing procedure consists of performing electrical measurements on sealed specimens that are stored in an isothermal condition at 23 °C, where sealed is defined as a condition that ensures the transfer of moisture to/from the specimen from/to the environment is prevented through an appropriate method.[33] These measurements may be made either at discrete times or continuously (and in-situ) by embedded probes.[30,41] By making measurements on sealed, isothermal specimens, the testing factors related to temperature, leaching, and microstructural development at elevated temperatures are all eliminated. It is further recommended that the pore solution conductivity be calculated using the online tool developed by Bentz,[42] using thermodynamic modeling,[43] or measured directly.[44,45] This leaves only the need to correct electrical measurements with a saturation function to calculate the formation factor, as described in Eq. (5), and the diffusion coefficient by extension using Eq. (3).

$$F = \frac{\rho_p^o}{\rho_c} \cdot f(S) \quad (5)$$

This paper examines the saturation function that can be used for air-entrained concretes. It should be noted that changes in the DOS have a highly nonlinear relationship with electrical measurements.[15,46] This is due to the physical construct of the electrical properties of concrete, where the formation factor is defined by the tortuosity multiplied by the volume of filled, conductive pore volume, which is directly analogous to the degree of saturation.[47] Further details on the derivation of this relationship can be found in related work.[48]

EXPERIMENTAL MEASUREMENTS

The experimental results in this paper correspond to four industrially produced, internally cured high-performance concrete (IC HPC) mixtures.[48,49] In addition, four reference high-performance concretes (HPCs) were tested, having been made on the same day by the same ready-mixed concrete producer using the same constituent materials as the corresponding IC HPC but without lightweight fine aggregate substitution of a similar volume of conventional fine aggregate. The typical design proportions of each of these concretes was similar, having a water-to-cementitious materials ratio (w/cm) of approximately 0.40, a paste volume of 24 % to 26 %, and a target air content by volume fraction of concrete of 6.5 %. Further details on the sample preparation and constituent materials are provided in the referenced work.[48] Table 1 provides the as batched mixture proportions.

A set of 100 mm x 200 mm (4 in x 8 in) cylinders were cast from industrially produced ready mixed concrete and field cured for up to 7 d prior to transportation to the laboratory. Sealed, bulk uniaxial resistivity measurements were made at discrete ages over time, with samples being stored between measurements in sealed bags inside a wet curing misting chamber (to minimize any potential drying), where the relative humidity was above (98 ± 2) % with a constant temperature of (23 ± 1) °C. At the age of 28 d or later (i.e., when the samples have reached a stable degree of hydration (DOH)), a minimum of two additional companion specimens that had been sealed-cured in molds and stored in the wet curing chamber were de-molded, and the sealed resistivity and masses were measured. The oven-dry mass of the specimens was then obtained after drying in an oven set to 105 °C until mass equilibrium was reached (drying time was more than 7 d). The specimens were then cut into three approximately equal pieces using a concrete wet saw, making it necessary to return the three pieces to the oven until mass equilibrium in the oven dry state was achieved once more. The mass was then measured and recorded for each of the three pieces of the cylinder.

The samples were then saturated to the fullest extent possible using an industrial vacuum saturator regulated to between 0.67 kPa to 1.33 kPa (5 Torr to 10 Torr) with the oven-dry samples under vacuum for 3 h. The samples were saturated with a supersaturated lime-water solution made with de-aired water, which was prepared by placing the water at a vacuum of 46.7 kPa (350 Torr) for approximately 15 min. The solution was added to the vacuum chamber such that the samples were entirely covered with lime-water (without releasing the vacuum) and held under vacuum for 1 h. The samples were then removed from the vacuum chamber and remained under solution for a minimum of 18 h prior to testing.

Once the samples were vacuum saturated, the saturated surface dry mass (m_S^o), buoyant mass (m_B), and resistivity at saturation (ρ_S^o) were measured. The degree of saturation, defined in Eq. (6) for any experimental measurement on a mass basis, was computed using the mass at any degree of saturation (m_S) and the oven dry mass (m_{OD}). This relationship was used to estimate the mass to which the samples needed to be dried to obtain varying levels of saturation, at which point corresponding resistivity measurements were made to generate the experimental relationship between the saturation function $f(S)$, and the degree of saturation (S). This procedure was performed on individual test specimens by drying them sequentially to the desired degree of saturation then sealing them in bags for a sufficient amount of time to allow the moisture to redistribute and minimize effects of moisture gradients throughout the geometry. In the present work, the test specimens were sealed in two bags to minimize further moisture loss, and a period of 7 d was chosen to allow for the redistribution of moisture prior to the measurement of mass and resistivity. This procedure was repeated with sequential drying until the initial degree of saturation of the original sealed sample was reached. The saturation function was then calculated by normalizing the results of the conductivity at any degree of saturation by the fully saturated conductivity of that specimen.

$$S = \frac{m_S}{m_S^o - m_{OD}} \quad (6)$$

DEGREE OF SATURATION

While the mass-based definition of the degree of saturation is convenient for use in experiments, it is equally important to review the volumetric definition of the degree of saturation (the mass and volume approaches are numerically equivalent). Eq. (7) defines the degree of saturation as a function of the volume of water (V_w), where consideration will be given to all voids that may be filled in the system including the gel (V_{gel}) and capillary pores (V_{cap}), empty void space formed due to chemical shrinkage (V_{cs}), and air voids (V_{air}).

$$S = \frac{V_w}{V_{gel} + V_{cap} + V_{cs} + V_{air}} \tag{7}$$

It is convenient to group these contributions into those that are a part of the matrix (gel pores, capillary pores, and chemical shrinkage) and those that are not, namely the air voids. This enables the degree of saturation to be represented as a function of the two separate groups of pore structures. The degree of saturation that delineates these two groups is the nick point (also referred to in literature as matrix saturation), a point that is commonly associated with the transition between initial and secondary sorption in the ASTM C1585 absorption test and frequently occurs within the first day of testing for 50 mm tall test specimens.[50] Research using neutron radiography to map moisture movement during absorption tests performed on mortars showed that the pores in the matrix fill rapidly (equal to the mass change during initial sorptivity) followed by a slower infilling of the air voids (corresponding to secondary sorptivity) when unimpeded absorption occurs.[51] Based on those findings, for the remainder of this work the nick point degree of saturation will therefore be equal to a condition in which all matrix pores are full while the air voids remain empty.

Powers' model can be used to estimate the nick point degree of saturation (S_{nick}).[52] The initial porosity is required and is calculated using Eq. (8).

$$P_i = \frac{w/c}{\frac{w}{c} + \frac{\rho_{water}}{\rho_{cement}}} \tag{8}$$

where (w/c) is the water to cement ratio, (ρ_{water}) is the density of water, and (ρ_{cement}) is the density of cement.

The nick point degree of saturation (S_{nick}) is computed using Eq. (9).

$$S_{nick} = \frac{P_i - 0.5(1 - P_i)\alpha}{(P_i - 0.5(1 - P_i)\alpha) + \left(\frac{V_{air}}{V_{paste}}\right)} \tag{9}$$

where (α) is the degree of hydration, (V_{air}) is the volume of entrained air, and (V_{paste}) is the volume of paste.

Eq. (10) provides a similar expression that may be used to estimate the sealed degree of saturation (S_{sealed}).

$$S_{sealed} = \frac{P_i - 0.7(1 - P_i)\alpha}{(P_i - 0.5(1 - P_i)\alpha) + \left(\frac{V_{air}}{V_{paste}}\right)} \tag{10}$$

Eq. (8), Eq. (9), and Eq. (10) are developed from mixtures with only cement, uncertainty in their accuracy may exist when extending to more complex binder systems if not accounted for. A companion study was performed that explores the role of mixture proportions and volume of entrained air on the nick point using these expressions and extensions, which include the contributions of silica fume.[48,53] The primary conclusion therein demonstrated that air entrainment reduces the degree of saturation associated with the nick point while standard water curing will result in an initial degree of saturation approximately equal to the nick point. It was also shown that the degree of saturation at the nick point is substantially lower than full saturation in air entrained concrete. Additionally, these expressions show that the

sealed degree of saturation is proportional to the nick point degree of saturation, a phenomenon that can be leveraged to simplify the electrical resistivity testing method and will be expanded upon in the latter portion of this paper.

This Powers' model has been shown schematically in Fig. 1(b) for the paste fraction of a concrete with a water-to-cement ratio of 0.40, a paste volume of 25 %, and an air content by volume fraction of concrete of 6.5 %, which closely resembles the initial design of the mixtures studied herein. Fig. 1(a) shows the experimentally measured saturation function for each of the mixtures in this study and indicates the theoretical nick point as calculated using Eq. (9) in the hatched region assuming a degree of hydration of 70 %. The location of this region is primarily a function of the volume of entrained air, which varies by mixture and batched load. The majority of the measured response of the saturation function for these concretes is associated with the infilling of air voids and their participation in the electrical conductance of the concrete void system. The theoretical and mathematical description of the direct contribution of the air voids on the overall conductivity of the concrete has been treated in greater depth in the companion study.[48]

Initial experimental evaluation of the saturation function for air-entrained concretes indicates that this is primarily a measure of the influence of air voids. Bu et al. showed that different levels of vacuum used in the saturation process resulted in varying levels of total porosity being filled.[28] For the level of vacuum corresponding to boiling water (boil saturation is a common specification measure, ASTM C642[54]), it was shown that the majority of the matrix pores are filled while the air voids remain empty, therefore yielding an initial degree of saturation that is consistent with the nick point saturation (S_{nick}). For vacuum levels approaching a perfect vacuum (i.e., under 1.3 kPa (10 Torr), as was implemented in this study) it was shown that the total measured porosity approached the theoretical total porosity. As an experimental check, the total volume of voids for each specimen is provided in Table 2 and were greater than 15 %, a lower-bound estimate for a cement-only system with a paste volume of 25 % and 6.5 % volume of air. As such, the experimental data shown here can therefore be primarily associated with the change in degree of saturation related to the emptying of the air voids. This observation has implications not only on the result of the resistivity test when applied to air entrained concretes in the field but also indicates the nonlinear effect of moisture content on diffusion measurements in general, which may lead to challenges when interpreting, comparing, and evaluating diffusion measurements obtained from accelerated tests that require specimens to be saturated but do not specify any specific level of vacuum for preparation.[48]

POWER SATURATION FUNCTION

Several studies assessing the influence of the degree of saturation on measured electrical properties begin with Archie's research on conductivity measurements in drilled rock cores where a simple power law was proposed,[55] shown in Eq. (11), where (n) is a fitting parameter typically determined to be in the range of 3 to 5 for non-air entrained cementitious materials.

$$\frac{\sigma_c}{\sigma_c^o} = f(S) = S^n \tag{11}$$

This relationship was extended by Weiss et al.[15] to cementitious materials by accounting for drying.[56] The result of the power law saturation function has been plotted for the typical upper and lower bound fitting parameters (n equals 3 and 5 respectively) overlaid on the experimental data in Fig. 1.

Analysis of the experimental data (Fig. 1) on a mixture-by-mixture basis indicated two notable findings. First, a single unique relationship may not describe the saturation function for a set of specimens cut from a single cylinder or a set of cylinders from a single concrete mixture. Second, the power law saturation function may not be adequate to describe the measured experimental relationship at high degrees of saturation. It is hypothesized that this is primarily associated with the effect on the electrical connectivity of the air voids, which are relatively isolated from one another and contain a large volume of conductive fluid at full saturation.

GEL-CAPILLARY-AIR (GCA) SATURATION FUNCTION

To address this shortcoming, a new saturation function was developed where it is assumed that the response can be divided into three regions with each being associated with the gel, capillary, and air voids, as shown schematically in Fig. 2. Measurements at a degree of saturation greater than the calculated nick point degree of saturation (Fig. 1) are

the response of the air void structure and take a general concave shape. The traditional power law, which has been observed experimentally, has been primarily a measure of the capillary pore network, as much of this data was collected from experiments on non-air-entrained systems.[15] A constant region associated with the gel pores was added, as tentatively supported by previous research,[21] to facilitate conceptual simplification. Water can, however, be lost from these smaller pores as the system dries so it may be expected that the saturation function continues to decrease as the degree of saturation approaches zero.[48] Most measurements made on concrete are performed at degrees of saturation greater than about 30 %, so this region is likely of lower interest for practical concrete field applications.

The proposed GCA saturation function is shown in Eq. (12) (based on the schematic concept shown in Fig. 2).

$$f(S) = \left[\frac{1}{1 + \left(\frac{S}{1-\varphi}\right)^{-4n}} + \sigma_{Gel}\right](1 - \sigma_{Gel})\left(1 + \left(\frac{1}{1-\varphi}\right)^{-4n}\right) \tag{12}$$

where (n) is a shape parameter, (φ) is a parameter that describes the curvature of the function, and (σ_{Gel}) is a constant to account for the conductivity of the gel pores. The primary form of the equation is shown in brackets, taking a similar form to experimentally derived moisture diffusion estimations,[57] while also retaining the power law (where (n) is generally still in the range of 3 to 5) and adding the contribution of the gel conductivity. The remainder of the expression is a mathematical necessity to balance the response function and ensure that the result of the expression at a degree of saturation of 1.0 results in 1.0 for reasonable inputs. In general, gel conductivity may be expected in a range of 0.0 to 0.2, and the shape parameter should fall between 0.0 and 0.3 and is associated with the volume and conductivity of air voids, however no definitive relationship based on first principles has yet been derived. The power function is shown in Fig. 3(a) while the GCA function is shown in Fig. 3(b). The GCA function shows its flexibility in being able to bound the majority of the data with its prediction interval while the power law saturation function shows some deficiencies at the higher saturation levels.

UNCERTAINTY ANALYSIS OF SATURATION FUNCTIONS

Eq. (12) is applied to experimental data by solving for optimum values of (n), (σ_{gel}), and (φ) for each individual specimen tested. This has been done for the present study and the results of the fitting parameters are provided in Table 2. Due to the experimental variability both throughout the height of each specimen and between samples, each of these parameters exhibits a distribution of fitted parameter values. To account for the variability in each parameter on the fitted function, the parametric bootstrap analysis method was implemented using Monte Carlo simulations. The general form of the analysis is described by Eq. (13), where random sampling of fitted probability distributions of each of the three individual variables were used in 5,000 trials to generate a distribution of the calculated saturation function. A coefficient of variation (COV) associated with the determination of the saturation function is calculated by normalizing the bootstrap distribution standard deviation by the mean and may be used as an estimator of the variability of the proposed testing method.

$$\begin{aligned}
\frac{\sigma_c}{\sigma_c^o} &\sim N\left(\mu_{f(S)}, \sigma_{f(S)}^2\right) \\
\mu_{f(S)} &\sim f\left(S \mid n_i, \sigma_{gel_i}, \varphi_i\right) \\
n_i &\sim N(\mu_n, \sigma_n^2) \\
\sigma_{gel_i} &\sim N\left(\mu_{\sigma_{gel}}, \sigma_{\sigma_{gel}}^2\right) \\
\varphi_i &\sim N\left(\mu_\varphi, \sigma_\varphi^2\right) \\
&for\ (i = 1, 2, \ldots, 5000)
\end{aligned} \tag{13}$$

where ($\sim N(\mu, \sigma^2)$) notates the independent parameter which was assumed to be normally distributed with respective mean (μ) and variance (σ^2), and ($f\left(S \mid n_i, \sigma_{gel_i}, \varphi_i\right)$) is the GCS saturation function from Eq. (12). Fig. 4(a) shows the results of the uncertainty analysis for experimental data fitted using the power law saturation function. Fig. 4(b)

and Fig. 4(c) shows the results of the independent (non-grouped) analysis for the IC HPCs and HPCs, respectively. Inspection of these results show that the coefficient of variation associated with the use of a power law saturation function may not work well for lower degrees of saturation. The proposed saturation function was applied for the four IC HPC mixtures with a sample size of 21 individual specimens cut from 7 cylinders and resulted in a maximum COV of approximately 0.30. The analysis for the HPC mixtures (7 cylinders, 21 total samples) resulted in a maximum COV of approximately 35 % and had similar trends observed in the IC HPC mixtures. When performing analysis for individual concrete mixtures, the COV improved for mixtures that were tested to a DOS at which the air voids were entirely empty (DOS of approximately 55 %), while data sets that were stopped at higher DOS inherently contained more variability in fitting parameters. For this reason, it is recommended that future testing be extended to DOS of 0.50 or lower to minimize variation due to a lack of data. Additionally, follow up testing indicated that measurement of the saturation function on an entire 100 mm x 200 mm cylindrical specimen (as opposed to dividing the specimen into three pieces) was able to reduce the COV to 10 %.[48] This was largely associated with the elimination of the varying volumes of air throughout the height of a single specimen when divided into smaller pieces and the prevention of creating new internal absorptive surfaces from saw cutting through aggregates, which resulted in some anomalous measurements at very high DOS.

ELECTRICAL RESISTIVITY, FORMATION FACTOR, AND DIFFUSION COEFFICIENT

The remainder of this paper focuses on implementing the DOS relationships for interpreting electrical measurements. Three applications are demonstrated. First and most generally, the proposed saturation function was applied to sealed resistivity measurements to determine the saturated resistivity, formation factor, and intrinsic chloride diffusion coefficient (all defined at DOS of 100 %). Second, resistivity measurements on samples submerged in a simulated pore solution were used to determine the apparent formation factor and chloride diffusion coefficient at the nick point DOS (or matrix saturation). Last, a simplified approach is proposed using sealed resistivity to approximately measure the apparent formation factor and chloride diffusion coefficient at the nick point DOS without the requirement to submerge samples in simulated pore solution.

Measuring Sealed Resistivity and Using Saturation Function

The resistivity of a sealed specimen was used with the saturation function to calculate the formation factor (Eq. (5)). The formation factor can be used in quality control, specifications, and service life predictions.[58] For example, the project special provisions specified a charge passed of 1,500 C in the RCP test,[49] which has an equivalent formation factor of 575. The corresponding equivalent intrinsic chloride diffusion coefficient has also been proposed for use in specification for service life design and is 3.3×10^{-12} m^2/s by Eq. (3).[48] It can readily be seen that these mixtures surpassed either threshold (solid line in Fig. 6) between 30 d and 120 d of age. Any formation factor or intrinsic diffusion coefficient above this line exceeds the specified value.

While the solid line shown in Fig. 6 was based average measured values, the measured coefficient of variation (COV) can also be plotted to show the production variation for the formation factors and diffusion coefficients (with 95 % confidence chosen here) as indicated by the dashed lines in Fig 6. Using this approach, a reliability-based service limit state calculation that accounts for the uncertainty in the measurement and the material could be used.[48] The results in Fig. 6 indicate that only the IC HPC/HPC 1 and IC HPC 4 mixtures achieved the design threshold to a 95 % level of confidence based on the measurements made.[48]

Nick Point Resistivity Based on Submersion in a Simulated Pore Solution

The resistivity was measured periodically using samples submerged in a simulated pore solution. As the specimens absorbed moisture, the resistivity decreased until the sample reached a degree of saturation associated with the nick point (around 1 d). After reaching a local minimum, the resistivity measurements were observed to continue to change, being governed by the slow infilling of the air voids, increased hydration of the binder, and/or any leaching. Fig. 7 shows the measured resistivity and mass gain for specimens that were cured in the sealed condition for 550 d to 600 d. The results show that the absorption of fluid (increase in mass) was relatively small and the resistivity remained relatively constant. Table 3 lists the resulting resistivity at the nick point (i.e., the local minimum of the measured resistivity curve) and the corresponding apparent formation factor and diffusion coefficients. Fig. 8(a) shows the measured sealed resistivity (starting measurement of the experiment) and the resistivity at the nick point. The results indicate that the starting sealed resistivity for the submersion test was approximately 80 % of the resistivity at the nick point except for some specimens from the IC HPC/HPC 1 mixtures.

Simplified Procedure Based on Sealed Resistivity

It is proposed that the resistivity at the nick point may be estimated simply by measuring concrete specimens in the sealed condition (Fig. 5). The difference in degree of saturation between samples in the sealed condition and measurements on the same samples at the associated theoretical nick point (Eq. (9)) was between 5 % to 15 %, as shown in Fig. 8(b). This is consistent with estimations for conventional mixtures, assuming a degree of hydration of 70 % or lower.[48] The corresponding differences in resistivity were found to be 3.7 % using the nearest actual measurement from sealed specimens and 11.1 % when using the saturation function (Fig. 8(a)). The upper bound of deviation was observed for the well-aged samples tested under submersion, with an average reduction of 17.7 % excluding outliers.

The difference between sealed and nick point degree of saturation resistivity is directly proportional to the self-desiccation that occurs due to the chemical shrinkage of the binder. This is a value that varies slightly due to changes in chemical composition of the cement or changes in binder composition associated with the use of supplementary cementitious materials; however, it is generally approximately 0.07 ml / g on a mass basis of cement. The magnitude of the resulting effect on the saturation function is related to the w/cm and the size of the pores undergoing self-desiccation. For the purposes of daily quality control measurements on the same mixture for a given project, these effects are expected to be well-behaved and relatively small. It may therefore be permissible to approximately evaluate the fundamental performance characteristic of the concrete (suggested as the resistivity at the nick point)[48] by simply performing measurements on sealed specimens.

Using this approach, the specimens used for resistivity measurements can be tested in a sealed condition by storing them in cylinder molds or a similar method that prevents the loss of moisture due to drying. The resistivity can be continually measured over time, which can be automated and measured using internal electrodes. This eliminates the need to store samples in a simulated pore solution. This also enables determination of whether the specified material property is achieved without waiting to test at a specific age. These advantages may have value in accelerating materials acceptance testing or estimating performance and have the potential to simplify practice.

CONCLUSIONS

The electrical properties of concrete are being increasingly used to assess concrete resistance to fluid transport. Electrical measurements are strongly dependent on sample conditioning, which includes the degree of saturation. This paper presented two mathematical expressions for the degree of saturation ($f(S)$). A power law saturation function (previously proposed) was used; however, this function may not be the best way to describe air-entrained concretes. An alternative saturation function was developed in this paper that accounts for changes in degree of saturation between the air voids, the capillary pores, and the gel pores (i.e., the GCA function). The GCA function includes a shape parameter, (n), a new parameter that describes the curvature of the function, (φ), and the conductivity of the gel pores, (σ_{Gel}).

Full saturation of a sample (i.e., DOS = 100 %) is defined herein as the filling of all of the voids in the concrete with fluid, including the gel and capillary pores, the volume of voids created due to chemical shrinkage, and entrained or entrapped air. This requires vacuum saturation at a vacuum level of less than 1.3 kPa (10 Torr), which can be considered as full saturation with air voids being filled (and is similar to what is standard for the common RCP test method).[28] Sample conditioning of air-entrained concretes by submerging them in water results in an initial degree of saturation that is substantially different from full saturation (i.e., the air voids remain largely empty).

The uncertainty associated with applying the saturation function was assessed using the parametric bootstrap analysis method and Monte Carlo simulations. The power function had a greater measured uncertainty than the GCA function. The GCA function performed better at both high and low degrees of saturation. The resistivity of specimens submersed in simulated pore solution was measured as were sealed specimens. The sealed specimens have a degree of saturation that is similar to those at the nick point (matrix saturation), with an offset (a reduction) consistently only due to the self-desiccation of the binder.

ACKNOWLEDGEMENTS

This research was performed at Purdue University in the Pankow Materials Laboratory with funding provided by the Joint Transportation Research Program, SPR-3752. As such, the authors gratefully acknowledge all those who contributed and provided the resources to make this work possible. The results and discussions presented here are the opinions of the authors and do not necessarily represent the viewpoints of any organizations with which the authors have been associated.

REFERENCES

1. AASHTO T277-07. Standard Test Method for Electrical Indication of Concrete's Ability to Resist Chloride Ion Penetration. Washington, DC: American Association of State Highway and Transportation Officials; 2007.
2. NT Build 492. Chloride Migration Coefficient from Non-Steady-State Migration Experiments. Espoo, Finland: NORDTEST; 1999.
3. SIMCO Technologies Inc. STADIUM Lab 3.0 User Guide. Quebec City, Quebec, Canada: SIMCO Technologies Inc.; 2013.
4. AASHTO T358-15. Standard Method of Test for Surface Resistivity Indication of Concrete's Ability to Resist Chloride Ion Penetration. Washington, DC: American Association of State Highway and Transportation Officials; 2015.
5. AASHTO T402. Standard Method of Test for Electrical Resistivity of a Concrete Cylinder Tested in a Uniaxial Resistance Test. Washington, DC: American Association of State Highway and Transportation Officials; 2023.
6. ASTM C1876-19. Standard Test Method for Bulk Electrical Resistivity or Bulk Conductivity of Concrete. West Conshohocken, PA: ASTM International; 2019.
7. Magnusson CE, Smith GH. Electrolytic Corrosion in Reinforced Concrete. Proc Am Inst Electr Eng. 1911;30(5):939–63.
8. Magnusson CE, Izhuroff B. Effect of Electrolysis on the Compressive Strength of Cement and Concrete. Trans Am Inst Electr Eng. 1914;33(1):673–84.
9. Monfore G. The Electrical Resistivity of Concrete. Bulletin 224. Skokie, IL: Portland Cement Association Research and Development Laboratories; 1968. p. 35–48.
10. Whittington HW, McCarter J, Forde MC. The Conduction of Electricity Through Concrete. Mag Concr Res. 1981;33(114):48–60.
11. Gjørv OE, Vennesland ØE, El-Busaidy AHS. Electrical Resistivity Of Concrete In The Oceans. In: Offshore Technology Conference. Houston, TX; 1977. p. 581–9.
12. Torquato S. Bulk Properties of Two-phase Disordered Media. III. New Bounds on the Effective Conductivity of Dispersions of Penetrable Spheres. J Chem Phys. 1986;84(11):6345–59.
13. Sant G, Rajabipour F, Weiss WJ. The Influence of Temperature on Electrical Conductivity Measurements and Maturity Predictions in Cementitious Materials During Hydration. Indian Concr J. 2008;82(April):7–16.
14. Spragg R, Castro J, Nantung T, Paredes M, Weiss W. Variability Analysis of the Bulk Resistivity Measured Using Concrete Cylinders. FHWA/IN/JTRP-2011/21. West Lafayette, IN; 2011.
15. Weiss J, Snyder K, Bullard J, Bentz D. Using a Saturation Function to Interpret the Electrical Properties of Partially Saturated Concrete. J Mater Civ Eng. 2013 Aug;25(8):1097–106.
16. Olsson N, Baroghel-Bouny V, Nilsson LO, Thiery M. Non-saturated Ion Diffusion in Concrete – A New Approach to Evaluate Conductivity Measurements. Cem Concr Compos. 2013 Jul;40:40–7.
17. Nadelman EI, Kurtis KE. A Resistivity-Based Approach to Optimizing Concrete Performance. Concr Int. 2014;(2):50–4.
18. Spragg RP, Vilani C, Weiss WJ, Pourasee A, Jones S, Bentz D, et al. Surface and Uniaxial Electrical Measurements on Layered Cementitious Composites Having Cylindrical and Prismatic Geometries. In: Proceedings of the 4th International Conference on the Durability of Concrete Structures. 2014. p. 317–26.
19. Spragg R, Jones S, Bu Y, Lu Y, Bentz D, Snyder K, et al. Leaching of Conductive Species: Implications to Measurements of Electrical Resistivity. Cem Concr Compos. 2017 May;79:94–105.
20. Tashiro C, Ishida H, Shimamura S. Dependence of the Electrical Resistivity on Evaporable Water Content in Hardened Cement Pastes. J Mater Sci Lett. 1987;6:1379–81.
21. Olson R, Christensen B, Coverdale S, Ford G, Moss M, Jennings H, et al. Interpretation of the Impedance Spectroscopy of Cement Paste via Computer Modelling: Part III Microstructural Analysis of Frozen Cement Paste. J Mater Sci. 1995;30:5078–86.
22. Morris W, Moreno EI, Sagüés AA. Practical Evaluation of Resistivity of Concrete in Test Cylinders Using a Wenner Array Probe. Cem Concr Res. 1996;26(12):1779–87.

23. Hunkeler F. The Resistivity of Pore Water Solution - A Decisive Parameter of Rebar Corrosion and Repair Methods. Constr Build Mater. 1996;10(5):381–9.
24. McCarter WJ, Garvin S. Dependence of Electrical Impedance of Cement-based Materials on Their Moisture Condition. J Phys D Appl Phys. 2000;22:1773–6.
25. Rajabipour F, Weiss WJ, Shane JD, Mason TO, Shah SP. Procedure to Interpret Electrical Conductivity Measurements in Cover Concrete During Rewetting. J Mater Civ Eng. 2005;17(5):586–94.
26. Rajabipour F. Insitu Electrical Sensing and Material Health Monitoring in Concrete Structures. Doctoral Dissertation. Purdue University; 2006.
27. Bentz DP. A Virtual Rapid Chloride Permeability Test. Cem Concr Compos. 2007 Nov;29(10):723–31.
28. Bu Y, Spragg R, Weiss WJ. Comparison of the Pore Volume in Concrete as Determined Using ASTM C642 and Vacuum Saturation. Adv Civ Eng Mater. 2014 Dec 31;3(1):308–15.
29. Spragg R, Bu Y, Snyder K, Bentz D, Weiss J. Electrical Testing of Cement-Based Materials: Role of Testing Techniques, Sample Conditioning. FHWA/IN/JTRP-2013/28. West Lafayette, Indiana; 2013 Dec.
30. Rajabipour F, Weiss J, Abraham DM. Insitu Electrical Conductivity Measurements to Assess Moisture and Ionic Transport in Concrete (A discussion of critical features that influence the measurements). Proceedings of the International RILEM Symposium on Concrete Science and Engineering: A Tribute to Arnon Bentur. Rilem. Paris, France; 2004.
31. Snyder KA. The Relationship Between the Formation Factor and the Diffusion Coefficient of Porous Materials Saturated with Concentrated Electrolytes : Theoretical and Experimental Considerations. Concr Sci Eng. 2001;3(12):216–24.
32. Yuan-Hui L, Gregory S. Diffusion of Ions in Sea Water and in Deep-sea Sediments. Geochim Cosmochim Acta. 1974;38(2):703–14.
33. Weiss WJ, Barrett TJ, Qiao C, Todak H. Toward a Specification for Transport Properties of Concrete Based on the Formation Factor of a Sealed Specimen. Adv Civ Eng Mater. 2016 Jul 29;5(1):179–94.
34. Isgor OB, Weiss WJ. A Nearly Self-sufficient Framework for Modelling Reactive-transport Processes in Concrete. Mater Struct. 2019;52(1):3.
35. ASTM C192/C192M-13. Standard Practice for Making and Curing Concrete Test Specimens in the Laboratory. West Conshohocken, PA: ASTM International; 2013.
36. Bu Y. Service Life Prediction of Concrete: Considerations of Specimen Conditioning and Testing Methods on the Measurement of Porosity and Diffusion Coefficient of Chloride. Doctoral Dissertation. Purdue University; 2014.
37. Li W, Pour-Ghaz M, Castro J, Weiss WJ. Water Absorption and Critical Degree of Saturation Relating to Freeze-Thaw Damage in Concrete Pavement Joints. J Mater Civ Eng. 2012;24(March):299–307.
38. Bu Y, Weiss J. Saturation of Air Entrained Voids and Its Implication on the Transport of Ionic Species in Concrete. In: 4th International Conference on the Durability of Concrete Structures. Purdue University West Lafayette, IN; 2014.
39. Todak H. Durability Assessments of Concrete Using Electrical Properties and Acoustic Emission Testing. Master's Thesis. Purdue University; 2015.
40. Federal Highway Administration. Considerations for Scalability of Alkali Concentrated Conditioning Solution. Washington, DC; 2024.
41. Poursaee A, Weiss W. An Automated Electrical Monitoring System (AEMS) to Assess Property Development in Concrete. Autom Constr. 2010;19(4):485–90.
42. Bentz DP. A Virtual Rapid Chloride Permeability Test. Cem Concr Compos. 2007;29(10):723–31.
43. Azad VJ, Isgor OB. Modeling Chloride Ingress in Concrete with Thermodynamically Calculated Chemical Binding. Int J Adv Eng Sci Appl Math. 2017;9(2):97–108.
44. Tuinukuafe A, Chopperla KST, Weiss J, Ideker J, Isgor B. Estimating Na+ and K+ Concentrations of the Pore Solution Based on Ex-situ Leaching Tests and Thermodynamic Modeling. RILEM Tech Lett. 2022 Oct 14;7:88–97.
45. Biever J, Chopperla K, Isgor O, Weiss W. Practical Measurement of Pore Solution Resistivity in Fresh Mixtures. ACI Mater J. 2023;120(5).
46. Weiss WJ. Prediction of Early-age Shrinkage Cracking in Concrete Elements. Doctoral Dissertation. Northwestern University; 1999.
47. Rajabipour F, Weiss J. Electrical Conductivity of Drying Cement Paste. Mater Struct. 2007;40:1143–60.
48. Barrett TJ. Improving Service Life of Concrete Structures Through the Use of Internal Curing: Impact on Practice. Doctoral Dissertation. Purdue University; 2015.
49. Barrett TJ, Miller AE, Weiss WJJ. Documentation of the INDOT Experience and Construction of the Bridge

Decks Containing Internal Curing in 2013. FHWA/IN/JTRP-2015/10. West Lafayette, IN: Joint Transportation Research Program, Indiana Department of Transportation and Purdue University; 2015.
50. ASTM C1585-11. Standard Test Method for Measurement of Rate of Absorption of Water by Hydraulic-Cement Concretes. West Conshohocken, PA: ASTM International; 2011.
51. Lucero C. Quantifying Fluid Transport in Cementitious Materials Using Neutron Radiography. Master's Thesis. Purdue University; 2015.
52. Jensen OM, Hansen PF. Water-entrained Cement-based Materials - I. Principles and Theoretical Background. Cem Concr Res. 2001 Apr;31(4):647–54.
53. Lura P. Autogenous Deformation and Internal Curing of Concrete. Delft: Delft University Press; 2003. p. 189.
54. ASTM C642-06. Standard Test Method for Density, Absorption, and Voids in Hardened Concrete. ASTM Int West Conshohocken, PA, USA. 2006;
55. Archie GE. Classification of Carbonate Reservoir Rocks and Petrophysical Considerations. Am Assoc Pet Geol Bull. 1952;36(2):278–98.
56. Snyder K, Feng X, Keen B, Mason T. Estimating the Electrical Conductivity of Cement Paste Pore Solutions from OH−, K+ and Na+ Concentrations. Cem Concr Res. 2003 Jun;33(6):793–8.
57. Xi Y, Bažant ZP, Molina L, Jennings HM. Moisture Diffusion in Cementitious Materials Moisture Capacity and Diffusivity. Adv Cem Based Mater. 1994 Nov;1(6):258–66.
58. Spragg R, Qiao C, Barrett T, Weiss J. Assessing a Concrete's Resistance to Chloride Ion Ingress Using the Formation Factor. In: Poursaee A, editor. Corrosion of Steel in Concrete Structures. Elsevier; 2016. p. 211–38.
59. De la Varga I. Increased Fly Ash Volume and Internal Curing in Concrete Structures and Pavements. Doctoral Dissertation. Purdue University; 2013.

Table 1—Concrete mixture proportions as batched.

		IC HPC 1	HPC 1	IC HPC 2	HPC 2	IC HPC 3	HPC 3	IC HPC 4	HPC 4
w/cm		0.405	0.428	0.396	0.403	0.447*	0.422	0.465*	0.398
Cement		394	398	443	443	432	432	438	458
Fly Ash[1]		125	125	–	–	113	113	–	–
GGBFS[2]		–	–	99	98	–	–	120	125
Silica Fume	**[lb/cyd]**	25	25	25	25	17	17	25	25
Coarse Aggregate		1825	1834	1802	1802	1731	1724	1827	1798
Fine Aggregate		745	1222	780	1335	819	1338	851	1384
Lightweight Aggregate		329	–	346	–	420	–	507	–
Air Entrainer		1.20	1.70	0.59	0.59	0.89	0.95	1.14	1.10
HRWRA[3]	**[oz/cwt]**	15.00	13.25	5.45	5.47	9.49	10.08	14.92	14.17
MRWRA[4]		–	–	–	–	1.96	1.90	3.60	3.46
Retarder		1.99	3.77	2.99	3.00	–	–	–	–
Measured Air Content	**[%]**	6.5	7.1	5.1	5.2	1.8*	5.9	8.1	7.1
Slump	**[in]**	3.5	6.0	8.0*	7.0*	2.0	2.0	9.0*	9.0*
Paste Content	**[%]**	24.0	25.0	24.4	24.6	26.0*	25.2*	24.5	25.3*

*Indicates non-conformance to project special provisions
–Indicates no data
[1]ASTM C618 Class C, source properties available from De la Varga[59]
[2]Ground granulated blast furnace slag
[3]High-range water reducing admixture
[4]Medium-range water reducing admixture
1 lb / cyd = 0.593 kg / m^3, 1 oz / cwt = 0.65 mL / kg, 1 in = 25.4 mm

Table 2—Fitted saturation function parameters, initial degree of saturation, total volume of voids, and resistivity at saturation for the third pieces of specimens used to determine the saturation function.

Mixture	n	σ_{gel}	φ	Volume of Voids	Air Content	Saturated Resistivity (Ωm)
HPC 1	3.10	0.23	0.09	19%	7.1%	91
	2.01	0.17	0.15	19%	7.1%	88
	2.48	0.24	0.11	19%	7.1%	98
HPC 1	2.80	0.26	0.10	19%	7.1%	92
	3.01	0.23	0.08	20%	7.1%	81
	2.53	0.23	0.12	19%	7.1%	96
IC HPC 1	3.60	0.24	0.09	20%	6.5%	116
	2.56	0.17	0.14	22%	6.5%	91
	3.11	0.21	0.09	22%	6.5%	97
IC HPC 1	3.49	0.25	0.08	20%	6.5%	120
	2.50	0.18	0.12	20%	6.5%	110
	2.90	0.23	0.09	20%	6.5%	115
HPC 2	2.45	0.19	0.10	18%	5.2%	45
	3.53	0.11	0.23	19%	5.2%	47
	3.75	0.36	0.05	17%	5.2%	49
HPC 2	2.65	0.22	0.08	18%	5.2%	51
	2.20	0.17	0.11	17%	5.2%	49
	4.03	0.42	0.04	16%	5.2%	54
IC HPC 2	3.57	0.31	0.04	22%	5.1%	48
	3.19	0.11	0.17	20%	5.1%	46
	2.00	0.14	0.18	19%	5.1%	82
IC HPC 2	3.21	0.23	0.06	21%	5.1%	50
	3.14	0.10	0.17	20%	5.1%	46
	4.48	0.42	0.04	20%	5.1%	51
HPC 3	2.67	0.11	0.21	19%	5.9%	42
	3.82	0.09	0.27	18%	5.9%	40
	4.74	0.17	0.21	19%	5.9%	42
HPC 3	2.45	0.12	0.18	17%	5.9%	44
	3.73	0.07	0.26	18%	5.9%	37
	3.37	0.11	0.19	18%	5.9%	44
IC HPC 3	5.33	0.35	0.04	18%	1.8%	49
	3.66	0.17	0.08	19%	1.8%	46
	4.66	0.2	0.06	20%	1.8%	46
IC HPC 3	2.73	0.21	0.12	18%	1.8%	73
	6.00	0.08	0.14	19%	1.8%	46
	4.46	0.19	0.07	20%	1.8%	44
HPC 4	2.01	0.15	0.15	17%	7.1%	86
	2.05	0.08	0.28	17%	7.1%	76
	2.00	0.12	0.24	17%	7.1%	88
IC HPC 4	3.47	0.17	0.09	24%	8.1%	48
	4.25	0.17	0.21	23%	8.1%	50
	2.00	0.14	0.19	21%	8.1%	82

Table 3—Summarized results of the submersion test, where (ρ_{nick}) ($\Omega \cdot m$) is the nick-point resistivity, (F^*) (unitless) is apparent formation factor and (D^*) (10^{-13} m^2/s) is the corresponding chloride diffusion coefficient.

	IC HPC 1	HPC 1	IC HPC 2	HPC 2	IC HPC 3	HPC 3	IC HPC 4	HPC 4
ρ_{nick}	540	445	265	160	310	215	545	415
F^*	5300	4350	2600	1600	2975	2050	5000	4040
D^*	2.2	2.7	4.5	7.4	4.0	5.8	2.4	2.9

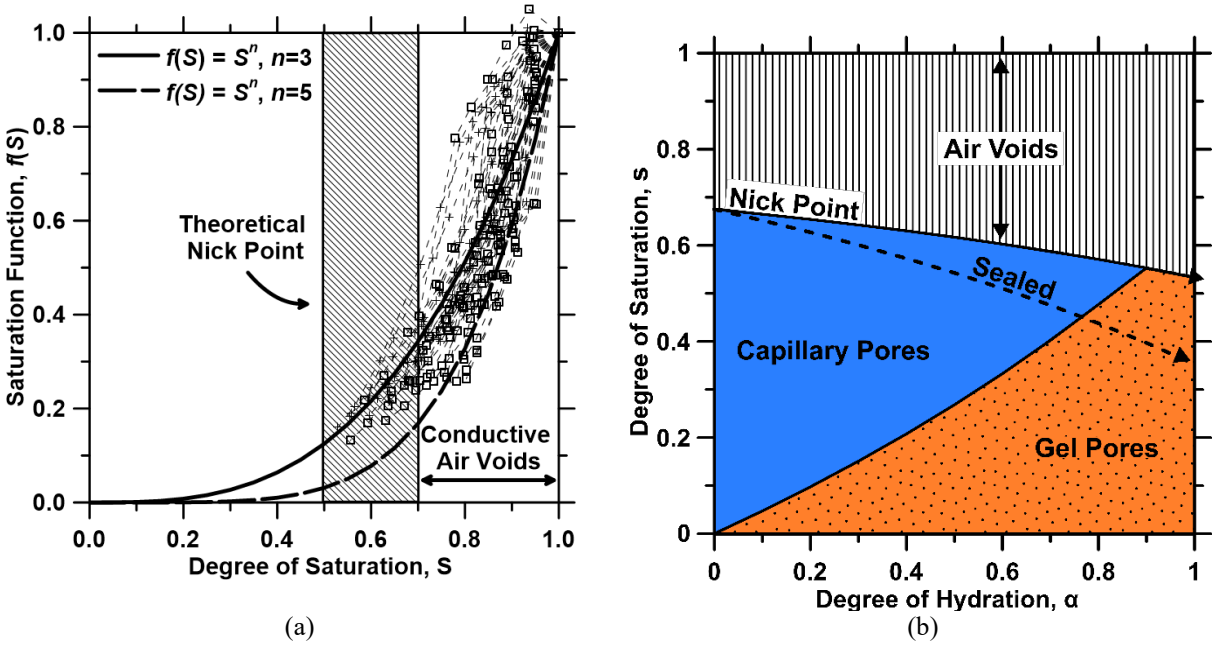

(a) (b)

Fig. 1—(a) Experimentally measured saturation function for IC HPC and HPC materials and (b) the contributions of each void type in the degree of saturation, shown as a function of the degree of hydration [33]. Source: FHWA.

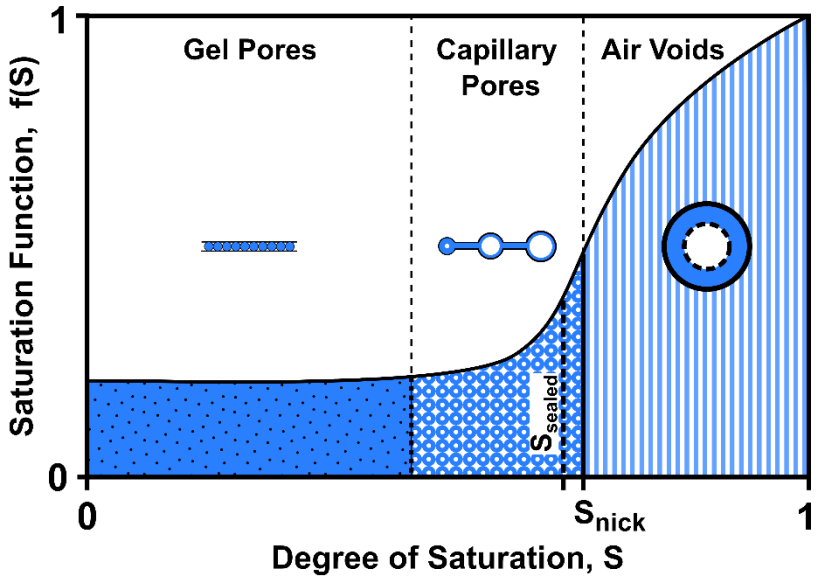

Fig. 2—Schematic representation of the proposed saturation function. Source: FHWA.

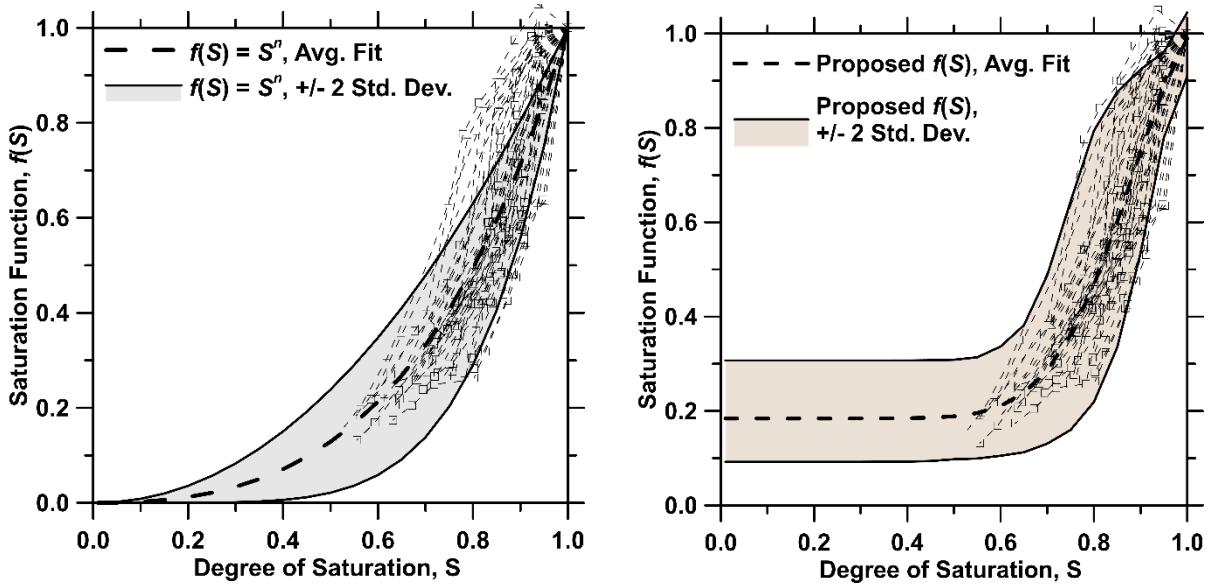

(a) (b)

Fig. 3—Demonstration of the range of (a) the power law saturation function and (b) the proposed saturation function. The shaded region represents the 95 % prediction interval for each saturation function. Source: FHWA.

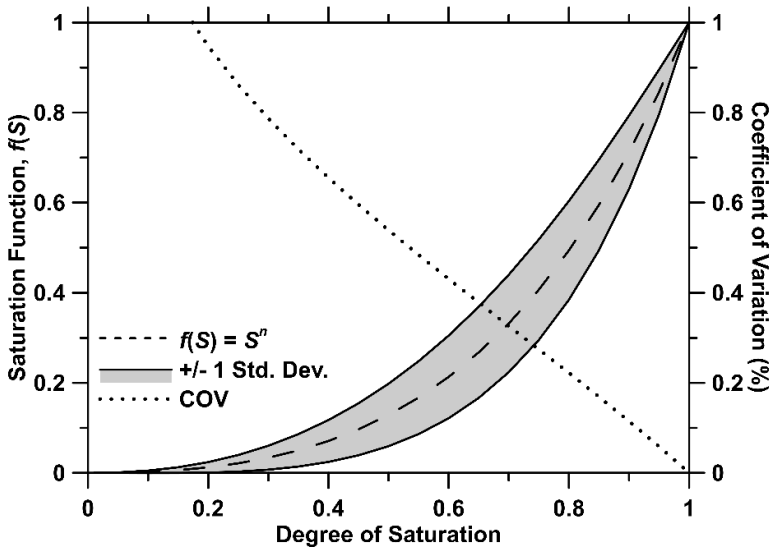

(a)

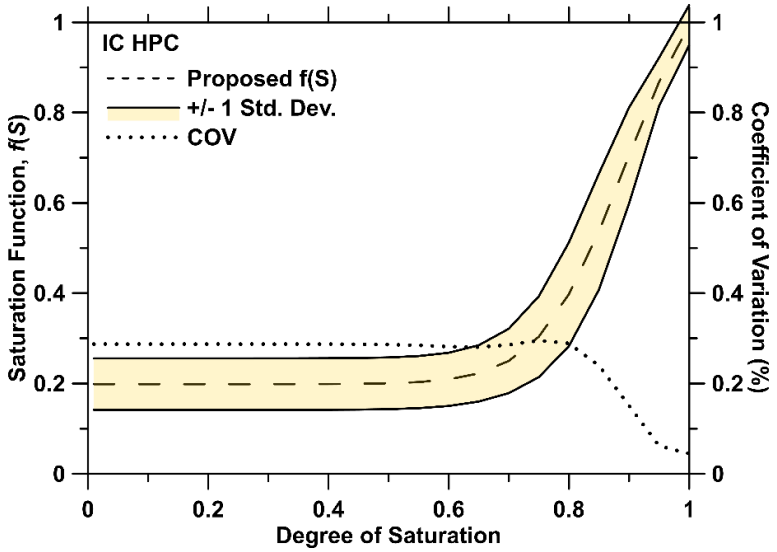

(b)

Fig. 4a, b—Results of uncertainty analysis to determine saturation function distribution and coefficient of variation for (a) all experimental data using a power law and the GCA function for (b) IC HPCs or (c) HPCs. Source: FHWA.

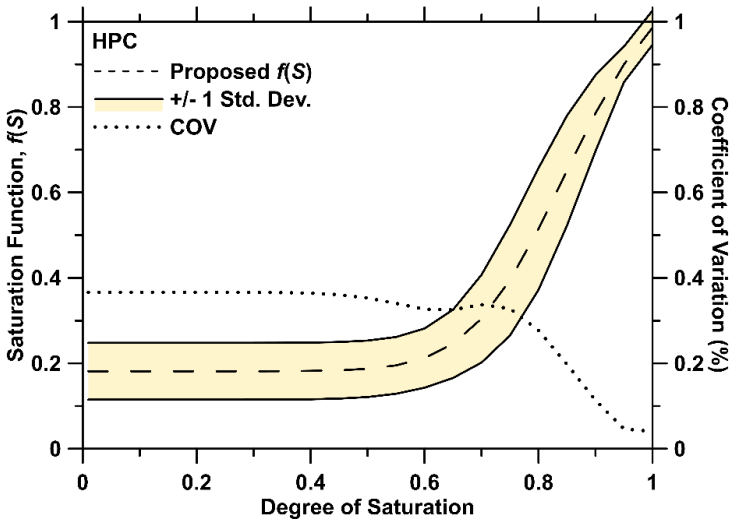

(c)

Fig. 5c—Results of uncertainty analysis to determine saturation function distribution and coefficient of variation for (a) all experimental data using a power law and the GCA function for (b) IC HPCs or (c) HPCs. Source: FHWA.

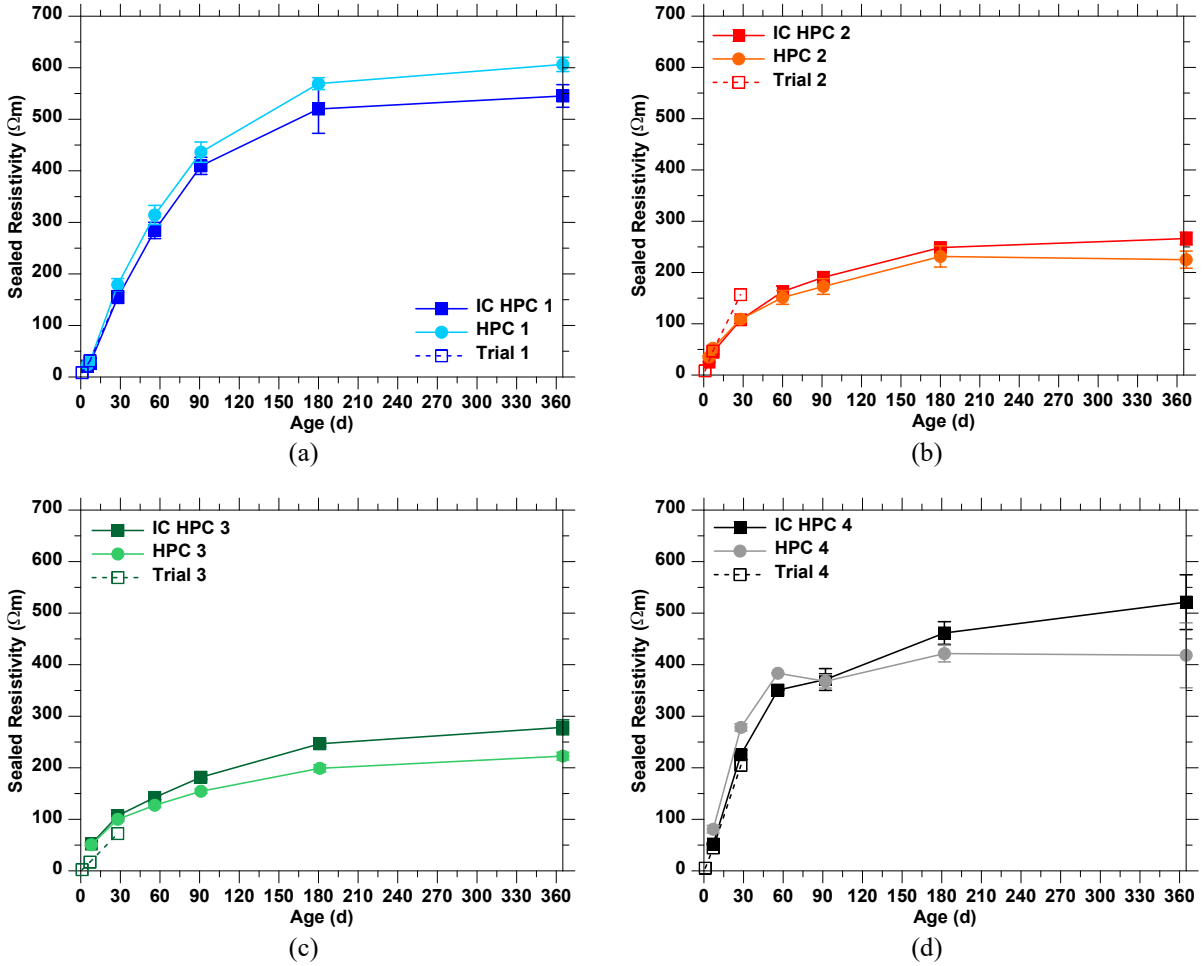

(a) (b) (c) (d)

Fig. 6—Sealed resistivity measurements for (a) IC HPC 1 and HPC 1, (b) IC HPC 2 and HPC 2, (c) IC HPC 3 and HPC 3, and (d) IC HPC 4 and HPC 4. Error bars indicate one standard deviation from the mean for n = 3 specimens. Source: FHWA.

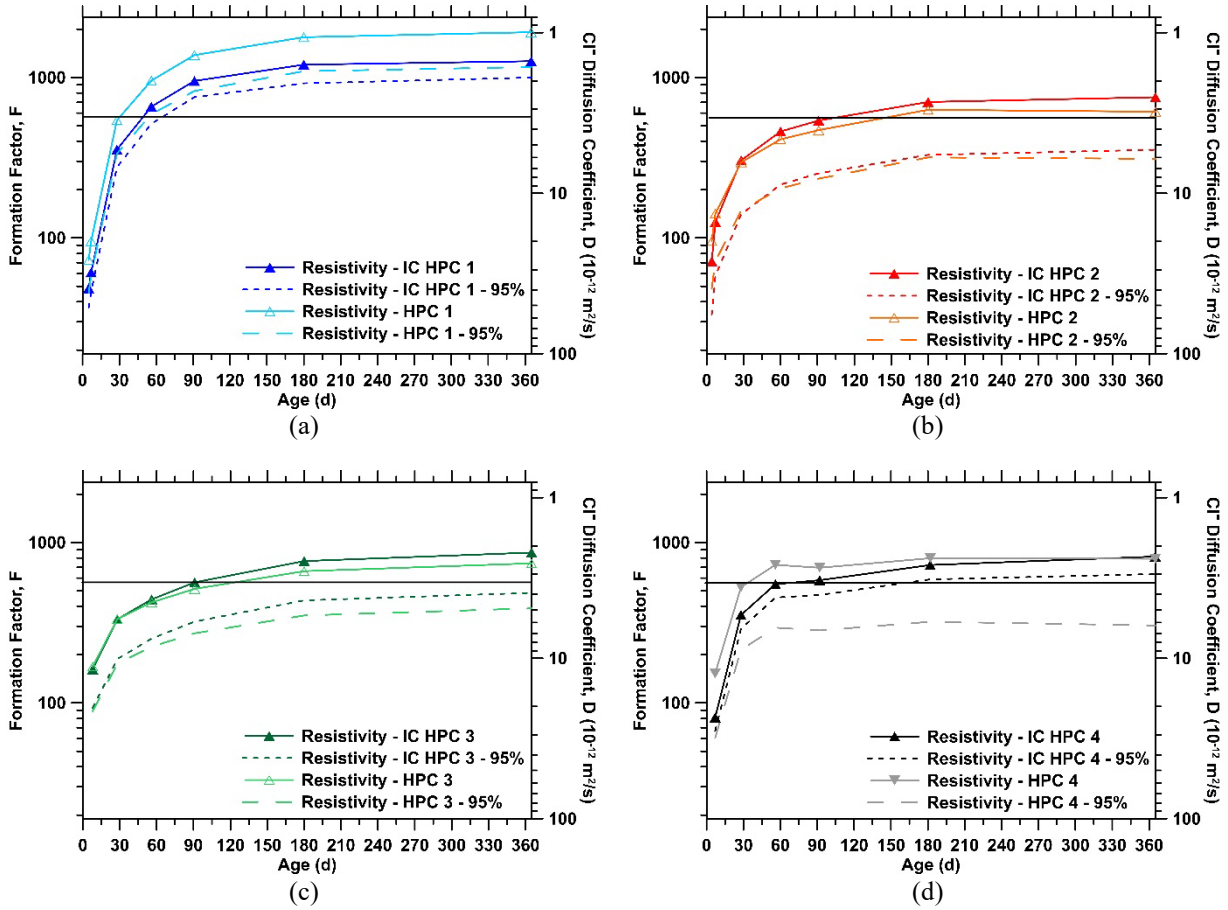

Fig. 7—Application of the saturation function to sealed resistivity measurements for (a) IC HPC 1 and HPC 1, (b) IC HPC 2 and HPC 2, (c) IC HPC 3 and HPC 3, and (d) IC HPC 4 and HPC 4. The horizontal line represents the project special provision specification for charge passed of 1,500 C in the RCP test, which has an equivalent chloride diffusion coefficient of 3.3 x 10^{-12} m^2/s. Dashed lines represent the 95 % confidence interval of the mean response. Source: FHWA.

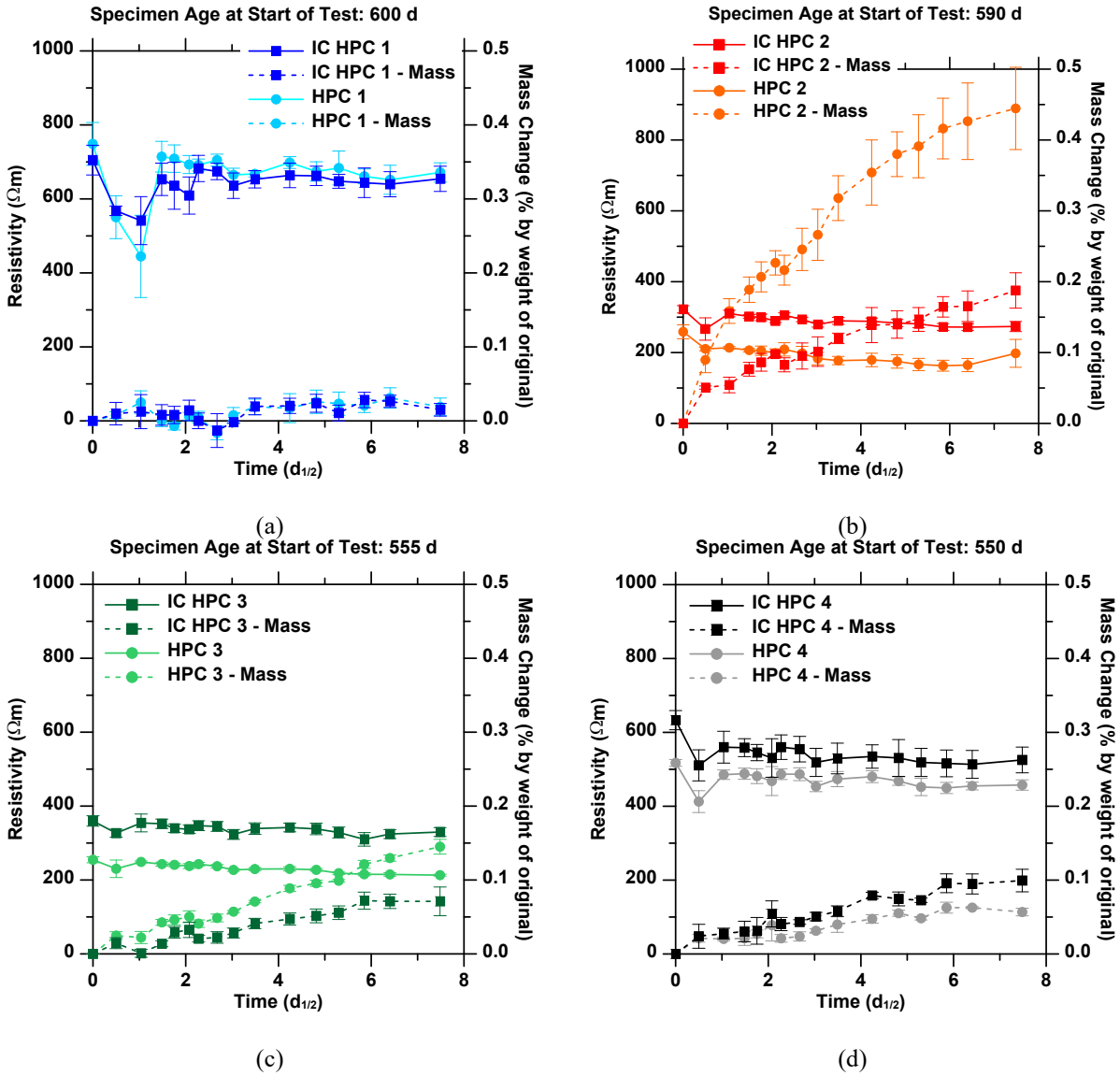

Fig. 8—Results of submersion testing for (a) IC HPC 1 and HPC 1, (b) IC HPC 2 and HPC 2, (c) IC HPC 3 and HPC 3, (d) IC HPC and HPC 4. Error bars indicate one standard deviation from the mean for n = 3 specimens. Source: FHWA.

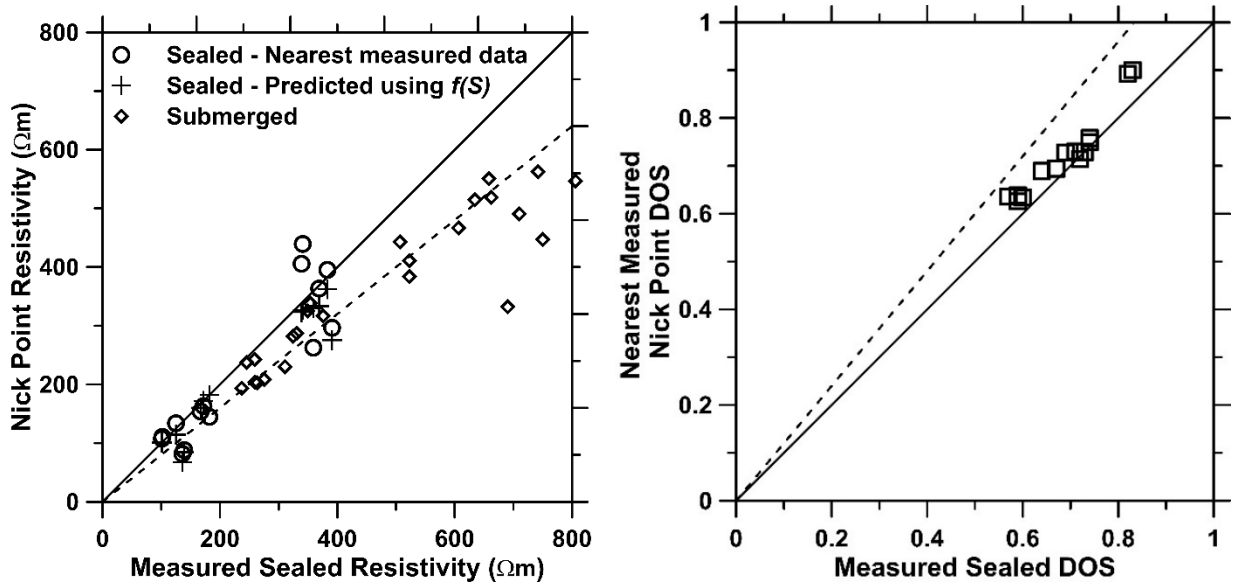

(a) (b)

Fig. 9—Comparison of (a) the average sealed resistivity and the average approximate nick point resistivity for sealed and submerged methods and (b) the corresponding measured degrees of saturation from the sealed method. The degree of saturation for the submerged test was not measured nor was any increase in the degree of hydration due to extended curing during testing. Solid lines represent equality, dashed lines represent a 20 % deviation from unity. Uncertainty of the sealed measurements may be taken from COV of the GCA saturation function, (*f(S)*), in Fig. 4. Source: FHWA.

Electrochemical Chloride Extraction: Mechanisms & Long-Term Impact

David Whitmore

Synopsis: Reinforced concrete is prevalent in construction for its strength and longevity. However, it can be susceptible to corrosion when exposed to chloride ions, particularly in areas affected by de-icing salts and marine environments. The technique known as Electrochemical Chloride Extraction (ECE) helps combat this corrosion by pulling chlorides away from the reinforcing steel and raising the concrete's pH around the steel. This paper examines the technique's development, the electrochemical reactions, and its effects on corrosion rates. Although ECE can dramatically lower chloride-induced corrosion, immediate post-treatment measurements often reveal increased corrosion rates as the passive oxide layer is re-established. A comparison of Linear Polarization Resistance (LPR) measurements before and after ECE illustrates the technique's effectiveness.

Keywords: cathodic protection, chloride-induced corrosion, concrete rehabilitation, corrosion mitigation electrochemical chloride extraction (ECE), electrochemical reactions, linear polarization resistance (LPR), steel-reinforced concrete, structural durability

ACI member **David Whitmore** is a Professional Engineer, NACE Cathodic Protection Specialist, and Founder/Chief Innovation Officer at Vector Corrosion Technologies. His career began in 1981, and in 1989, he led North America's first electrochemical chloride extraction project, which sparked his interest in corrosion and cathodic protection. Whitmore actively contributes to various ACI, ICRI, and AMPP committees, advancing industry knowledge in corrosion prevention and concrete rehabilitation.

INTRODUCTION

Reinforced concrete is extensively used in construction for its strength, durability, and cost-effectiveness. However, when exposed to chloride ions from sources such as de-icing salts or marine environments, the steel within concrete structures becomes susceptible to corrosion [3]. This corrosion results in the formation of expansive rust products, leading to cracks and spalling that compromise structural integrity. To address this issue, various rehabilitation methods have been developed, including electrochemical chloride extraction (ECE). This technique removes chlorides from the concrete and increases the pH surrounding the steel. ECE applies a high current density for a short duration, effectively mitigating corrosion and extending the lifespan of structures while reducing long-term maintenance costs. Although this method may be less labour-intensive and more economical than alternatives like cathodic protection, there are instances where the applied electric field may impact the concrete's chemistry and microstructure if industry standard procedures are not adhered to[3][4].

A brief history of electrochemical chloride extraction

ECE originated in the 1970s through initial studies by American researchers [14]. This technique was first studied by the Kansas Department of Transportation (KDOT) and Battelle Columbus Laboratories and both studies were funded by the Federal Highway Administration (FHWA) which offered a solution to costly maintenance problems [8][13][14]. By the 1980s, field tests were underway, and a Norwegian ECE patent was commercially released [10]

Since then, most ECE projects have focused on highway bridges and overpasses in North America and Europe. In these regions, chloride contamination primarily stems from de-icing salts applied to roads during winter, which are then carried by vehicle tires onto concrete structures. Conversely, coastal areas, especially those where structures are directly exposed to salt water, have encountered challenges in applying ECE due to the impracticality of its methods in such environments [10]. Despite these limitations, ECE remains a widely adopted technique for extending the service life of historic concrete bridges.

Theoretical background of electrochemical reactions in concrete

Electrochemical Reactions—Anodic dissolution and cathodic oxygen reduction are the two primary electrochemical mechanisms that take place when steel corrodes in concrete [5][6].

The anodic dissolution of iron occurs at the anode (reinforcing steel), as depicted in Eq. (1):

$$Fe \rightarrow Fe^{2+} + 2e^{-}$$

This reaction releases iron ions into the concrete pore solution and generates electrons [5][6].

The electrons produced at the anode migrate to the cathode, typically a non-corroding area of the steel, where they participate in the oxygen reduction reaction, as shown in Eq. (2):

$$O_2 + 4e^{-} + 2H_2O \rightarrow 4OH^{-}$$

This cathodic reaction consumes oxygen and water, generating hydroxyl ions that contribute to the alkalinity of the concrete. The combined action of these anodic and cathodic reactions leads to the formation of corrosion pits on the steel surface, which progressively worsen as the corrosion rate increases [3][6].

ELECTROCHEMICAL CHLORIDE EXTRACTION (ECE)

Electrochemical chloride extraction (ECE) is a corrosion mitigation technique that applies a direct current (DC) through concrete to remove chloride ions from the vicinity of reinforcing steel, halting further deterioration. This process also generates hydroxyl ions, which contribute to re-passivating the steel surface, and may produce hydrogen

gas at the cathode. At the external anode, water oxidation generates oxygen gas, and chloride ions may convert to hypochlorite. By carefully regulating the electrolyte's pH, potential damage to the concrete surface is minimized, ensuring a safer and more effective treatment.

ECE is one of two primary electrochemical treatments used to mitigate corrosion in reinforced concrete, alongside re-alkalization [3][4][5][6]. While re-alkalization restores the pH of carbonated concrete, reversing the effects of carbonation, ECE not only increases alkalinity but also removes chloride ions (Cl-), helping to restore the steel's passive layer and re-establish a protective alkaline environment [3][4].

The process involves attaching an external anode, typically made of titanium or steel, to the concrete surface and immersing it in a conductive electrolyte. This electrolyte, often a non-toxic, biodegradable paste, can be applied to various concrete orientations, including vertical, overhead, and horizontal surfaces [6]. When the DC electric field is applied, the anode becomes positively charged, while the reinforcing steel becomes negatively charged. This potential difference initiates a cathodic reaction at the steel surface, producing hydroxyl ions (OH-), which raise the pH and further stabilize the steel. Simultaneously, chloride ions are repelled from the steel and migrate through the concrete pores toward the anode, accumulating in the electrolyte. The combined effect of chloride removal and increased alkalinity strengthens the passive oxide layer, protecting the steel from further corrosion [3].

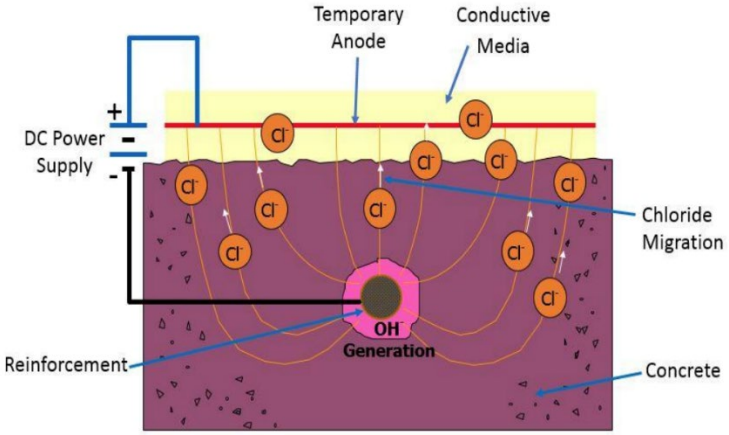

Figure 1: Visual diagram of ECE process, Electric Field Applied [15][16][17].

The efficiency of the external anode depends on its material composition. Consumable anodes, such as steel, degrade over time as they participate in the electrochemical reaction, whereas inert anodes, like titanium, remain stable, making them a preferred choice for long-term applications [1].

BURLINGTON SKYWAY CASE STUDY

The Burlington Skyway consists of two parallel high-level bridges that carry the Queen Elizabeth Way expressway over the Burlington Bay in Ontario, allowing Great Lakes freight vessels to pass beneath. The original bridge opened in 1958, followed by a second parallel bridge in 1985 to accommodate increasing traffic. Decades of exposure to de-icing salts from leaking deck joints led to chloride contamination of the reinforced concrete substructure, initiating corrosion of the steel reinforcement [17].

By the late 1980s, although chloride levels in the concrete had reached critical levels, the damage was largely limited to minor cracking and spalling, making the structure an ideal candidate for an innovative corrosion mitigation approach. In 1989, the Ontario Ministry of Transportation (MTO) approved a pilot demonstration of Electrochemical Chloride Extraction (ECE) on Pier S19 of the Burlington Skyway [11][15]. This trial marked the first North American application of the experimental Norwegian electrochemical treatment. The goal was to remove chlorides and restore

the passive layer on the steel reinforcement without requiring complete concrete removal or additional encasement [17].

Following eight years of monitoring, the success of the trial led to full-scale ECE implementation in 1997 and 1999. These projects treated 20,000 ft² (1,850 m²) of chloride-contaminated reinforced concrete substructure components, extending the service life of the bridge. The MTO later applied ECE to five additional bridges across Ontario, reinforcing its effectiveness as a corrosion mitigation technique [11].

Figure 2: Burlington Skyway, Burlington, Ontario, Canada [17].

Methodology

Effective system installation is essential for optimal performance. Before starting, ensure the concrete surface is cleaned, removing any coatings that could hinder current flow. Although ECE can conduct current through certain coatings, it's important to seal any open cracks or exposed steel with cement slurry, mortar, or non-conductive epoxy to avoid short circuits. Once the surface is ready, secure the external anode and apply the electrolytic paste (Figure 3). For the electrochemical process to function, the anode must be immersed in the electrolyte paste [15][17].

Connect the anode and reinforcing steel to the positive and negative terminals of a specially supplied AC/DC controllable rectifier. Once the rectifier is energized, ensure continuous operation, as ion migration occurs only in the presence of an electric field, after verifying that the electrochemical process has been sustained for a sufficient duration to raise the pH of the concrete and reduce the chloride concentration around the reinforcing steel, the electrolyte paste, and external anode are removed [15][17].

Figure 3: Application of anode and electrolyte (1989).

Installation

On July 4-5, 1989, the initial installation was performed on the west column's lower 13 feet (4 meters). Three sides of the square column were treated. The system was not applied to the north side of the column, leaving it as a control area. Initial readings revealed that chloride ion concentration at the reinforcement level averaged 4lb/yd^3 (0.106 percent by weight of concrete), considerably exceeding the typical corrosion initiation threshold values (Figure 4). Nevertheless, the pier remained mostly in good condition, with no visible cracks or delamination in the trial area, and the reinforcement was electrically continuous [11] [15-17].

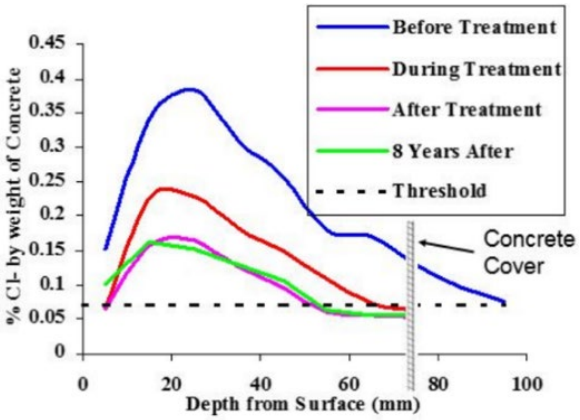

Figure 4: Representative chloride testing results for Pier S-19 before, during, and after the electrochemical treatment. [7][11][17].

Throughout the treatment, the electrochemical system was closely observed—often every day—to gather as much data as possible. Concrete cores were taken during and following the treatment, and it was determined that up to 87% of the chloride ions above the reinforcing steel had been removed from the concrete. Figure 4 displays typical chloride test results [11].

According to corrosion potential and corrosion rate measurements made using the linear polarization resistance method, the steel was corroding before treatment. 10% of the corrosion potential readings obtained on Pier S-19 were in the active corrosion range (more negative than -350 mV), and 90% of the measurements were in the uncertain range (between -200 and -350 mV (vs. $Cu/CuSO_4$)). Before treatment, no measurements were found in the passive region (more positive than -200 mV) [11][15][16][17].

Pre-treatment corrosion rates, as determined by a commercial linear polarization resistance device (3 LP), averaged 0.97 mA/ft^2(1.04 (1.04 mVuA/cm^2). Light corrosion on the reinforcing steel was confirmed by petrographic analysis of cores taken before treatment [11][15][16][17].

The initial area was treated in the autumn of 1989, and the Ontario Ministry of Transportation (MTO) has continuously monitored its condition. This first segment underwent treatment at a rate of 600–700 $A - hr/m^2$. Monitoring activities have included visual inspections, delamination surveys, corrosion potential surveys, coring to evaluate chloride ion remigration, and adjustments to various concrete parameters such as electrical resistivity and permeability process [11][15][16][17].

Table 1 summarizes the corrosion potential measurements for Pier S-19. Before treatment, corrosion potentials fell within the uncertain to active corrosion ranges, reflecting a mild to moderate level of corrosion. One year after the treatment was completed and the steel fully depolarized, all corrosion potentials on the treated surfaces were in the passive range (more positive than -200 $mV\ vs\ CuSO_4$). The data in Table 1 illustrates a significant decrease in corrosion activity due to the electrochemical treatment [11][15][16][17].

Long-term testing demonstrates the efficiency of the ECE treatment, and the concrete remains in good condition 30 years after treatment [17]

Table 1: Pier S-19 (1989) [17]

Percentage of Corrosion Potential Readings	North Face (Untreated)			South Face (Electrochemically Treated)		
	> -200 mV	-200 to -350	<-350	> -200 mV	-200 to -350	<-350
Pre-Treatment	0	85	15	0	96	4
1 Yr. After	41	59	0	100	0	0
2 Yr. After	41	59	0	100	0	0
3 Yr. After	26	74	0	96	4	0
4 Yr. After	26	70	4	96	4	0
5 Yr. After	19	74	7	96	4	0
6 Yr. After	26	59	15	93	7	0
7 Yr. After	30	63	7	96	4	0
8 Yr. After	11	78	11	93	7	0
15 Yr. After	0	74	26	100	0	0
20 Yr. After	25	75	0	100	0	0

Electrochemical treatments improve the electrical resistivity of concrete and reduce its permeability due to the formation of low-solubility calcium compounds within its pores. The MTO gathered concrete cores from Pier S-34 and the South Abutment both before and after the ECE treatment. The MTO materials lab analyzed these cores to assess their electrical resistance and air permeability. Consequently, the surface permeability of the concrete diminished, while its bulk electrical resistance significantly increased [15][16].

CASE STUDY RESULTS

Impact of electrochemical chloride extraction on corrosion rates

The effect of electrochemical chloride extraction (ECE) on steel corrosion rates in concrete has been extensively studied, yet the outcomes can be complex and varied. In the 1990s, using linear polarization resistance techniques, [2] observed that before the ECE treatment, corrosion rates of laboratory samples (Figure 5) ranged from 80 to 350 mA/m². Following the treatment, the corrosion rate spiked to 3.2 A/m² but then dropped to 80 mA/m² after 21 days [3].

The explanation for this outcome lies in the effects ECE has on local conditions surrounding the steel rebar. Green et al. concluded that the ECE process led to localized oxygen depletion and an increase in pH at the steel-concrete interface, attributed to oxygen reduction and water hydrolysis, respectively [2]. This elevated pH could cause temporary increases in the corrosion rate, although it remained lower than the active corrosion rates typically induced by the presence of chlorides. The higher pH resulting from cathodic polarization likely produced magnetite (Fe_3O_4) as a corrosion product due to the oxygen and water deficiencies brought about by the ECE process. This observation aligns with findings by Odden and Buenfeld and Broomfield [7][9], who noted the presence of black-brown rust on steel surfaces following extraction treatment (Figure 5).

It is further suggested that corrosion rate measurements taken immediately after ECE likely overestimated the equilibrium corrosion rate, as the system had not yet fully stabilized [3]. Oxygen replenishment and the restoration of the stable passive oxide film, along with equilibrium pH levels at the steel-concrete interface, were identified as potential areas for future investigation. Furthermore, the study highlighted that corrosion rates prior to treatment were averaged over the total steel area, while chloride-induced corrosion is highly localized, typically affecting less than 10% of the steel surface. This implies that the actual corrosion rates in pitted areas were likely much higher than what was reported prior to ECE, whereas the post-treatment values better represented the overall corrosion behaviour.

Although ECE can reduce corrosion rates, the immediate post-treatment period may exhibit elevated rates due to the re-establishment of the passive oxide film following ECE treatment. Long-term effects and the actual equilibrium corrosion rates require additional time to be established, as the pH around the steel stabilizes, particularly in a wet, low-oxygen environment [7].

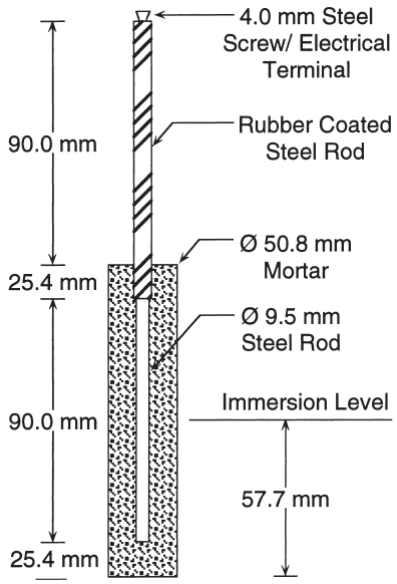

Figure 5: Schematic diagram of cylindrical mortar specimens showing dimensions and key features. [7]

Comparison of linear polarization resistance measurements before and after electrochemical chloride extraction

Linear polarization resistance (LPR) measurements provide insight into the corrosion rate of steel-reinforced concrete and can be used to assess the effectiveness of electrochemical chloride extraction (ECE). Before ECE treatment, corrosion rates may appear passive based on initial data, which defines corrosion rates below 1 mA/m² as representing passive conditions. However, this assumption may be misleading for chloride-contaminated specimens [7], as this is an average measurement that may not represent the actual corrosion rate in pits.

When the observed corrosion current was adjusted to account for the fact that corrosion only occurred on approximately 5% of the steel's polarized surface area, it became clear that all specimens containing chloride were actively corroding prior to the extraction treatment. This finding highlights the importance of considering localized corrosion when interpreting pre-treatment LPR data.

After ECE, corrosion rates remained significant one-month post-treatment, as re-establishing equilibrium conditions takes time. The treatment electrochemically depleted the dissolved oxygen in the concrete pore solution, and it requires time for oxygen to return to equilibrium and for the passive oxide film to reform, especially in wet or saturated environments.

The comparison of LPR measurements before and after ECE highlights the complexities of assessing the treatment's true impact on long-term corrosion behavior unless sufficient time is allowed for equilibrium to be re-established.

CONCLUSION

Electrochemical chloride extraction effectively addresses chloride-induced corrosion in steel-reinforced concrete. Although corrosion rates may seem to increase temporarily following treatment due to localized chemical alterations until the passive oxide layer regenerates, extensive research indicates that ECE can considerably prolong the lifespan of structures by diminishing corrosion over time. To enhance the treatment's efficiency and avoid potential negative impacts, it is crucial to manage the applied voltage and current carefully and to select suitable anode and electrolyte materials.

Pier S-19 of the Burlington Skyway has undergone regular monitoring for the last 30 years. In 1989, the deck joint above Pier S-19 was replaced (prior to the ECE treatment), and subsequent inspection reports showed no visible leakage through the joints for several years. However, in 2004, the inspection report indicated that the joint had failed, and chloride-contaminated water was leaking onto the pier once more. Throughout the 20-year period during which these readings were taken, corrosion potentials and rates have remained low, with none indicating localized or general corrosion activity.

REFERENCES

[1] Buenfeld, N.R. & Broomfield, J.P. (1994) Effect of chloride removal on rebar bond strength & concrete properties, in: R.N. Swamy (Ed.), Proceedings of the Conference on Corrosion and Corrosion Protection of Steel and Concrete, Vol. 2, Sheffield Academic Press, pp. 1438–1450.

[2]Green, W.K., Lyon, S.B., Scantlebury, J.D. (1993) Electrochemical Changes in Chloride-Contaminated Reinforced Concrete Following Cathodic Polarization, Corrosion Science 35, 1627-1631

[3] Ihekwaba, N., Hope, B., & Hansson, C. (1996). Carbonation and Electrochemical Chloride Extraction from Concrete. Cement and Concrete Research, 26(7), 1095-1107.

[4] Ihekwaba, N., Hope, B., & Hansson, C. (1996). Pull-out and bond degradation of steel rebars in ECE concrete. Cement and Concrete Research, 26(2), 267–282. https://doi.org/10.1016/0008-8846(95)00210-3

[5] Ihekwaba, N., Hope, B., & Hansson, C. (1996). Structural Shape Effect on Rehabilitation of Vertical Concrete Structures by ECE Technique. Cement and Concrete Research, 26(1), 165-175.

[6] Marcotte, T. D., Hansson, C. M., & Hope, B. B. (1999). The effect of the electrochemical chloride extraction treatment on steel-reinforced mortar Part I: Electrochemical measurements. Cement and Concrete Research, 29 1555-1560.

[7] Marcotte, T. D., Hansson, C. M., & Hope, B. B. (1999). The effect of the electrochemical chloride extraction treatment on steel-reinforced mortar Part II: Electrochemical measurements. Cement and Concrete Research, 29 1561-1568.

[8] Morrison, G.L., Virmani, Y.P., Stratton, F.W., and Gilliland, J. (1976). Chloride Removal and Monomer Impregnation of Bridge Deck Concrete by Electro-Osmosis, Report No. FHWA-KS-RD 74-1, Kansas Department of Transportation, Topeka, KS.

[9] Odden, L., (1994) The re-passivating effect of electrochemical realkalisation and chloride extraction, in: R.N. Swamy (Ed.), Proceedings of the Conference on Corrosion and Corrosion Protection of Steel and Concrete, Vol. 2, Sheffield Academic Press, 1473–1488.

[10] Palmer, T., Goncalves, H. S., & McGuiness, B. (2013) Electrochemical Chloride Extraction: Re-injecting Sustainability Into The Australian Market, CIA Conference

[11] Pianca, F., Shell, H., Lai, D. & Raven, R. (2003). The Ministry of Transportation of Ontario's Experience With Electrochemical Chloride Extraction (ECE) 1989-2002, Corrosion 2003, Paper 03294.

[12] Rasheeduzzafar, Ali, M. G., & Al-Sulaimani, G. J. (1993). Degradation of bond between reinforcing steel and concrete due to cathodic protection current. ACI Materials Journal, 90(1), 8-15.

[13] Slater, J.E., Lankard, D.R., and Moreland, P.J. (1976). "Electrochemical Removal of Chlorides from Concrete Bridge Decks," Transportation Research Record 604, 6–15, Transportation Research Board, Washington, DC

[14] Sohanghpurwala, A., & Scannell, W. T. (2011). Long-Term Effects of Electrochemical Chloride Extraction on Laboratory Specimens and Concrete Bridge Components. https://rosap.ntl.bts.gov/view/dot/41677

[15] Whitmore, D. (1996). Electrochemical Chloride Extraction from Concrete Bridge Elements: Some Case Studies. NACE, Corrosion 96, Paper No. 299.

[16] Whitmore, D. (1998). Rapid Electrochemical Treatment of Concrete: A Short Term Process can Give Long Term Benefits. NACE, Corrosion 98, Paper No. 656.

[17] Whitmore, D., & Ball, C. (2022). Burlington Skyway electrochemical chloride extraction – 30 years later. Cathodic & Anodic Protection. Paper presented at the AMPP Annual Conference + Expo, San Antonio, Texas, USA

Service Life of Reinforced Concrete Structures in Coastal Environments

Ceki Halmen, David Trejo, Momn Telfah

Synopsis: Corrosion of reinforcement is a common deterioration problem for reinforced concrete structures at coastal areas causing early failure, increased maintenance costs, and significant safety problems. This paper combines a well-established diffusion-based service life estimation method with recently developed data-driven models on surface chloride concentration accumulation and critical chloride threshold distribution data to probabilistically analyze the effect of design parameters such as water-cement ratio (w/c), cover depth, and admixed chloride content in various coastal exposure zones. Results indicate that the used probabilistic analysis can result in changes to estimated service life values by an order of magnitude. Although w/c and cover depth were the most significant factors affecting the service life, parameters such as wind speed, temperature, exposure zone, and distance from the coast were identified as influencing the service life of coastal structures.

Keywords: Corrosion, service life, marine environment, probabilistic, allowable chlorides, exposure conditions

ACI member **Ceki Halmen** is an Associate Professor at the University of Missouri-Kansas City. He received his BS in civil engineering from Bosphorus University, Istanbul, Turkey, and his MS and PhD from Texas A&M University, College Station, TX. He is a member of ACI Committees 201, Durability of Concrete; and 222, Corrosion of Metals in Concrete.

David Trejo, FACI, is Professor and Hal D. Pritchett Endowed Chair in the School of Civil and Construction Engineering at Oregon State University. He is past Chair of ACI Committee 222, Corrosion of Metals in Concrete, and a member of ACI Committees 201, Durability of Concrete; and 236, Material Science of Concrete. His research interests include corrosion of steel in cementitious materials, service life analyses, innovative concrete materials and systems for improved construction, and modeling deterioration mechanisms

INTRODUCTION

Corrosion of steel reinforcement is one of the main deterioration mechanisms causing damage and early failure of reinforced concrete structures. In good quality concrete, reinforcement steel is unlikely to corrode due to the formation of a thin protective oxide film (passive film) in the highly alkaline concrete pore solution environment.[1] Steel reinforcement remains passive as long as the high alkalinity of concrete pore solution is sustained. However, the passive film can break down causing initiation of active corrosion due to two major causes; presence of a threshold amount of chlorides at the steel/concrete interface and a reduction in alkalinity of the concrete cover due to carbonation.[2] Although both are important causes, in coastal environments, chloride induced corrosion is the most common problem due to chloride exposure, both from the water and carried by water in the air.[3] These chlorides accumulate on the concrete surface and penetrate the concrete deeper over time. When the chloride content at the steel reinforcement surface reaches a certain threshold value, called the critical chloride threshold, the protective passive film gets disturbed and corrosion is believed to initiate in the presence of moisture and oxygen.[4] Especially in windy and dry coastal climates, such as Florida and the North Peninsula of Yucatan, corrosion may be aggravated.[5] A recently published report on the collapse of Champlain Towers South in Florida includes many references to corrosion's role in the deterioration of buildings, which can accelerate in salt air environments.[6]

Poor design decisions and inadequate construction practices, especially in coastal regions, can decrease protection of reinforced concrete structures from corrosion, decrease their service life, which consequently affects their sustainability and safety. Designers and owners need methods to help them understand the effects of certain decisions, such as water cement ratio (w/c) of concrete or cover depth of reinforcement, on the service life of structures. This paper aims to provide such a methodology for designers based on recently published data and developed models to improve their understanding and help them make better informed decisions.

BACKGROUND AND METHODOLOGY

Although different limit states can be used to define the end of service life of a structure, typically the initiation of reinforcement corrosion due to chloride concentration reaching the critical chloride threshold at the cover depth is accepted as the end of service life.[7] In certain cases, the time period from the initiation of corrosion to the cracking of concrete, a.k.a. the corrosion propagation period, can be a significant part of the service life and multiple researchers have developed models to estimate the length of propagation period.[8-10] In this paper, service life is defined as the time until the initiation of corrosion but these values can be further combined by engineers with existing corrosion propagation models to make feasibility analysis and design decisions.

Time dependent transport of accumulated chlorides from the concrete surface into the concrete can be modelled using a diffusion model based on Fick's second law.[11] This models can estimate the chloride concentration various concrete depths at different times under the influence of a surface chloride concentration. In addition to chlorides penetrating from the external environment, typical concrete mixtures will also have chlorides that were introduced from the constituent materials, in the water, cement, and aggregates. These chlorides are referred to as initial chlorides or admixed chlorides. The diffusion model modified to include the effect of initial chloride content of concretes is shown in Eq. 1[12]

$$C_{(x,t)} = C_i + (C_s - C_i)\left(1 - \text{erf}\left(\frac{x}{2\sqrt{D\,t}}\right)\right) \quad \text{Eq. 1}$$

Where $C_{(x,\,t)}$ denotes the chloride ion concentration at depth x and time t, C_i denotes the initial (admixed) chlorides, C_s denotes the surface chloride concentration, and D denotes the apparent diffusion coefficient of chlorides in concrete. Using the cover depth of reinforcement as x in Eq. 1, the chloride concentration at the reinforcement surface can be calculated for set C_s, C_i, and D values. Corrosion initiation time (service life) of concrete can then be calculated by finding the time that will set the chloride concentration at the reinforcement surface equal to the critical chloride concentration, C_{crit}. There are a couple of issues that need to be addressed when doing these calculations. The first issue is that C_{crit} and $C_{(x,\,t)}$ are not deterministic values but distributions. Therefore, setting them equal can significantly overestimate the service life. Additionally, C_s and D values are not constants but functions of time. These issues are addressed in the following sections.

Distribution of Critical Chloride Threshold, C_{crit}

Currently there is no standardized test method to determine the C_{crit} of a reinforced concrete system. A literature survey reported that 29 authors published a wide range of different C_{crit} values based on over 20 different test methods, criterion, and/or materials. The published C_{crit} data obtained using these different methods exhibits significant scatter and varies between ~ 0.1 and 3.1 % by weight of binder.[13] Important differences between the test methods used and differences between the physical and chemical properties of materials used in different studies contribute to the large scatter of published data. A recent multi-laboratory validation study sponsored by ACI committee 222, corrosion of metals in concrete, evaluated a critical chloride test method developed at Oregon State University and reported good repeatability and reproducibility.[14, 15] A follow up multi-laboratory study evaluated variability of observed C_{crit} distribution due to differences in sources of steel and cement and found that although different sources were increasing the variability of observed values, the difference in the mean C_{crit} value was statistically insignificant. Results showed that for ASTM 615 steel and Type I/II cement systems C_{crit} values were normally distributed with a mean value of 0.396% by weight of cement and a coefficient of variation (COV) of 39.1%.[16] It should be noted that the reported C_{crit} values were acid-soluble (total chloride) chloride contents. However, a later study reported that water-soluble chloride concentrations are sufficiently conservative even for cases when alkalinity of the concrete environment decreases and recommended the use of water-soluble chloride concentrations in standards for engineers evaluating service life of their structures.[17] Therefore in this study, water-soluble C_{crit} values were used to determine service life values. Water soluble C_{crit} is taken as a normal distribution with a mean of 0.336% by weight of cement with a COV of 39.1%. The acid soluble to water soluble conversion was performed based on their reported relationship in the literature.[18]

Distribution of Chlorides in Concrete

To compare the chloride concentration $C_{(x,\,t)}$ obtained at the cover depth with the C_{crit} distribution, we need to know about the variability of chloride concentration. Trejo and Vasudevan evaluated a group of 81 concrete samples for water soluble admixed chloride contents and observed that they exhibited a skewed distribution. The distribution was transformed to a normal distribution by using a square root transformation and the COV of the resulting normal distribution was reported to be 51.7%.[19] Another study evaluated the spatial distribution of chlorides in uncracked concrete subjected to homogeneous exposure using embedded potentiometric sensors and reported COV values between 30 and 70% for straight portland cement concrete mixtures with w/c between 0.4 and 0.6. [20] This study also reported that the variability of chloride concentration at a certain depth was not strongly affected by the exposure conditions (such as the surface chloride concentration). Observed variability was also similar to predicted variability values by a finite element analysis and primary cause of variability was the presence of coarse aggregates rather than w/c ratio, cement type, or exposure conditions.[21] In this paper we used a COV of 51.7% for distribution of chlorides at the cover depth but we also evaluated the impact of different COV values on the service life results.

Surface Chloride Concentration, C_s

As shown in Eq. 1, C_s of concrete provides a boundary condition for solving the diffusion equation based on Fick's law and can have a significant impact on the estimated service life values.[22] Therefore, accumulation of external chlorides on concrete surface was investigated and modeled by multiple researchers.[23-28] Some of these models ignore the time varying behavior of C_s and the rest use different time-varying functions such as square root , power, exponential, and logarithmic functions. Major service life estimation models, such as DuraCrete, LNEC E456, and JTS 153-2015 also include quantitative computational models for C_s of concrete in marine environments.[25] A recent study evaluated 929 sets of field test data and developed a reciprocal time varying multi factor model for C_s as shown in Eq. 2.[27]

$$C_s = \beta \cdot A_{cb} \cdot R_{\frac{w}{b}} \cdot \left(\frac{\alpha \cdot A_{ct} \cdot t}{1 + \alpha \cdot A_{ct} \cdot t}\right)\left(1 - e^{-\theta_1 C_{sw}}\right) \cdot e^{-\theta_2 d} \cdot (\theta_4 \nu)^{\theta_3} \quad \text{Eq. 2}$$

Where α and β are fitted model parameters based on the exposure zone, $R_{w/b}$ denotes the water binder ratio, t is time, and C_{sw}, d, and ν denote water salinity, distance from the shore, and wind speed, respectively. A_{cb} and A_{ct} are dimensionless parameters related to cementitious material type of concrete. The units for θ_1 and θ_2 are m^{-1} and s/m, respectively and θ_3 and θ_4 are again dimensionless parameters. The values of the fitted parameters and A_{cb} and A_{ct} are defined for four different exposure zones: tidal zone, splash zone, submerged zone, and atmospheric zone. The model requires salinity of the water as an input for the submerged zone and the distance from the shore and wind speed for the atmospheric zone. This model was validated using 456 sets of data that were not used for the development of the model and compared with other existing models. This model was reported to have a better accuracy compared to other models including the DuraCrete, JTS, and the Life-365 models. This paper will use the time varying multi factor model shown in Eq. 2 to estimate the C_s values at different time intervals and will use the estimated values in Eq. 1 to calculate the service life of structures in 4 different exposure zones. In the submerged zone, corrosion mainly depends on the diffusion of chlorides and salinity of water is a significant factor. In tidal and splash zones, migration of chlorides are mainly driven by capillarity and diffusion and continuous wetting and drying cycles exacerbate the accumulation of chlorides within the concrete. In the atmospheric zone corrosion is influenced by factors such as salt spray deposition, wind speed, humidity, temperature, rainfall, coastal distance, and building orientation and exhibits the most complex diversity.[28]

Diffusion Coefficient, D

Diffusion coefficient that is used in Eq. 1 is strongly related to the permeability of concrete which is mostly determined by w/c for ordinary portland cement concrete. The Life-365 service life software uses Eq. 3 shown below to estimate the diffusion coefficient of concrete at 28 days.[29]

$$D_{ref} = 1x10^{(-12.06+2.4\cdot\frac{w}{c})} \quad \text{Eq. 3}$$

Where D_{ref} is the diffusion coefficient for chloride ions at 28 days in m^2/s, and w/c is the water cement ratio. As a result of continued hydration reactions in concrete, over time the diffusion coefficient decreases with pore structure refinement. The change in diffusion coefficient over time can be calculated with the relation shown in Eq. 4[29, 30]

$$D(t) = D_{ref}\left(\frac{t_{ref}}{t}\right)^m \quad \text{Eq. 4}$$

Where $D(t)$ is the diffusion coefficient at time t, and D_{ref} is the reference diffusion coefficient measured at time t_{ref}. The diffusion decay coefficient, m, defines the reduction in diffusion coefficient with time. A study evaluated the decrease of diffusion coefficient values for ordinary portland cement mixtures at different w/c's and established the empirical formula for the decay factor shown in Eq. 5.[31]

$$m_{OPC} = 0.06\left(\frac{w}{c}\right)^{-1.66} \quad \text{Eq. 5}$$

In this study, when calculating the service life values of reinforced concrete structures with different w/c values, equations 3, 4, and 5 were used to estimate the diffusion coefficient and its variance over time. If the service life increased beyond 25 years, hydration and pore refinements were assumed to be complete and the diffusion coefficient at 25 years was taken as a constant. In addition to changing with time, the diffusion coefficient of concrete is also affected by the ambient temperature and may cause differences in observed corrosion initiation times at different geographic locations.[30, 32] To account for the effect of ambient temperature, the diffusion coefficient at a time *t* can be further modified using the Arrhenius equation shown in Eq. 6.[29]

$$D_{(t,T)} = D(t) \cdot e^{\frac{U}{R}\left(\frac{1}{T_{ref}} - \frac{1}{T}\right)} \quad \text{Eq. 6}$$

Where $D_{(t,\ T)}$ is the diffusion coefficient at time *t* and temperature *T*, $D(t)$ is the time adjusted diffusion coefficient, *U* is the activation energy of the diffusion process (35,000 J/mol), and *R* is the universal gas constant (8.31 J/mol K) and T_{ref} is 293 K.

Methodology

As stated earlier, in this paper, service life was defined as the time to initiation of corrosion, which takes place when the chloride concentration at the cover depth exceeds the critical chloride threshold. Service life of a reinforced concrete structure was calculated for 6 different cases in 4 coastal exposure zones; submerged, tidal, splash, and atmospheric at 15, 50, and 100 m (16.4, 54.7, and 109 yard) from the shore. Service life values were calculated using Eq. 1 and using daily incremental time steps. Additionally, calculations were performed at different initial (admixed) chloride concentrations to evaluate the effect of this parameter.

At each time step, the time-dependent surface chloride concentration, C_s, was calculated based on the exposure zone using Eq. 2. Water salinity was set to 3% by weight for the submerged zone and the wind speed was assumed to be 5 m/s (11.2 mph) for the atmospheric zone. At each time step, the diffusion coefficient was calculated using equations 3, 4, and 5 based on the w/c of concrete. To evaluate the effect of design decisions, 3 different w/c values (0.35, 0.4, and 0.5) and 3 different cover depths (25.4, 58, and 76.2 mm [1, 2.3, and 3 in]) were evaluated. Bulk of the analysis was performed using average monthly temperatures of a coastal location in Maine. The time-adjusted diffusion coefficients were adjusted for temperature using Eq. 6. Keeping all other variables constant, the effect of temperature was also evaluated in the atmospheric zone by using the monthly average temperature values of Keys area in Florida.

After setting the C_s, C_i, $D_{(t,\ T)}$, and cover depth (x) values at each time step, the chloride concentration at the cover depth, $C_{(x,\ t)}$ was calculated. This value was taken as the mean chloride concentration of a normal distribution curve at the cover depth with a COV of 51.7%. This distribution was compared to the C_{crit} distribution with a mean value of 0.336% and a COV of 39.1% using the probabilistic approach described by Trejo and Vasudevan.[19] Figure 1 shows how at each time step the calculated $C_{(x,\ t)}$ at the cover depth would increase with increasing variance based on the constant COV value. At each time step, the probability of chloride concentration at the cover depth exceeding the C_{crit} value, in other words probability of failure - P_f, can be calculated using the distribution shown in Eq. 7.

$$N\left[\left(C_{(x,t)} - \mu_{C_{crit}}\right), \left(\sigma^2_{C_{(x,t)}} + \sigma^2_{C_{crit}}\right)\right] \quad \text{Eq. 7}$$

Because the chloride concentration at the cover depth and the C_{crit} distribution are both normally distributed, their difference is also normally distributed as shown in Eq. 7. Time iteration was stopped when a limit probability of failure was reached to determine the service life. The typical service life determination method where $C_{(x,\ t)}$ is simply set equal to the mean C_{crit} value translates to using a limit probability of 50% when using this method, i.e. there is a 50% probability that the chlorides at the cover depth may be over the critical chloride threshold and 50% probability to be under. The effect of using different P_f values for service life determination is discussed in the results section.

RESULTS AND ANALYSIS

Figure 2 shows the calculated service life values at three different cover depths in tidal, splash, and submerged zones at three different water cement ratios. The service lives were calculated by setting the calculated chloride content at

each cover depth equal to the mean water-soluble critical chloride threshold value of 0.336% (i.e., P_f of 50% that the chloride level will be above the critical chloride threshold) and admixed chlorides were assumed to be zero. Although the service life values calculated at the tidal zone defines the lower boundary of service lives, the figure clearly shows that the w/c of the concrete and the cover depth have a much larger impact on the service life compared to the exposure zones. At a low cover depth of 25.4 mm (1 in), the service life values at all w/c's and at all zones are less than 5 years. Service life values are less than 10 years, even with a cover depth up to 76.2 mm (3 in), when using a w/c of 0.5. A service life of 10 years can be achieved only at a cover depth of 58 mm (2.3 in) or more when using a w/c of 0.4 and at the same cover depth using a w/c of 0.35 can increase the service life to about 30 years. As expected, longer service lives up to 50 years can be achieved using a combination of lower w/c and larger cover depths in the absence of supplementary cementitious materials, corrosion resistant reinforcement, or other measures such as liners.

Figure 3 shows the calculated service life values at three different cover depths and w/c values for the tidal zone where the shortest service life values were calculated. The values are calculated either by matching the chloride content at the reinforcement depth to the critical chloride threshold (50% P_f) or by calculating when the probability of chloride content being above the critical chloride threshold becomes 10% or more based on their probability distributions (10% P_f). Admixed chlorides are assumed to be zero. Although the difference between service life values due to different P_f values is not large when using a w/c of 0.5, the difference between the estimated corrosion initiation times at w/c of 0.4 at a cover depth of 58 mm (2.3 in) is about 5 years. This difference goes up to 13 years (~ 45% reduction) for a w/c of 0.35. The difference is almost 20 years when w/c of 0.35 with a cover depth of 76.2 mm (3 in) is used showing that using a failure probability of 10% is much more conservative than setting the chloride content at the reinforcement level equal to the critical chloride threshold.

Figure 4 shows the service life values calculated for the same cover depths in the atmospheric zone at 15, 50, and 100 m (16.4, 54.7, and 109 yard) distance from the shore. Service life values are calculated using 10% probability of failure and results are plotted for w/c's of 0.4 and 0.5. In this figure admixed chlorides are again assumed to be zero. For comparison, the service life values calculated for the splash zone are also shown on the figure. Service life increases with increasing distance from the shore, increasing cover depths, and decreasing w/c as expected. At a w/c of 0.5, corrosion initiation time for a structure 100 m (109 yard) from the shore is still lower than the splash zone at a w/c of 0.4, showing the importance of w/c of the concrete. At a w/c of 0.4 and a cover depth of 58 mm (2.3 in), corrosion initiation can be delayed to 25 years at 100 m (109 yard) from the shore. It is not shown on the figure but a service life of 60 years with a 10% failure probability, can be achieved at 100 m (109 yard) from the shore using a w/c of 0.35 and a cover depth of 58 mm (2.3 in). All the atmospheric service life values were estimated for a light breeze of 5 m/s (11.2 mph) assumption. At a w/c of 0.4 and cover depth of 58 mm (2.3 in) the service life can be increased by 120% by increasing the distance from 15 to 100 m (16.4 to 109 yard).

Figure 5 shows the service life values in tidal zone at three cover depth values. Service life values are calculated at two w/c (0.35, 0.4) using 10% and 50% probability of failure for two initial chloride contents of 0 and 0.08% by weight of cement. Dashed and solid lines show the 50% and 10% probability of failure and empty and solid markers indicate 0 and 0.08% admixed chlorides, respectively. Trejo and Vasudevan in their paper proposed an admixed chloride limit of 0.08% for exposure classes where structures are exposed to chlorides in the environment.[19] This figure shows that at w/c of 0.4 initiation of corrosion is accelerated by two years due to the presence of 0.08% admixed chlorides at a cover depth of 58 mm (2.3 in). The effect of admixed chlorides is the same whether 10 or 50% probability of failure is used. The effect of admixed chlorides is larger at w/c of 0.35 and they shortened the service life by 4 and 5 years using 50% and 10% probability of failure, respectively. The difference in service life goes up to 9 years for w/c of 0.35 using 10% probability of failure for a cover depth of 76.2 mm (3 in). At w/c of 0.5 the decrease in service life due to admixed chlorides is less than a year at all cover depths. This shows that the impact of admixed chlorides is negligible if the initial design provides a service life less than 5 years to begin with. Figure 6 shows the service life values in atmospheric zone at 50 and 100 m (54.7 and 109 yards) distance from the shore using 0 and 0.08% admixed chlorides. All values shown are for a w/c of 0.4. Dashed and solid lines show the 50% and 10% probability of failure and empty and solid markers indicate 0 and 0.08% admixed chlorides, respectively. In atmospheric zone 50 m (54.7 yard) from the shore and at a cover depth of 58 mm (2.3 in) the admixed chlorides shortened the service life by 6 (~ 43%) and 7 (~18%) years using 10% and 50% probability of failure, respectively. Like the tidal zone, probability of failure did not make a big difference in terms of effect of admixed chlorides.

However, for the atmospheric zone 100 m (109 yards) from the shore, admixed chlorides shortened the service life by 11 and 28 years using 10% and 50% probability of failure. Admixed chlorides of 0.08% decreased the service life in the atmospheric zone 100 m (109 yards) from the shore by about 56% which shows the importance of limiting the admixed chlorides especially when longer service lives are expected.

Figure 7 shows the decrease in calculated service life values in the splash and atmospheric zones with the increase in admixed chlorides using a 10% probability of failure criteria. Solid and dashed lines indicate the w/c values of 0.35 and 0.4 and all results are for a cover depth of 58 mm (2.3 in.) Results show that the initiation of corrosion becomes immediate when using 10% failure probability criteria at an admixed chloride content of 0.15% by weight of cement. The effect of admixed chlorides is more pronounced when permeability of concrete decreased by using a lower w/c ratio. Because the transport of chlorides is slowed down, existence of admixed chlorides results in larger percent decreases of estimated duration of corrosion initiation at lower w/c's. Results show that a service life of 15 years can be achieved for structures 100 m (109 yards) or more from the shore when using w/c of 0.4 and limiting the admixed chlorides to 0.06%. This value increases to 38 years when using a w/c of 0.35. Figure 8 shows the change in calculated service life values with increasing admixed chlorides for the same cases but using a 50% failure probability. This figure shows that not using the chloride distributions for a probabilistic estimation, can underestimate the effect of admixed chlorides significantly. This figure indicates a corrosion initiation time of 67 years even with 0.1% by weight of cement admixed chlorides for concrete in atmospheric zone 100 m (109 yards) from the shore at w/c 0.4 with a cover depth of 58 mm (2.3 in).

Figure 9 shows the effect of used failure probability on service life for the splash and atmospheric zones at w/c of 0.4 and cover depth of 58 mm (2.3 in.) The service life values were calculated for an admixed chloride content of 0.06% by weight of cement. As stated earlier, in this study the variability of admixed chlorides at the cover depth before and after the start of diffusion of external chlorides was assumed to be constant with coefficient of variation (COV) of 51.7%. This COV was applied at each time step to the chloride concentration at the cover depth to calculate the service life based on a required probability. Figure 9 shows the calculated service life values at different failure probabilities using three different COVs of 30% (short-dashed lines), 51.7% (solid lines), and 70% (long-dashed lines). To improve the legibility of the figure by limiting the maximum value of y-axis, the service life values for the atmospheric zone, 100 m (109 yards) or more from the shore, are shown only up to 30% failure probability. The figure shows that at w/c of 0.4 the estimated service life can vary between 3 and 33 years for the atmospheric zone, 50 m (54.7 yards) or more from the shore, when varying the probability of failure between 2.5% and 50%. However, the difference for the service life in the splash zone for the same conditions was only about 8 years. The figure also shows that the difference in COV values used for the distribution of chlorides do not affect the estimated service life values in the splash zone but have a bigger impact for the atmospheric zone. At 30% probability of failure, changing the COV from 0.3 to 0.7% shortened the estimated service life by 4 years (~ 18%) for the atmospheric zone, 50 m from the shore. Similar percent decrease of service life was observed for the atmospheric zone, 100 m (109 yards) from the shore. Since the variation in the distribution does not have an effect in the initiation of corrosion, when the mean chloride concentration is set equal to the mean critical chloride concentration, the estimated service life at 50% probability of failure is equal for all COV values. The effect of COV on the service life for the atmospheric zone, 100 m (109 yards) from the shore, and at a w/c of 0.35, was also 19% which translates to a difference in service life of 24 years between 0.3 and 0.7% COV values.

All service life values shown in earlier figures for the atmospheric zone at different distances were calculated using an average wind speed of 5 m/s (11.2 mph). Also, as discussed earlier, all service life values were calculated using the average monthly temperature values of a coastal location in Maine. Figure 10 shows the effect of using a higher wind speed of 7 m/s (15.7 mph) and higher temperatures matching the average monthly temperatures in the Keys area of Florida (high temperature). Solid lines show the service life values calculated at different failure probabilities at three distances in the atmospheric zone for a w/c of 0.4 and cover depth of 58 mm (2.3 in.) The dashed lines show the decrease in service life values with increased wind speed for the corresponding similar conditions. At 10% failure probability the difference in service life is 1, 2, and 3 years at 15, 50, and 100 m (16.4, 54.7, and 109 yard) distance, respectively, indicating that the effect of wind speed was not very important. However, the figure shows that the differences between the calculated service life values increase with increasing failure probabilities, e.g. when using a 30% failure probability, the service life value in atmospheric zone at 100 m (109 yard) distance may reduce by 30%.

The double red lines in Figure 10 show the service life values calculated using high monthly average temperature values and indicate that the effect of temperature is larger compared to the wind speed even at lower failure probabilities. At 10% failure probability, service life values in the atmospheric zone at all distances decrease by 50% or more due to increased temperature.

SUMMARY AND CONCLUSIONS

A well-established diffusion-based service life estimation method was combined with recently developed data-driven models on surface chloride concentration accumulation and critical chloride threshold distribution data to analyze the effect of design parameters such as w/c and cover depth in various coastal exposure zones. A key distinction of this method is its use of a probabilistic failure limit to define the end of service life instead of a deterministic approach Designers can apply the described methodology to assess the impact of design parameters based on the exposure zones of their structures and to establish admixed chloride limits according to required probabilistic service life criteria. However, it is important to note that the simulations presented in this study have not been experimentally validated. Important findings of the performed analysis using this methodology are:

- Cover depth and w/c have a much larger impact on service life than exposure zones. At the same cover depth and exposure zone, reduction of w/c from 0.5 to 0.4 can improve the service life by 70%
- Using a P_f of 10% instead of setting chloride concentration at the steel level equal to critical chloride threshold (P_f of 50%) can reduce the estimated service life by more than 50%. Changing the required failure probability limit from 2.5% to 50% can increase the estimated service life an order of magnitude.
- Analysis using a 10% P_f shows that admixed chlorides of 0.15% by weight of cement can initiate corrosion immediately even at low w/c values and atmospheric zones with large distances.
- When performing the described probabilistic analysis, varying the COV value between 30 and 70% for chlorides at a certain depth, can affect the service life by about 19%.
- The effect of varying wind speed from 5 to 7 m/s (11.2 to 1.7 mph) had a limited effect on service life but the effect increased with increased P_f values. The effect of temperature was relatively more important and could shorten service life values up to 50%

FIGURES

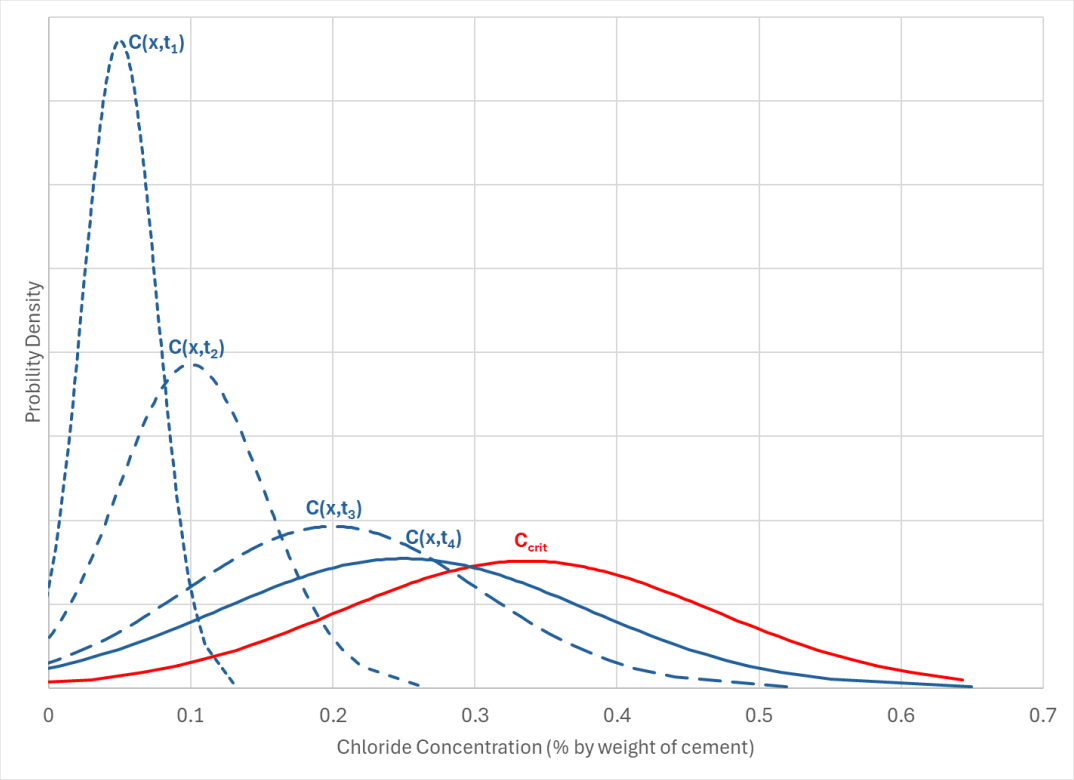

Figure 1 – Change and comparison of $C_{(x,\ t)}$ probability distributions with the C_{crit} distribution

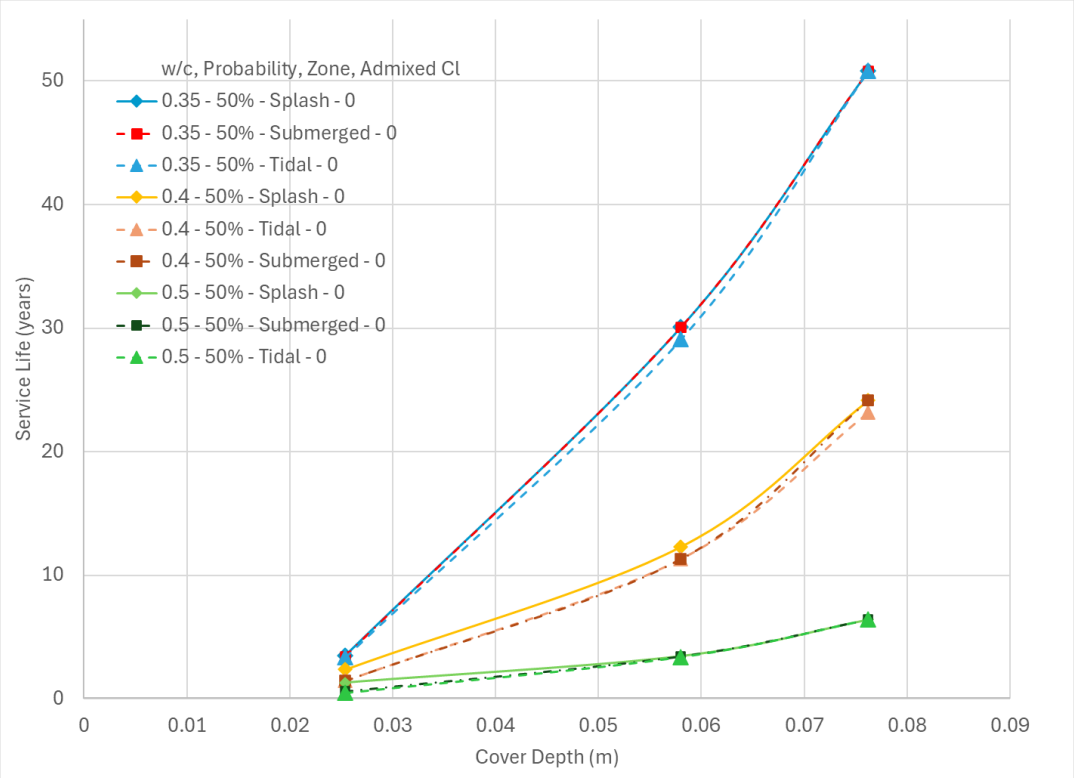

Figure 2 – Service Life values at 3 cover depths, exposure zones, and w/c's

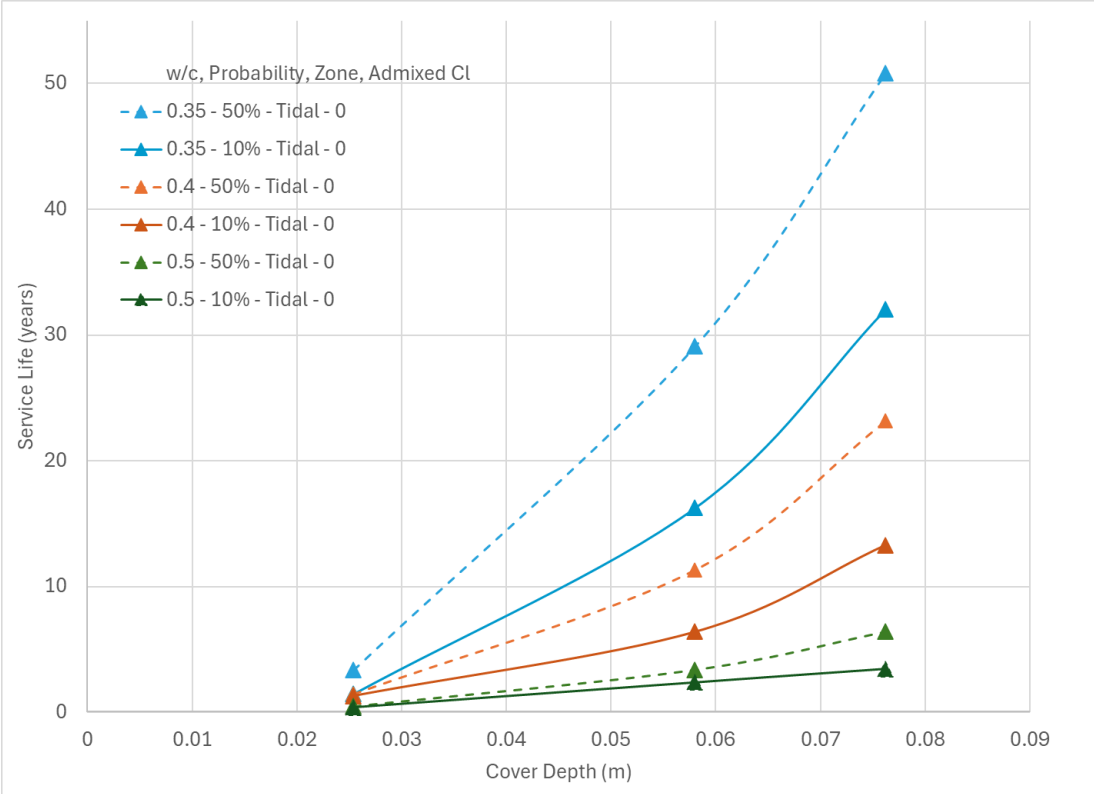

Figure 3 – Service Life values at the tidal zone for 10 and 50% P_f

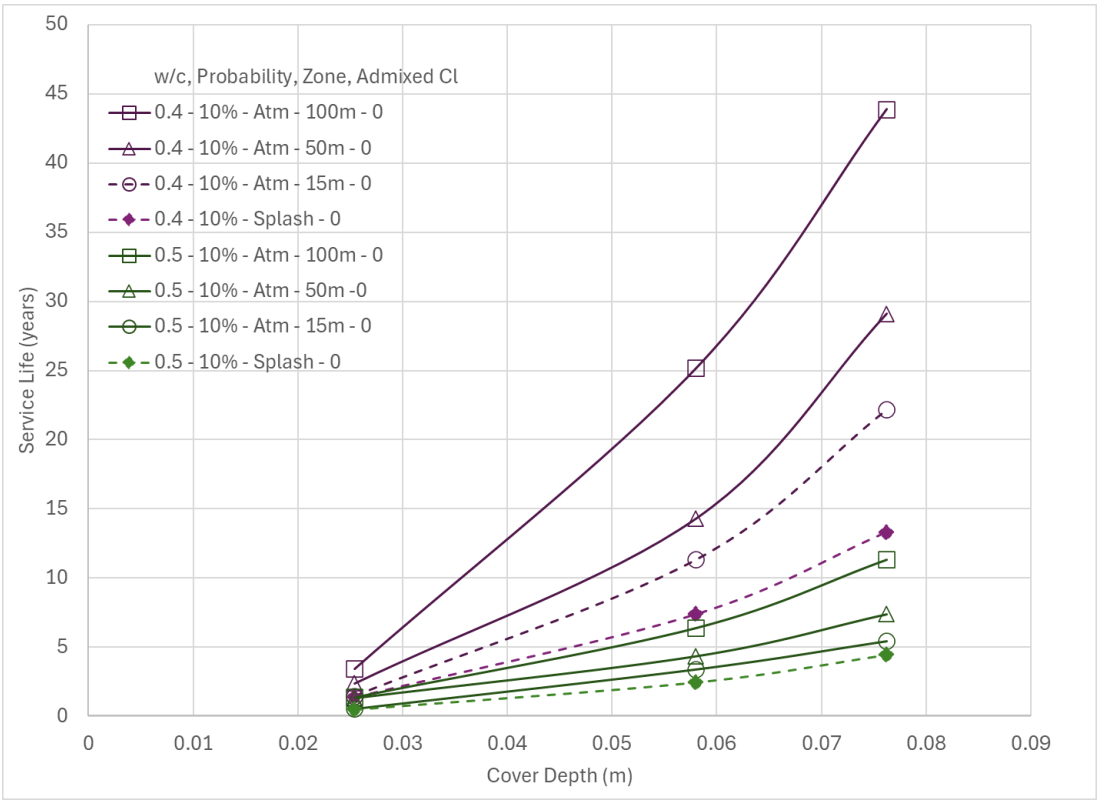

Figure 4 – Service Life values at the atmospheric zone at different w/c's and cover depths

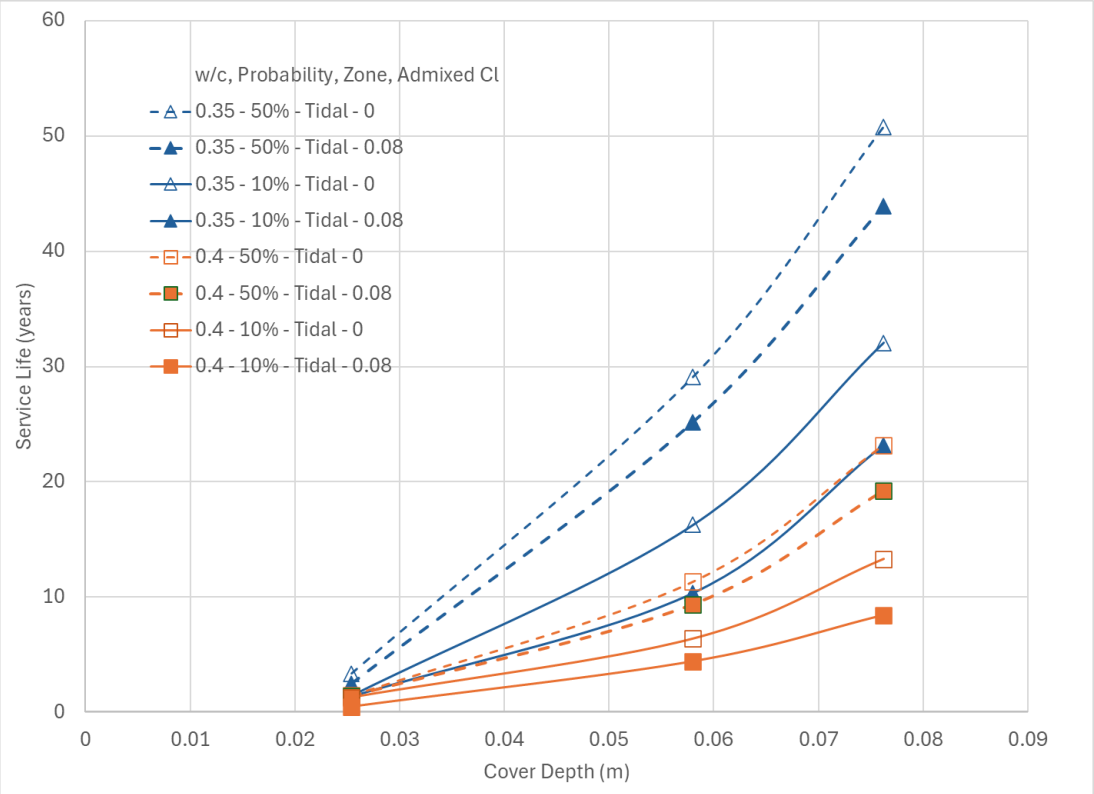

Figure 5 – Effect of 0.08% admixed chlorides in tidal zone

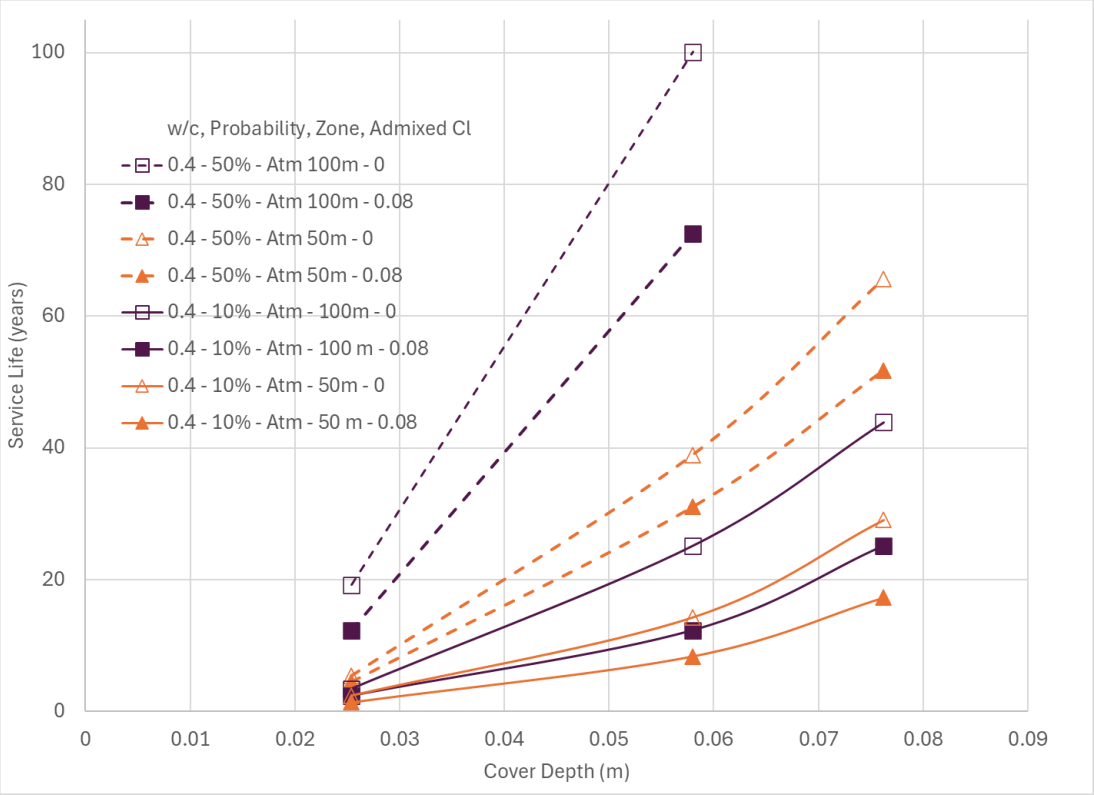

Figure 6 – Effect of 0.08% admixed chlorides in the atmospheric zone

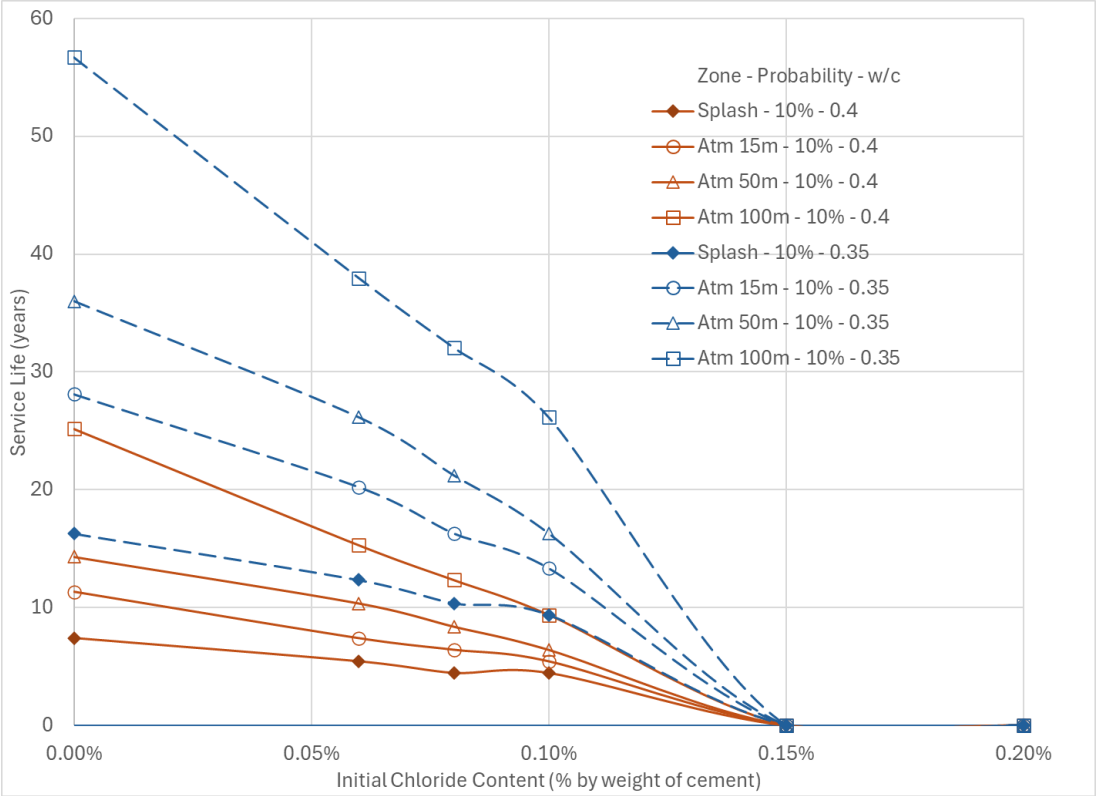

Figure 7 – The effect of increasing admixed chlorides using P_f of 10%

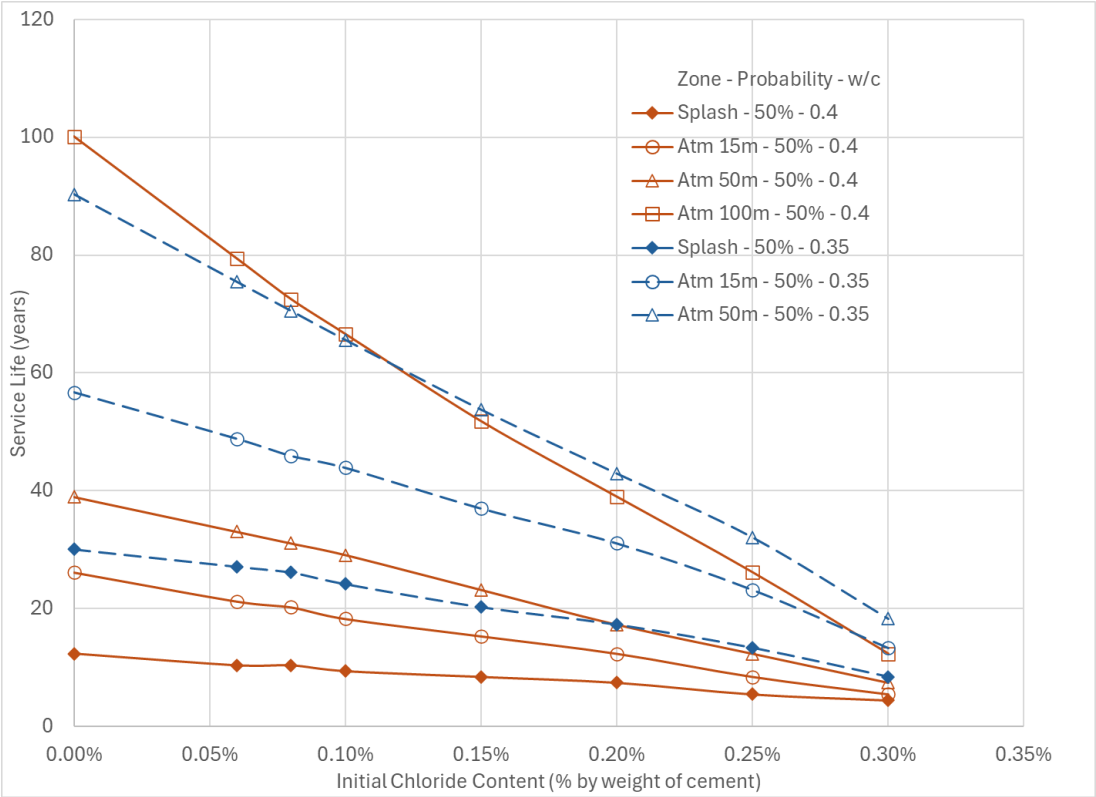

Figure 8 – The effect of increasing admixed chlorides using P_f of 50%

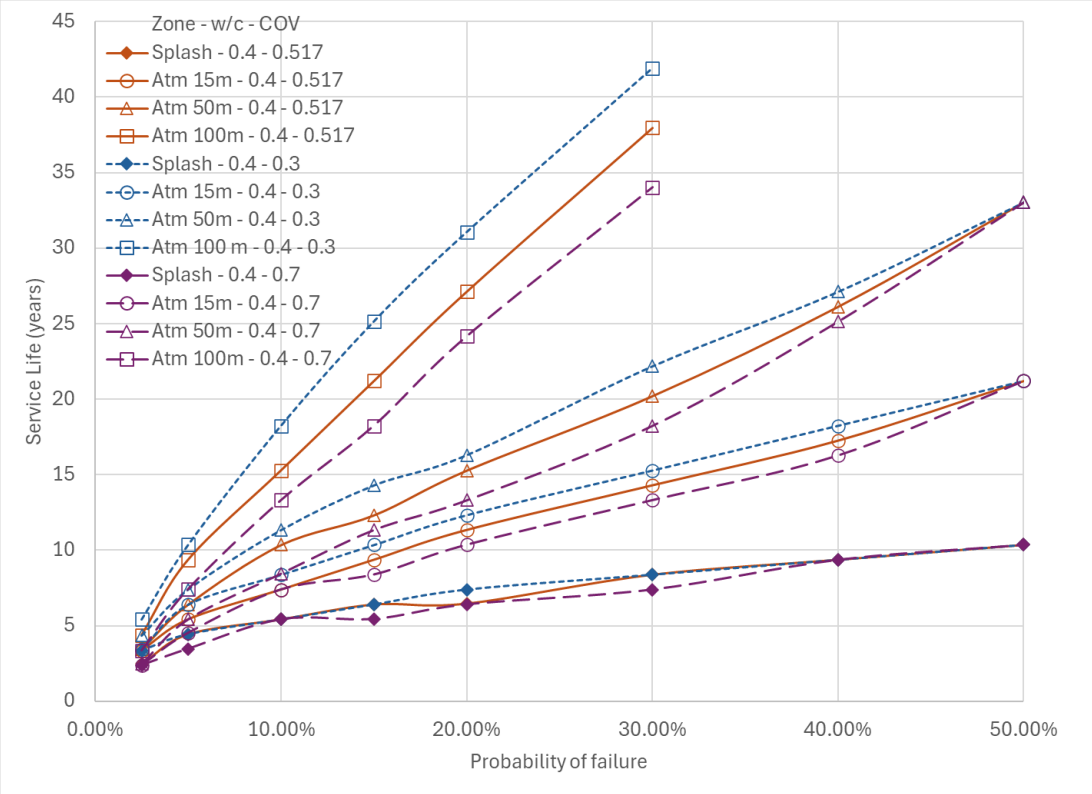

Figure 9 – Change in service life for different P_f values using different COVs

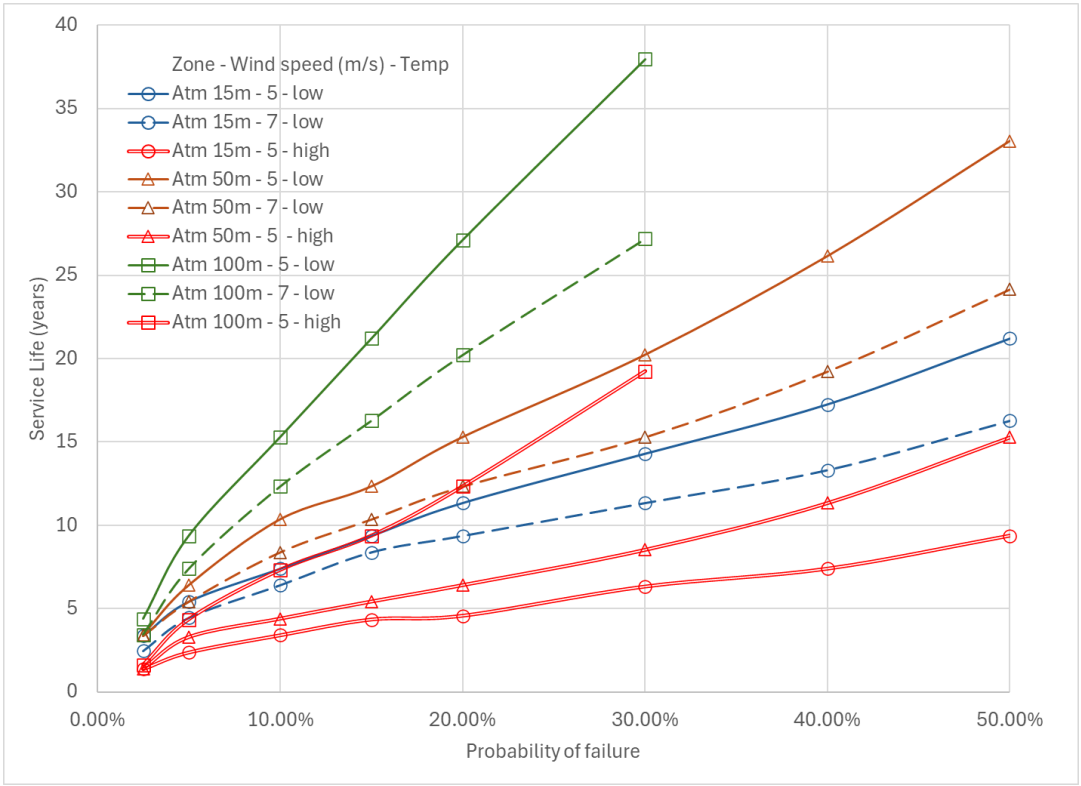

Figure 10 – The effect of wind speed and temperature on service life

REFERENCES

1. Elsener, B., *Macrocell corrosion of steel in concrete - implications for corrosion monitoring.* Cement and Concrete Composites, 2002. **24**(1): p. 65-72.
2. Broomfield, J.P., *Corrosion of Steel in Concrete: Understanding, Investigation, and Repair* 2006, London and New York: Spon Press.
3. Carvajal, A., R. Vera, F. Corvo, and A. Castañeda, *Diagnosis and rehabilitation of real reinforced concrete structures in coastal areas.* Corrosion engineering, science and technology, 2012. **47**(1): p. 70-77.
4. Montemor, M., A. Simoes, and M. Ferreira, *Chloride-induced corrosion on reinforcing steel: from the fundamentals to the monitoring techniques.* Cement and concrete composites, 2003. **25**(4-5): p. 491-502.
5. Pech-Canul, M.A. and P. Castro, *Corrosion measurements of steel reinforcement in concrete exposed to a tropical marine atmosphere.* Cement and Concrete Research, 2002. **32**(3): p. 491-498.
6. Marquez, L.E., *In South Florida and coastal areas worldwide, corrosion is a cry for help.* Materials Performance Magazine, 2022(April 2022).
7. Tepl, yacute, Bretislav, Vorechovsk, aacute, and Dita, *Reinforcement Corrosion: Limit States, Reliability and Modelling.* Journal of Advanced Concrete Technology, 2012. **10**(11): p. 353-362.
8. Munoz, A., C. Andrade, and A. Torres, *Corrosion products pressure needed to crack the concrete cover.* Advances in Construction Materials 2007, 2007: p. 359-370.
9. Liu, T. and R. Weyers, *Modeling the dynamic corrosion process in chloride contaminated concrete structures.* Cement and Concrete research, 1998. **28**(3): p. 365-379.
10. Yang, S., X. Xi, K. Li, and C.-Q. Li, *Numerical modeling of nonuniform corrosion-induced concrete crack width.* Journal of Structural Engineering, 2018. **144**(8): p. 04018120.
11. Collepardi, M., A. Marcialis, and R. Turriziani, *Penetration of chloride ions into cement pastes and concretes.* Journal of the American Ceramic Society, 1972. **55**(10): p. 534-535.
12. Chen, R., J. Liu, and S. Mu, *Chloride ion penetration resistance and microstructural modification of concrete with the addition of calcium stearate.* Construction and Building Materials, 2022. **321**: p. 126188.
13. Angst, U., B. Elsener, C.K. Larsen, and Ø. Vennesland, *Critical chloride content in reinforced concrete — A review.* Cement and Concrete Research, 2009. **39**(12): p. 1122-1138.
14. Trejo, D., N.P. Vaddey, and C. Halmen, *Standardizing test to quantify chloride threshold of steel in concrete.* ACI Materials Journal, 2021. **118**(1): p. 177-187.
15. Adil, G., C. Halmen, P. Vaddey, J. Pacheco, and D. Trejo, *Multi-Laboratory Validation Study of Critical Chloride Threshold Test Method.* ACI Materials Journal, 2022. **119**(6).
16. Isgor, B., C. Halmen, D. Trejo, and D. Tepke. *Recent Initiatives of ACI Committee 222 on Corrosion of Metals in Concrete*. Presented at *RILEM Spring Convention and Conference*. Springer. 2024
17. Ahmed, A.A. and D. Trejo, *Quantifying Conservativeness of Water-Soluble Chloride Testing.* ACI Materials Journal, 2023. **120**(2): p. 13-24.
18. Vaddey, N.P., M. Shakouri, and D. Trejo, *Predicting chloride testing outcome of different cementitious systems.* ACI Materials Journal, 2020. **117**(1): p. 139-151.
19. David, T. and V. Gokul Dev, *Chlorides in Concrete: Science-Based Exposure Classifications and Allowable Limits.* ACI Materials Journal, 2024. **121**(1).
20. Angst, U.M. and R. Polder, *Spatial variability of chloride in concrete within homogeneously exposed areas.* Cement and Concrete Research, 2014. **56**(Supplement C): p. 40-51.
21. Soive, A. and V. Baroghel-Bouny, *Influence of gravel distribution on the variability of chloride penetration front in saturated uncracked concrete.* Construction and Building Materials, 2012. **34**: p. 63-69.
22. Shakouri, M., D. Trejo, and P. Gardoni. *A risk-based model for determining allowable admixed chloride limits in concrete*. Presented at *International RILEM Conference on Materials, Systems and Structures in Civil Engineering: Conference segment on service life of cement-based materials and structures*. Lyngby Denmark. 2016
23. Shakouri, M., *Time-dependent concentration of chlorides at the concrete surface revisited.* Sustainable and Resilient Infrastructure, 2021. **8**: p. 1-18.
24. Ann, K.Y., J.H. Ahn, and J.S. Ryou, *The importance of chloride content at the concrete surface in assessing the time to corrosion of steel in concrete structures.* Construction and Building Materials, 2009. **23**(1): p. 239-245.
25. Guo, Z., R. Guo, and S. Lin, *Multi-factor fuzzy prediction model of concrete surface chloride concentration with trained samples expanded by random forest algorithm.* Marine Structures, 2022. **86**: p. 103311.
26. Liu, J., K. Tang, D. Pan, Z. Lei, W. Wang, and F. Xing, *Surface Chloride Concentration of Concrete under Shallow Immersion Conditions.* Materials (Basel), 2014. **7**(9): p. 6620-6631.

27. Yang, L., L. Wang, and B. Yu, *Time-varying behavior and its coupling effects with environmental conditions and cementitious material types on surface chloride concentration of marine concrete.* Construction and Building Materials, 2021. **303**: p. 124578.
28. Zhao, R., C. Li, and X. Guan, *Advances in Modeling Surface Chloride Concentrations in Concrete Serving in the Marine Environment: A Mini Review.* Buildings, 2024. **14**(6): p. 1879.
29. Ehlen, M.A. and A.N. Kojundic, *Life-365™ v2. 2.* Concrete international, 2014. **36**(5): p. 41-44.
30. Sakr, M.R., O. El-Mahdy, and K. El-Dash, *Effect of Different Factors on the Service Life of Concrete Structures in Chloride Environments: A Parametric Study–Part One.* International Journal of Advanced Engineering Research and Science, 2016. **3**(8): p. 40-48.
31. Park, J.-I., K.-M. Lee, S.-O. Kwon, S.-H. Bae, S.-H. Jung, and S.-W. Yoo, *Diffusion decay coefficient for chloride ions of concrete containing mineral admixtures.* Advances in Materials Science and Engineering, 2016. **2016**(1): p. 11.
32. Yuan, Y. and J. Jiang, *Prediction of temperature response in concrete in a natural climate environment.* Construction and Building Materials, 2011. **25**(8): p. 3159-3167.

Model for corrosion initiation and propagation based on the resistivity

Carmen Andrade

Synopsis: Concrete is an efficient material in terms of mechanical strength and functionality, but whose durability is one of present challenges that need particular attention to preserve the reinforcement absent of corrosion during the nominal service life. Present trends on modelling by performance make more complex the quality control testing and lengthens the characterization of new low carbon cement concretes. In present work is presented concrete resistivity as the single parameter able to characterize both corrosion periods through the corresponding mathematical expressions. Resistivity is a non-destructive test which could qualify concrete from its early ages. Based in the relation between diffusivity-corrosion current and resistivity, an integral model based in the resistivity measured at short term in the same specimens than mechanical strength (cured humid), is described. It is also analysed the analogies between the diffusivity and corrosion current and the influence of climate in the resistivity for future challenge of predicting the impact of climatic change.

Keywords: model, service-lie, corrosion, initiation, propagation, resistivity

ACI member **Carmen Andrade** is a Research Professor at the International Center of Numerical Methods in Engineering (CIMNE) in Madrid-Spain. She is Dr. in Industrial Chemistry and has been Research Professor at the Institute of Construction Sciences of the CSIC of Spain devoting his research to concrete durability and reinforcement corrosion. She is Doctor Honoris Causa by the University of Trondheim (Norway) and of Alicante (España). She has been President of several international organizations (UEAtc, RILEM, WFTAO, Liaison Committee and ALCONPAT International) and Rilem and fib Fellow. She has been General Director of Technological Policy of the Ministry of Education and Science and Advisor to the Secretary of State Universities in the Ministry of Science and Innovation, Spain. At present she is Honorary President of ALCONPAT Int. and her Director of International relations.

INTRODUCTION

The electrical resistivity of concrete was one property regarding concrete durability identified comparatively early with respect to the application of other electrochemical techniques, because studies are reported from the 1940-50's (1-2) related to the characterization of concrete as an electrical insulator to be used in train sleepers and with the non-destructive measurement of cement setting (3). The electrochemical techniques, (4-6), were starting to be applied, to corrosion of reinforcement studies, first only the polarization curves, from the 1960's and was not until the beginning of 1970's that the Polarization Resistance technique, R_p, was used to measure the instantaneous corrosion rate (7-8). The needed systematic measurement of the concrete ohmic drop affecting R_p measurements enabled the evidence that the concrete resistivity is a direct function of the corrosion rate, which in turn depends on the concrete porosity (pore structure and pore water chemistry) and its degree of water saturation (9-11). The interest on resistivity arises again in the decade of the 1990's when the relation between chloride diffusion and concrete resistivity was demonstrated (12-13). This relation between diffusivity and resistivity was shaded by the higher interest to explore the accelerated testing of chlorides by migration (14).

Concrete resistivity has numerous applications (15) in addition to that of the relation with the steel corrosion current, in particular it is important its relation to concrete microstructure (16) and the possibility to predict the reinforcement service life from its characterization (17). In present work is presented the updated knowledge with respect to this last possibility, emphasizing that the resistivity alone is not enough as it only represents the pore structure (porosity and tortuosity) (17,18), but not inform on the binding of chlorides with the hydrated cement phases, and its evolution with time (aging) or on the influence of the process of the chloride concentration. These aspects should be part of a model, if the resistivity is used more than as a simple durability Indicator.

CONCRETE RESISTIVITY FUNDAMENTALS

Concrete electrical resistance, R, is the relation between the voltage drop, V, and the current, I, induced by it.

$$R = \frac{V}{I} = \rho \frac{l}{A} \quad (1)$$

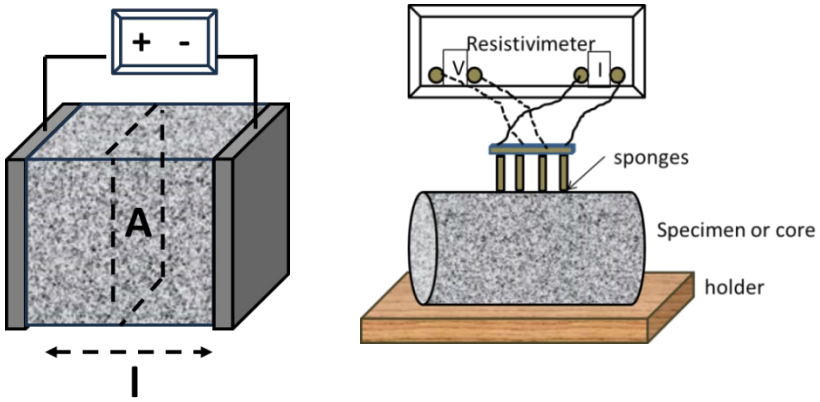

Figure 1: Left: Bulk method to measure resistivity. Right: four points or Wenner method. Concrete resistivity is an indication of the concrete porosity, tortuosity and and degree of water saturation.

This is Ohm's law where Resistance R is equal to the voltage drop (V) divided by the current (I) and if standardized to a regular geometry (a cube for example), enables to know the resistivity as indicated in the equation (l= the distance between electrodes and A is the cross-section area in figure 1).

The most common method of measurement of resistivity is the "direct" or "bulk" method (figure 1-left). Two electrodes as placed in two parallel faces of a concrete specimen or disc and a voltage is applied and the circulated current is measured. The other common method is that known as "four points or Wenner method" (19) shown right in the same figure. This last one value is calculated following equation (2) where the term "2πd" is the "geometrical factor" where d is the distance between electrodes and f_s is the "form factor" that takes into account the shape and size of the specimen (20):

$$\rho = 2 \cdot \pi \cdot d \cdot R \cdot f_s \quad (2)$$

Features of concrete resistivity

Evolution during setting and hardening

The resistivity is evolving during the hydration (3) because the pore solution does in composition and because the porosity (pore structure and water chemistry) is changing. At the mixing time the resistivity is very low as shown in figure 2-left. When setting there is produced an progressive increase of the resistivity which later evolves more slowly (figure 2-right). This increase with time obliges to suggest a reference time for its representative value and serves to monitor the "aging factor", aspects that will be addressed later.

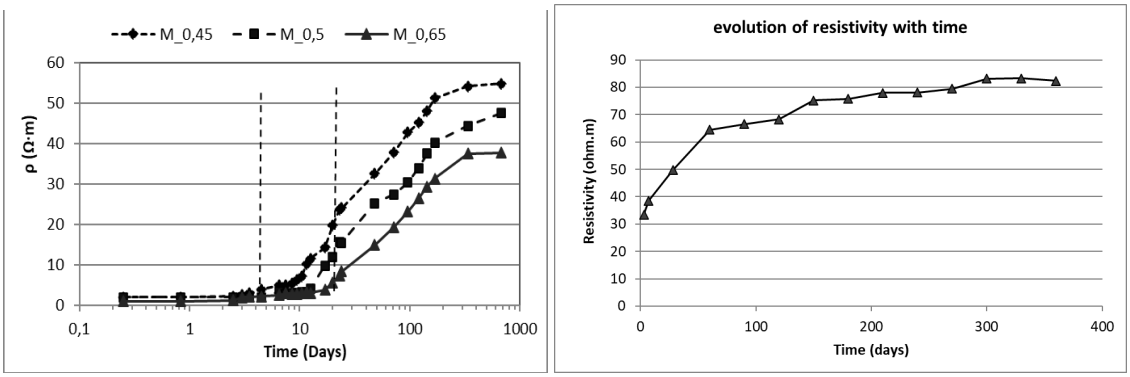

Figure 2: Left: Evolution of resistivity of mortar during cement setting with several w/c ratios (the vertical lines show the staring and end of setting. Right: example of evolution of concrete resistivity during hardening

Relation resistivity and mechanical strength

The mechanical strength increases with time as the resistivity as is illustrated in figure 3 because of the continuous refinement of the pore network due to the hydration. In this figure is shown their behaviour for numerous concretes. It indicates that the resistivity may be used to predict mechanical strength, but for establishing a precise equation of evolution it is recommended that the specimens are of the same cement type and cured in standarized conditions.

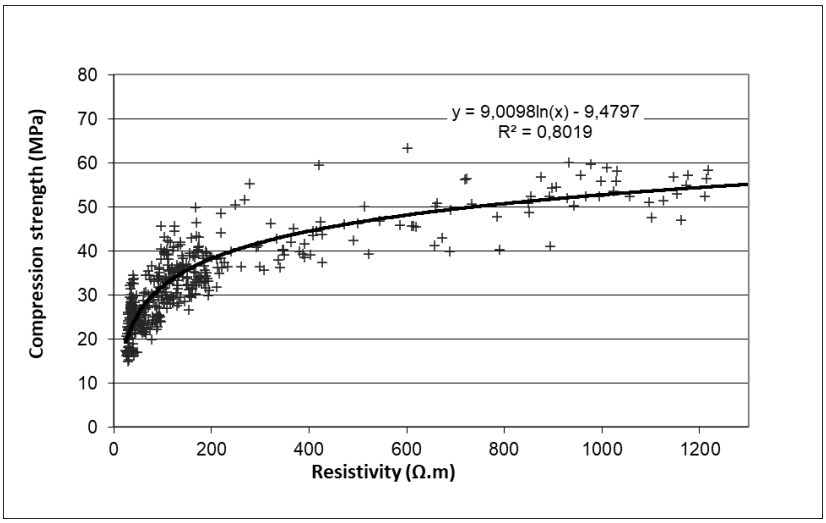

Figure 3: Relation of compressive strength of concretes at different ages and resistivity.

Relation of Resistivity with pore microstructure and water saturation. Formation factor

The resistivity value depends on the concrete porosity, tortuosity and its degree of saturation (9-11,17) and in consequence, on its pore size distribution. Concrete is a porous body in which the solid phases are non-conductive, but the conductive phase is the pore solution. Then, the resistivity/conductivity of the concrete will depend on the total pore volume, its pore size distribution and on the pore chemistry, in addition of the water saturation. As higher is the porosity, lower is the resistivity providing the concrete is water saturated..

This relation can be expressed through a modification of Archie's law (18), where the constant of Archie is substituted by ρ_0 that is the resistivity of the pore solution (value from 10 to 100 Ω.cm), W is the volumetric fraction of water and the exponent of the porosity in Archie's law is named as τ, the tortuosity factor,τ:

$$\rho = \rho_0 \cdot W^{-\tau} \quad (3)$$

This law was applied to rocks by Archie (18) and because of the difficulty to know the pore solution chemistry in the times of the original research, the term [$W^{-\tau}$] was named by Archie as "Formation factor" F, representing the impact in the variation of the resistivity for different pore shapes of both together, the porosity and its pore size distribution. If the F is used, the expression turns from having nonlinear relation between W and τ , to be linear this relation and therefore, errors may be introduced in the calculations. The F is only a simplified expression of the effect of the pore structure on the resistivity. The most accurate is to use the values of resistivity as such. and even to use the expression substituting the resistivity of the pore solution by that in saturated conditions. ρ_{sat}:

$$\rho = \rho_{sat} \cdot W^{-\tau} \quad (3')$$

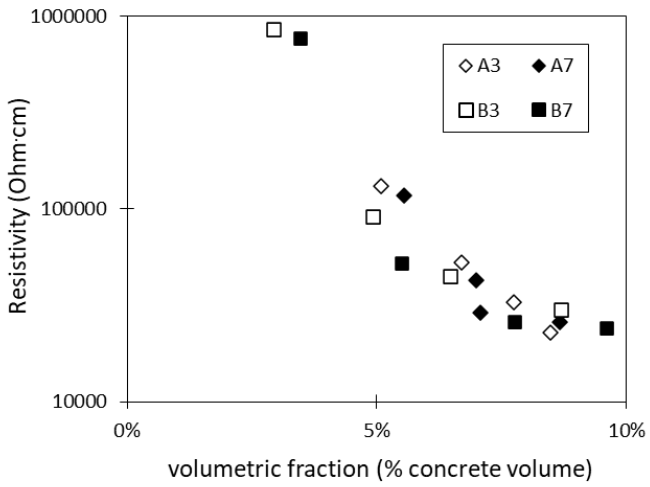

Figure 4: Relation between volumetric fractions of porosity saturated with water and resistivity of four different mixes. The value of τ of equation 3 is 2.52 (15).

An illustration of this empirical relation is given in figure 4 (16) where four concrete mixes have been conditioned to several relative humidities, and the resistivity was measured together with the weight. It indicates that below a RH of 65% the resistivity rises exponentially, while the RH is above 85-90% when the capillary pores are starting to be filled with evaporable water.

Influence of temperature in the Resistivity

The temperature has an important effect on resistivity, because it increases when temperature decreases and viceversa. The impact of temperature can be standarized using Arrhenius law, however it has been detected (22) that the Activation energy depends on the type of cement and on the degree of saturation and a single value has not still been quantified with precision. Furthermore, even knwong the activation energy of the particular concrete, for practical applications the resistivity should not be standardized by Arrhenius' law, because what is influencing the process is the actual value at the actual temperature. On the other hand, an increase in temperature usually means evaporation of pore water, which in turn means an increase of resistivity. That is, the final effect of temperature in the diffusion or corrosion rate is counter-influencing, as an increase in temperature may produce a slowing of the Diffusion coefficient and the corrosion rate due to the drying. Therefore, the incorporation of temperature effects on models cannot be generalized through Arrhenius law as independently on the moisture content.

RELATION BETWEEN RESISTIVITY, DIFFUSIVITY AND CORROSION RATE

Resistivity-Diffusivity

The relation was established by Einstein (see equation 4) in solution and was Garboczi (12) one of the first applying it for the concrete:

$$D_e = F \cdot \sigma = \frac{F}{\rho} \tag{4}$$

where D_e = effective diffusion coefficient, F = a factor, which depends on the external ionic concentration, ρ_e= resistivity of the solution,σ = conductivity (inverse of resistivity). A value of F of $20x10^{-5}$ can be used for external chloride concentrations of 0.5 to 1 M (13).

Resistivity- Corrosion Rate

The relation of the resistivity and the corrosion rate is related to the degree of water saturation as can be deduced from figure 5 in a graph corrosion current I_{corr}-resistivity (16).

$$I_{corr}(\frac{\mu A}{cm2}) = \frac{K}{\rho\ (K\Omega \cdot cm)} \quad (5)$$

The K is a constant that has been determined empirically to be around 26 mV. If the I_{corr} is given as V_{vorr} in mm/year this expression (5) results in expression (6):

$$V_{corr} = \frac{0.0116 \cdot 26000}{\rho} = \frac{301.6}{\rho} \quad (6)$$

Where V_{corr} = (mm/year), 0.0116 = conversion factor between V_{corr} and I_{corr} and ρ = concrete resistivity (ohm·cm).

This relation has opened the door to derive the corrosion rate from resistivity providing the corrosion is in active state, because when the steel is passive the resistivity cannot be used to forecast corrosion rates.

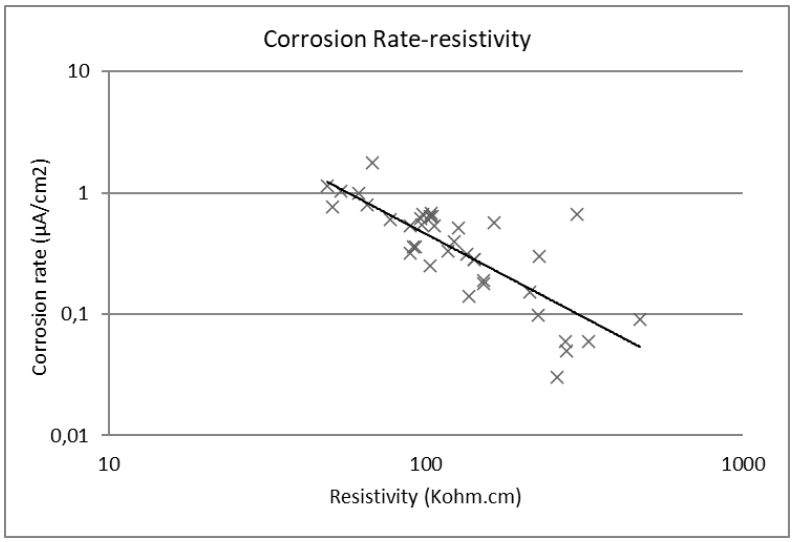

Figure 5: Example of the Graph I_{corr}- ρ_{ef} which indicates the relation between the I_{corr} and the resistivity that is a consequence of the degree of concrete saturation.

Resistivity- Coulombs in the RCPT

It has to be added on the relations of resistivity with chloride transport, that also there is a relation with the Coulombs (Q) recorded in the Rapid Chloride Permeability test, as published years ago in collaboration with D. Whiting (23). In that paper it was shown that the RCPT is a resistivity test and that the relation for the particular geometry of the equipment standardized now by ASTM-1202 (24) is approximately (see Table 1):

$$\rho[\Omega \cdot m] = \frac{200000}{Q} \quad (7)$$

SERVICE LIFE MODEL BASED IN THE RESISTIVITY MEASUREMENTS

The resistivity as mentioned before can be related to the transport though the pore network, but it does neither take into account the reactive transport nor the evolution with time of the concrete, or the external aggressivity. Then, the need to have an expression with the time explicit and factors were proposed to account for these

effects (17). The first was to have an expression where resistivity is related to time life and the cover depth. The needed resistivity cannot be the same for 50 or 100 years life or with different cover depths.This will be explained next.

The complementary factors were:

- Ageing exponent: The evolution with time of the resistivity.
- Reaction factor: to account for the bound chlorides with the hydrated cement phases because the ρ is only proportional to the effective diffusion coefficient in the pore solution,
- Exposure factor: to consider the chloride concentration and the degree of saturation.

If the value of resistivity is used without these complementary factors, the prediction is less precise than when complemented with them.

Time explicit relation for the initiation period and complementary factors

The first is to relate the value with the time life designed and with the cover depth. For that the resistivity has been introduced in a "square root law" enabling the relation between time and the resistivity. Thus, if using the standard square root law:

$$x = V_{CO2,Cl} \cdot \sqrt{t} = \sqrt{\mathrm{D} \cdot t} \quad (8)$$

where x= depth of carbonation or chloride threshold penetration [cm], V= velocity of the aggressive front [cm/year$^{0.5}$], D is the diffusion coefficient [cm^2/s] and t= time life [year]. The model based in the resistivity (17) was proposed by substituting the value of D by expression (7) which gives the following where F_{env} is now the "Environmental factor" which would take into account the exposure aggressivity and ρ_{ef} is the resistivity after wet curing for 28 days:

$$x = \sqrt{\frac{F_{env}}{\rho_{ef}} \cdot t_i} \quad (9)$$

where:

- x= penetration depth of the aggressive front (chlorides or carbonation) [cm]
- t_i= initiation period [year]
- ρ_{ef} = effective resistivity (at 28 days of wet curing) [ohm.cm]
- F_{env} = environmental factor depending on exposure class [cm^3·ohm/year]

Based on this relation, a service life model considering the initiation period has been developed (17). In equation (10) is presented using the time of initiation as the independent variable and c= cover depth [cm]:

$$t_l = \frac{c^2 \cdot \rho_{ef}}{F_{env}} \quad (10)$$

Knowing the value of the resistivity in the same specimen than that used for mechanical strength at 28 days, this model enables the calculation of the time to corrosion and the corrosion propagation period, but without taking into account the chloride binding and the aging factor. Both have to be incorporated into the expression, but first it will be explained the environmental factor.

Time explicit model for the propagation period.

The propagation period has been modelled based in the following time explicit expression where P_{corr} [μm] is the corrosion penetration after the time "t" [years] and I_{corr} is the corrosion rate [μA/cm^2]:

$$P_{corr} = I_{corr} \cdot 11.6 \cdot \mathrm{t} \quad (11)$$

In turn, as given in equation (5) the corrosion rate is a function of the resistivity and then, the expression can be written as:

$$P_{corr} = \frac{26}{\rho_{ef}} \cdot \mathrm{t} \tag{12}$$

Additional terms are necessary to take into account the degree of saturation, the pH (carbonation) and the chloride content. The most complete expression would be:

$$P_{corr} = \frac{26}{\rho_{ef}} \cdot S_w \cdot f(pH) \cdot f[Cl] \cdot \mathrm{t} \tag{13}$$

where S_w= saturation degree, f(pH) is a function to relate pH to the corrosion rate and f[Cl] is a function of the chloride concentration.

COMPLEMENTARY FACTORS IN THE RESISTIVITY MODEL

The complementary factors needed in expression (10) and (13) are:

Initiation

- ***F_{env}*** has been named "**environmental factor**". It depends on chloride concentration and in the case of carbonation, on the concrete moisture content (13,17).
- **r_b "reaction factor"** (17, 25) which multiplies the resistivity to account for the "retarder" effect of chloride binding during the penetration of chlorides. It can also be applied to the case of carbonation. This is due to carbonation progresses when the concrete is partially saturated. That is, as higher is the porosity (pore structure) or the empty pores due to dry conditions, higher the carbonation depth will be but a minimum certain moisture level is necessary for the carbonation reaction to proceed.
- Finally, an "**aging factor"** q (17, 26) which accounts for the evolution with time of the porous microstructure.
- **Degree of saturation**, **S_w**: it should be applied to account for the unsaturated periods

Propagation

- **Saturation degree** also critical in the propagation of corrosion.
- **f(pH)** to indicate that at high pH values corrosion is not proceeding whatever is the value of the resistivity
- **f[Cl]** A function of the chloride concentration indicating that at values below the threshold there will not be active corrosion

The explanation and values of these factors is presented below, except the functions of the pH and Cl that are not yet developed enough.

Environmental factor F_{env}

The environmental factors F_{Cl} and F_{CO2} depend on the exposure conditions (17). In the expression (9) and (10) was explained that it comes from the dependence between the diffusion coefficient and the chloride concentration in the electrolyte. Table 2 presents values that were calculated by inverse analysis of test results obtained from real structures.

Reaction factor "r_{Cl}"

The reaction factors r_{Cl} and r_{CO2} (17, 25) depends on the type and amount of cement and therefore on the reaction of the chlorides with the hydrated cement phases. It can be introduced in Equation (4) as follows:

$$D_{CO2} = \frac{F_{Cl,CO2}}{\rho_{ef} \cdot r_{Cl,CO2}} \tag{14}$$

The values of the reaction factor can be calculated either by direct measurement on the same specimen of the resistivity and the apparent diffusion coefficient, or by measuring both diffusion coefficients, effective (from steady-state tests) and apparent (from non-steady-state tests), in a multiregime test (25). Table 3 presents examples of r_{Cl} values that were calculated based on test results obtained by comparing steady and non-steady diffusion coefficients.

Aging Factor q

It accounts for the refinement of the concrete pore system because of hydration and reaction with chlorides or carbon dioxide, that aims into an increase of resistivity with time (17, 26) (figures 2 and 3). It can be calculated through the expression:

$$\rho_t = \rho_0 \left(\frac{t}{t_0} \right)^q \tag{15}$$

where:

ρ_t = resistivity at any age t

ρ_0 = resistivity at the age of the first measurement t_0

Values of *q* found for different cement types are given in table 4. The relation between *q a*nd the aging factor *n* of the chloride diffusion coefficient gives the expression (26):

$$q = 0.8\, n \tag{16}$$

Saturation degree (S_w) or volumetric fraction of water (W_s)

Its quantification is a future task because, in spite of the critical influence of the moisture content in the durability and the numerous literature on laboratory tests, its measurement on site has been seldom made and it changes with not only the external climate, but also with the concrete pore size distribution. However average values can be assumed, for example in continental weather with average annual temperature of 15ºC and RH of 50% with around 400 l/m^2 of rain, the S_w may vary from 10% protected from rain conditions to 55% in concrete exposed to rain.

FULL EXPRESSION OF THE MODEL

By the incorporation of all the complementary factors mentioned and considering the initiation and the propagation periods, the expression of a model based on the resistivity (equation (18)) results:

$$t_l = t_i + t_p = \frac{x_i^2}{V_{CO_2,Cl}} + \frac{P_{corr}}{V_{corr}} \tag{17}$$

Substituting all the factors explained before in it:

$$t_l = \frac{x^2 \cdot \rho_{ef} \left(\frac{t}{t_0} \right)^q}{F_{Cl,CO_2}} \cdot r_{Cl,CO2} \cdot S_w + \frac{P_{corr} \cdot \left(\rho_{ef} \cdot \left(\frac{t}{t_0} \right)^q \cdot S_w^{-\tau} \right)}{K \cdot 0.0116} \tag{18}$$

Example of application

For the initiation period the application by way of an example can be made by assuming a concrete with a cover depth of 4 cm made with cement type I with silica fume (reaction factor = 1.5 and aging factor = 0,22) to be placed in exposure class XS3 (tidal and splash conditions). Considering a service life of 100 years, the values of the reaction, as well as the environmental and aging factors are presented in Table 5. The calculations indicate that the resistivity needed at 28 days of age, measured in saturated conditions, is 215 Ω m.

$$4 = \sqrt{\frac{25000}{\rho_0 (\frac{100}{0.0767})^{0.22} \cdot 1.5}} \cdot 100 \; \{ \; \rho_0(\Omega \cdot cm) = 21497 \rightarrow \boxed{\rho_0(\Omega \cdot m) = 215}$$

With this resistivity the length of the propagation period following values in Table 6 is:

$$t_l = \frac{0.01 \cdot \left(21.5 \cdot \left(\frac{100}{0.0767} \right)^{0.22} \cdot 1 \right)}{26 \cdot 0.00116} = 34.54 \text{ years}$$

This propagation period may be included in the 100 years or considered apart as an additional safe time until cracking is produced.

PRODUCTION OF CONCRETE FOR A SPECIFIED APPARENT RESISTIVITY

Once known the resistivity which is needed to reach a nominal service life, it remains to describe how the concrete producer can design a mix to fulfil the service life specification. This can be done (27), in a simplified manner, by considering the modification of Archie's law linking resistivity and porosity:

$$\rho_{2_{8d}} = \rho_o \cdot \varepsilon^{-\tau} \tag{19}$$

where ρ_{28d} is the resistivity of concrete under saturated condition at 28 days, ρ_0 is the resistivity of the pore solution that can be taken an average of 50 Ω·cm and τ is the tortuosity coefficient, which is estimated by fit to the experimental data, and ε is the total porosity.

The coefficient τ depends on the concrete composition which is identified to the tortuosity and could be determined from type or family of cement type by means of measuring the porosity and the resistivity. The values found in present research are, for type I cement τ= 1.9, for type II-AV τ= 2.3 and for type II AP τ= 1.6.

From the specified resistivity the paste porosity can be obtained through Power's relation on capillary porosity and w/c ratio, whose application to cements with mineral additions is not fully precise but that may serve as an approximation:

$$\varepsilon_p(\%volumen) \approx \frac{\left(w/c\right) - 0{,}36\alpha}{\left(w/c\right) + 0{,}32} \times 100 \tag{20}$$

This would give the capillary porosity of the cement paste. To calculate the porosity of the concrete it can be obtained by multiplying it by the percentage in volume of paste (γ) in the concrete.

$$\varepsilon = \varepsilon_p \cdot \gamma \tag{21}$$

It is feasible to prepare a mix with the needed effective resistivity at 28 days, providing the consideration of the type of cement and its retarder factor. The concrete producer should verify by testing the reaching of the specified resistivity, while the cement producer should give the retarder factor of his cements.

So, the following concrete design methodology model is proposed to achieve the prescribed value ρ_{28d}:

1. Select a type of cement. It fixes the values of reaction factor (r) and tortuosity (τ).
2. Select a w/c ratio and calculate capillary porosity of the paste following Powers' model.
3. Then calculate the expected resistivity of the concrete through $\rho = \rho_o \cdot \left(\varepsilon_p \cdot \gamma\right)^{-\tau}$.

FINAL COMMENTS

Concrete is a very complex material, but which is fabricated onsite by relatively simple practices. Being a complex material evolving with time, sophisticated models can model it, but to be practical also simple ones should be applied which could help to improve its quality and durability. The electrical resistivity, being a non-destructive method simplifies the control of the durability very much. On the other hand, it enables multiple applications in concrete technology and the quantification of the expected life. Its main advantage is that the measurement is non-destructive, and the concrete in the structure can be monitored with time.

In present paper is shown the fundamental relations of resistivity with diffusivity and with the reinforcement corrosion rate. Resistivity is the parameter enabling to link microstructure with the macro-performance. Also, the model for service life prediction is based on Einstein law relating conductivity with the diffusion coefficient, but also the relation between resistivity and corrosion rate. Making certain assumptions this basic law can be applied to the advance of carbonation front or chloride threshold, and to the representation of steel corrosion propagation and then, enabling the calculation of the cover thickness.

The resistivity can also be used as an "Indicator" of the service life by ranking the limiting values as made with the coulombs, but in this case, the limiting values should be related to the time life and to the cover depth.

ACKNOWLEDGMENT

The author would like to recognize the contributions to the subject of reinforcement corrosion by Carolyn Hansson. The author met her when she worked for FORCE Institute in Copenhagen with the occasion of the first Workshop on Corrosion of reinforcement organized by H. Arup in 1981. In the attached historical photo Carolyn is in the first row in the left and the author is just behind in the second row. Later we met with the occasion of congresses and committees. Her interest for understanding the basic mechanisms was always remarkable.

Participants in the workshop entitled 'Corrosion of steel in concrete' organized by Hans Arup at Copenhagen in 1981. In the *first row from right to left*: XX, K. Tuutti, XX, J.A. Gonzalez, Wilkins, C. Locke, C. Hansson, *second row*: O. Vennesland, O. Gjorv, C. Page, R. Bakker, J. Dawson, K. Byfors, P. Schiessl, XX, XX, G. John, C. Andrade, *third row*: in the center behing K. Byfors H. Aru, the other could not be identified.

REFERENCES

1. Hammond E., Robson Td., 1955, The Engineer January, pp78-80 and 114.115.
2. Monfore G. E., 1968, The electrical resistivity of concrete. Journal PCA, Applied Research Section. May pp. 35
3. Calleja J. 1953, Determination of Setting and Hardening Time of High-Alumina Cements by Electrical Resistance Techniques. Journal of ACI, vol 50 issue 11 pp249
4. Gjorv O. E., Vennesland O., & El-Busaidy A. H.,1987, Diffusion of dissolved oxygen through concrete. Mater. Performance *25*(12) pp 39-44
5. Page C.L., Treadaway K.W.J., 1982, Aspects of the electrochemistry of steel in concrete. Nature 297 No. 5862, 109-115
6. Gouda V. K., Monfore, G. E., 1965, A rapid method for studying corrosion inhibition of steel in concrete. Journal of PCA, vol 7 no.3, Sep. pp. 24.
7. Andrade, C. and Gónzalez, J.A., 1978, Quantitative measurements of corrosion rate of reinforcing steels embedded in concrete using polarization resistance measurements. Werkstoffe und Korrosion 29, pp. 515.
8. González J.A., Algaba S., Andrade C., 1980, Corrosion of reinforcing bars in carbonated concrete. British Corrosion Journal, 3, pp.135-139.
9. Andrade C., Fullea J., Alonso C., 2000, The use of the graph corrosion rate-resistivity in the measurement of the corrosion current- Proceedings of the International Workshop on "Measurement and interpretation of the on-site corrosion rate-. MESINA- RILEM Proc. No. 18. Ed. C. Andrade, C. Alonso, J. Fullea, J. Polimon and J. Rodriguez. Rilem Publications S.A.R.L. pp. 157-166.
10. Page, C.L., Lambert, P., Vassie, P.R.W., 1991, Investigations of reinforcement corrosion, 2: Electrochemical monitoring of steel in chloride-contaminated concrete. Materials & Structures, 24, pp. 351-358.
11. McCarter, W. J., and Garvin, S., 1989, Dependence of Electrical Impedance of Cement-Based Materials on their Moisture Condition. J. Phys. D: Appl. Phys., Vol. 22, pp. 1773 – 6.
12. Garboczi E.J. 1990. Permeability, diffusivity, and microstructural parameters: A critical review. Cement and Concrete Research, 20, (4), 591-601.
13. Andrade C., 1993, Calculation of chloride diffusion coefficients in concrete from ionic migration measurements. Cement and Concrete Res., 23, pp. 724-742.
14. Tang, L., 1996, Electrically accelerated methods for determining chloride diffusivity in concrete—current development. Magazine of concrete research, 48(176), 173-179.
15. Andrade. C., Alonso C., Goñi S., 1993, Possibilities for electrical resistivity to universally characterize mass transport processes in Concrete. Proceedings International Conference "Concrete 2000. Economic and durable construction through excellence". Dundee, UK, Sep pp 1639-1653. Dhir R.K. and jones R. Editors. University of Dundee Pub.
16. Andrade C., Bolzoni F., Fullea J., 2011, Analysis of the relation between water and resistivity isotherms in concrete. Materials and Corrosion, 62, no.2, pp. 130-138.
17. Andrade, C., 2004, Calculation of initiation and propagation periods of service-life of reinforcements by using the electrical resistivity. International Symposium on Advances in Concrete through Science and Eng., RILEM Symposium, March, pp. 22-24, Evanston (Illinois, USA).
18. Archie, G.E., 1942, "The electrical resistivity log as an aid in determining some reservoir characteristics" AIME Trans. 146, 54.
19. Wenner, F., 1915, A method of measuring earth resistivity. Bureau of Standards, Bull. 12((4) 258): p. 478-496.
20. EN 12398-19 Testing of hardened concrete. Determination of electrical resistivity. - Part 19: Determination of resistivity
21. Morris W., Moreno E.I., Sagüés A.A., 1996, Practical evaluation of resistivity of concrete in test cylinders using a Wenner array probe, Cement and Concrete Research, 26, pp. 1779-1787.
22. Andrade C., Zuloaga P., Martinez I., Castillo A., Briz S., 2011, Effect of temperature on the corrosion parameters and apparent activation energy measured by embedded sensors in a pilot container in "El Cabril" repository. Corrosion Engineering, Science and Technology. Vol 46 No 2, pp 182-189.

23. Andrade C. Whiting D., 1995, Comparison of AASHTO T-277 (Electrical) and AASHTO T-257 (90d ponding) results. Proceedings 1st RILEM workshop on Chloride Penetration into Concrete 15-18 october, St Rémy lès Chevreuse, France
24. ASTM C1202-22e1 -Standard Test Method for Electrical Indication of Concrete's Ability to Resist Chloride Ion Penetration
25. Andrade, C., d'Andrea R., and Rebolledo N., 2014, Chloride ion penetration in concrete: The reaction factor in the electrical resistivity model, Cement and Concrete Composites, **47**, pp. 41-46.
26. Andrade C., Castellote M., D'Andrea R., 2011, Measurement of ageing effect of chloride diffusion coefficients in cementitious matrices. Journal of Nuclear Materials, 412, pp. 209-216.
27. Andrade C., d`Andréa R**.,** 2010, Concrete mix design based on the electrical resistivity. 2nd International Conference on Sustainable Construction Materials and Technologies. Ancona- Italy June. Ed. Coventry University UK.

TABLES

Table 1: Equivalence between resistivity and Coulombs in the test now ASTM 1202 calculated in (24)

Coulombs (A·sg)	**ρ (Ω·cm)**	**D_{ef} (cm^2/sg)**
4000	5295	5.52 ·10-8
2000	10590	2.75 ·10-8
1000	21179	1.38 ·10-8
100	211792	0.138 ·10-8

Table 2: Values of environmental factors, k_{Cl} and k_{CO2}, following the exposure classification of EN206

Exposure class	**F ($cm^3\Omega$/year)**
X0,XC1,XC2	200
XC3 moderate humidity	1000
XC4 cycles wet and dry	3000
XS1 (d > 500 m distance to the coast line)	5000
XS1 (d < 500 m distance to the coast line)	10000
XS2 submerged	17000
XS3 tidal	25000

Table 3: Examples of values of the reaction factor of chlorides, r_{Cl}, for 3 types of cement

Cement	r_{Cl}
CEM I	1.9
CEM I + silica fume	1.5
CEM IIA (with pozzolan and fly ash, in ≤ 20%)	3

Table 4: Values of the ageing factor

Cement	*q*	Standard Deviation
I	0.22	0.01
II/A -P	0.37	0.06
II/A-V	0.57	0.08

Table 5: Input data for a calculation of the concrete resistivity

Cement type I with silica fume	r_{Cl} = 1,85
Exposure class (XS3)	F ($cm^3\Omega$/year) = 25000
Service life	t (years) = 100
Cover depth	X_{Cl} (cm) = 4
Ageing factor during 10 years	q = 0.22

Table 6: Input data for the propagation period

Limit of Diameter loss, P_{corr}	100 μm = 0.01 cm
ρ_{ef} at 28 days	21.5 Kohm.cm
q applied during 100 years	0.22
S_w in saturated conditions	1